Programa de doctorado en Química Teórica y Modelización Computacional

Enlace químico en Topología Química Cuántica: enlaces de hidrógeno y otros

José Manuel Guevara Vela

Mayo, 2019

Departamento de Química Física y Analítica
Grupo de Química Cuántica

Universidad de Oviedo
Universidá d'Uviéu
University of Oviedo

Universidad de Oviedo
Universidá d'Uviéu
University of Oviedo

RESUMEN DEL CONTENIDO DE TESIS DOCTORAL

1.- Título de la Tesis	
Español/Otro Idioma: Enlace químico en Topología Química Cuántica: enlaces de hidrógeno y otros	Inglés: Chemical bonding in quantum chemical topology: hydrogen bond and more

2.- Autor	
Nombre: José Manuel Guevara Vela	DNI/Pasaporte/NIE:
Programa de Doctorado: Doctorado en Química Teórica y Modelización Computacional	
Órgano responsable: Centro Internacional de Posgrado	

F O R - M A T - V O A - 0 1 0 1 (R e g . 2 0 1 8)

RESUMEN (en español)

El crecimiento inusitado de la química teórica en general y de la química computacional ha traído un problema que ya quisieran haber tenido nuestros predecesores: contamos con demasiados datos. La función de onda resultante de un cálculo es un objeto que contiene toda la información de un sistema. Ante esta situación, surgieron diversos métodos de análisis que son, en gran medida, esfuerzos por recuperar conceptos propios de la química, como las cargas atómicas, de los resultados computacionales. La topología químico cuántica (QCT) es un conjunto de metodologías de análisis que se dedica a analizar observables invariantes ante el cambio de orbitales, típicamente escalares construidos a partir de matrices de densidad reducidas en el espacio real y que funciona como un puente entre los conceptos químicos tradicionales (aquellos derivados de la teoría de enlace de Lewis) y los resultados de los métodos mecánico-cuánticos desarrollados a partir de primeros principios. Con esta idea de recuperar conceptos químicos a partir de cálculos teóricos, la presente tesis está centrada en el estudio del enlace en situaciones no convencionales. En particular estudiamos la función del enlace de hidrógeno como catalizador de la formación de lluvia ácida, el debilitamiento de un enlace a través de su interacción con una cadena de enlaces π conjugados, el enlace de halógeno en clatratos, diferentes interacciones en complejos de oro pero en particular la interacción aurofílica, el efecto de distintas aproximaciones en la descripción de la densidad electrónica, y finalmente la localización espacial de la correlación electrónica. Los resultados obtenidos han sido satisfactorios. Más allá de la variedad de sistemas considerados, esta investigación ha permitido poner en relieve la importancia de las interacciones secundarias en la química, a la vez que ha demostrado la eficacia de la QCT para elucidar la respuesta a problemas donde la gran cantidad de variables hacen de ello una tarea complicada.

RESUMEN (en Inglés)

The unusual growth of theoretical chemistry in general and of computational chemistry in particular has brought in a problem that our predecessors would have liked to face: we have too much data. The wave function resulting from a calculation is an object that contains all the information of a system. In this situation, various methods of analysis have emerged that are, to a great extent, efforts to recover concepts specific to chemistry, such as atomic charges, from the results of the computations. What we know as Quantum chemical topology (QCT) is a set of analysis methodologies that are devoted to analyzing observables that are invariant to the orbital transformations, typically scalars constructed from reduced density matrices in real space, and that works as a bridge between the concepts of traditional chemistry (those derived from the Lewis Bond theory) and the results of the quantum-mechanical methodologies developed from first principles. With this idea of recovering chemical concepts from theoretical calculations, this thesis is focused on the study of chemical bonding in unconventional situations. In particular, we have studied the role of hydrogen bonding as a catalyst in the formation of

acid rain, the weakening of a bond through its interaction with a chain of conjugated π bonds, the halogen bond in clathrates, different interactions in gold complexes but in particular the aurophylic interaction, the effect of different approaches in the description of the electron density, and finally the spatial localization of electron correlation. The results obtained have been satisfactory. Beyond the variety of systems considered, this research has allowed to highlight the importance of secondary interactions in chemistry, while demonstrating the effectiveness of QCT to elucidate the solution to problems where the large number of unknowns involved make of it a complicated task.

Universidad de Oviedo
Universidá d'Uviéu
University of Oviedo

FORMULARIO RESUMEN DE TESIS POR COMPENDIO

1.- Datos personales solicitante	
Apellidos: Guevara Vela	Nombre: José Manuel

Curso de inicio de los estudios de doctorado	16/17

	SI	NO
Acompaña acreditación por el Director de la Tesis de la aportación significativa del doctorando		
Acompaña memoria que incluye		
Introducción justificativa de la unidad temática y objetivos		
Copia completa de los trabajos *		
Resultados/discusión y conclusiones		
Informe con el factor de impacto de la publicaciones		
Se acompaña aceptación de todos y cada uno de los coautores a presentar el trabajo como tesis por compendio		
Se acompaña renuncia de todos y cada uno de los coautores a presentar el trabajo como parte de otra tesis de compendio		

* Ha de constar el nombre y adscripción del autor y de todos los coautores asi como la referencia completa de la revista o editorial en la que los trabajos hayan sido publicados o aceptados en cuyo caso se aportará justificante de la aceptación por parte de la revista o editorial

FOR-MAT-VOA-033

Artículos, Capítulos, Trabajos

Trabajo, Artículo 1

Titulo (o título abreviado)	**The bifunctional catalytic role of water clusters in the formation of acid rain**
Fecha de publicación	28/03/2017
Fecha de aceptación	07/02/2017
Inclusión en Science Citation Index o bases relacionadas por la CNEAI (indíquese)	Sí
Factor de impacto	6.290

Coautor2 □ Doctor □ No doctor . Indique nombre y apellidos	Eduardo Romero-Montalvo
Coautor3 □ Doctor □ No doctor . Indique nombre y apellidos	Wilmer Esteban Vallejo Narváez
Coautor4 □ Doctor □ No doctor . Indique nombre y apellidos	Aurora Costales
Coautor5 □ Doctor □ No doctor . Indique nombre y apellidos	Ángel Martín Pendás
Coautor6 □ Doctor □ No doctor . Indique nombre y apellidos	Marcos Hernández-Rodríguez
Coautor7 □ Doctor □ No doctor . Indique nombre y apellidos	Tomás Rocha-Rinza

Universidad de Oviedo
Universidá d'Uviéu
University of Oviedo

Trabajo, Artículo 2

Titulo (o título abreviado)	Chemical bonding in excited states: Energy transfer and charge redistribution from a real space perspective
Fecha de publicación	15/05/2017
Fecha de aceptación	07/03/2017
Inclusión en Science Citation Index o bases relacionadas por la CNEAI (indíquese)	Sí
Factor de impacto	3.221

Coautor2 □ Doctor □ No doctor . Indique nombre y apellidos	Jesús Jara-Cortés
Coautor3 □ Doctor □ No doctor . Indique nombre y apellidos	Ángel Martín Pendás
Coautor4 □ Doctor □ No doctor . Indique nombre y apellidos	Jesús Hernández-Trujillo

Trabajo, Artículo 3

Titulo (o título abreviado)	Performance of the RI and RIJCOSX approximations in the topological analysis of the electron density
Fecha de publicación	12/04/2017
Fecha de aceptación	29/03/2017
Inclusión en Science Citation Index o bases relacionadas por la CNEAI (indíquese)	Sí
Factor de impacto	1.545

Coautor2 □ Doctor □ No doctor . Indique nombre y apellidos	Ángel Martín Pendás
Coautor3 □ Doctor □ No doctor . Indique nombre y apellidos	Tomás Rocha-Rinza

Trabajo, Artículo 4

Titulo (o título abreviado)	π-Backbonding and non-covalent interactions in the JohnPhos and polyfluorothiolate complexes of gold(I)
Fecha de publicación	07/10/2017
Fecha de aceptación	22/06/2017
Inclusión en Science Citation Index o bases relacionadas por la CNEAI (indíquese)	Sí
Factor de impacto	4.099

Coautor2 □ Doctor □ No doctor . Indique nombre y apellidos	Guillermo Moreno-Alcántar
Coautor3 □ Doctor □ No doctor . Indique nombre y apellidos	Kristopher Hess
Coautor4 □ Doctor □ No doctor . Indique nombre y apellidos	Tomás Rocha-Rinza
Coautor5 □ Doctor □ No doctor . Indique nombre y apellidos	Ángel Martín Pendás
Coautor6 □ Doctor □ No doctor . Indique nombre y apellidos	Marcos Flores-Álamo
Coautor7 □ Doctor □ No doctor . Indique nombre y apellidos	Hugo Torrens

Universidad de Oviedo
Universidá d'Uviéu
University of Oviedo

Trabajo, Artículo 5

Titulo (o título abreviado)	Structural effects of trifluoromethylation and fluorination in gold(I) BIPHEP fluorothiolates
Fecha de publicación	07/10/2017
Fecha de aceptación	31/08/2017
Inclusión en Science Citation Index o bases relacionadas por la CNEAI (indíquese)	Sí
Factor de impacto	3.201

Coautor2 □ Doctor □ No doctor . Indique nombre y apellidos	Guillermo Moreno-Alcántar
Coautor3 □ Doctor □ No doctor . Indique nombre y apellidos	Rafael Delgadillo-Ruíz
Coautor4 □ Doctor □ No doctor . Indique nombre y apellidos	Tomás Rocha-Rinza
Coautor5 □ Doctor □ No doctor . Indique nombre y apellidos	Ángel Martín Pendás
Coautor6 □ Doctor □ No doctor . Indique nombre y apellidos	Marcos Flores-Álamo
Coautor7 □ Doctor □ No doctor . Indique nombre y apellidos	Hugo Torrens

Trabajo, Artículo 6

Titulo (o título abreviado)	Hydrogen-Bond Weakening through π Systems: Resonance-Impaired Hydrogen Bonds (RIHB)
Fecha de publicación	21/11/2017
Fecha de aceptación	05/09/2017
Inclusión en Science Citation Index o bases relacionadas por la CNEAI (indíquese)	Sí
Factor de impacto	5.160

Coautor2 □ Doctor □ No doctor . Indique nombre y apellidos	Eduardo Romero-Montalvo
Coautor3 □ Doctor □ No doctor . Indique nombre y apellidos	Alejandra del Río-Lima
Coautor4 □ Doctor □ No doctor . Indique nombre y apellidos	Ángel Martín Pendás
Coautor5 □ Doctor □ No doctor . Indique nombre y apellidos	Marcos Hernández-Rodríguez
Coautor6 □ Doctor □ No doctor . Indique nombre y apellidos	Tomás Rocha-Rinza

Trabajo, Artículo 7

Titulo (o título abreviado)	Where Does Electron Correlation Lie? Some Answers from a Real Space Partition
Fecha de publicación	15/12/2017
Fecha de aceptación	05/10/2017
Inclusión en Science Citation Index o bases relacionadas por la CNEAI (indíquese)	Sí
Factor de impacto	2.947

Coautor2 □ Doctor □ No doctor . Indique nombre y apellidos	José Luis Casalz-Sainz
Coautor3 □ Doctor □ No doctor . Indique nombre y apellidos	Evelio Francisco
Coautor4 □ Doctor □ No doctor . Indique nombre y apellidos	Tomás Rocha-Rinza
Coautor5 □ Doctor □ No doctor . Indique nombre y apellidos	Ángel Martín Pendás

Universidad de Oviedo
Universidá d'Uviéu
University of Oviedo

Trabajo, Artículo 8

Titulo (o título abreviado)	Halogen Bonds in Clathrate Cages: A Real Space Perspective
Fecha de publicación	05/10/2018
Fecha de aceptación	22/06/2018
Inclusión en Science Citation Index o bases relacionadas por la CNEAI (indíquese)	Sí
Factor de impacto	2.947

Coautor2 □ Doctor □ No doctor . Indique nombre y apellidos	David Ochoa-Resendiz
Coautor3 □ Doctor □ No doctor . Indique nombre y apellidos	Aurora Costales
Coautor4 □ Doctor □ No doctor . Indique nombre y apellidos	Ramón Hernández-Lamoneda
Coautor5 □ Doctor □ No doctor . Indique nombre y apellidos	Ángel Martín Pendás

Trabajo, Artículo 9

Titulo (o título abreviado)	Stability and trans Influence in Fluorinated Gold(I) Coordination Compounds
Fecha de publicación	01/11/2018
Fecha de aceptación	14/09/2018
Inclusión en Science Citation Index o bases relacionadas por la CNEAI (indíquese)	Sí
Factor de impacto	2.507

Coautor2 □ Doctor □ No doctor . Indique nombre y apellidos	Guillermo Moreno-Alcántar
Coautor3 □ Doctor □ No doctor . Indique nombre y apellidos	Hugo Hernández-Toledo
Coautor4 □ Doctor □ No doctor . Indique nombre y apellidos	Tomás Rocha-Rinza
Coautor5 □ Doctor □ No doctor . Indique nombre y apellidos	Ángel Martín Pendás
Coautor6 □ Doctor □ No doctor . Indique nombre y apellidos	Marcos Flores-Álamo
Coautor7 □ Doctor □ No doctor . Indique nombre y apellidos	Hugo Torrens

En caso de compendio de un número de artículos superior a seis, se incorporarán hojas suplementarias conforme a este modelo

Índice general

Capítulo 1

Introducción

El mundo es un lugar complicado. Es tan complicado, de hecho, que el mero hecho de que seamos capaces de percibirlo debería ser considerado en sí mismo como un milagro. Este entendimiento está mediado por un marco de referencia, con su propias estructura y lógica internas, que es medianamente consistente.

El primer marco de referencia de la humanidad, el primer modelo de entendimiento del mundo, fue la religión. Una religión, cualquiera que sea esta, coloca los acontecimientos del mundo en un contexto, de modo que la erupción de un volcán no es un hecho fortuito, si no la expresión de enojo del dios de la tierra, y la imposibilidad de concebir hijos se debe no a un impedimento biológico, si no que se convierte en un castigo divino. Sin embargo, este marco de referencia, el religioso, es limitado en el sentido que permite explicar el pasado pero su poder predictivo hacia los acontecimientos futuros es limitado. Sí, los mayas fueron capaces de predecir eclipses con muchos años de antelación, pero fueron incapaces de entender quienes eran los visitantes que llegaron a sus costas a principios del siglo XVI.

Tal vez uno de los primeros intentos por entender el mundo en términos no religiosos se dio en la Antigua Grecia. Algunos filósofos griegos teorizaron sobre el funcionamiento del mundo y propusieron sistemas varios, como el panteísmo radical de Parménides, el mundo de las ideas de Platón, o la visión del mundo constituido por cuatro elementos de Aristóteles. Entre estos filósofos, se encuentra Demócrito, y su teoría atomística: la postulación de que todo en cuanto existe en el mundo está constituido por átomos, partículas, indestructibles e indivisibles, y que las propiedades de la materia varían dependiendo de diferentes agrupamientos de átomos [1].

Sin embargo, todas estas teorías se desarrollaron únicamente utilizando la lógica de las ideas, sin contrastarse con la realidad a través de la experimentación. Esto se debió en gran medida a

que en la cultura griega el trabajo manual siempre fue visto como algo propio de esclavos, por lo que el desarrollo de la técnica fue limitado y apenas hubo innovaciones tecnológicas asociadas al trabajo manual. En el mundo antiguo, una teoría filosófica era juzgada por la belleza de sus argumentos, no por su valor como explicación fenomenológica. Las teorías, sin importar lo hermosas que sean, una vez formuladas requieren ser contrastadas con la realidad, de otro modo son poco más que cuentos de hadas.

Con la caída del Imperio romano de occidente, la enorme tradición filosófica griega encontró refugio en dos lugares bastante disímiles, por un lado en los monasterios cristianos donde monjes dedicaron incontables horas a transcribir una y otra vez las obras de los antiguos filósofos y por otro en la cultura árabe, donde la apreciación por la cultura griega perduró durante siglos.

Durante el renacimiento, humanistas de distinta índole se dieron a la tarea de rescatar los trabajos de la antigüedad buscando en monasterios por toda Europa. Esta intensa búsqueda resultó en la reaparición de un gran número de ideas, entre ellas de la teoría atómica de Demócrito. El redescubrimiento de esta teoría, materialista y de intenso contraste con la tradición cristiana y neoplatónica, fue un estímulo importante en el posterior desarrollo de la modernidad en general y de la ciencia moderna en particular. [2]

Por otra parte, en el mundo islámico una parte de la ciencia de los griegos sobrevivió al colapso romano y se asimiló dentro de su tradición cultural. De esta manera las ideas griegas sobre astronomía, botánica, geografía, cartografía, matemáticas, medicina, física, y demás perduraron y pudieron llegar a los pensadores de la modernidad. Entre estas ideas la más relevante para el posterior desarrollo de la química moderna fue la alquimia.

La alquimia fue una filosofía natural que mezcló tradiciones filosóficas y protocientíficas originada en Egipto cuando este era parte de la Antigua Grecia. Su objetivo, como práctica filosófica, fue la purificación. En términos mundanos esto significó dos cosas: Primero, la (imposible) búsqueda del elíxir de la vida y el intento (no menos imposible) de conseguir transmutar el plomo en oro. A pesar de la futilidad de ambos ejercicios, muchos conocimientos prácticos antiguos sobrevivieron como parte de esta tradición; cómo producir pigmentos, pinturas, gemas preciosas artificiales, la manera de limpiar y fabricar perlas, o cómo manufacturar imitaciones de oro y plata [3].

Es en este contexto histórico en el que se dio el nacimiento de la ciencia moderna en general y de la química en particular; quehacer que combina el entendimiento del mundo dentro de un marco teórico propio con una vocación eminentemente práctica. Al final, la química es la única ciencia que crea su propio objeto de estudio.

1.1. La ciencia moderna

Durante el renacimiento la ciencia moderna surgió usando como pilares el conocimiento técnico conservado en la cultura islámica y el redescubrimiento de los antiguos filósofos griegos. Usando estas dos herramientas, los nuevos humanistas se dedicaron a explorar el mundo, pero, a diferencia de sus antecesores, ellos combinaron sus indagaciones filosóficas con experimentos para validar estas. Así tenemos por ejemplo el famoso experimento de Galileo en la torre inclinada de Pisa, donde dejó caer dos esferas de diferente masa para comprobar que el tiempo que tardaban en caer era independiente de ésta [4].

Esta interacción entre teoría y experimento generó un círculo virtuoso de aprendizaje que propició el crecimiento de la ciencia moderna. Muchos filósofos naturales, como se llamaban a sí mismos, de la época se dedicaron al estudio y entendimiento de la naturaleza, pero, de manera crucial, ahora parte de esta exploración consistió en comprobar experimentalmente las teorías existentes, tanto las que formulaban ellos mismos como aquellas de los filósofos de la antigüedad. sí durante los siglos entre el renacimiento y el final del siglo XVIII se dieron muchos avances, entre ellos los principales tal vez sean la ley de los gases de Boyle-Mariotte y el descubrimiento de elementos químicos como el fósforo, el cobalto, el níquel, el hidrógeno o el cloro.

Este proceso de acumulación del conocimiento no fue sencillo ni inmediato. Las comunicaciones entre investigadores eran lentas y aún se daban casos donde algunos confiaban más en escritos atribuidos a Aristóteles que a los experimentos que ellos o sus contemporáneos realizaban. Así, por ejemplo, de la observación que el óxido metálico era más pesado que el metal mismo surgió la teoría del flogisto, con peso negativo, de ahí la masa ganada por el material, y atraído por el aire. Durante casi dos siglos esta fue la teoría dominante sobre la combustión, en parte debido a que se apoyaba y convivía con la concepción aristotélica del los cuatro elementos. Sin embargo, hacia finales del siglo XVIII experimentos hechos por Antoine Lavoisier desmintieron esta teoría, demostrando que la combustión no cambia la masa total del sistema cuando éste es cerrado [5]. Además de proponer la teoría de combustión con oxígeno, Lavoisier fue un pionero en el desarrollo de la estequiometría y en nomenclatura química.

A principios del siglo XIX, John Dalton propuso la teoría atómica, reminiscente de aquella postulada por Demócrito y sus discípulos, la cual sostenía que la materia estaba formada por partículas indivisibles llamadas átomos, que los átomos de diferentes elementos eran distintos entre sí, y que los compuestos químicos se forman al unirse dos o más elementos distintos. Dalton rescataba así una concepción puramente materialista del mundo que por casi dos milenios estuvo

enterrada debajo del mundo platónico prevaleciente en el cristianismo.

Los experimentos y las teorías de Lavoisier junto con la teoría atómica de Dalton pueden ser consideradas como el principio de la química tal y como la entendemos actualmente. La teoía atḿica propone una visión material del mundo físico, donde todo lo que sucede tiene su origen en este mismo, poniendo fin a la difícil convivencia entre los elementos filosóficos de la Antigua Grecia, a través de la alquimia y los textos redescubiertos, los experimentos, y teorías de la ciencia moderna.

1.1.1. La tabla periódica

Este cambio de paradigma en la comprensión del universo que constituyó la nueva ciencia fue acompañado del descubrimiento de cuantiosos elementos químicos. Mientras que el mundo antiguo únicamente conoció 9 elementos, para comienzos del siglo XIX este número había llegado a más de 30. Desde este punto, y durante el resto de la primera mitad del siglo XIX, el número de elementos químicos conocidos no dejó de aumentar, en gran medida por la aplicación de nuevas técnicas como la electrólisis o la espectroscopía en su búsqueda.

Ante esta superabundancia, los científicos se dieron a la tarea de ordenar los elementos químicos. Al principio, el acomodo de los elementos y la descricipción de las relaciones entre ellos fue rudimentaria; el propio Lavoisier propuso la separación de los elementos en gases, no metales, metales, y tierras [6]. Posteriores intentos de sistematización, como las tríadas o las octavas, se basaron en las relaciones entre los pesos atómicos de cada elemento. Esto significó un paso importante pues se dejó de lado las similitudes aparentes en pos de encontrar un orden subyacente, pero su resultado como sistemas era aún insatisfactorio.

En 1869, Dimitri Mendeleiev, propuso una clasificación sistemática de los elementos químicos en una tabla estructurada en función de sus pesos atómicos y de la proporción de dichos elementos en sus hidruros y óxidos correspondientes. Es decir, Mendeleiev utilizó argumentos tanto físicos, los pesos, como químicos, lo que hoy conocemos como valencia, para dar forma a su tabla periódica. La primera tabla periódica como tal fue publicada en la revista alemana *Zeitschrift für Chemie*, y se puede ver en la Figura 1.1.

La adopción de la tabla periódica de Mendeleiev fue un proceso relativamente rápido, principalmente debido a un hecho muy poco común entre las propuestas de sistematización de la época: Mendeleiev no solo ordenó los elementos químicos conocidos, si no que predijo la existencia de varios elementos nuevos, de modo que las tendencias observadas en su tabla se cumplieran de mejor manera. Esta arriesgada decisión fue reinvindicada por posteriores descubrimientos y significó un

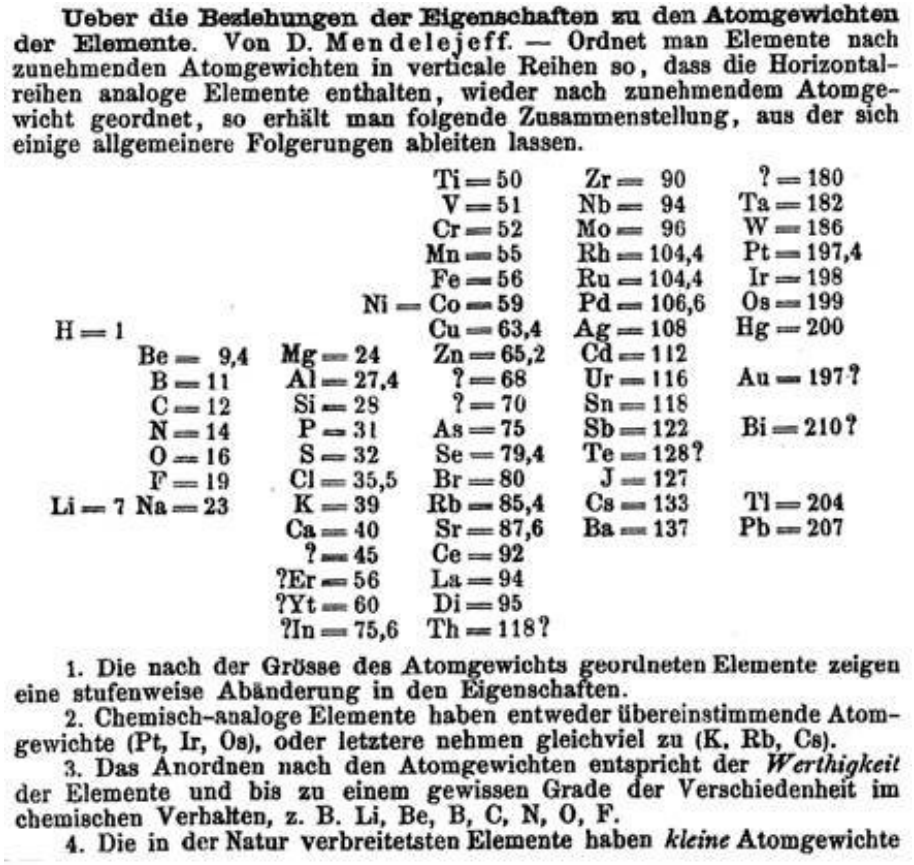

Ueber die Beziehungen der Eigenschaften zu den Atomgewichten der Elemente. Von D. Mendelejeff. — Ordnet man Elemente nach zunehmenden Atomgewichten in verticale Reihen so, dass die Horizontalreihen analoge Elemente enthalten, wieder nach zunehmendem Atomgewicht geordnet, so erhält man folgende Zusammenstellung, aus der sich einige allgemeinere Folgerungen ableiten lassen.

			Ti = 50	Zr = 90	? = 180	
			V = 51	Nb = 94	Ta = 182	
			Cr = 52	Mo = 96	W = 186	
			Mn = 55	Rh = 104,4	Pt = 197,4	
			Fe = 56	Ru = 104,4	Ir = 198	
		Ni =	Co = 59	Pd = 106,6	Os = 199	
H = 1			Cu = 63,4	Ag = 108	Hg = 200	
	Be = 9,4	Mg = 24	Zn = 65,2	Cd = 112		
	B = 11	Al = 27,4	? = 68	Ur = 116	Au = 197?	
	C = 12	Si = 28	? = 70	Sn = 118		
	N = 14	P = 31	As = 75	Sb = 122	Bi = 210?	
	O = 16	S = 32	Se = 79,4	Te = 128?		
	F = 19	Cl = 35,5	Br = 80	J = 127		
Li = 7	Na = 23	K = 39	Rb = 85,4	Cs = 133	Tl = 204	
		Ca = 40	Sr = 87,6	Ba = 137	Pb = 207	
		? = 45	Ce = 92			
		?Er = 56	La = 94			
		?Yt = 60	Di = 95			
		?In = 75,6	Th = 118?			

1. Die nach der Grösse des Atomgewichts geordneten Elemente zeigen eine stufenweise Abänderung in den Eigenschaften.
2. Chemisch-analoge Elemente haben entweder übereinstimmende Atomgewichte (Pt, Ir, Os), oder letztere nehmen gleichviel zu (K, Rb, Cs).
3. Das Anordnen nach den Atomgewichten entspricht der *Werthigkeit* der Elemente und bis zu einem gewissen Grade der Verschiedenheit im chemischen Verhalten, z. B. Li, Be, B, C, N, O, F.
4. Die in der Natur verbreitetsten Elemente haben *kleine* Atomgewichte

Figura 1.1: La tabla periódica de Mendeleiev como fue publicada en 1869. Presenta los periodos en una dispoción vertical mientras que los grupos se acomodan horizontalmente [7]

éxito rotundo en el progreso de la química como ciencia: La química pasó de ser eminentemente descriptiva a ocupar una posición desde la cual era capaz de predecir lo desconocido.

1.2. El mundo cuantizado

Durante el siglo XIX la ciencia y la técnica avanzaron de manera impresionante. Entre algunos de los descubrimientos científicos más significativos del siglo se encuentran la anestesia, las vacunas, la teoría de la evolución, las leyes de la termodinámica, o las leyes de Maxwell sobre el electromagnetismo. Por otro lado, entre las invenciones más importantes de esta pica se encuentran la locomotora a vapor, la máquina de combustión interna, el motor eléctrico, el telégrafo, la dinamita, o la bombilla eléctrica. De esta manera, es comprensible que hacia finales del siglo el optimismo respecto al progreso, y al poder de la ciencia que impulsaba dicho progreso, se encontraba por los cielos. Tal era el grado de confianza que se respiraba en ese entonces que en

1984 el físico estadounidense Albert Michelson, quien posteriormente ganaría el premio Nobel de física por su contribución a la medición de la velocidad de la luz, afirmó:

> "...parece probable que la mayoría de los principios fundamentales más importantes han sido ya establecidos. Un eminente físico observó que los futuros descubrimientos de la física deben ser buscados en el sexto número decimal [8]."

Sin embargo, hoy podemos decir que los principios fundamentales de la física estaban muy lejos de estar ya establecidos, como lo demostraró el vertiginoso ritmo de descubrimientos que sobrevino en las décadas siguientes y que cambió, una vez más, nuestro entendimiento del mundo.

1.2.1. Max Planck y el problema del cuerpo negro

Hacia el final del siglo XIX un problema hacía difícil la vida a los físicos de la época: el espectro de luz emitido por un cuerpo negro. Para los físicos, un cuerpo negro es un material ideal tal que absorbe toda la luz incidente sin reflejar nada. Dado que no existe ningún material con estas características, los físicos experimentales utilizaron una cavidad hueca con un agujero en medio como modelo, pues así la luz absorbida podría reflejarse entre las paredes del interior de la cavidad y únicamente una pequeña parte saldría por el agujero.

Al calentarse, un cuerpo negro emite luz, produciendo lo que se conoce como espectro de emisión. El problema surgió cuando los conocimientos físicas existentes fueron incapaces de explicar los espectros obtenidos experimentalmente. Usando termodinámica clásica, Wilhelm Wien propuso una teoría que funcionaba solamente cuando la frecuencia de emisión era alta. En cambio, Lord Rayleigh intentó otra explicación fundamentada en física clásica y hechos empíricos, que también tuvo éxito parcialmente, explicando correctamente el fenómeno solo a bajas frecuencias.

Es ante este problema que Max Planck propuso un enfoque totalmente diferente y propuso que la cantidad de energía que una onda lumímica intercambia con la materia no es contínua sino discreta. Es decir, en el caso del cuerpo negro, que la energía intercambiada por las paredes de la cavidad pudiera ser únicamente múltiplos enteros de una constante h, que hoy conocemos como la constante de Planck.

La formulación de Planck fue capaz de predecir de manera correcta el espectro de emisión del cuerpo negro, indicando que el mundo no era un continuo si no que estaba discretizado. El trabajo de Albert Einstein sobre el efecto fotoeléctrico no hizo sino confirmar esto. Así, al comenzar el nuevo siglo, estos desarrollos junto a la amplia aceptación de la teoía atómica establecían un

nuevo paradigma: La física de Newton y Maxwell no era ya suficiente para modelar el mundo ahora que estaba cuantizado.

1.2.2. La forma del átomo

La aceptación de la teoría atómica como el paradigma dominante en el mundo científico generó inmediatamente la pregunta correspondiente: ¿Qué forma tiene un átomo por dentro? El átomo de Dalton consistía en una unidad indivisible, sin embargo, el descubrimiento del electrón por parte de J. J. Thomson vino a trastocar esta idea. Ante esto, Thomson propuso que el átomo consistía en una nube de carga positiva con electrones, cientos de veces más pequeños, repartidos a lo largo de esta de manera aleatoria. A esta teoría se le denominó afectuosamente el "Plum pudding model", o modelo del pudín de ciruelas [9] y tuvo poca una aceptación debido a que requería de cargas opuestas interpenetrantes.

En 1909, Ernest Rutherford, diseño un experimento para probar la estructura interna del átomo: Bombardeó una delgada hoja de oro con un haz de partículas alfa provenientes del decaimiento de gas radón. El modelo de Thomson predecía que el grado de dispersión de las partículas alfa dependería del grosor de la lámina de oro, y sería mínimo para una hoja delgada. Sin embargo, el resultado fue sorprendente, algunas partículas alfa no desviaban ligeramente su trayectoria, si no directamente rebotaban. En palabras de Rutherford:

> Eso fue el evento más increíble que me ocurrió jamás en la vida. Fue casi tan increíble como si disparases una bala de 15 pulgadas contra una pieza de papel y esta rebotase y te diera.[10]

Era claro que el modelo de Thomson no describía la realidad adecuadamente. Rutherford entonces propuso una explicación alternativa: la estructura del átomo consistía en un núcleo muy pequeño cargado positivamente que contenía casi la totalidad de la masa rodeado de electrones con masas órdenes de magnitud inferiores. Es decir, el átomo estaba vacío.

1.2.3. El átomo de Bohr

El modelo atómico de Rutherford, conceptualmente, era muy atractivo. Proponer que la materia se comportaba de manera similar a nivel atómico, un núcleo rodeado de electrones, y estelar, una estrella en el centro que contiene toda la masa y planetas orbitando alrededor. No obstante, había un problema: de acuerdo a la mecánica clásica, un electrón orbitando al núcleo

emitiría radiación electromagnética. Teóricamente, al perder energía el electrón debería colapsar hacia el interior del núcleo. Esto es, el átomo sería inestable [11].

Para solventar este inconveniente, Niels Bohr propuso un modelo atómico nuevo, que fuera consistente tanto con el experimento de Rutherford como con la teoría de radiación de Planck. El modelo de Bohr postula que los electrones se mueven únicamente en órbitas estacionarias alrededor del núcleo sin emitir energía alguna. Estas órbitas son un múltiplo entero de la constante de Planck, $m_e \nu r = n\hbar$, donde $n = 1, 2, 3, ...$ es el número cuántico principal.

Entre las consecuencias lógicas de este modelo se encuentran la existencia de una distancia mínima entre núcleo y electrón, el llamado radio de Bohr (0.0529 nm), y el hecho que los electrones solo puedan ganar y perder energía cambiando de orbita. Este intercambio energético está, por tanto, cuantizado.

El principal éxito de la teoría atómica de Bohr fue su capacidad para explicar las líneas en el espectro de emisión del átomo de hidrógeno y por qué estas estaban descritas correctamente por el modelo empírico de Rydberg. Sin embargo, el modelo de Bohr era incapaz de describir correctamente varios fenómenos, como el espectro de emisión de átomos multielectrónicos o las intensidades relativas de las líneas espectrales por poner dos ejemplos. Además, como se descubriría más adelante, el átomo de Bohr tenía otra carencia fundamental: al considerar que la posición y la órbita de los electrones podían conocerse simultáneamente, se violaba el principio de incertidumbre de Heisenberg.

Así, con estos errores y aciertos, la teoría atómica de Bohr es fiel representante de la revolución científica que estaba viviendo el mundo en las primeras décadas del siglo XX. En unos pocos años el mundo pasó de ser continuo a discreto, de estar lleno de materia a ser vacío, y las dudas más que las certezas.

1.3. Química teórica

La química, como se entiende actualmente, es en gran medida la ciencia del enlace. El modelo de Bohr, incapaz de describir un sistema biatómico es, por tanto, totalmente insuficiente para responder a la que puede ser la interrogante central en química: ¿Qué es un enlace? Fue un científico austriaco, Erwin Schrödinger, quien comenzaría a indicar el camino hacia la respuesta a esta pregunta, o algo suficientemente parecido a ello.

1.3.1. La ecuación de Schrödinger

Hacia principios de los años 20 el desarrollo de la mecánica cuántica la llevó a convertirse en la formulación más aceptada en física de los átomos, aunque su interpretación última siguió siendo controvertida. Particularmente complicado de explicar fue el descubrimiento, mediante el experimento de la doble rejilla, que demostró que ambos luz y partículas podían comportarse como ondas o como partículas dependiendo de cómo se observasen.

En 1926, Schrödinger introdujo al mundo una ecuación para describir una onda para sistemas independientes del tiempo que, al ser aplicada sobre un sistema análogo al átomo de hidrógeno, resultaba en la solución correcta para sus energías propias. Esta ecuación diferencial parcial tiene la forma $\widehat{H}\psi = E\psi$, donde $\widehat{H}$ es el Hamiltoniano y E es la energía del sistema. Sin embargo, debido a que electrones y núcleos se mueven a velocidades de diferente orden de magnitud, es posible considerar a estos últimos como estáticos respecto a los primeros. Por tanto la ecuación anterior se puede reescribir bajo esta aproximación como:

$$\widehat{H}_{\text{elec}}\psi_{\text{elec}} = E_{\text{elec}}\psi_{\text{elec}}. \tag{1.1}$$

Cuando aplicamos la ecuación 1.1 sobre un sistema de M núcleos y N electrones e ignoramos el espín y otros efectos relativistas, obtenemos lo siguiente:

$$\widehat{H}_{\text{elec}} = -\frac{1}{2}\sum \nabla_i^2 - \sum_{i=1}^{N}\sum_{A=1}^{M}\frac{Z_A}{r_{iA}} + \sum_{i=1}^{N-1}\sum_{j>i}^{N}\frac{1}{r_{ij}} + \sum_{A=1}^{M-1}\sum_{B>A}^{M}\frac{Z_A Z_B}{R_{AB}}, \tag{1.2}$$

donde A y B son etiquetas para los núcleos e i y j denotan los electrones del sistema. Asimismo, Z_X denota la carga del núcleo X y r_{iA}, r_{ij} y r_{AB} las distancias entre núcleo y electrón, electrones y núcleos, respectivamente. La ecuación 1.2 es entonces capaz de describir sistemas multielectrónicos. No obstante, su solución, aún aproximada, se encontraba más allá de lo que era posible calcular en la época.

1.3.2. El método de Hartree-Fock

Un par de años después de la publicación de la ecuación de Schrödinger, Douglas Hartree usó los conocimientos sobre ecuaciones diferenciales y análisis numérico, desarrollados durante su trabajo en ecuaciones de balística durante la primera guerra mundial [12], para darle una solución aproximada a esta. Su ingeniosa idea consistió en aproximar la función de onda multielectrónica, la solución de la ecuación de Schrödinger, como el producto de funciones de onda monoelectrónicas. Esas funciones generaban un campo $v(r)$ que a su vez era añadido a la ecuación original

y recalculado de manera iterativa hasta converger. A este procedimiento se le denominó como método del campo autoconsistente debido a que el campo obtenido debía ser consistente con el campo de prueba usado originalmente.

Este método tal y como fue planteado por Hartree no satisfacía el principio de exclusión de Pauli, pues no discernía entre electrones de difernte espín. En 1930, Vladimir Fock señaló que un determinante de Slater[1] satisface el principio de antisimetría, y por tanto el principio de exclusión de Pauli. Así, el uso del procedimiento de Hartree con un determinante de Slater, que tomaba en cuenta la energía de intercambio entre electrones, se conoció como método de Hartree-Fock.

La nueva metodología tenía el problema que calcular la solución bajo esta estaba fuera de las posibilidades de los procedimientos matemáticos desarrollados por Hartree para su aproximación original. Fue entonces que el padre de Hartree, William Hartree, participó en el trabajo de su hijo calculando los valores de una solución numérica que incluyese el intercambio para distintos átomos, entre ellos el Berilio [13]. Este momento puede ser considerado como el inicio de la química computacional, aunque el verdadero auge de esta debió esperar al desarrollo de la computadorada electrónica en los años cincuenta.

1.4. La química computacional hoy

Durante el resto del siglo XX y el comienzo del siglo XXI la química computacional creció junto con el vertiginoso desarrollo de los microprocesadores, que hacían posible llevar a cabo cálculos matemáticos que 10 años antes parecían una fantasía. Conjuntamente con la evolución de las tecnologías que hacían posible el cálculo, se dieron diversos avances metodológicos en darle solución aproximada a la ecuación de Schrödinger. A partir del método de Hartree-Fock, se desarrollaron diversas propuestas, como la teoría de perturbaciones de Møller-Plesset (MP), el método de interacción de configuraciones (CI), o la teoría de cúmulos acoplados (CC). Estos métodos se conocen colectivamente como métodos post-Hartree-Fock. Otra importante aproximación en la química computacional actual es la teoría del funcional de la densidad, que da solución a un problema multielectrónico utilizando como base la densidad electrónica (DFT).

De esta manera, la química computacional pasó de estudiar átomos, a moléculas pequeñas, y de ahí a proteínas con el mismo grado de exactitud en cuestión de menos de un siglo. El estudio

[1] Un determinante de Slater es una expresión que describe a la función de onda de un sistema con dos o más fermiones. Por ejemplo, para el caso de dos partículas con coordenadas x_1 y x_2 el determinante de Slater correspondiente es $\Psi(x_1, x_2) = ||\chi_1(x_1)\chi_2(x_2)||$

de sistemas cuya complejidad y tamaño harían palidecer a nuestros antecesores se han vuelto rutinarios a una velocidad apabullante.

Hoy, la química computacional se dedica a estudiar fenómenos tan diversos como complejos que por diferentes razones no es posible estudiar utilizando simplemente técnicas experimentales. En ciertos casos el modelado de un sistema revela características de este que no serían apreciables de otra manera, como en el caso de la absorción de un fotón por parte de una base de ADN [14]. En otros casos, el cálculo computacional puede ofrecer una perspectiva sobre fenómenos que por su corta duración es difícil apreciar de otra manera, como la estructura de compuestos de elementos transuránicos [15].

Los pasos que se han dado en este siglo en el campo de la química teórica han sido enormes, pero tal vez el más grande ha sido la aceptación de esta dentro de la comunidad científica en general. En nuestros días, más y más químicos buscan no solo explicaciones a lo que observan en sus experimentos, si no que poco a poco entienden a la simulación como una herramienta más para descifrar las complejidades de la naturaleza. Esto es, estamos hoy más cerca de ese ideal científico de comunión entre teoría y la técnica.

1.5. La visión desde el espacio real: este trabajo de tesis

El crecimiento inusitado de la química teórica en general y de la química computacional ha traído un problema que ya quisieran haber tenido nuestros predecesores: contamos con demasiada información. La función de onda resultante de un cálculo es un objeto que contiene toda la información de un sistema. La densidad, en sí misma muchísimo más simple, es aún demasiado complicada para nuestras mentes homínidas.

Ante esta situación, casi desde el comienzo de la química computacional como tal, surgieron distintos métodos de análisis para dar sentido a los resultados obtenidos. La necesidad de dar significado a la abundancia de números era urgente. En los años cincuenta Robert S. Mulliken propuso un método para analizar la población de distintos orbitales. Tiempo después este método fue la base de un procedimiento para estimar la carga parcial de un átomo a partir de los resultados del cálculo de la energía de una molécula. De esta manera, los métodos de análisis son, en gran medida, esfuerzos por recuperar conceptos propios de la química, como las cargas atómicas, de los resultados computacionales.

La topología químico cuántica (QCT por sus iniciales en inglés), una rama de la química teórica que se dedica a analizar observables invariantes ante el cambio de orbitales, típicamente

escalares construidos a partir de matrices de densidad reducidas en el espacio real. Esta tiene su origen en la investigación de Richard F.W. Bader sobre "Átomos en Moléculas" (AIM) en la que, analizando la topología de la densidad electrónica, funciona como un puente entre los conceptos químicos derivados de la teoría de enlace de Lewis y los resultados de los métodos mecánico-cuánticos desarrollados a partir de primeros principios [16].

De esta manera, la presente tesis se enmarca dentro del mundo de la química computacional en el contexto del análisis de la densidad electrónica en el espacio real. En particular, la investigación llevada a cabo a lo largo de esta tesis se centró en el uso de la QCT para escudriñar los misterios que guarda aún hoy el enlace químico.

Lo que sigue es un resumen del trabajo realizado y se organiza de la siguiente manera: primero se hará una breve exposición de los métodos computacionales más utilizados durante el trabajo de tesis, con especial énfasis en las metodologías de la QCT. A continuación, se hará una recapitulación de los principales resultados obtenidos. Seguidamente, se presentarán el conjunto de artículos publicados tal como aparecen en la revista original. Finalmente, se enumerarán las conclusiones obtenidas.

Capítulo 2

Methodology

This chapter explains briefly the theory behind the procedures most used in the articles included in the present work. Firstly, the Hartree-Fock, as the underlying foundation for the approximations used in computational chemistry, and the density functional theory are explained. Later, a short summary of the methods of analysis employed, namely the Quantum Theory of Atoms in Molecules (QTAIM), the Interacting Quantum Atoms (IQA) energy partition and, the Non-Covalent Interaction (NCI) index method, is carried out. The methods of analysis used are encompassed by the term Quantum Chemical Topology (QCT), a branch of theoretical chemistry that characterizes chemical systems using quantitative descriptors [17].

The importance of the methodologies within QCT for chemist resides in two important qualities. The first is that they allow for the extraction of additional information from theoretical calculations, being these wavefunction or density-based methods that can be related to concepts that are central to chemistry, such as bond or atom, that are absent from quantum mechanics. The second is that QCT methodologies are rooted in physical quantities, which makes them highly robust with regards to changes in the computational level of theory used.

2.1. Hartree-Fock and post-Hartree Fock methodologies

In the present summary we will consider the Hartree-Fock theory as concerning only to one determinant wave functions for simplicity. Thus, we know that the energy of the N-electron system is determined by the Hamiltonian, $\mathscr{H}$, as:

$$E_0 = \langle 0|\mathscr{H}|0\rangle\,, \tag{2.1}$$

where

$$|0\rangle = |\chi_1, \chi_2 \cdots \chi_a, \chi_b \cdots \chi_N\rangle \tag{2.2}$$

is a determinant made of a set of spin-orbitals, χ_a, to be found such as to get the best possible description of the corresponding ground state. According to the variational principle, this set has to correspond to those that minimize the energy.

$$\begin{aligned} E_0 &= \langle 0|\mathscr{H}|0\rangle \\ &= \sum_a \langle a|h|a\rangle + \frac{1}{2}\sum_{ab}\langle ab||ab\rangle \qquad (2.3) \\ &= \sum_a \langle a|h|a\rangle + \frac{1}{2}\sum_{ab}[aa|bb] - [ab|ba]. \qquad (2.4) \end{aligned}$$

We can then vary the orbitals with the only constrain that the remain orthonormal to each other,

$$\langle \chi_a|\chi_b\rangle = \delta_{ab}, \tag{2.5}$$

until the energy E_0 is minimized. In this way, we get a formalism to obtain an equation that defines the best spin orbitals. Thus, we have the Hartree-Fock equation:

$$\epsilon_a\chi_a(1) = h(1)\chi a + \sum_{b\neq a}\left[\int d\mathrm{x}_2|\chi_b(2)|^2 r_{12}^{-1}\right]\chi_a(1) - \sum_{b\neq a}\left[\int d\mathrm{x}_2\chi_b(2)^*\chi_a(2)r_{12}^{-1}\right]\chi_b(1) \tag{2.6}$$

where

$$h(1) = -\frac{1}{2}\nabla_1^2 - \sum_A \frac{Z_A}{r_{1A}}. \tag{2.7}$$

Here the first part represents the kinetic energy of the electron and the second one is the potential energy between the electron and the nucleus.

The lasts two terms of equation (2.6) represent the interaction between electrons. Without them, the energy of an orbital would be reduced to the Schrödinger equation of a single electron trapped in the field of the nuclei.

The second to last term of equation (2.6) is called the Coulomb term, and it represents the averaged potential of the N-1 other electrons acting over the remaining electron. We can define

the coulomb operator in order to represent, individually, the action of an electron in orbital χ_b over the position x_1 as:

$$\mathscr{J}_b(1) = \int d\mathrm{x}_2 |\chi_b(2)|^2 r_{12}^{-1}. \tag{2.8}$$

Now, the last term of equation (2.6) is known as the exchange part. It arises from the antisymmetric nature of the single determinant but, unlike the Coulombic term, it lacks a straightforward interpretation beyond noticing that it is quantum in nature. It is possible to get an expression comparable to equation (2.8) for the exchange operator:

$$\mathscr{K}_b(1) = \int d\mathrm{x}_2 \chi_b(2)^* \chi_a(2) r_{12}^{-1}. \tag{2.9}$$

By combining equations (2.7), (2.8), and (2.9) we can rewrite the expression (2.6) in a simpler form:

$$\epsilon_a \chi_a(1) = \left[h(1) + \sum_{b \neq a} \mathscr{J}_b(1) - \sum_{b \neq a} \mathscr{K}_b(1) \right] \chi_a(1). \tag{2.10}$$

Now we can stop for a moment to observe the differences between the coulomb and exchange operators by multiplying both by $\chi_a(1)$:

$$\mathscr{J}_b(1)\chi_a(1) = \left[\int d\mathrm{x}_2 \chi_b(2)^* \chi_b(2) r_{12}^{-1} \right] \chi_a(1). \tag{2.11}$$

and

$$\mathscr{K}_b(1)\chi_a(1) = \left[\int d\mathrm{x}_2 \chi_b(2)^* \chi_a(2) r_{12}^{-1} \right] \chi_b(1). \tag{2.12}$$

Here we can see that the exchange operator involves the "exchange" of the positions of electrons 1 an 2 for $\mathscr{K}_b(1)$ relative to $\mathscr{J}_b(1)$. Unlike the coulomb operator, the nature of the exchange operator is nonlocal since there is not a simple potential $\mathscr{K}_b(\mathbf{x}_1)$ univocally defined at a local point in space $\mathbf{x}_1$. Namely, the result of $\mathscr{K}_b(\mathbf{x}_1)$ operating over $\chi_a(\mathbf{x}_1)$ depends on the value of χ_a throughout all the space.

By inspecting the coulomb and exchange operators in equations (2.11) and (2.12) we can infer that

$$[\mathscr{J}_a(1) - \mathscr{K}_a(1)]\chi_a(1) = 0. \tag{2.13}$$

Then, it is possible to add this zero term to equation (2.10) and skip the restriction on the summation in order to get the Fock operator:

$$f(1) = h(1) + \sum_b \mathscr{J}_b(1) - \mathscr{K}_b(1). \tag{2.14}$$

The Fock operator is thus the sum of a core Hamiltonian operator and an effective electron potential operator, v^{HF}, that accounts for the electron-electron interaction:

$$v^{HF} = \sum_b \left(\mathscr{J}_b(1) - \mathscr{K}_b(1)\right). \tag{2.15}$$

Using the relation (2.14) we got the Fock operator

$$f(1) = h(1) + v^{HF}, \tag{2.16}$$

and finally, we have the Hartree-Fock equation

$$f\,|\chi_a\rangle = \epsilon_a\,|\chi_a\rangle \tag{2.17}$$

which is an eigenvalue equation that has the spin orbitals as eigenfunctions and the corresponding energies as eigenvalues. Although the exact solutions to this equation give as a result the exact Hartree-Fock spin orbitals, its exact solution is only known for atoms. For molecules, the usual procedure is to use a set of basis functions to expand the spin orbitals and to solve a set of matrix equations[1] that offer an approximate answer. Only as the size of the basis set approaches infinity the approximate spin orbitals approach the exact Hartree-Fock spin orbitals [18].

There is an alternative formalism to describe an analyze many-body systems that contain indistinguishable particles, like electrons, known as second quantization. This approach is mainly used because it allow us to incorporate the essential information in a very succinct way. In

[1]The usual procedure of solution is known as the self-consistent field method, an iterative scheme that involves selecting an approximate Hamiltonian, solving the Schrödinger equation to obtain a more accurate set of orbitals, and then solving the Schrödinger equation again with these until the results converge

it, the single particle operators, as position or momentum, are rewritten to a new basis of operators $\{\hat{c}_r^\dagger, \hat{c}_r\}_{r=1}^{\infty}$ that create and destroy a particle in single particle states $|r\rangle$. We will use this formalism later in this chapter to facilitate the exposition of two post Hartree-Fock methodologies.

Electronic correlation

The term electronic correlation refers to the forces, mostly repulsive, that an electron experience by the presence of the rest of the electrons within an atom or molecule. Within the Hartree-Fock methodology, an electron only senses the rest of electrons in a mean-field manner. That is to say, within the Hartree-Fock approximation, there is no explicit correlation between the position of the electrons.

The energy difference between the one corresponding to the Hartree-Fock solution for an electronic system and the exact one at the non-relativistic limit, usually approximated by means of the Configuration Interaction (CI) procedure, is known as the correlation energy

$$E_{\text{corr}} = E_{\text{exact}} - E_{\text{HF}}. \tag{2.18}$$

Usually, E_{corr} is much, much smaller than E_{HF}, which is an indication about how good an approximation the Hartree-Fock methodology is. However, unfortunately for chemists, often the correlation energy is of the same order of magnitude than the energy involved in the processes that they want to study. It then becomes necessary to use methods beyond Hartree-Fock in order to take into account, at least partially, electronic correlation. Below, maybe the two most common of such methods are promptly summarized.

2.1.1. Rayleigh-Schrödinger perturbation theory

One of the first corrections to be applied over the Hartree-Fock methodology was the use of perturbation theory to approximate the unknown portion of the energy, intuiting that the difference between the exact energy and the Hartree-Fock one was small. The most successful implementation of perturbation theory is the proposed by Møller-Plesset (MP).

The MP methodology is based in the theory of non-degenerated perturbations as introduced by Rayleigh and Schrödinger (RS), which fundamental tenets will be exposed here [19]. First, we assume that our system is described by a time-independent Hamiltonian, $\widehat{H}$, which solves the Schrödinger equation

$$\widehat{H}\psi_i = E_i\psi_i. \tag{2.19}$$

Now, we consider another Hamiltonian, $\widehat{H}^0$, which is slightly different from $\widehat{H}$,

$$\widehat{H} = \widehat{H}^0 + \widehat{H}^p, \tag{2.20}$$

where $\widehat{H}^p$ is a term that can be presumed small. The eigenvalues and eigenfunctions of $\widehat{H}_0$ are known

$$\widehat{H}^0\psi_i^{(0)} = E_i^0\psi_i^{(0)}. \tag{2.21}$$

The system described by $\widehat{H}$ is denominated as "perturbed", the one described by $\widehat{H}^0$ is known as "unperturbed". The RS perturbation theory consists in obtaining the eigenvalues and eigenfunctions of the perturbed system in terms of those of the unperturbed one. It order to do this, a perturbation is gradually applied to produce a continuous change, in such a way as to be able to rewrite equation (2.20) as

$$\widehat{H} = \widehat{H}^0 + \lambda\widehat{H}^p, \tag{2.22}$$

where λ goes from 0, the unperturbed system, up to 1, the perturbed one. The substitution of expression (2.22) in equation (2.19) gives us

$$\widehat{H}\psi_i = (\widehat{H}^0 + \lambda\widehat{H}^p)\psi_i = E_i\psi_i. \tag{2.23}$$

Expanding eigenfunctions and eigenvalues of $\widehat{H}$ as a Taylor series of λ

$$E_i = E_i^{(0)} + \lambda E_i^{(1)} + \lambda^2 E_i^{(2)} + \cdots + \lambda^k E_i^{(k)} + \cdots, \tag{2.24}$$

$$\psi_i = \psi_i^{(0)} + \lambda\psi_i^{(1)} + \lambda^2\psi_i^{(2)} + \cdots + \lambda^k\psi_i^{(k)} + \cdots, \tag{2.25}$$

and using this into equation (2.23) results in

$$(\widehat{H}^0+\lambda\widehat{H}^p)(\psi_i^{(0)}+\lambda\psi_i^{(1)}+\lambda^2\psi_i^{(2)}+\dots) = (E_i^{(0)}+\lambda E_i^{(1)}+\lambda^2 E_i^{(2)}+\dots)(\psi_i^{(0)}+\lambda\psi_i^{(1)}+\lambda^2\psi_i^{(2)}+\dots), \tag{2.26}$$

where $\psi_i^{(k)}$ and $E_i^{(k)}$ are known as *order-k corrections* to the wavefunction and the energy, respectively. It is to be expected that for small perturbations taking into account only the first terms of the expansion will produce a solution that is close enough to the exact one.

If the so called *intermediate normalization* condition is required

$$\langle \psi_i^{(0)} | \psi_i \rangle = 1, \tag{2.27}$$

then, the substitution of equation (2.25) into the expression (2.27) results in

$$1 = \langle \psi_i^{(0)} | \psi_i^{(0)} \rangle + \lambda \langle \psi_i^{(0)} | \psi_i^{(1)} \rangle + \lambda^2 \langle \psi_i^{(0)} | \psi_i^{(2)} \rangle + \cdots . \tag{2.28}$$

The theorem of uniqueness of power series [20] implies that the coefficients of λ for the same power on each side of equation (2.28) must be identical. If we equalize the coefficients we get

$$\langle \psi_i^{(0)} | \psi_i^{(0)} \rangle = 1, \tag{2.29}$$

$$\langle \psi_i^{(0)} | \psi_i^{(n)} \rangle = 0 \quad \text{for } n = 1, 2, 3..., \tag{2.30}$$

which implies that the wavefunction of zero order is orthogonal to the corrections of order one and above to the wavefunction.

In order to obtain expressions of $\psi_i^{(k)}$ and $E_i^{(k)}$, we first multiply both sides of equation (2.26) by $\psi_i^{(0)*}$ and integrate over all the space, and then we separate the coefficients of each power of λ. For powers of λ smaller than three we get

$$\langle \psi_i^{(0)} | \, \widehat{H}^0 \, | \psi_i^{(0)} \rangle = E_i^{(0)} \langle \psi_i^{(0)} | \psi_i^{(0)} \rangle , \tag{2.31}$$

$$\langle \psi_i^{(0)} | \, \widehat{H}^0 \, | \psi_i^{(1)} \rangle + \langle \psi_i^{(0)} | \, \widehat{H}^p \, | \psi_i^{(0)} \rangle = E_i^{(0)} \langle \psi_i^{(0)} | \psi_i^{(1)} \rangle + E_i^{(1)} \langle \psi_i^{(0)} | \psi_i^{(0)} \rangle , \tag{2.32}$$

$$\langle \psi_i^{(0)} | \, \widehat{H}^0 \, | \psi_i^{(2)} \rangle + \langle \psi_i^{(0)} | \, \widehat{H}^p \, | \psi_i^{(1)} \rangle = E_i^{(0)} \langle \psi_i^{(0)} | \psi_i^{(2)} \rangle + E_i^{(1)} \langle \psi_i^{(0)} | \psi_i^{(1)} \rangle + E_i^{(2)} \langle \psi_i^{(0)} | \psi_i^{(0)} \rangle . \tag{2.33}$$

Considering equations (2.29) and (2.30), as well as the following equivalences

$$\langle \psi_i^{(0)} | \, \widehat{H}^0 \, | \psi_i^{(1)} \rangle = E_i^{(0)} \langle \psi_i^{(0)} | \psi_i^{(1)} \rangle = 0, \tag{2.34}$$

$$\langle \psi_i^{(0)} | \, \widehat{H}^0 \, | \psi_i^{(2)} \rangle = E_i^{(0)} \langle \psi_i^{(0)} | \psi_i^{(2)} \rangle = 0, \tag{2.35}$$

$$\tag{2.36}$$

allow us to simplify considerably the expressions (2.31), (2.32) and (2.33) resulting in

$$E_i^{(0)} = \langle \psi_i^{(0)} | \, \widehat{H}^0 \, | \psi_i^{(0)} \rangle , \tag{2.37}$$

$$E_i^{(1)} = \langle \psi_i^{(0)} | \, \widehat{H}^p \, | \psi_i^{(0)} \rangle , \tag{2.38}$$

$$E_i^{(2)} = \langle \psi_i^{(0)} | \, \widehat{H}^p \, | \psi_i^{(1)} \rangle . \tag{2.39}$$

Equations (2.37), (2.38) and (2.39) imply that in order to obtain the correction to the energy of order k it is necessary only to know the correction to the wavefunction of order $k-1$. However, it is possible to show that $\psi_i^{(k)}$ determines the corrections to the energy up to order $2k+1$ [19].

The next step consists in determining the correction to the wavefunction of first order. To that end, we consider the coefficients of λ raised to the first power in equation (2.26)

$$\widehat{H}^0\psi_i^{(1)} + \widehat{H}^p\psi_i^{(0)} = E_i^{(0)}\psi_i^{(1)} + E_i^{(1)}\psi_i^{(0)}. \tag{2.40}$$

When we integrate over all the space after multiplying by $\psi_m^{(0)*}$ we get

$$\langle\psi_m^{(0)}|\,\widehat{H}^0\,|\psi_i^{(1)}\rangle + \langle\psi_m^{(0)}|\,\widehat{H}^p\,|\psi_i^{(0)}\rangle = E_i^{(0)}\,\langle\psi_m^{(0)}|\psi_i^{(1)}\rangle + E_i^{(1)}\,\langle\psi_m^{(0)}|\psi_i^{(0)}\rangle\,. \tag{2.41}$$

Reordering the above expression we get

$$\langle\psi_m^{(0)}|\,\widehat{H}^0\,|\psi_i^{(1)}\rangle - E_i^{(0)}\,\langle\psi_m^{(0)}|\psi_i^{(1)}\rangle = E_i^{(1)}\,\langle\psi_m^{(0)}|\psi_i^{(0)}\rangle - \langle\psi_m^{(0)}|\,\widehat{H}^p\,|\psi_i^{(0)}\rangle\,. \tag{2.42}$$

After considering equation (2.21) and that $\langle\psi_m^{(0)}|\psi_i^{(0)}\rangle = \delta_{mi}$ we arrive at

$$(E_m^{(0)} - E_i^{(0)})\,\langle\psi_m^{(0)}|\psi_i^{(1)}\rangle = E_i^{(1)}\delta_{mi} - \langle\psi_m^{(0)}|\,\widehat{H}^p\,|\psi_i^{(0)}\rangle\,. \tag{2.43}$$

For the case $m = i$, the left-hand side of the previous equation becomes zero and we recover expression (2.38)

$$E_i^{(1)} = \langle\psi_i^{(0)}|\,\widehat{H}^p\,|\psi_i^{(0)}\rangle \tag{2.44}$$

$$= \int \psi_i^{(0)*}\widehat{H}^p\psi_i^{(0)}d\tau. \tag{2.45}$$

On the other hand, if $m \neq i$ then, being $\delta_{mi} = 0$, the equation (2.43) becomes

$$(E_i^{(0)} - E_m^{(0)})\,\langle\psi_m^{(0)}|\psi_i^{(1)}\rangle = \langle\psi_m^{(0)}|\,\widehat{H}^p\,|\psi_i^{(0)}\rangle\,. \tag{2.46}$$

By expressing $|\psi_i^{(1)}\rangle$ as a lineal combination of the basis set $\alpha = \{\psi_m^{(0)}\}$, i.e. the eigenfunctions of $\widehat{H}^{(0)}$, we obtain

$$|\psi_i^{(1)}\rangle = \sum_m a_m\,|\psi_m^{(0)}\rangle$$

$$= \sum_{m\neq i} |\psi_m^{(0)}\rangle\,\langle\psi_m^{(0)}|\psi_i^{(1)}\rangle\,, \tag{2.47}$$

where i is excluded from the sum because of intermediate normalization condition (expression (2.27)). Equations (2.46) and (2.47) imply that

$$\begin{aligned} a_m &= \langle \psi_m^{(0)} | \psi_i^{(1)} \rangle \\ &= \frac{\langle \psi_m^{(0)} | \, \widehat{H}^p \, | \psi_i^{(0)} \rangle}{(E_i^{(0)} - E_m^{(0)})} \qquad \text{with } m \neq i, \end{aligned} \tag{2.48}$$

and hence

$$|\psi_i^{(1)}\rangle = \sum_{m \neq i} \frac{\langle \psi_m^{(0)} | \, \widehat{H}^p \, | \psi_i^{(0)} \rangle}{(E_i^{(0)} - E_m^{(0)})} \, |\psi_m^{(0)}\rangle \, . \tag{2.49}$$

An analogous procedure leads to the second order correction to the wave function. The substitution of equation (2.49) into the expression(2.39) results in

$$E_i^{(2)} = \sum_{m \neq i} \frac{\langle \psi_m^{(0)} | \, \widehat{H}^p \, | \psi_i^{(0)} \rangle}{(E_i^{(0)} - E_m^{(0)})} \, \langle \psi_i^{(0)} | \, \widehat{H}^p \, | \psi_m^{(0)} \rangle \, , \tag{2.50}$$

and given the hermiticity of $\widehat{H}^p$, the previous equation implies that the second order correction to the energy can be written as

$$E_i^{(2)} = \sum_{m \neq i} \frac{| \, \langle \psi_m^{(0)} | \, \widehat{H}^p \, | \psi_i^{(0)} \rangle \, |^2}{(E_i^{(0)} - E_m^{(0)})}. \tag{2.51}$$

2.1.2. Møller-Plesset perturbation theory

The MP perturbation theory is based in the partition of the electronic Hamiltonian

$$\widehat{H}_{\text{elec}} = \widehat{f} + \widehat{\Phi} + h_{\text{nuc}}, \tag{2.52}$$

where $\widehat{f}$ is the Fock operator, h_{nuc} corresponds to the nuclei-nuclei repulsion, and $\widehat{\Phi}$ is the fluctuation operator, which is equal to the electronic repulsion minus Fock's monoelectronic effective potential, which in the language of second quantization is written as

$$\widehat{\Phi} = \frac{1}{2} \sum_{PQRS} g_{PQRS} a_P^\dagger a_R^\dagger a_S a_Q - \sum_{PQ} V_{PQ} a_P^\dagger a_Q. \tag{2.53}$$

being $\widehat{a}_P^\dagger$ y $\widehat{a}_R^\dagger$ and $\widehat{a}_S$ and $\widehat{a}_Q$ creation and annihilation operators, respectively, and where

$$h_{PQ} = \int \chi_p^*(\mathbf{x}) \left(-\frac{1}{2}\nabla^2 - \sum_A \frac{Z_A}{r_A} \right) \chi_q(\mathbf{x}) \mathrm{d}\mathbf{r}, \tag{2.54}$$

$$g_{PQRS} = \int\int \frac{\chi_P^*(\mathbf{x}_1)\chi_Q(\mathbf{x}_1)\chi_R^*(\mathbf{x}_2)\chi_S(\mathbf{x}_2)}{r_{12}} \mathrm{d}\mathbf{x}_1 \mathrm{d}\mathbf{x}_2. \tag{2.55}$$

and χ_P, χ_Q, χ_R and χ_S indicate spin orbitals both occupied and virtual.

The electronic states of order zero are Slater Determinants formed with the spin orbitals that satisfy the Hartree-Fock equations, such that

$$\widehat{f} \left| \mathrm{SD} \right\rangle_i = \sum_j \epsilon_{ji} \left| \mathrm{SD} \right\rangle_i, \tag{2.56}$$

where $\sum_j \epsilon_{ji}$ is the sum of the energies of the occupied spin orbitals in $\left| \mathrm{SD} \right\rangle_i$. The zero order states are all those determinants of the full configuration interaction expansion formed from the Hartree-Fock canonical orbitals.

The application of MP theory on the ground state $\left| \mathrm{SD} \right\rangle_0 = \left| \mathrm{HF} \right\rangle$ together with the Condon-Slater rules [19] lead to the expressions for the zero, first, and second order energies

$$E_{\mathrm{MP0}}^{(0)} = \left\langle \mathrm{HF} \right| \widehat{f} \left| \mathrm{HF} \right\rangle = \sum_I \epsilon_I, \tag{2.57}$$

$$E_{\mathrm{MP1}}^{(1)} = \left\langle \mathrm{HF} \right| \widehat{\Phi} \left| \mathrm{HF} \right\rangle, \tag{2.58}$$

$$\begin{aligned} E_{\mathrm{MP2}}^{(2)} &= \sum_{j \neq 0} \frac{\left| \left\langle \mathrm{HF} \right|_0 \widehat{\Phi} \left| \mathrm{SD} \right\rangle_j \right|^2}{E_0^{(0)} - E_j^{(0)}} \\ &= - \sum_{A>B, I>J} \frac{|g_{AIJB} - g_{AJBI}|^2}{\epsilon_A + \epsilon_B - \epsilon_I - \epsilon_J}, \end{aligned} \tag{2.59}$$

where A y B (I y J) stand for the virtual (occupied) Hartree-Fock spin orbitals, g_{PQRS} are bielectronic integrals.

The Hartree-Fock energy equals the sum of the nuclear repulsion, the zero and first order energies from the Møller-Plesset method

$$\begin{aligned} E_{\mathrm{HF}} &= \left\langle \mathrm{HF} \right| \widehat{H} \left| \mathrm{HF} \right\rangle \\ &= \left\langle \mathrm{HF} \right| \widehat{f} \left| \mathrm{HF} \right\rangle + \left\langle \mathrm{HF} \right| \widehat{\Phi} \left| \mathrm{HF} \right\rangle + \left\langle \mathrm{HF} \right| h_{\mathrm{nuc}} \left| \mathrm{HF} \right\rangle \\ &= E_{\mathrm{MP}}^{(0)} + E_{\mathrm{MP}}^{(1)} + h_{\mathrm{nuc}}, \end{aligned} \tag{2.60}$$

while the correction to this energy according to the MP methodology is given by the expression (2.59) which results in

$$\begin{aligned} E_{\mathrm{MP2}} &= E_{\mathrm{HF}} + E^{(2)}_{\mathrm{MP}} \\ &= E_{\mathrm{HF}} - \sum_{A>B,I>J} \frac{|g_{AIJB} - g_{AJBI}|^2}{\epsilon_A + \epsilon_B - \epsilon_I - \epsilon_J}. \end{aligned} \tag{2.61}$$

2.1.3. The Coupled Cluster method

The coupled cluster (CC) theory is a methodology used to characterize systems of many bodies. It was originally developed to study problems of nuclear physics but later on it was reformulated as a method to take into account the electronic correlation in atoms or molecules.

The wave functions in the Hartree-Fock ($|\mathrm{HF}\rangle$) and CC ($|\mathrm{CC}\rangle$) methodologies are related by the expression

$$|\mathrm{CC}(\mathbf{t})\rangle = e^{\widehat{T}(\mathbf{t})} |\mathrm{HF}\rangle \,, \tag{2.62}$$

where

$$\widehat{T}(\mathbf{t}) = \widehat{T}_1(\mathbf{t}) + \widehat{T}_2(\mathbf{t}) + \widehat{T}_3(\mathbf{t}) + \widehat{T}_4(\mathbf{t}) + \ldots, \tag{2.63}$$

and at the same time the operator $\hat{T}_i(\mathbf{t})$ is a lineal combination of operators with excitation range[2] i. For instance, $\hat{T}_1$ and $\hat{T}_2$ are given by

$$\widehat{T}_1(\mathbf{t}) = \sum_{IA} t_I^A a_A^\dagger a_I, \tag{2.65}$$

$$\widehat{T}_2(\mathbf{t}) = \frac{1}{4} \sum_{IJAB} t_{IJ}^{AB} a_A^\dagger a_I a_B^\dagger a_J, \tag{2.66}$$

where I and J stand for canonical spin orbitals while A and B indicate virtual spin orbitals. The parameters t_I^A and t_{IJ}^{AB} are known as simple and double amplitudes, respectively. The amplitudes

[2]The range of excitation of a chain $\widehat{A}$ of elemental creation and annihilation operators is

$$S = \frac{1}{2}(n_v^c + n_o^a - n_v^a - n_o^c), \tag{2.64}$$

where n_v^c and n_o^c (n_v^a and n_o^a) are the number of operators of creation (annihilation) in $\widehat{A}$ of virtual and occupied Hartree-Fock canonical orbitals, respectively.

are the parameters that form the tensor $\mathbf{t}$ and that determine the wave function $|\mathrm{CC}\rangle$ (equation (2.62)) and hence its associated energy.

In day to day work, the operator $\widehat{T}$ is truncated, which generates a hierarchy of wave functions $|\mathrm{CC}\rangle$

$$\mathrm{CCS}\ \widehat{T} = \widehat{T}_1, \tag{2.67}$$

$$\mathrm{CCSD}\ \widehat{T} = \widehat{T}_1 + \widehat{T}_2, \tag{2.68}$$

$$\mathrm{CCSDT}\ \widehat{T} = \widehat{T}_1 + \widehat{T}_2 + \widehat{T}_3, \tag{2.69}$$

which on its own generates the coupled clusters levels with singles excitations, with singles and doubles excitations, and with singles, doubles and triples excitations (CCS, CCSD, and CCSDT, respectively).

In order to establish the used equations in obtaining the amplitudes $\mathbf{t}$, we can start from the coupled-cluster's Schrödinger equation

$$\widehat{H}e^{\widehat{T}}\,|\mathrm{HF}\rangle = E_{\mathrm{CC}}e^{\widehat{T}}\,|\mathrm{HF}\rangle\,. \tag{2.70}$$

First, the Condon-Slater rules imply that

$$\langle\mathrm{HF}|\,e^{\widehat{T}}\,|\mathrm{HF}\rangle = \langle\mathrm{HF}|\mathrm{HF}\rangle = 1, \tag{2.71}$$

hence, when we multiply equation (2.70) by $\langle\mathrm{HF}|$ we got

$$\langle\mathrm{HF}|\,\widehat{H}e^{\widehat{T}}\,|\mathrm{HF}\rangle = E_{\mathrm{CC}}\,\langle\mathrm{HF}|\mathrm{HF}\rangle = E_{\mathrm{CC}}. \tag{2.72}$$

By expanding the left side of equation (2.72) we arrive to

$$\begin{aligned} E_{\mathrm{CC}} &= \langle\mathrm{HF}|\widehat{H}e^{\widehat{T}}|\mathrm{HF}\rangle \\ &= \langle\mathrm{HF}|\widehat{H}\overbrace{\left(1 + \left(\widehat{T}_1 + \widehat{T}_2 + \widehat{T}_3 + \ldots\right) + \frac{1}{2}\left(\widehat{T}_1 + \widehat{T}_2 + \widehat{T}_3 \ldots\right)^2 + \ldots\right)}^{e^{\widehat{T}}}|\mathrm{HF}\rangle \\ &= \langle\mathrm{HF}|\widehat{H}\left(1 + \widehat{T}_2 + \frac{1}{2}\widehat{T}_1^2\right)|\mathrm{HF}\rangle, \end{aligned} \tag{2.73}$$

where the Condon-Slater rules were used to discard triple and higher excitations as well as the Brillouin theorem [18] to remove single excitations. Even though the energy depends only of

single and double excitations, the presence of higher order excitations change the shape of the equations that determine $\widehat{T}_1$ and $\widehat{T}_2$.

On the other hand, if we multiply the left side of expression (2.70) with the operator $e^{-\widehat{T}}$ we get

$$e^{-\widehat{T}}\widehat{H}e^{\widehat{T}}\left|\mathrm{HF}\right\rangle = E_{\mathrm{CC}}\left|\mathrm{HF}\right\rangle. \tag{2.74}$$

After multiplying both sides of equation (2.74) by *i)* $\langle\mathrm{HF}|$ we arrive to

$$\langle\mathrm{HF}|\, e^{-\widehat{T}}\widehat{H}e^{\widehat{T}}\left|\mathrm{HF}\right\rangle = E_{\mathrm{CC}}, \tag{2.75}$$

or by *ii)* $\langle\mu| = \langle\mathrm{HF}|\,\widehat{T}_\mu^\dagger$, where $\widehat{T}_\mu$ is an excitation operator within the truncated $\widehat{T}$, we obtain

$$\langle\mu|\, e^{-\widehat{T}}\widehat{H}e^{\widehat{T}}\left|\mathrm{HF}\right\rangle = E_{\mathrm{CC}}\left\langle\mu|\mathrm{HF}\right\rangle = 0. \tag{2.76}$$

Expressions (2.76) constitute a coupled set of equations from which the amplitudes that determine the state $|\mathrm{CC}\rangle$ are obtained. This equations can be further simplified by taking into account that:

- The Baker-Campbell-Hausdorff (BCH) expansion [21] of $e^{-\widehat{T}}\widehat{H}e^{\widehat{T}}$

$$e^{-\widehat{T}}\widehat{H}e^{\widehat{T}} = \widehat{H} + [H,\widehat{T}] + \frac{1}{2}[[\widehat{H},\widehat{T}],\widehat{T}] + \frac{1}{3!}[[[\widehat{H},\widehat{T}],\widehat{T}],\widehat{T}] + \frac{1}{4!}[[[[\widehat{H},\widehat{T}],\widehat{T}],\widehat{T}],\widehat{T}], \tag{2.77}$$

  for which it is possible to show that because $\widehat{H}$ is a lineal combination of operators of range 1 and 2[3]. The rest of the nested commuters in the BCH expansion of expression (2.77) are equal to 0.

- The fact that if m_0 is the range of the operator $\widehat{\mathscr{O}}$, then the ket

$$[[...[[\widehat{\mathscr{O}},\widehat{T}_{n_1}],\widehat{T}_{n_2}],...],T_{n_k}]\left|\mathrm{HF}\right\rangle,$$

[3]The range of a chain $\widehat{A}$ of creation and annihilation operators is the number of creation and annihilation elemental operators divided by two.

is a lineal combination of Slater determinants with excitations s within the interval

$$\sum_{i=1}^{k} n_i - m_0 \leq s \leq \sum_{i=1}^{k} n_i + m_0 - k. \tag{2.78}$$

Considering the expressions (2.77) and (2.78) we get, for instance, the equations for the single and double amplitudes of CCSD

$$\begin{aligned}
&\langle \mu_1 | \, \widehat{H} \, | \mathrm{HF} \rangle + \langle \mu_1 | \, [\widehat{H}, \widehat{T}_1] \, | \mathrm{HF} \rangle + \langle \mu_1 | \, [\widehat{H}, \widehat{T}_2] \, | \mathrm{HF} \rangle + \frac{1}{2} \langle \mu_1 | \, [[\widehat{H}, \widehat{T}_1], \widehat{T}_1] \, | \mathrm{HF} \rangle \\
&+ \langle \mu_1 | \, [[\widehat{H}, \widehat{T}_1], \widehat{T}_2] \, | \mathrm{HF} \rangle + \frac{1}{6} \langle \mu_1 | \, [[[\widehat{H}, \widehat{T}_1], \widehat{T}_1], \widehat{T}_1] \, | \mathrm{HF} \rangle = 0, \qquad (2.79) \\
&\langle \mu_2 | \, \widehat{H} \, | \mathrm{HF} \rangle + \langle \mu_2 | \, [\widehat{H}, \widehat{T}_1] \, | \mathrm{HF} \rangle + \langle \mu_2 | \, [\widehat{H}, \widehat{T}_2] \, | \mathrm{HF} \rangle + \frac{1}{2} \langle \mu_2 | \, [[\widehat{H}, \widehat{T}_1], \widehat{T}_1] \, | \mathrm{HF} \rangle \\
&+ \langle \mu_2 | \, [[\widehat{H}, \widehat{T}_1], \widehat{T}_2] \, | \mathrm{HF} \rangle + \frac{1}{2} \langle \mu_2 | \, [[\widehat{H}, \widehat{T}_2], \widehat{T}_2] \, | \mathrm{HF} \rangle + \frac{1}{6} \langle \mu_2 | \, [[[\widehat{H}, \widehat{T}_1], \widehat{T}_1], \widehat{T}_1] \, | \mathrm{HF} \rangle \\
&+ \frac{1}{2} \langle \mu_2 | \, [[[\widehat{H}, \widehat{T}_1], \widehat{T}_1], \widehat{T}_2] \, | \mathrm{HF} \rangle + \frac{1}{24} \langle \mu_2 | \, [[[[\widehat{H}, \widehat{T}_1], \widehat{T}_1], \widehat{T}_1], \widehat{T}_1] \, | \mathrm{HF} \rangle = 0. \qquad (2.80)
\end{aligned}$$

2.2. Density Functional Theory

The density functional theory approximation is an alternative formulation of quantum mechanics that has the electronic density as its fundamental variable. It essentially tries to replace the complicated N-electron wave function (which depends on 3N spatial plus N spin variables) by the much simpler electron density. It states that there is a universal functional that relates the electronic density with the energy of the system. This idea has its inception in the Thomas-Fermi model and in the Slater approximation of Hartree-Fock exchange. However, it was until Hohenberg and Kohn formulated their now famous theorems that DFT as we know it today was born. The theorems state that [22]:

- The external potential $V_{ext}(\mathbf{r})$ is a unique functional[4] of $\rho(\mathbf{r})$.
- The ground state energy can be obtained variationally: the density that minimizes the total energy is the exact ground state density[5].

The first theorem offers a recipe for obtaining the electronic energy of the ground state as a function of $\rho(\mathbf{r})$. The electronic density determines the external potential, $V_{ext}(\mathbf{r})$. From

[4] In mathematics, a functional is a map from vector space to its field of scalars.

[5] Although the original theorems are only valid for non-degenerate ground states in the absence of a magnetic field, they have been generalized out of those limitations [23].

the external potential we can form the Hamiltonian of the system, which allow us to get the corresponding wave function, and solving the equations we obtain the electronic energy. Thus, the electronic energy (and all other properties of the system) has to be a unique functional of the density. This can be better understood by following the scheme in figure 2.1.

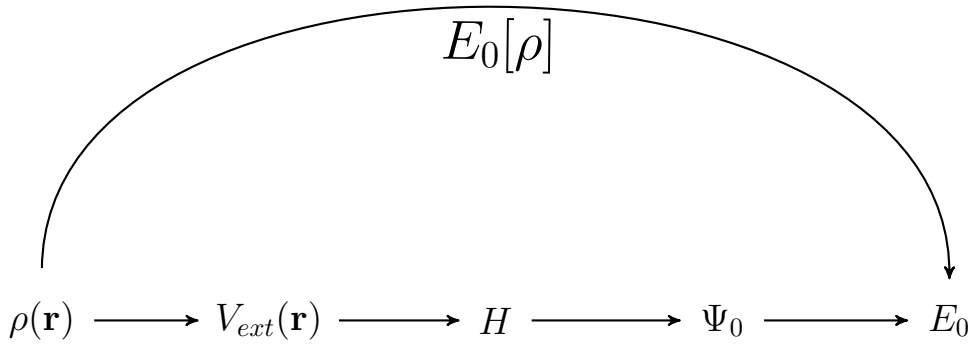

Figure 2.1: Scheme of the relationships between density, external potential, Hamiltonian, wave-function, and Energy.

Given that the ground state energy is a functional of the ground state electronic density, its individual components have to be as well, resulting in

$$\mathrm{E}_0[\rho] = \mathrm{T}[\rho_0] + \mathrm{E}_{\mathrm{ee}}[\rho_0] + \mathrm{E}_{\mathrm{Ne}}[\rho_0], \tag{2.81}$$

where $T[\rho_0]$, $E_{ee}[\rho_0]$, and $E_{Ne}[\rho_0]$ are the kinetic energy, the electron-electron repulsion, and the electron-nuclei attraction, respectively.

We can rearrange the terms of equation 2.81 in order to separate those that depend on the system itself and those which are independent of the number of electrons, atomic number, or distance to the nuclei. Considering then the electron-nuclei attraction as $E_{Ne}[\rho_0] = \int \rho_0(\mathbf{r}) V_{\mathrm{Ne}} d\mathbf{r}$ and the two remaining terms as the Hohenberg-Kohn functional, $F_{HK}[\rho_0(\mathbf{r})]$, we get to

$$\mathrm{E}_0[\rho] = \mathrm{F}_{\mathrm{HK}}[\rho_0(\mathbf{r})] + \int \rho_0(\mathbf{r}) V_{\mathrm{Ne}} d\mathbf{r} \tag{2.82}$$

A characteristic of the Hohenberg-Kohn functional is that when it is fed with some arbitrary density it returns the expectation value

$$F_{HK}[\rho] = T + V_{ee} = \langle \Psi | \hat{T} + \hat{V}_{ee} | \Psi \rangle \,. \tag{2.83}$$

Now, the second Hohenberg and Kohn theorem indicates that if we use a trial density we will always obtain an energy larger or equal than the one we would obtain using the ground density of the system, i.e. the variational principle. This is, a trial density follows the next equation:

$$E_0 \leq E[\tilde{\rho}] \tag{2.84}$$

and represents an upper bound to the true ground state energy.

Any trial density defines its own Hamiltonian and hence its own wave function. We can then use the trial wave function on the exact Hamiltonian in order to approximate the solution for the ground state energy as

$$\langle \tilde{\Psi} | \hat{H} | \tilde{\Psi} \rangle = E[\tilde{\rho}] \geq E_0 = \langle \Psi_0 | \hat{H} | \Psi_0 \rangle \,. \tag{2.85}$$

Summarizing, all the properties of a system defined by an external potential V_{ext} are determined by the ground state density. For the energy, we obtain its minimum value if and only if we use the true ground state density. However, from a practical point of view this is of little help since the problem is as hard to solve as before. The Hohenberg and Kohn theorems only tell us that there is a unique mapping, the Hohenberg-Kohn functional, between the ground state density, $\rho(\mathbf{r})$, and the ground state energy, E_0. Beyond this proof of existence, the theorems offer no guidance at all about how said functional could be build. They do not even give a clue regarding the kind of approximations that should be used to construct the unknown functional.

2.2.1. The Kohn-Sham approach

In a breaking contribution in 1965 Kohn and Sham introduced a way to approximate the unknown, universal functional in a practical way [24]. They realized that most of the problems with the construction of density functionals resided in how the kinetic energy of the system is determined. Noticing that the Hartree-Fock methodology perform the estimation of this energy well enough, Kohn and Sham introduced the concept of non-interacting reference system built from one electron functions as a way to compute the major part of the kinetic energy. Then, they suggested that the remainder had to be merged with the non-classical contributions to the

electron-electron repulsion. By doing this, the Kohn-Sham method leaves only a very small part of the energy to be determined by an approximate functional.

The first step then is to build the non-interacting system. For this, we compute the kinetic energy in the same way as in the Hartree-Fock approximation:

$$\mathrm{T_s} = -\frac{1}{2}\sum_{\mathrm{i}}^{\mathrm{N}} \langle\phi|\nabla^2|\phi\rangle\,. \tag{2.86}$$

We separate the electron-electron repulsion of Hohenberg and Kohn functional in two parts, a classic, or Coulombic, and a non-classic

$$\mathrm{E_{ee}}[\rho] = \mathrm{J}[\rho] + \mathrm{E_{ncl}}[\rho], \tag{2.87}$$

and the total kinetic energy as the sum of the non-interaction kinetic energy and the difference between them

$$\mathrm{T}[\rho] = \mathrm{T_s}[\rho] + \mathrm{T_c}[\rho]. \tag{2.88}$$

Then, we can define the exchange-correlation energy as the sum of the differences of the kinetic and the non-interacting kinetic energies, and the electron-electron repulsion and its Coulombic interaction

$$\mathrm{E_{XC}}[\rho] \equiv (\mathrm{T}[\rho] - \mathrm{T_s}[\rho]) + (\mathrm{E_{ee}}[\rho] - \mathrm{J}[\rho]) = \mathrm{T_c}[\rho] + \mathrm{E_{ncl}}. \tag{2.89}$$

This is, the exchange-correlation term is the functional that contains everything that is unknown, the non-classical effects of self-interaction correction, exchange and correlation, and a portion of the kinetic energy that is not encompassed by $\mathrm{T_s}$.

Now, we can rewrite the equation (2.81) as

$$\mathrm{E}[\rho] = \mathrm{T_s}[\rho] + \mathrm{J}[\rho + \mathrm{E_{XC}}[\rho] + \mathrm{E_{Ne}}[\rho]. \tag{2.90}$$

Here the only unknown term is $\mathrm{E_{XC}}[\rho]$. Now, in a similar fashion to what is done in the Hartree-Fock approximation, we apply the variational principle to determine the equations needed to solve this problem given the constrain of $\langle\phi_i|\phi_j\rangle = \delta_{ij}$. We arrive to the Kohn-Sham equations

$$\left(-\frac{1}{2}\nabla^2\left[\int\frac{\rho(\mathrm{r}_2)}{\mathrm{r}_{12}}\mathrm{dr}_2+\mathrm{V_{XC}}(\mathrm{r}_1)-\sum_{\mathrm{A}}^{\mathrm{M}}\frac{\mathrm{Z_A}}{\mathrm{r_{1A}}}\right]\right)\phi_\mathrm{i}=\left(-\frac{1}{2}\nabla^2+\mathrm{V_{eff}}(\mathrm{r}_1)\right)\phi_\mathrm{i}=\epsilon_\mathrm{i}\phi_\mathrm{i}. \tag{2.91}$$

where the term $\mathrm{V_{XC}}$ is the potential due to the exchange-correlation energy term. Given that we do not know how to compute this energy, we of course have no idea of the shape of the corresponding potential, and thus simply define it as the functional derivative of $\mathrm{E_{XC}}$ with respect to ρ, or

$$\mathrm{V_{XC}}\equiv\frac{\delta E_{XC}}{\delta\rho}. \tag{2.92}$$

It is important to note that $\mathrm{V_{eff}}$ depends, through the Coulomb term, on the density and hence of the orbitals. As a consequence, the Kohn-Sham equations have to be solved iteratively.

The problem of DFT for scientists then resides in finding a way to approach the unknown exchange-correlation functional. Many different strategies have been tried so far with different degrees of success. Regarding the strategies there are two schools of thought. The first one claims that a functional has to be universal and be derived from first principles. The second one says that it is acceptable to use empirical data in the construction of functionals if that improves the results.

The first principles school advances the construction of functionals by making them fulfill certain criteria and including more terms in them. In the earliest approximations the functional depended only of the local density (LDA). Subsequent developments included not only the density but its first derivative and are known as generalized gradient approximations (GGA). Finally, meta-GGA DFT functional are those that go beyond and include the second derivative of the electron density.

The most famous functional developed so far by the second school of though is B3LYP, which uses three empirical parameters in its formulation to fit the results of other, more complex, calculations [25]. B3LYP was developed in the decade of 1990 and its structure is somewhat simple. The functionals developed nowadays, as those introduced by the group of Donald Thrular [26], can have up to hundreds of parameters and are usually fitted to huge sets of data.

2.3. Quantum Theory of Atoms in Molecules

Everything is in the charge density, $\rho(\mathbf{r})$, because it is the physical manifestation of the forces acting within the system [27]. This is the central proposition within the Quantum Theory

of Atoms in Molecules (QTAIM), a theory dedicated to link physical quantities to chemical concepts, such as atom and bond, to physical observables through the topology of the charge density.

The QTAIM is based on a topological analysis of $\rho(\mathbf{r})$. According to QTAIM, within a molecule, each nucleus generates a substantial local cusp of the charge density at its position [28]. This way, the space of a molecule is partitioned into disjoint regions, Ω, each containing an nucleus, that can be identified with an atom.

The separation between regions is determined by the gradient of the electronic density, $\nabla\rho(\mathbf{r})$, which can be characterized by its flux lines, which are trajectories $\sigma(t) : R \to R^n$ defined by the expression $\sigma'(t) = \nabla\rho(\sigma(t))$. Within each atom, this flux lines point towards each nuclei, while at the frontier between atoms, the flux lines satisfy the zero-flux condition:

$$\nabla\rho(\mathbf{r}) \cdot \widehat{\mathbf{n}} = 0 \tag{2.93}$$

where $\widehat{\mathbf{n}}$ is a unitary vector that is normal to the boundaries separating the basins Ω. These frontiers are denominated interatomic surfaces.

The basins enclosed by a zero flux surface are proper quantum subsystems and therefore, atomic average values of quantum observables can be calculated. For example, the charge of an atom Ω is given by

$$q(\Omega) = Z_\Omega - \int_\Omega \rho(\mathbf{r})\mathrm{d}\mathbf{r} \tag{2.94}$$

while the atomic dipole reads

$$\mu_\alpha(\Omega) = -\int_\Omega r_\alpha \rho(\mathbf{r})\mathrm{d}\mathbf{r} \tag{2.95}$$

wherein Z_Ω is the atomic number of Ω and α denotes a Cartesian component.

2.3.1. Critical points

The topological properties of the electronic density can be investigated in a convenient way by studying its critical points. A critical point, $\mathbf{r_c}$, of a scalar field is that point where its gradient is equal to the zero vector:

$$\nabla\rho(\mathbf{r_c}) = \frac{\partial\rho(\mathbf{r_c})}{\partial x}\mathbf{i} + \frac{\partial\rho(\mathbf{r_c})}{\partial y}\mathbf{j} + \frac{\partial\rho(\mathbf{r_c})}{\partial z}\mathbf{k} = 0. \tag{2.96}$$

Table 2.1: Types of stable critical points of the charge density, $\rho(\mathbf{r})$.

(ω, σ)	Description
(3,-3)	All the curvatures are negative and ρ is a local maximum of $\mathbf{r}$. They are identified with nuclei.
(3,-1)	Two curvatures are negative and the third is positive. This is, it is a maximum on the plane defined by the first two axis while in the third axis is a minimum. They are identified with bonds.
(3,+1)	Two curvatures are positive and the third is negative. It corresponds to a minimum on the plane formed by the first to axis while it is a maximum in the third axis. They are identified with rings.
(3,+3)	All the curvatures are positive and ρ is a local minimum. They are identified with cages.

For a critical point, it is possible to know if it is a local minimum, local maximum, or a saddle point by examining the second derivatives of the scalar field on its position. In three dimensions, the Hessian produced by the second derivatives is a nine-element matrix that can be diagonalized to produce three eigenvalues, λ_1, λ_2, and λ_3, that correspond to the curvatures with respect to the three principal axis. Notice that the Laplacian of the density, $\nabla^2\rho(\mathbf{r})$, is equal to the trace of the Hessian matrix.

The critical points of the charge density can be classified according to its range and firm. The range, ω, refers to the number of curvatures of ρ at point $\mathbf{r_c}$ different from zero. A critical point with $\omega < 3$ is unstable with regards to any minimal perturbation of the density, like one generated by an infinitesimal change in the position of the nuclei. This kind of critical points are indicative of a change in the topology of the density and hence of a change in the molecular structure and are in systems close to equilibrium. The firm, σ, is the sum of the signs of the curvatures of the critical point. Thus, there are four types of stable critical points that are shown in table some table 2.1.

Each type of critical point are related with an element of chemical structure. The points characterized as (3,-3) are related with electronic density attractors as the nuclei. The points (3,-1) are known as bond critical points (BCP), the points (3,+1) as ring critical points, and those signaled as (3,+3) are the cage critical points. They are known as such because they coincide with the corresponding structural elements.

Among the types of critical points, the most important one for describing the interaction

between two atoms is the BCP. Every flux line of $\nabla\rho(\mathbf{r})$ in an interatomic surface ends in a BCP. There are also two pairs of trajectories that start at a BCP and finish at two different nuclei. These pair of trajectories are known as a bond path. The existence of a bond path and a BCP linking two nuclei has been used as an indicator of a chemical bond between the corresponding atoms [29]. This issue has caused some controversy in the literature [30; 31; 32], however, the use of different descriptors related with the BCP in the characterization of an interatomic interaction is not that controversial.

The simplest descriptor of this kind is the value of the electron density at the BCP. It has a direct relationship with the strength of the interaction between two atoms, i.e. larger electron density at the BCP indicates a stronger interaction. Another useful descriptor is the Laplacian of the density. For covalent interactions $\nabla^2\rho(\mathbf{r})$ is large and negative, while for closed-shell interactions its value is positive [28]. The density and the Laplacian at the BCP are convenient descriptors for compounds with conventional bonds, like most organic molecules, however, for systems where the bonding situation is not as simple other physical quantities are usually needed.

For instance, for transition metal complexes, one kind of system widely studied in the present thesis, the value of both the density and the Laplacian at the BCP are small because of the diffuse nature of its electron distribution, which reduce the utility of those quantities as descriptors. Instead, we can study the type of interaction by determining the kind of energy, kinetic or potential that dominates locally. One way to assess this is to compute the energy density at the BCP, H, i.e. the sum of the kinetic energy density, G, which is always positive, and the potential energy density, V, which is always negative. An interaction could be considered as covalent if $H > 0$ ($H < 0$), and indication that the kinetic (potential) energy dominates [33]. Another quantity that assess which type of energy dominates is the ratio between the potential and the kinetic energy at the BCP, $|V_{BCP}|/G_{BCP}$. For closed-shell interactions this ratio would be of less than one and for covalent ones it is larger than 2. The interactions where the ratio sits between 1 and 2 can be considered as intermediate [34].

Finally, the ellipticity is an assessment of how the density is preferentially accumulated in a given plane containing the bond path. It is calculated as the deviation of the density distribution along the bond from a cylindrical shape as

$$\epsilon = \frac{\lambda_1}{\lambda_2} - 1 \quad \text{with } |\lambda_1| \geq |\lambda_2|. \tag{2.97}$$

where λ_1 and λ_2 are the eigenvalues of the Hessian matrix of the second derivatives of the

density. If $\lambda_1 = \lambda_2$ then $\epsilon = 0$ and the bond is perfectly cylindrical, like in the case of the C-C bond in ethane. For reference, the double C-C bond in ethylene has an ellipticity of 0.45. Thus, computing ellipticity provides a reasonable way to study the amount of π character in a bond [28].

2.3.2. Localization and delocalization indices

Electron localization and delocalization indices can be obtained by considering the Fermi and Coulomb holes as the difference between the pair density, $\rho_2(\mathbf{r}_1, \mathbf{r}_2)$ and the product of independent densities $\rho(\mathbf{r}_1)$ and $\rho(\mathbf{r}_2)$

$$\rho(\mathbf{r}_1)\rho(\mathbf{r}_2)f(\mathbf{r}_1, \mathbf{r}_2) = \rho_2(\mathbf{r}_1, \mathbf{r}_2) - \rho(\mathbf{r}_1)\rho(\mathbf{r}_2) \tag{2.98}$$

A necessary and sufficient condition to have a certainty in the number of electrons in Ω, i.e. that every measurement of the number of electrons inside the basin Ω yields $N(\Omega)$, is given by

$$|F(\Omega, \Omega)| = \int_\Omega \rho(\mathbf{r})\mathrm{d}\mathbf{r} = N(\Omega) \tag{2.99}$$

wherein

$$F(\Omega, \Omega) = \int_\Omega \int_\Omega \rho(\mathbf{r}_1)\rho(\mathbf{r}_2)f(\mathbf{r}_1, \mathbf{r}_2)\mathrm{d}\mathbf{r}_1\mathrm{d}\mathbf{r}_2 \tag{2.100}$$

According with 2.99, the condition that the probability of finding $N(\Omega)$ electrons in Ω be equal to 1 or, equivalently, that there are $N(\Omega)$ electrons localized in Ω, requires that the Fermi and Coulomb holes of an electron in Ω is completely contained in this basin. Hence, the localization index, $\lambda(\Omega)$, inside the basin Ω is

$$\lambda(\Omega) \equiv |F(\Omega, \Omega)| \tag{2.101}$$

Similarly, the delocalization index, $\delta(\Omega, \Omega')$ is defined in terms of the integrals of the Fermi and Coulomb holes in regions Ω and Ω' as

$$\delta(\Omega, \Omega') \equiv |F(\Omega, \Omega')| + |F(\Omega', \Omega)| \tag{2.102}$$

in which

$$F(\Omega, \Omega') = \int_\Omega \int_{\Omega'} \rho(\mathbf{r}_1)\rho(\mathbf{r}_2)f(\mathbf{r}_1, \mathbf{r}_2)\mathrm{d}\mathbf{r}_1\mathrm{d}\mathbf{r}_2 \tag{2.103}$$

The fact that $f(\mathbf{r}_1, \mathbf{r}_2)$ is a symmetric function i.e, $f(\mathbf{r}_1, \mathbf{r}_2) = f(\mathbf{r}_2, \mathbf{r}_1)$ implies $|F(\Omega, \Omega')| = |F(\Omega', \Omega)|$. The normalization of the Fermi and Coulomb hole involved in equation 2.98

$$\int\int \rho(\mathbf{r}_1)\rho(\mathbf{r}_2)f(\mathbf{r}_1, \mathbf{r}_2) = -N \tag{2.104}$$

and the definitions of the indices $\lambda(\Omega)$ and $\delta(\Omega, \Omega')$ in equations 2.101 and 2.102 imply

$$N = \sum_{\Omega} N(\Omega) = \sum_{\Omega} \lambda(\Omega) + \frac{1}{2}\sum_{\Omega \neq \Omega'} \delta(\Omega, \Omega') \tag{2.105}$$

which means that the electrons in a molecular system can be divided in those localized in the basins, i.e., $\sum_{\Omega} \lambda(\Omega)$ and those delocalized between two basins, i.e., $\frac{1}{2}\sum_{\Omega' \neq \Omega} \delta(\Omega, \Omega')$. The larger the delocalization index between two basins, Ω and Ω', the more covalent the interaction between these two basins [35] and therefore $\delta(\Omega, \Omega')$ is useful to characterize both intra- and intermolecular interactions.

2.4. Interacting Quantum Atoms approach

The Interacting Quantum Atoms approach is a QCT methodology that allows for the partition of the total electronic energy of a multielectronic system into intra- and interatomic terms, thus allowing the measurement of individual interactions within a molecule. This is possible by explicitly computing the one- and two-electron contributions to the total energy by means of operating over the corresponding density matrices [36]: the first order reduced density matrix, $\rho_1(\mathbf{r}_1; \mathbf{r}_1{}')$ and the pair density, $\rho_2(\mathbf{r}_1, \mathbf{r}_2)$.

Under the Born-Oppenheimer approximation, we can compute the total electronic energy in terms of $\rho_1(\mathbf{r}_1; \mathbf{r}_1{}')$ and $\rho_2(\mathbf{r}_1, \mathbf{r}_2)$ using the following expression:

$$E_{\text{elec}} = \frac{1}{2}\sum_{A \neq B} \frac{Z_A Z_B}{r_{AB}} + \int \widehat{h}\rho_1(\mathbf{r}_1; \mathbf{r}_1{}')\mathrm{d}\mathbf{r}_1 + \frac{1}{2}\int\int \frac{\rho_2(\mathbf{r}_1, \mathbf{r}_2)}{r_{12}}\mathrm{d}\mathbf{r}_1\mathrm{d}\mathbf{r}_2, \tag{2.106}$$

$$E_{\text{elec}} = V_{\text{nn}} + \langle \widehat{T} + \widehat{V}_{\text{ne}} \rangle + \langle \widehat{V}_{\text{ee}} \rangle, \tag{2.107}$$

where the monoelectronic part of the Hamiltonian corresponds to the sum of the kinetic energy ($\widehat{T}$) and the nuclei-electron attraction ($\widehat{V}_{\text{ne}}$). In other words, $\widehat{h} = \widehat{T} + \widehat{V}_{\text{ne}}$, while Z_X, $\widehat{V}_{\text{nn}}$ and $\widehat{V}_{\text{ee}}$ are the atomic number of X, the nuclei-nuclei repulsion, and the electron-electron repulsion operator, respectively.

If we use the space partition proposed by QTAIM, we can rewrite equation 2.106 in terms of the interaction between disjoint regions Ω_A as:

$$\begin{aligned} E_{elec} &= \frac{1}{2}\sum_{A\neq B}\frac{Z_A Z_B}{r_{AB}} - \frac{1}{2}\int \nabla^2\rho_1(\mathbf{r}_1;\mathbf{r}_1{}')\mathrm{d}\mathbf{r}_1 - \sum_A \int \frac{Z_A\rho(\mathbf{r}_1)}{r_{1A}}\mathrm{d}\mathbf{r}_1 + \frac{1}{2}\int\int\frac{\rho_2(\mathbf{r}_1,\mathbf{r}_2)}{r_{12}}\mathrm{d}\mathbf{r}_1\mathrm{d}\mathbf{r}_2, \\ &= \frac{1}{2}\sum_{A\neq B}\frac{Z_A Z_B}{r_{AB}} - \frac{1}{2}\sum_A\int_A \nabla^2\rho_1(\mathbf{r}_1;\mathbf{r}_1{}')\mathrm{d}\mathbf{r}_1 - \sum_{AB}\int_B \frac{Z_A\rho(\mathbf{r}_1)}{r_{1A}}\mathrm{d}\mathbf{r}_1 + \frac{1}{2}\sum_{AB}\int_A\int_B\frac{\rho_2(\mathbf{r}_1,\mathbf{r}_2)}{r_{12}}\mathrm{d}\mathbf{r}_1\mathrm{d}\mathbf{r}_2, \\ &= \frac{1}{2}\sum_{A\neq B}V_{\mathrm{nn}}^{AB} + \sum_A T_A + \sum_A V_{\mathrm{ne}}^{AA} + \sum_{A\neq B}V_{\mathrm{ne}}^{AB} + \sum_A V_{\mathrm{ee}}^{AA} + \frac{1}{2}\sum_{A\neq B}V_{\mathrm{ee}}^{AB}, \end{aligned} \tag{2.108}$$

where

$$V_{\mathrm{nn}}^{AB} = \frac{Z_A Z_B}{r_{AB}}, \tag{2.109}$$

$$T_A = -\frac{1}{2}\int_A \nabla^2\rho_1(\mathbf{r}_1;\mathbf{r}_1{}')\mathrm{d}\mathbf{r}_1, \tag{2.110}$$

$$V_{\mathrm{ne}}^{AB} = -Z_A\int_B\frac{\rho(\mathbf{r}_1)}{r_{1A}}\mathrm{d}\mathbf{r}_1, \tag{2.111}$$

$$V_{\mathrm{ee}}^{AB} = \frac{2-\delta_{AB}}{2}\int_A\int_B\frac{\rho_2(\mathbf{r}_1,\mathbf{r}_2)}{r_{12}}\mathrm{d}\mathbf{r}_1\mathrm{d}\mathbf{r}_2. \tag{2.112}$$

If we regroup the monoatomic terms we can rewrite the energy of each atom, as:

$$E_{\mathrm{net}}^A = T^A + V_{\mathrm{ne}}^{AA} + V_{\mathrm{ee}}^{AA}. \tag{2.113}$$

Using a similar procedure it is possible to separate those terms that correspond to the interaction energy between two atoms, which produce the following expression:

$$E_{\mathrm{int}}^{AB} = V_{\mathrm{nn}}^{AB} + V_{\mathrm{ne}}^{AB} + V_{\mathrm{ne}}^{BA} + V_{\mathrm{ee}}^{AB}. \tag{2.114}$$

If we add equations (2.113) and (2.114) for each atom and pair of atoms within a molecule we reach the next form for the electronic energy:

$$E_{\mathrm{elec}} = \sum_A E_{\mathrm{net}}^A + \frac{1}{2}\sum_{A\neq B}E_{\mathrm{int}}^{AB}. \tag{2.115}$$

Equation (2.115) is the central tenet of the IQA procedure, as it allows the dissection of E_{elec} into its intra and interatomic parts. In the same vein, we can now consider atoms as part of different groups $\mathscr{G}, \mathscr{H}, \mathscr{I}\ldots$ Thus, we can define the energy of a group, $\mathscr{G}$, as:

$$E_{\text{net}}^{\mathscr{G}} = \sum_{A\in\mathscr{G}} E_{\text{net}}^{A} + \frac{1}{2}\sum_{A\in\mathscr{G}}\sum_{\substack{B\in\mathscr{G}\\B\neq A}} E_{\text{int}}^{AB}, \tag{2.116}$$

while the interaction energy between two groups corresponds to the expression:

$$E_{\text{int}}^{\mathscr{G}\mathscr{H}} = \sum_{A\in\mathscr{G}}\sum_{B\in\mathscr{H}} E_{\text{int}}^{AB}. \tag{2.117}$$

Reorganizing the atoms into groups this way allows us to get an equation similar to equation (2.115) for the electronic energy, but in this case as a function of the energy of each group and the interaction energy between the groups:

$$E_{\text{elec}} = \sum_{\mathscr{G}} E_{\text{net}}^{\mathscr{G}} + \frac{1}{2}\sum_{\mathscr{G}\neq\mathscr{H}} E_{\text{int}}^{\mathscr{G}\mathscr{H}}. \tag{2.118}$$

The ability of IQA to separate the electronic system into groups is particularly convenient for the study of non-additive contributions, such as the non-covalent interactions between two atoms or molecules when a third species is present.

Another important concept in the IQA approximation is the so called *deformation energy*. If the groups $\mathscr{G}, \mathscr{H}, \mathscr{I}\ldots$ represent molecules, it is possible to express the energy associated to the formation of the molecular cluster $\mathscr{G}\cdots\mathscr{H}\cdots\mathscr{I}$ as:

$$\begin{aligned}
E_{\text{form}} &= E^{\mathscr{G}\cdots\mathscr{H}\cdots\mathscr{I}\cdots} - \left(E_{\text{ais}}^{\mathscr{G}} + E_{\text{ais}}^{\mathscr{H}} + E_{\text{ais}}^{\mathscr{I}} + \ldots\right)\\
&= \sum_{\mathscr{G}} E_{\text{net}}^{\mathscr{G}} + \frac{1}{2}\sum_{\mathscr{G}}\sum_{\mathscr{H}\neq\mathscr{G}} E_{\text{int}}^{\mathscr{G}\mathscr{H}} - \left(E_{\text{ais}}^{\mathscr{G}} + E_{\text{ais}}^{\mathscr{H}} + E_{\text{ais}}^{\mathscr{I}} + \ldots\right)\\
&= \sum_{\mathscr{G}} (E_{\text{net}}^{\mathscr{G}} - E_{\text{iso}}^{\mathscr{G}}) + \frac{1}{2}\sum_{\mathscr{G}}\sum_{\mathscr{H}\neq\mathscr{G}} E_{\text{int}}^{\mathscr{G}\mathscr{H}}\\
&= \sum_{\mathscr{G}} E_{\text{def}}^{\mathscr{G}} + \frac{1}{2}\sum_{\mathscr{G}}\sum_{\mathscr{H}\neq\mathscr{G}} E_{\text{int}}^{\mathscr{G}\mathscr{H}}.
\end{aligned} \tag{2.119}$$

In expression (2.119), $E_{\text{iso}}^{\mathscr{G}}$ represents the energy of an isolated molecule of $\mathscr{G}$, while the deformation energy is computed as:

$$E_{\text{def}}^{\mathscr{G}} = E_{\text{net}}^{\mathscr{G}} - E_{\text{iso}}^{\mathscr{G}}, \tag{2.120}$$

This energy is the representation of the distortion happening upon the electronic density of a system when it interacts with other atoms or molecules. Equation (2.119) suggest that generating a molecular cluster can be considered as a two-steps virtual process where in the first step

the electronic density is distorted and the position of the nuclei is modified with regards to the configuration of the isolated molecule while the second step corresponds to the interaction between the resulting, deformed species.

It is possible to obtain a more complete picture of the intra- and intermolecular interactions if we separate the pair density into its Coulombic (ρ_2^{C}), exchange (ρ_2^{X}) and correlation (ρ_2^{corr}) parts:

$$\begin{aligned}\rho_2(\mathbf{r}_1,\mathbf{r}_2) &= \rho_2^{\mathrm{C}}(\mathbf{r}_1,\mathbf{r}_2) + \rho_2^{\mathrm{X}}(\mathbf{r}_1,\mathbf{r}_2) + \rho_2^{\mathrm{corr}}(\mathbf{r}_1,\mathbf{r}_2) \\ &= \rho_2^{\mathrm{C}}(\mathbf{r}_1,\mathbf{r}_2) + \rho_2^{\mathrm{xc}}(\mathbf{r}_1,\mathbf{r}_2),\end{aligned} \tag{2.121}$$

where

$$\rho_2^{\mathrm{C}}(\mathbf{r}_1,\mathbf{r}_2) = \rho(\mathbf{r}_1)\rho(\mathbf{r}_2), \tag{2.122}$$

$$\rho_2^{\mathrm{X}}(\mathbf{r}_1,\mathbf{r}_2) = -\rho_1(\mathbf{r}_1;\mathbf{r}_2)\rho_1(\mathbf{r}_2;\mathbf{r}_1) \tag{2.123}$$

$$\rho_2^{\mathrm{corr}}(\mathbf{r}_1,\mathbf{r}_2) = \rho_2(\mathbf{r}_1,\mathbf{r}_2) - \rho_2^{\mathrm{C}}(\mathbf{r}_1,\mathbf{r}_2) - \rho_2^{\mathrm{X}}(\mathbf{r}_1,\mathbf{r}_2) \text{ y} \tag{2.124}$$

$$\rho_2^{\mathrm{xc}} = \rho_2^{\mathrm{X}}(\mathbf{r}_1,\mathbf{r}_2) + \rho_2^{\mathrm{corr}}(\mathbf{r}_1,\mathbf{r}_2) = \rho_2(\mathbf{r}_1,\mathbf{r}_2) - \rho(\mathbf{r}_1)\rho(\mathbf{r}_2). \tag{2.125}$$

The separation of $\rho_2(\mathbf{r}_1,\mathbf{r}_2)$ in (2.121) makes possible the partition of the electron-electron energy between two different atoms, $A \neq B$, into its Coulombic, exchange, correlation, and exchange-correlation components.

$$\begin{aligned}V_{\mathrm{ee}}^{AB} &= \int_A\int_B \frac{\rho_2(\mathbf{r}_1,\mathbf{r}_2)}{r_{12}}\mathrm{d}\mathbf{r}_1\mathrm{d}\mathbf{r}_2 \\ &= \int_A\int_B \frac{\rho_2^{\mathrm{C}}(\mathbf{r}_1,\mathbf{r}_2)}{r_{12}}\mathrm{d}\mathbf{r}_1\mathrm{d}\mathbf{r}_2 + \int_A\int_B \frac{\rho_2^{xc}(\mathbf{r}_1,\mathbf{r}_2)}{r_{12}}\mathrm{d}\mathbf{r}_1\mathrm{d}\mathbf{r}_2 \\ &= \int_A\int_B \frac{\rho_2^{\mathrm{C}}(\mathbf{r}_1,\mathbf{r}_2)}{r_{12}}\mathrm{d}\mathbf{r}_1\mathrm{d}\mathbf{r}_2 + \int_A\int_B \frac{\rho_2^{\mathrm{X}}(\mathbf{r}_1,\mathbf{r}_2)}{r_{12}}\mathrm{d}\mathbf{r}_1\mathrm{d}\mathbf{r}_2 + \int_A\int_B \frac{\rho_2^{\mathrm{corr}}(\mathbf{r}_1,\mathbf{r}_2)}{r_{12}}\mathrm{d}\mathbf{r}_1\mathrm{d}\mathbf{r}_2 \\ &= V_{\mathrm{C}}^{AB} + V_{\mathrm{xc}}^{AB} = V_{\mathrm{C}}^{AB} + V_{\mathrm{X}}^{AB} + V_{\mathrm{corr}}^{AB},\end{aligned} \tag{2.126}$$

where

$$V_\sigma^{AB} = \int_A\int_B \frac{\rho_2^{\sigma}(\mathbf{r}_1,\mathbf{r}_2)}{r_{12}}\mathrm{d}\mathbf{r}_1\mathrm{d}\mathbf{r}_2 \quad \text{with } \sigma = \mathrm{C},\ \mathrm{X},\ \text{corr o xc and } A \neq B. \tag{2.127}$$

Equation (2.126) suggest that the interaction energy between two atoms can be separated into two components, a classic one:

$$V_{\mathrm{cl}}^{AB} = V_{\mathrm{C}}^{AB} + V_{\mathrm{ne}}^{AB} + V_{\mathrm{ne}}^{BA} + V_{\mathrm{nn}}^{AB}, \tag{2.128}$$

and a quantum mechanical one (that corresponds to exchange-correlation), and therefore we can rewrite the interaction energy in equation (2.114) as:

$$E_{\mathrm{int}}^{AB} = V_{\mathrm{cl}}^{AB} + V_{\mathrm{xc}}^{AB}. \tag{2.129}$$

The partition of $\rho_2(\mathbf{r}_1, \mathbf{r}_2)$ as appears in equation (2.121) can also be used to divide the interaction energy between two groups of atoms, $\mathscr{G}$ y $\mathscr{H}$

$$V_{\sigma}^{\mathscr{G}\mathscr{H}} = \sum_{A\in\mathscr{G}} \sum_{B\in\mathscr{H}} V_{\sigma}^{AB}, \tag{2.130}$$

where we used equation (2.117) and σ has the same meaning as in expression (2.127). Then, it follows that the same partition used in equation (2.129) can be applied to the interaction between groups

$$E_{\mathrm{int}}^{\mathscr{G}\mathscr{H}} = V_{\mathrm{cl}}^{\mathscr{G}\mathscr{H}} + V_{\mathrm{xc}}^{\mathscr{G}\mathscr{H}}, \tag{2.131}$$

in which the classic interaction is

$$V_{\mathrm{cl}}^{\mathscr{G}\mathscr{H}} = V_{\mathrm{C}}^{\mathscr{G}\mathscr{H}} + V_{\mathrm{ne}}^{\mathscr{G}\mathscr{H}} + V_{\mathrm{ne}}^{\mathscr{H}\mathscr{G}} + V_{\mathrm{nn}}^{\mathscr{G}\mathscr{H}}, \tag{2.132}$$

and $V_{\mathrm{xc}}^{\mathscr{G}\mathscr{H}}$ is given by equation (2.130) in the case of $\sigma = \mathrm{xc}$.

Finally, it is important to note that the components of the electronic repulsion energy within an atom can be also obtained using an expression very similar to equation (2.127). However, it is important to consider the corresponding $1/2$ factor in expressions (2.112), (2.126) and (2.127).

At the present time it is possible to carry out the energy partition of IQA based on Hartree-Fock and most Hartree-Fock methodologies, such as MP2 and Coupled Cluster for which the pair density is available. For the DFT formalism, given the unavailability of the pair density, a method to scale the one- and two-atom terms of the Kohn-Sham exchange-correlation energy to fit the additive exchange-correlation energies as defined within the IQA approach [37]. Thus, it is possible to make an exact partition of the DFT energy of a molecule into intra-atomic and inter-atomic contributions.

2.5. The Non Covalent Interaction (NCI) index

The structure of molecules is determined by an interplay between covalent and non covalent interactions. The covalent interactions, or bonds, are defined by the three-dimensional molecular structure while the non covalent interactions are hidden within voids in the bonding network [38]. The non-covalent interactions (NCI) index is an approach to map and analyze non covalent interactions using the density and its derivatives. It allows for simultaneous analysis and visualization of a wide range of different types of non covalent contacts, it is very fast to compute, and its results are usually transferable to a large range of chemical problems.

The NCI analysis is based in an index that enables the identification of non covalent interactions based on a two-dimensional plot of the density ρ and the corresponding reduced density gradient, s, where

$$s = \frac{1}{2(3\pi^2)^{1/3}} \frac{|\nabla\rho|}{\rho^{4/3}}. \tag{2.133}$$

The reduced density gradient is a dimensionless quantity used widely in DFT that has been applied in the development of more accurate functionals [39] and it represents the deviation of the electronic density from a homogeneous distribution [40]. The reduced density gradient values grow to very large values when the density goes to zero in regions far away from the molecule, and approach zero in the regions where covalent and non covalent interactions appear.

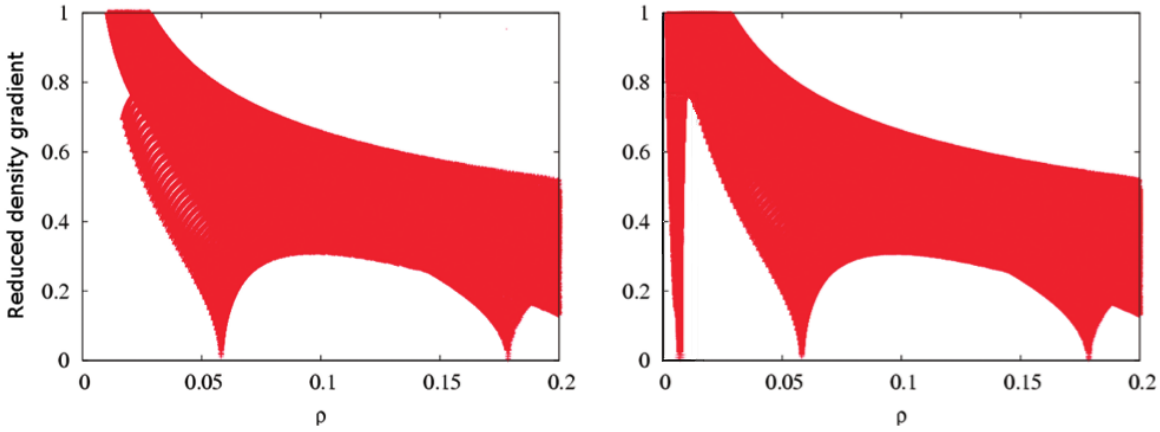

Figure 2.2: Reduced density gradient plot of the benzene monomer (left) and dimer (Right).

When we plot s as a function of ρ we can observe the fundamental shape of different interactions. Figure 2.2 shows the reduced density gradient as a function of the density for the

benzene molecule and the benzene dimer. The upper left side of the plots corresponds to the regions that are far from the nuclei and where, as a consequence, the density is very small. The points on the lower right side are those that characterize the covalent interactions, in this case the carbon-hydrogen covalent bond. Finally, we can see that on the plot on the right there is a spike that does not appear on the plot on the left. That spike is a signature of non-covalent interactions.

In order to understand the origin of this feature we have to consider the process of formation of the aggregate. For each molecule, the reduced density gradient is zero far away from the molecular frame, but when the two get closer there is a change in the profile of s in the region between them. Upon the formation of the dimer, a low-density region appear, which is reflected in the graph as a spike. Non covalent interactions are identified with regions of low density and low reduced gradient.

The power of the NCI analysis is amplified by the fact that it can distinguish between classically attractive and repulsive interactions by examining the second derivatives of ρ along the main axis of variation [41]. The sign of the Laplacian, $(\nabla^2\rho)$, of the density specify whether the gradient flux of density is entering $(\nabla^2\rho > 0)$ or leaving $(\nabla^2\rho < 0)$ an infinitesimal volume. Thus, the sign of $\nabla^2\rho$ determines if the density is concentrated or depleted at a point relative to its surroundings.

Given that for weak interactions the sign of the Laplacian is dominated by the negative contribution of the nuclei it is of no use to distinguish between interactions. However, by analyzing the contributions to the Laplacian along the different axes of maximal variation we can do it. These contributions are the eigenvalues, λ_i, of the Hessian matrix of the density, and hence

$$\nabla^2\rho = \lambda_1 + \lambda_2 + \lambda_3 \tag{2.134}$$

In molecules, the value of λ_3 changes along the inter nuclear direction, while λ_1 and λ_2 vary in a normal plane with respect to the λ_3 eigenvector. From this three, the second, λ_2 has the characteristic of assuming negative or positive values depending on the type of interaction studied. For attractive interactions, such as the hydrogen bond, there is accumulation of density perpendicular to the bond, and thus $\lambda_2 < 0$. For non bonding interactions, like in the case of steric repulsions, there is density depletion and $\lambda_2 > 0$. For van der Waals interactions the density overlap is minimal, almost negligible, which results in a $\lambda_2 \lesssim 0$

If we use the product of the sign of λ_2 and the density instead of the density, we would have a

reduced density gradient graph that separates into attractive (left side, $\lambda_2 < 0$), repulsive (right side, $\lambda_2 > 0$), and weak interactions (near zero, $\lambda_2 \lesssim 0$). Figure 2.3 shows such graph, with a color palette that makes the analysis easier: blue for attractive, red for repulsive, and green for weak interactions.

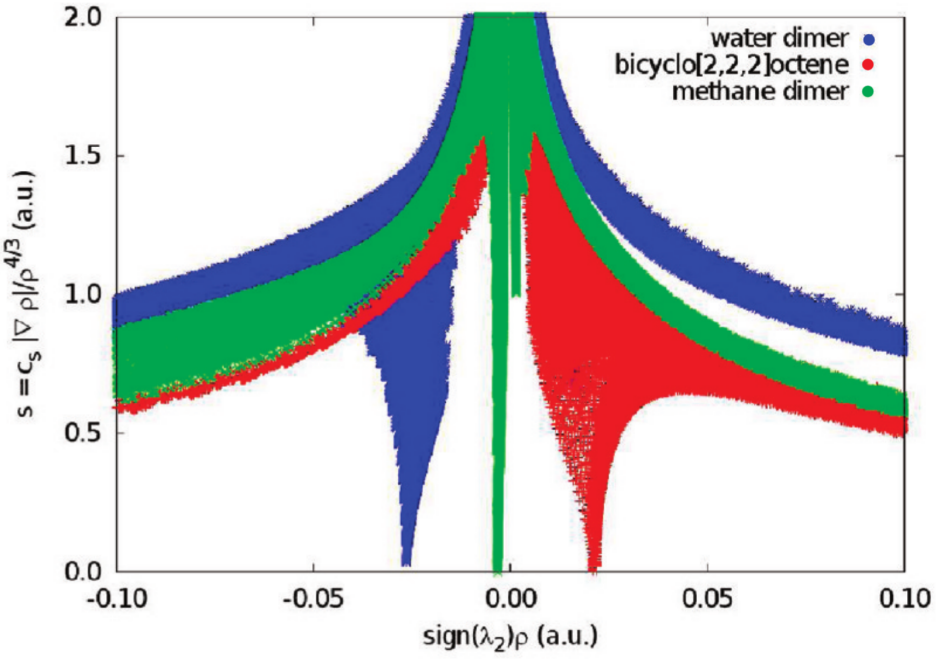

Figure 2.3: Plots of the reduced density gradient as a function of $\text{sign}(\lambda_2)\rho$. Attractive interactions appear on the left (blue), repulsive on the right (red), and van der Waals ones near zero (green.)

Finally, we can generate isosurfaces of s that enclose regions that fulfill the profile of the non covalent interactions described above, i.e. that have low density and reduced gradient density values. Further on, by using the values of $\text{sign}(\lambda_2)\rho$ to color those surfaces, we are able to better appreciate the different types of interactions that can be present in a molecule or molecular cluster. An example of the resulting 3D plots can be seen in Figure 2.4.

This way the NCI index analysis is a very powerful tool to investigate non covalent interaction because it not only points out to their spatial presence but also reveals its nature. This methodology thus enable us to have a clearer representation of those interactions hiding within the voids of molecular structure.

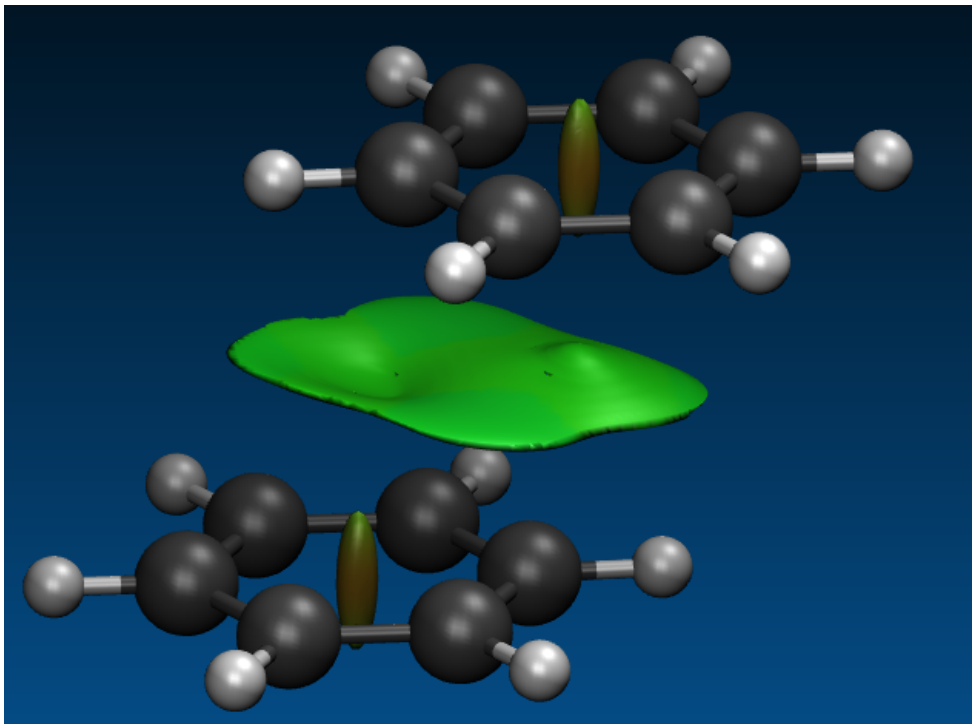

Figure 2.4: Gradient isosurface for a dimer of benzene. The green color indicates that the nature of the interaction is the van der Waals type.

Capítulo 3

Resultados

En este capítulo se presentarán los trabajos originales que conforman el cuerpo principal de esta tesis. El hilo conductor de este proyecto ha sido el análisis de diversas interacciones químicas cuya naturaleza, por diversas razones, no es evidente. Para ello, nos hemos servido de las herramientas de la topología químico cuántica (QCT). Los frutos de esta labor han sido exitosos. Más allá de la variedad de sistemas considerados, esta investigación ha permitido poner en relieve la importancia de las interacciones secundarias en la química, a la vez que ha demostrado la eficacia de la QCT para elucidar la respuesta a problemas donde la gran cantidad de variantes hacen de ello una tarea complicada. Estudiar el enlace entre dos átomos no es baladí. Hacerlo cuando estos átomos se ecuentran rodeados por decenas, cientos, de otros átomos lo es aún menos.

La exposición de los artículos generados se hará primeramente exponiendo de manera breve, en español, los principales resultados obtenidos y posteriormente se presentarán en su versión original en el apéndice correspondiente. La presentación seguirá un orden temático: primeramente se presentarán los artículos relacionados con el estudio de enlaces no covalentes: el rol del agua en la formación de lluvia ácida [42], el debilitamiento del enlace de hidrógeno a través de su interacción con un sistema π [43], y la la existencia, o no, de un enlace de halógeno [44]. Después, se comentarán los artículos donde se estudiaron las interacciones no covalentes en compuestos de coordinación [45; 46; 47]. Finalmente, se discutirán los resultados concernientes al resto de los artículos publicados. El primero de estos artículos versa sobre la validez del uso de modelos aproximados para la obtención de la densidad electrónica en el análisis QTAIM [48]. El segundo es un estudio de la localización espacial de la correlación electrónica mediante la partición de esta en términos intra e interatómicos [49].

3.1. Interacciones no covalentes

Se denominan interacciones no covalentes a las interacciones que unen a dos átomos o moléculas pero que no incluyen la formación de un enlace propiamente. Estas comprenden un amplio rango de fuerzas de unión, como el enlace de hidrógeno, la interacción dipolo-dipolo, la repulsión estérica, o la dispersión de London [50].

Las interacciones no covalentes son muy importantes en química, biología, y ciencia de materiales pues juegan un papel fundamental en diversos fenómenos. Por ejemplo, participan en la interacción entre fármaco y proteína así como en la formación de agregados moleculares [51].

Los métodos de la QCT son especialmente idóneos para el estudio de interacciones no covalentes por su capacidad de describir interacciones de corto y largo alcance en igualdad de condiciones. Además de esto, las metodologás de la QCT están basados en cantidades invariantes ante el cambio de orbitales, específicamente en la densidad de primer orden y la densidad de pares. Los resultados de la QCT tienen un significado físico bien definido que no depende de parámetros arbitrarios. En este sentido, estos análisis ofrecen respuestas que no dependen del método utilizado para llevar a cabo los cálculos de estructura electrónica subyacentes y por tanto están libres de sesgos introducidos por estos.

En el pasado, hemos usado las metodologás de la QCT para estudiar una variedad de sistemas y problemas, entre los que se encuentran los efectos cooperativos [52] y anticooperativos [53] en agregados pequeños de agua, la interacción entre un sistema π y un enlace de hidrógeno [54] o varios de estos [55]. En estos trabajos, la QCT ha probado su eficacia para elucidar los mecanismos internos que provocan los fenómenos observados.

3.1.1. The bifunctional catalytic role of water clusters in the formation of acid rain

Se puede argumentar que el enlace de hidrógeno es la interacción intermolecular más importante. El enlace de hidrógeno juega un papel fundamental en una gran variedad de fenómenos, entre los que caben destacar que confiere propiedades físicas particulares al agua en fase condensada. Al igual que el enlace de hidrógeno afecta la estructura de agregados moleculares [56], este puede modificar las propiedades químicas de un sistema. Un ejemplo de esta situación es la formación de lluvia ácida [57; 58].

La lluvia ácida es un subproducto de la industrialización. Se produce cuando la humedad en el aire se combina con dióxido o trióxido de azufre generados por la quema de productos derivados del petróleo o carbón que contengan azufre. La lluvia ácida se considera un problema no local pues los contaminantes atmosféricos que la provocan son capaces de viajar cientos de kilómetros antes de precipitar. El proceso de producción de lluvia ácida se puede esquematizar como:

$$\begin{aligned} SO_3 + (H_2O)_n &\xrightarrow{(1)} SO_3\cdots(H_2O)_n \xrightarrow{(2)} [SO_3\cdots(H_2O)_n]^{\ddagger} \\ [SO_3\cdots(H_2O)_n]^{\ddagger} &\xrightarrow{(3)} H_2SO_4\cdots(H_2O)_{n-1}. \end{aligned} \tag{3.1}$$

Este artículo ofrece una descripción detallada de de los cambios en la reactividad de las moléculas de H_2O y SO_3 en la formación de H_2SO_4 causados por la cooperatividad del enlace de hidrógeno en moléculas de agua que a primera vista podrían parecer no reactivas. Así, el objetivo es doble: Por un lado, este trabajo muestra la manera como la cooperatividad en el enlace de hidrógeno puede modificar el caracter nucleofílico y electrofílico de distintas especies en una reacción química. Por otro lado, se pretende que este estudio sirva para entender mejor el proceso de producción de lluvia ácida en sí mismo.

Para ello consideramos únicamente la reacción de SO_3 con $(H_2O)_n$ (n = 1–3) para producir H_2SO_4. Las curvas de energía potencial correspondientes a este proceso se pueden ver en la figura 3.1. La selección de estos procesos se debe a que la formación de H_2SO_4 es un proceso de segundo orden, y en circunstancias específicas de tercer orden, respecto al vapor de agua [59; 58]. Además, cálculos teóricos indican que el dímero y el trímero de agua, y sus correspondientes aductos con SO_3 son considerablemente más abundantes en la atmósfera que sus análogos de mayor tamaño [60; 61].

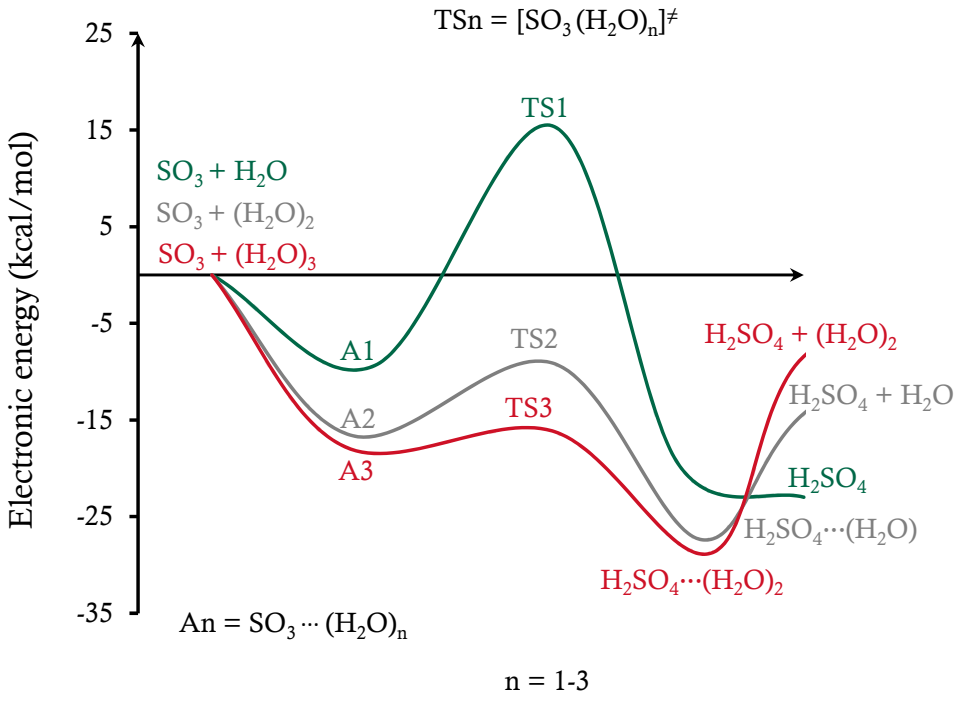

Figura 3.1: Curvas de energía potencial a nivel MP2/aug-cc-pVTZ para la formación de H_2SO_4 a partir de la reacción entre SO_3 y los cúmulos de agua $(H_2O)_n$ (n = 1, 2, 3). Todos los valores están referenciados respecto al valor correspondiente de la suma $E(SO_3) + E((H_2O)_n)$.

Las geometrías así como las densidades electrónicas de todos los sistemas estudiados fueron obtenidas usando el nivel de teoría MP2 [62]/aug-cc-pVTZ [63] tal como está implementado en el programa GAUSSIAN-09 [64]. Los análisis QTAIM e IQA se llevaron a cabo con el programa AIMAll [65]. Para la partición energética IQA se usó la aproximación de Müller [66].

Como ha sido reportado [57; 58] y como se muestra en el lado izquierdo de la figura 3.1, el primer paso de la reacción es la formación de los aductos moleculares $H_2O\cdots SO_3$ (A1), $(H_2O)_2\cdots SO_3$ (A2) y $(H_2O)_3\cdots SO_3$ (A3), cuyas estructuras se muestran en la figura 3.2. Es notable que los complejos $(H_2O)_n\cdots SO_3$ son más estables conforme aumenta el número de moléculas de agua participantes. Esta observación se explica debido a los efectos cooperativos que se dan en los cúmulos de agua. En efecto, la estructura de los sistemas $(H_2O)_2\cdots SO_3$ y $(H_2O)_3\cdots SO_3$ son similares a las conformaciones cíclicas del trímero y tetrámero de agua [52].

La figura 3.2 (d) muestra como durante la formación del dímero de agua se da un desplazamiento de la densidad electrónica desde la molécula que acepta el hidrógeno hacia la molécula donadora. Esto hace al oxígeno de la molécula donadora más rico en electrones y por tanto favorece su interacción con especies químicas deficientes en electrones, es decir, incrementa su

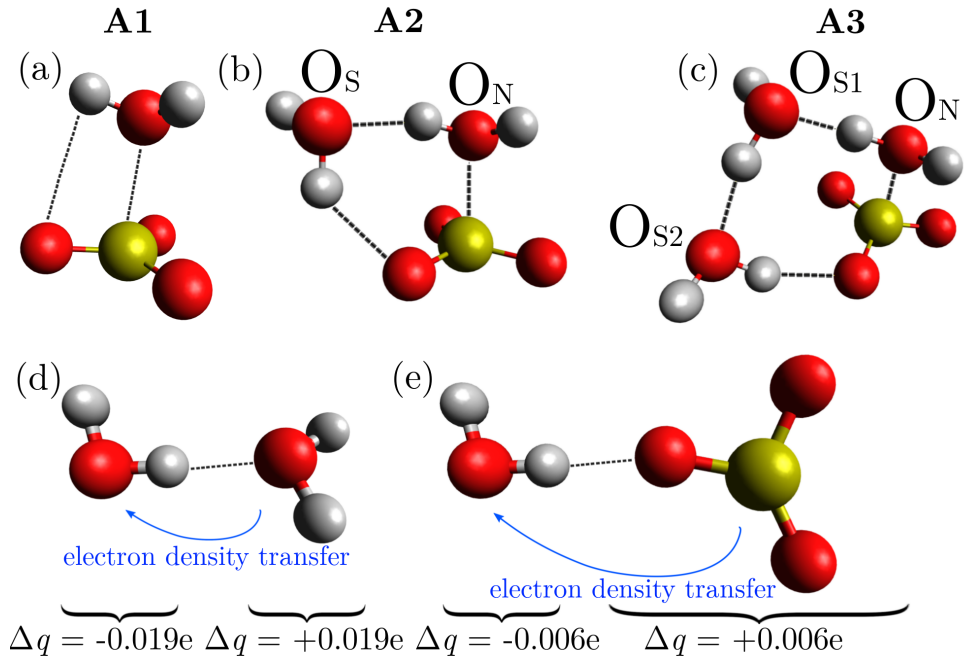

Figura 3.2: Arriba: Estructuras en el equilibrio de (a)–(c), los complejos supramoleculares $(H_2O)_n\cdots SO_3$ con n = 1, 2, 3. Las etiquetas O_N, O_{S_1}, y O_{S_2} se refieren al caracter nucleofílico de la molécula de H_2O en el caso de la primera, y a su papel como espectadores en el caso de las restantes durante la formación del complejo. Abajo: Transferencia de carga en los enlaces de hidrógeno (d) $H_2O\cdots H_2O$ y (e) $O_2S{=}O\cdots H_2O$. Los corchetes indican el cambio de carga total para una molécula al formar el aducto correspondiente.

carácter nucleofílico. El mismo proceso aumenta la acidez de los hidrógenos de la molécula aceptora de protón. De manera análoga, una molécula de trióxido de azufre, mostrada en la figura 3.2 (e), pierde densidad electrónica con respecto a una molécula de SO_3 aislada. De esta manera, el átomo de azufre, que es el que más pierde densidad electrónica en este proceso, se hace más propenso a interaccionar con una especie rica en electrones. En otras palabras, la formación de enlaces de hidrógeno donde el trióxido de azufre es el aceptor de hidrógeno, como en el caso de los complejos $HO_S{-}H\cdots O{=}SO_2$ y $HO_{S2}{-}H\cdots O{=}SO_2$ en las figura 3.2 (b) y (c) respectivamente, hacen del azufre un mejor electrófilo.

Para ilustrar esta idea, la figura 3.3 muestra la carga del átomo de azufre y del oxígeno nucleofílico (O_N) como función del número de moléculas de agua que participan en el complejo molecular. Al igual que el azufre, el oxígeno nucleofílico pierde carga también, pero en menor medida. Cuando una molécula de agua interacciona con SO_3, el O_N pierde densidad electrónica que se aloja en el átomo de oxígeno del trióxido de azufre. La inclusión de una segunda molécula

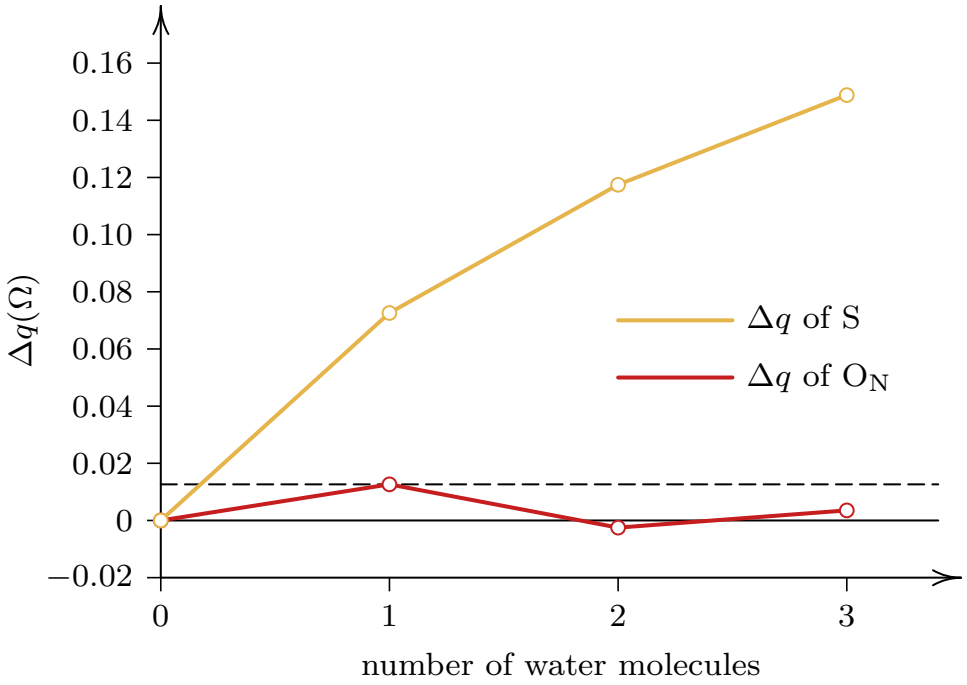

Figura 3.3: Cambios en las cargas QTAIM de los átomos de azufre y de oxígeno nucleofílico en los cúmulos moleculares $(H_2O)_n\cdots SO_3$ with n = 1, 2, 3. Los puntos en n = 0 representan a las moléculas aisladas. Los valores de $\Delta q(\Omega)$ están reportados en unidados atómicas.

aumenta el número de electrones del oxígeno nucleofílico, como se muestra en la figura 3.2 (d). A pesar de la pequeña perdida de electrones por parte de O_N que se da al agregar la tercera molécula de agua, el número de electrones en el oxígeno nucleofílico es aún más grande que en el sistema A1. Para el azufre, podemos ver claramente como la carga del átomo de S aumenta al incrementar el número de moléculas de agua en el aducto. La diferencia en la electrofília del azufre es considerablemente más grande que el efecto correspondiente para el O_N.

Los flujos de carga considerados hasta ahora evocan las estrategias seguidas en la catálisis orgánica bifuncional [67] para promover adiciones nucleofílicas a un sustrato mediante la formación de enlaces de hidrógeno. En otras palabras, la estrategia de diseño seguida últimamente en química orgánica de activar nucleófilos y electrófiles mediante el uso de enlaces de hidrógeno [68; 69; 70] ayuda a explicar la el mecanismo de formación de lluvia ácida aquí estudiado.

Para poder evaluar de manera cuantitativa el efecto de las moléculas de agua circundantes en la reacción entre H_2O y SO_3, determinamos los valores de la energía de interacción entre las distintas moléculas en los procesos descritos por el primer paso de la ecuación (3.1). La tabla 3.1 muestra que la presencia de la segunda molécula de agua incrementa la magnitud de la interacción

de la ecuación (3.1), las energías de activación para estos procesos disminuyen conforme aumenta el número de aguas en el sistema, lo que es consistente con observaciones previas [57; 58]. La descomposición de la energía en parejas (mostrada en la parte (b) de la tabla 3.1) muestra que los valores absolutos de $E_{\text{int}}^{\mathscr{F}\mathscr{G}\prime}$ son considerablemente más pequeños conforme aumenta el número de moléculas de agua alrededor de la reacción, un hecho que conduce a una estabilización del estado de transición. Esto implica que el escenario químico en la formación de lluvia ácida cambia menos drasticamente cuando más moléculas de aguaa son incluidas en el sistema.

En el lado derecho de la figura 3.4 se muestran los cambios en DI para distintos pares de átomos involucrados en la formación y ruptura de enlaces químicos en el paso 2 de la ecuación (3.1). Ciertamente, los cambios en DI para la interacción de $(H_2O)_2$ y $(H_2O)_3$ con SO_3 son más leves que para el sistema $H_2O + SO_3$. Sobre esta situación el postulado de Hammond [71] indica que *las estructuras próximas en energía que se transforman directamente una en la otra son también similares en estructura* [72].

Tabla 3.1: Particiones IQA de (a) la energía de formación de los aductos A1, A2, y A3 mostrados en la figura 3.2 (Primer paso en la ecuación 3.1) así como de (b) la energía de activación del paso limitante de la reacción en la figura 3.1 (Segundo paso en la ecuación 3.1). Las etiquetas N, S, S1 y S2 se definieron en la figura 3.2. Los valores están reportados en kcal/mol.

(a) Molecular cluster

	A1	A2		A3		
$\mathscr{G}\backslash\mathscr{F}$	H_2O(N)	H_2O(N)	H_2O(S)	H_2O(N)	H_2O(S1)	H_2O(S2)
SO_3	−8.65	−20.16	−8.98	−31.11	−3.70	−15.27
H_2O(N)	—	—	13.43	—	8.20	23.25
H_2O(S1)	—	—	—	—	—	0.88
Total	−8.65	−15.71		−17.75		

(b) Transition state

	TS1	TS2		TS3		
$\mathscr{G}\backslash\mathscr{F}$	H_2O(N)	H_2O(N)	H_2O(S)	H_2O(N)	H_2O(S1)	H_2O(S2)
SO_3	20.89	13.10	−7.18	4.63	−6.24	0.69
H_2O(N)	—	—	2.28	—	−1.73	−0.91
H_2O(S1)	—	—	—	—	—	4.96
Total	20.89	8.20		1.40		

Podemos apreciar entonces que las moléculas de agua que acompañan a la reacción de adición

ácido/base de Lewis SO_3 + H_2O no únicamente incrementan la magnitud de la interacción entre los átomos de azufre y oxígeno en el aducto molecular al inicio de la reacción, sino que también mitigan los cambios en los enlaces químicos que llevan a la formación del etado de transición. Esta moderación en el grado de modificación de las interacciones covalentes y no covalentes involucradas disminuye en gran medida la energía de activación del paso limitante de la formación de la lluvia ácida.

3.1.2. Hydrogen Bond Weakening through π Systems: Resonance Impaired Hydrogen Bonds RIHB

El enlace de hidrógeno es una interacción muy compleja pues está sujeta a efectos cooperativos y anticooperativos con otros enlaces de hidrógeno [56]. El enlace de hidrógeno puede verse afectado, además de por otros enlaces de hidrógeno adyacentes, por otras características de la moléculas involucradas, como por su aromaticidad [73] o su esqueleto σ rígido [74]. Los enlaces de hidrógeno asistidos por resonancia (RAHB por sus iniciales inglés) son enlaces de hidrógeno donde el donador de protón y el aceptor de protón están conectados a través de una cadena de dobles enlaces conjugados π y que son particularmente fuertes [75; 76].

La explicación habitual para la exagerada fuerza asociada a los RAHB es que al estar conectados a través de una cadena de enlaces conjugados π se da un efecto de resonancia que provoca una igualación en las distancias de los enlaces involucrados en el pseudo anillo. Esta idea es consistente con la creencia firmemente establecida en la comunidad química de que la existencia de estructuras de resonancia equivalentes es en sí misma estabilizadora. Dos ejemplos clásicos de RAHB son el malondialdehido **1** y el 3-aminoacrilmaldehido **2**, mostrados ambos en la figura 3.5.

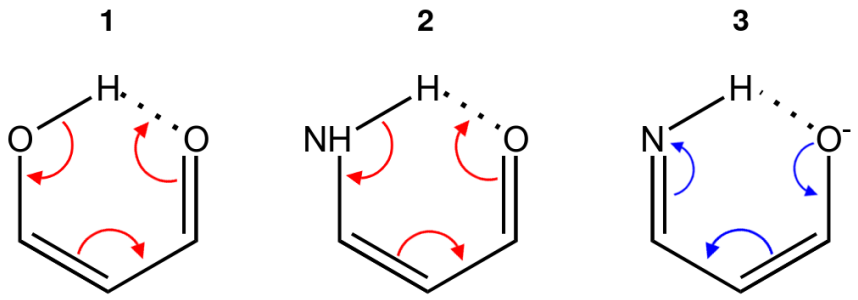

Figura 3.5: Enlaces de hidrógeno asistidos por resonancia en malonaldeido **1**, y 3-aminoacrilaldehido **2**. El enlace de hidrógeno impedido por resonancia en el compuesto **3**, que es la base conjugada del compuesto **2**, también se muestra. Las flechas mostradas en rojo/azul fortalecen/debilitan los enlaces de hidrógeno del esquema

Las estructuras de resonancia de **1** y **2** mostradas en la figura 3.5 sugieren un fortalecimiento de la interacción H···O en el aceptor de protón, y un debilitamiento del enlace X−H (X = O, N en **1** y **2** respectivamente). Ambos hechos contribuyen a hacer el enlace de hidrógeno intramolecular en **1** y **2** más fuertes que un enlace σ OH···O y NH···O.

QTAIM e IQA se llevaron a cabo con ayuda del código PROMOLDEN [79] usando densidades obtenidas con el funcional B3LYP y la base aug-cc-pVTZ. Para realizar la partición energética IQA consideramos una aproximación a los términos de uno y dos átomos de la energía de intercambio y correlación de Kohn-Sham [37]. Los índices de aromaticidad $I_{\text{ring}}(\mathscr{A})$, $I_{\text{NG}}(\mathscr{A})$ $I_{\text{NB}}(\mathscr{A})$ y MCI($\mathscr{A}$) fueron calculados con la ayuda del programa Esi-3D [80].

Tabla 3.2: Energía de formación (en kcal/mol) así como las distancias O···H and N···O (en ångstroms) para los enlaces de hidrógeno en los sistemas **2**, $\mathbf{2}_{\text{inter}}$, **3** y $\mathbf{3}_{\text{inter}}$

System	$\Delta E_{\text{form}}^{\text{H bond}}$	d(H···O)	d(N···O)
2	−7.9	1.896	2.665
$\mathbf{2}_{\text{inter}}$	−3.6	2.024	3.030
3	−2.6	2.135	2.979
$\mathbf{3}_{\text{inter}}$	−14.3	1.714	2.752

La tabla 3.2 muestra la los resultados de los cálculos de estructura electrónica de la formación de enlaces de hidrógeno en los sistemas estudiados. Como se esperaba, la interacción entre el enlace de hidrógeno y el sistema π en el RAHB provoca un aumento en la energía de formación. Podemos estimar este aumento como la diferencia entre E_{form}

$$\Delta\Delta E_{\text{RAHB}} = \Delta E_{\text{form}}(\mathbf{2}) - \Delta E_{\text{form}}(\mathbf{2}_{\text{inter}}) = -4{,}3 \text{ kcal/mol}. \tag{3.2}$$

En contraste, la interacción entre el donador y el aceptor del enlace de hidrógeno en **3** reduce apreciablemente la energía de formación de este respecto al sistema de referencia $\mathbf{3}_{\text{inter}}$. En una estimación análoga a la ecuación (3.2), tenemos que el efecto del RIHB es

$$\Delta\Delta E_{\text{RIHB}} = \Delta E_{\text{form}}(\mathbf{3}) - \Delta E_{\text{form}}(\mathbf{3}_{\text{inter}}) = 11{,}7 \text{ kcal/mol}. \tag{3.3}$$

En efecto, el valor asociado a la energía de formación del enlace de hidrógeno para el anión **3**, 2.6 kcal/mol, es significativamente más bajo que las energías correspondientes para enlaces σ típicos que incluyen especies cargadas. Usualmente, las magnitudes de ΔE_{form} para estos sistemas son de más de 10 kcal/mol, como es el caso de **3**, ($\mathbf{3}_{\text{inter}}$) = 14.3 kcal/mol), y pueden llegar al rango de $30 - 40$ kcal/mol para los complejos $[H_2O{\cdots}H{\cdots}OH_2]^+$ y $[F{\cdots}H{\cdots}F]^-$. [56]

La estabilización y desestabilización no se ve únicamente en los valores para la energía de formación. En las distancias H···O y N···O también es posible observar estos efectos. La tabla 3.2

cidad, $I_{ring}(\mathscr{A})$ [81], el cual mide la deslocalización de 6 centros en el anillo formado por los enlaces, MCI($\mathscr{A}$) [82], que agrega todas las otras posibles interacciones, así como sus versiones normalizadas, $I_{NG}(\mathscr{A})$ y $I_{NB}(\mathscr{A})$ [83]. Todos indican, en diferentes grados, que el compuesto **3** es más aromático que el compuesto **2**. Por tanto, a pesar de que usualmente se considera a la aromaticidad como una fuente de estabilización, lo que econtramos aquí es que el compuesto más estable es el menos aromático. Este sorprendente resultado coincide con las conclusiones de uno de nuestros trabajos previos que indica que la fuerza del RAHB no se origina en sus estructuras resonantes [54].

Tabla 3.3: Índices de aromaticidad $I_{ring}(\mathscr{A})$, MCI($\mathscr{A}$), $I_{NG}(\mathscr{A})$ ay $I_{NB}(\mathscr{A})$ para las conformaciones cerradas de **2** y **3**.

Índice	**2**	**3**
I_{ring}	0.001211	0.001668
MCI	0.022377	0.023604
I_{NG}	0.001618	0.002265
I_{NB}	0.021824	0.023082

Los cambios en los índices de deslocalización mostrados en la figura 3.7 generados por la formación de RAHB y RIHB se confirman también en el análisis de la ELF. La figura 3.8 muestra varias isosuperficies de la ELF para los sistemas **2** y **3**. La población electrónica de una región es directamente proporcional al tamaño de la isosuperficie. Los enlaces C_1-C_2 y C_2-C_3 (La numeración de los átomos se muestra en la figura 3.7) en el compuesto **2** son cualitativamente más parecidos después de la formación del enlace de hidrógeno, mientras que para el anión **3** ocurre lo contrario.

Adicionalmente, la revisión de la ELF en la molécula **2** en su confórmero abierto revela la presencia de un solitario par libre (Figura 3.8 (a)) que desaparece cuando se forma el RAHB. Esto indica una conjugación sustancial de este par libre con el enlace C−N adyacente cuando se forma el enlace de hidrógeno. La base **3** no presenta dicho par libre en ninguna de sus conformaciones.

Como se ha discutido previamente [54], el hecho que los órdenes de enlace se hagan más uniformes después de la formación del RAHB no implica que el número total de electrones localizados aumente también. De manera similar, que se reduzca la uniformidad de los DI con la formación del enlace de hidrógeno en el caso del compuesto **3** no necesariamente nos asegura que el número total de electrones deslocalizados disminuya.

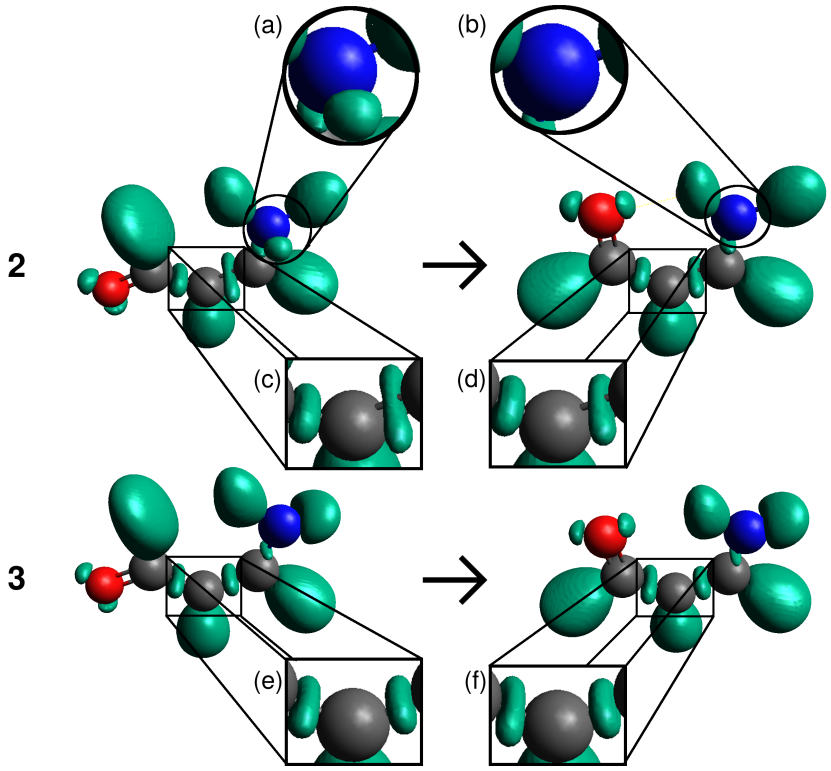

Figura 3.8: ELF isosurfaces at isovalue 0.9 for the RAHB **2** in its open (a) and closed (b) conformations and the RIHB **3** in its open (c) and closed (d) dispositions.

El número total de electrones en una molécula sigue la siguiente ecuación

$$N = \sum_{\mathrm{X}} \lambda(\mathrm{X}) + \frac{1}{2} \sum_{\mathrm{X} \neq \mathrm{Y}} \delta(\mathrm{X}, \mathrm{Y}) \tag{3.4}$$

donde N es el número de electrones totales, λ es el número de electrones localizados en X y δ representa a los electrones deslocalizados entre X y Y.

La tabla 3.4 muestra que el número total de electrones deslocalizados disminuye ligeramente después de la formación del RAHB en el compuesto **2** mientras que este se mantiene prácticamente constante para el sistema **3** cuando se forma el RIHB. El incremento en el número de electrones localizados en **2** como consecuencia de la formación de RAHB es acompañado de un incremento substancial en el componente intratómico de la energía de intercambio y correlación IQA, $\Delta|\sum_{\mathrm{A}} V_{\mathrm{xc}}^{\mathrm{A}}| = 23{,}9$ kcal/mol. En cambio, el componente interatómico, $V_{\mathrm{xc}}^{\mathrm{AB}}$ se vuelve sustancialmente menos negativo, $\sum_{\mathrm{A>B}} \Delta V_{\mathrm{xc}}^{\mathrm{AB}} = 17{,}5$ kcal/mol.

Como se dijo previamente [54], una importante fuente de estabilidad para el RAHB es la disminución que se da en la energía intratómica, no en la interatómica como sugieren las estruc-

Tabla 3.4: Cambio en el número de electrones deslocalizados y en los componentes intra e intermoleculares del componente de intercambio y correlación de la energía IQA (en kcal/mol) como consecuencia de la formación de los enlaces de hidrógeno en **2**, $\mathbf{2}_{\text{inter}}$ **3**, y $\mathbf{3}_{\text{inter}}$.

Sistema	$\sum_{\text{A>B}} \Delta\delta(\text{A},\text{B})$	$\sum_{\text{A}} \Delta V_{\text{xc}}^{\text{A}}$	$\sum_{\text{A>B}} \Delta V_{\text{xc}}^{\text{AB}}$
2	−0.08	−23.9	17.5
$\mathbf{2}_{\text{inter}}$	−0.03	−14.9	6.2
3	0.01	−0.7	4.0
$\mathbf{3}_{\text{inter}}$	−0.01	−24.7	14.6

turas mesoméricas en la figura 3.5 (a) y (b). En cambio, para el RIHB la reorganización de la densidad electrónica desde los enlaces hacia los átomos apenas tiene lugar. El desplazamiento de carga que se muestra en la figura 3.5 (c) es perjudicial para la estabilidad del sistema.

3.1.3. Halogen bonds in clathrate cages: A real space perspective

La IUPAC define a un enlace de halógeno como una relación entre dos átomos donde

> "...hay evidencia de una interacción neta atractiva entre una región electrofílica asociada a un átomo de halógeno en una entidad molecular y una región nucleofílica en otra, or la misma, entidad molecular." [84]"

La naturaleza de las interacciones huésped-anfitrión en el caso de las moléculas de dihalógeno dentro de jaulas de clatrato de agua[3] ha sido objeto de controversia en una serie de artículos tanto experimentales [85; 86; 87] como teóricos [88; 89; 90; 91]. Inicialmente se pensó que la interacción era de tipo dispersivo únicamente, debido a que todos los pares libres de las moléculas de agua en el clatrato forman puentes de hidrógeno y por tanto no están disponibles para formar enlaces de halógeno [85]. Sin embargo, calculos computacionales sugieren la presencia del enlace [90; 92].

En este artículo utilizamos una serie de metodologías de QCT para dar respuesta a la pregunta sobre la naturaleza de la interacción desde el punto de vista del espacio real. Especfíficamente, investigamos las moléculas Cl_2 y Br_2 atrapadas en las cajas de clatrato 5^{12} y $5^{12}6^2$, respectivamente. Un esquema de los sistemas estudiados puede verse en la figura 3.9.

Las geometrías de los complejos fueron tomadas de un estudio computacional previo [90]. En dicho estudio se encontró evidencia de enlace de halógeno para el sistema $Cl_2@5^{12}$ en la conformación de mínimo global pero no para $Br_2@5^{12}6^{12}$, donde se encontró evidencia para una geometría que no corresponde con el mínimo global. Usando un método basado en orbitales moleculares para particionar la energía de correlación se encontrp que dhica geometría corresponde con un mínimo de la energía iónica de interacción. Por esa razón se decidió agregar esta geometría a los sistemas aquí estudiados.

Los cálculos de estructura electrónica necesarios para obtener la densidad electrónica de los distintos clatratos se llevaron a cabo usando el nivel de teoría M06-X/aug-cc-pVTZ [26; 63] como está implementado en el programa `Gaussian09` [64]. Los análisis QTAIM e IQA fueron realizados con el programa AIMAll [65] mientras que los cálculos de la función de localización electrónica (ELF por sus iniciales en ingés) fueron hechos usando el código PROMOLDEN [79]. Finalmente, las isosuperficies de NCI fueron obtenidas usando el programa NCIPlot [41].

El análisis QTAIM revela que para ambos complejos, en todas las conformaciones estudiadas, existen varias trayectorias de enlace entre los átomos de halógeno y los oxígenos de la jaula del

[3]Los clatratos son compuestos donde la molécula huésped se encuentra en una jaula formada por la molécula anfitrión.

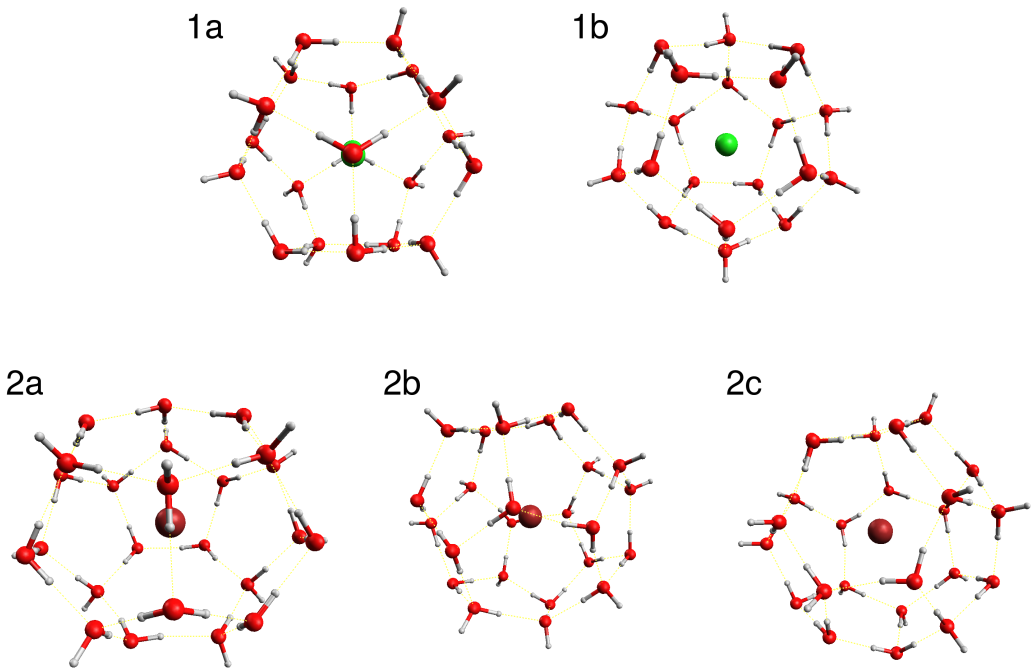

Figura 3.9: Esquema de los sistemas estudiados; Cl_2 in la jaula 5^{12} en las conformaciones de mínimo global (1a) y máximo global (1b), y Br_2 en la jaula $5^{12}6^2$ en tres conformaciones, mínimo global (2a), aquel donde la interacción iónica es mínima (2b, ver el texto para más información) y el máximo global (2c).

clatrato, como se puede ver en la figura 3.10. Más allá de la interpretación tradicional de Bader de las trayectorias de enlace como enlaces químicos, en situaciones controversiales se puede considerar a las trayectorias de enlace como canales de intercambio mecánico-quántico entre átomos [93]. Su presencia es un primer indicador de que existe una interacción no despreciable entre estos átomos.

La tabla 3.5 contiene los parámetros geométricos y algunos descriptores de QTAIM para las interacciones que tienen más posibilidades de ser consideradas como enlaces de halógeno, así como los mismos datos para los sistemas de referencia $Cl_2 \cdots H_2O$ y $Br_2 \cdots H_2O$.

La densidad en el BCP depende en gran medida de la distancia entre los átomos que conecta la trayectoria de enlace por lo que ofrece poca información respecto a la naturaleza del enlace. El Laplaciano de la densidad en el BCP es para todos los casos pequeño y positivo, lo que implica una interacción débil de capa cerrada. A partir de esta información no es posible obtener conclusiones respecto a la naturaleza del enlace.

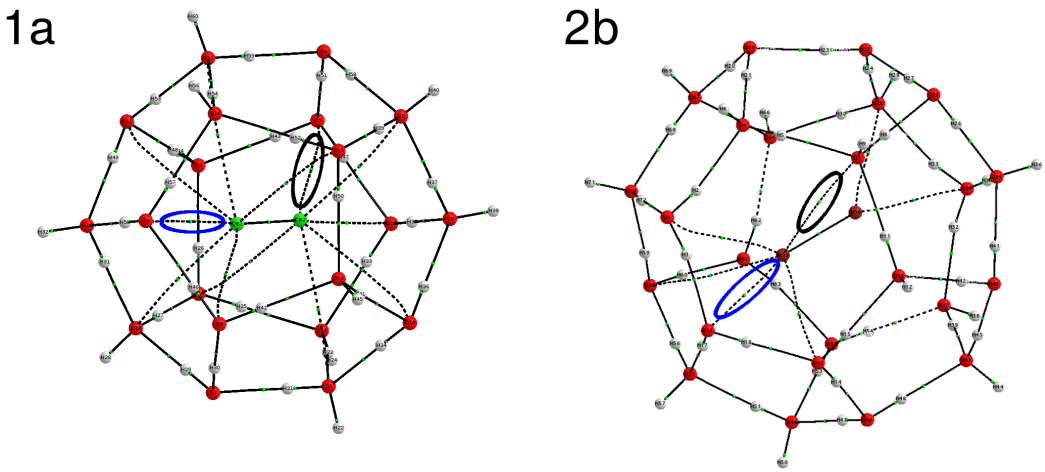

Figura 3.10: QTAIM bond paths for systems 1a and 2b. In blue we highlight two oxygen-halogen interactions that are (near) colinear to the halogen-halogen bond (Cl61-O4 and Br73-O16). Similarly, two representative of nonlinear interactions are indicated in black (Cl62-O5 and Br73-O7).

Tabla 3.5: Parámetros geométricos y algunas propiedades QTAIM de algunas trayectorias de enlace presentes en las diferentes conformaciones estudiadas.

Sistema	Par	Distancia/å	∠ OXX/°	ρ_b/u.a.	$\nabla^2\rho_b$/a.u.
Cl_2-H_2O	Cl2-O3	2.771	180.0	0.0157	0.0698
1a	Cl61-O4	2.790	175.2	0.0174	0.0731
	Cl62-O5	3.204	130.3	0.0096	0.0348
1b	Cl61-O18	2.835	133.9	0.0153	0.0696
Br_2-H_2O	Br2-O3	2.796	179.5	0.0181	0.0732
2a	Br74-O7	3.159	165.1	0.0081	0.0334
2b	Br73-O7	4.237	84.2	0.0014	0.0047
	Br73-O16	2.788	167.0	0.0209	0.0803
	Br74-O31	2.895	162.4	0.0176	0.0705
2c	Br73-O31	3.044	141.2	0.0146	0.0548

El análisis de la ELF permite detectar la presencia de pares de electrones libres. El modeloo de enlace de halógeno depende en gran medida de la disposición geométrica de estos pares libres. Típicamente, la presencia de un hueco σ en el halógeno junto con un par libre en la otra molécula es signo de la presencia de un enlace de halógeno. En el caso de los clatratos, se supone que el hecho que los pares libres de los oxígenos se encuentren formando ya enlaces de hidrógeno es un

indicador para negar la presencia de enlace de halógeno.

La figura 3.11 muestra isosuperficies relevantes de la ELF. Lo primero que es interesante notar es la estructura arquetípica de enlace de halógeno que observamos para los complejos $Cl_2 \cdots H_2O$ y $Br_2 \cdots H_2O$. En ambos casos, los pares libres del halógeno forman una especie de dona alrededor del átomo. De manera complementaria vemos uno de los pares libres del oxígeno apuntando hacia el agujero de la dona. Esto en completo acuerdo con el paradigma donador-aceptor del enlace de halógeno.

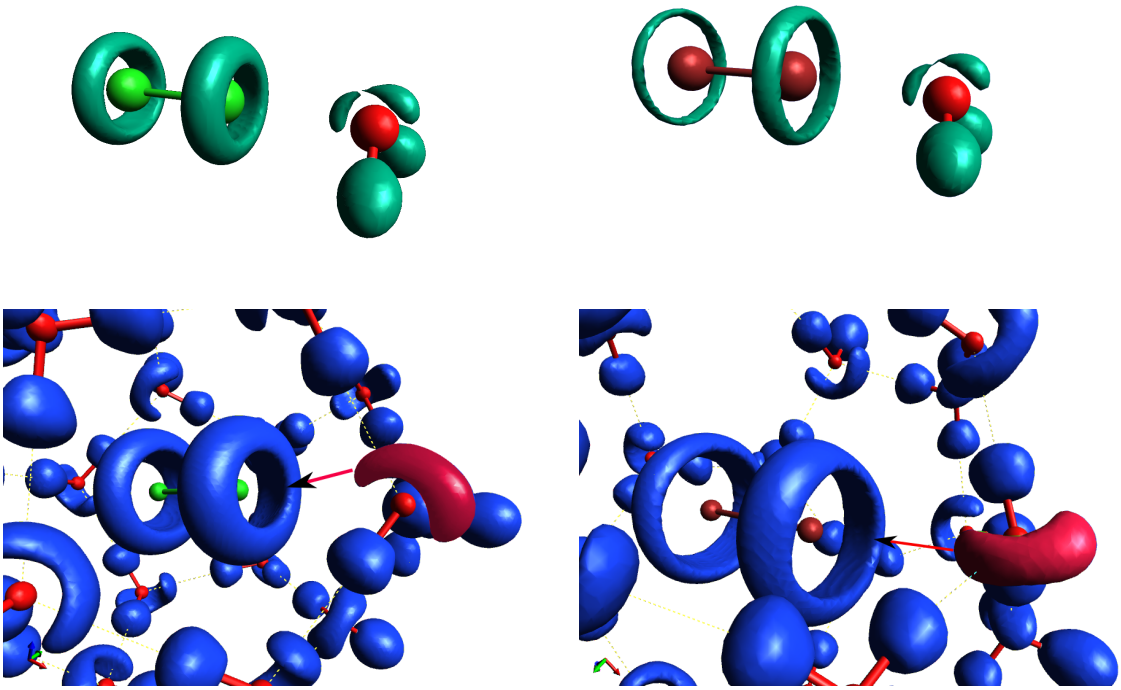

Figura 3.11: Isosuperficies de la ELF ($\eta = 0{,}9$) para los complejos $Cl_2 \cdots H_2O$ y $Br_2 \cdots H_2O$ (arriba, de izquierda a derecha), y para los sistemas 1a y 2b (abajo, también de izquierda a derecha). En este caso, una flecha señala a los pares libres del oxígeno (en rojo) involucrados en el enlace de halógeno que apuntan hacia el correspondiente agujero σ.

La isosuperficie de la ELF de los clatratos 1a y 2b muestra que a pesar de que los átomos de oxígeno de la jaula se encuentran participando ya en enlaces de hidrógeno, para los contactos $X \cdots O$ más cercanos el par libre participa en la interacción con el agujero σ. Es decir, este par libre participa en un enlace de hidrógeno y, al mismo tiempo, en un enlace de halógeno parcial. Es importante tener en cuenta que para el resto de los oxígenos en la jaula, sus pares libres apuntan o bien hacia el exterior de esta o bien a la densidad electrónica alrededor de los átomos de halógeno.

La figura 3.12 muestra las superficies NCI de los mismos sistemas que la figura 3.11. Es interesante notar que en las referencias, Cl_2...H_2O y Br_2...H_2O, aparecen superficies azules con forma de disco entre el átomo de halógeno y el oxígeno. Esto coincide con las superficies de la ELF en que pone en relieve la importancia de los pares libres para esta interacción. Para el caso de los clatratos 1a y 2b también se confirma lo visto en la ELF. La figura 3.12 nos permite apreciar los enlaces de hidrógeno y como su existencia no excluye la presencia de superficies de color azul intenso, indicador de atracción, entre los átomos de cloro o bromo y los oxígenos más cercanos. Como era de espearse, la interacción entre el dihalógeno y la jaula involucra un número considerable de átomos, pero deja claro que las interacciones más atractivas son aquellas que previamente se han identificado como enlaces de halógeno.

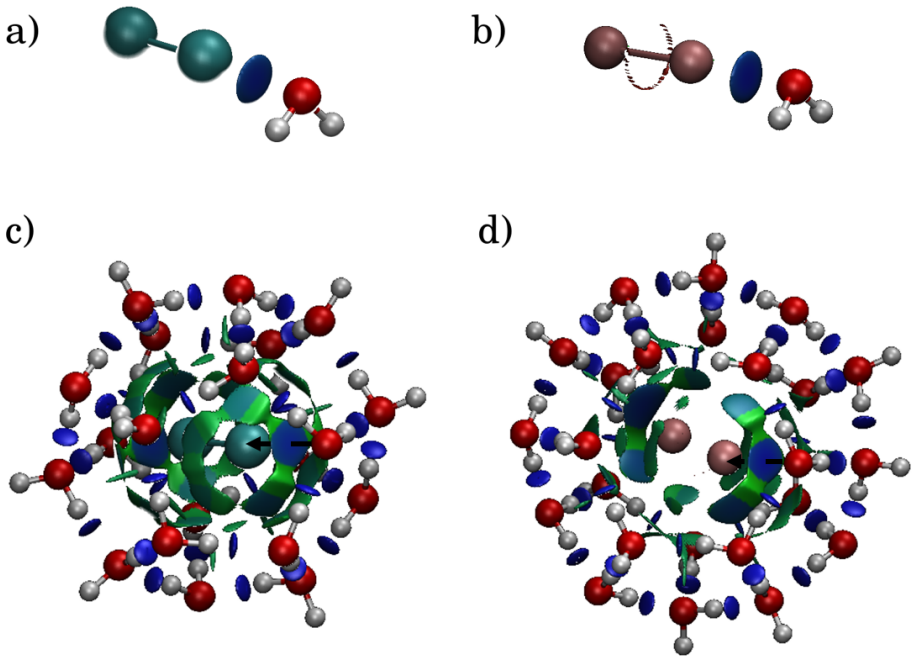

Figura 3.12: Isosuperficies de NCI para los complejos $Cl_2 \cdots H_2O$ y $Br_2 \cdots H_2O$ (arriba, de izquierda a derecha), y por los sistemas 1a y 2b (abajo, también de izquierda a derecha). La superficie atractiva correspondiente a la interacción oxígeno-halógeno está intersectada por una flecha negra que apunta desde el oxígeno hacia el átomo de halógeno.

Las descripciones de la ELF y de las superficies de NCI ofrecen interpretaciones compatibles, ambas favoreciendo la existencia de un enlace de halógeno en los confómeros 1a y 2b.

La metodología IQA es capaz de calcular de manera independiente las interacciones entre dos átomos dentro de una molécula. En este caso esta metodología fue utilizada para comparar la

fuerza relativa de las interacciones en los clatratos con respecto a los sistemas modelo, $X_2 \cdots H_2O$. La tabla 3.6 contiene un resumen de estos datos. El primer resultado que destaca de esta tabla es que para los complejos de referencia, $X_2 \cdots H_2O$, la energía de interacción es relativamente grande, alrededor de -24 y -34 kcal/mol para cloro y bromo, respectivamente. Para los enlaces dentro de la jaula, los que más se asemejan son la interacción Cl61-O4 en el sistema 1a y el par Br73-O16 en el sistema 2b. El valor de E_{int} para el primero es de -22 kcal/mol mientras que para el segundo es de -38 kcal/mol. De esta manera podemos confirmar la existencia de enlace de halógeno en dos de los sistemas estudiados.

Tabla 3.6: Descriptores IQA para interacciones oxígeno-halógeno seleccionadas. Energías en kcal/mol e índices de deslocalización en u.a.

Sistema	Interacción	$E_{\text{int}}^{\text{AB}}$	$V_{\text{cl}}^{\text{AB}}$	$V_{\text{xc}}^{\text{AB}}$	DI(A,B)
$Cl_2 \cdots H_2O$	Cl2-O3	-24.48	-10.36	-14.12	0.131
1a	Cl61-O4	-21.74	-7.20	-14.54	0.131
	Cl62-O5	-5.61	0.63	-6.25	0.063
1b	Cl61-O18	-12.12	-1.60	-10.52	0.092
$Br_2 \cdots H_2O$	Br2-O3	-34.07	-17.06	-17.01	0.158
2a	Br74-O7	-13.30	-7.02	-6.18	0.060
2b	Br73-O7	-2.06	-1.35	-0.70	0.009
	Br73-O16	-37.78	-19.49	-18.29	0.165
	Br74-O31	-19.61	-5.36	-14.24	0.133
2c	Br73-O31	-14.62	-3.61	-11.01	0.106

De manera un tanto inesperada, los resultados indican que ambos componentes de la energía de interacción contribuyen de manera importante a la energía de interacción.. V_{cl} es ligeramente más relevante en $Br_2 \cdots H_2O$, de acuerdo con el mayor tamaño del agujero σ en este caso. Por otro lado, los valores de V_{xc} coinciden con trabajo previo acerca del enlace de hidrógeno [94]. En el contexto de IQA, la presencia de una energía $V_{\text{cl}}^{\text{AB}}$ atractiva de cierto tamaño podría considerarse una señal de la existencia de un enlace de halógeno, pues confirma el requisito de ser una interacción electrostática atractiva.

Los valores de V_{cl} reportados en la tabla 3.6 son negativos, es decir, atractivos. Esto puede ser sorprendente si consideramos que tanto los halógenos como el oxígeno tienen una carga QTAIM negativa. Sin embargo, el signo de la interacción es el resultado de la suma de más

términos además del monopolo-monopolo de las cargas, como es la interacción dipolo-dipolo y la cuadripolo-cuadripolo. Por ejemplo, para la interacción Cl61-O4 las cargas QTAIM son -0.008 y -1.295 u.a. para el cloro y el oxígeno, respectivamente. Esto genera una interacción monopolo-monopolo de 1.3 kcal/mol, muy lejos de la interacción electrostática total de -7.2 kcal/mol. La atribución de esta diferencia a términos multipolares superiores es de naturaleza qualitativa, no cuantitativa. En realidad, la interacción multipolar en este tipo de interacciones no converge a su valor exacto debido a que la condición para una convergencia adecuada no se cumple.

Una corroboración de que el signo negativo de V_{cl} puede ser atribuido a la interacción entre el par libre y el agujero σ es el par de átomos Cl62-O5 en el confómero 1a. Aquí, la parte clásica de la interacción es ligeramente positiva, pues en en este caso la interacción ocurre entre el par libre de un oxígeno y los pares libre del átomo de cloro adyacente.

Finalmente, un indicador del papel que juega la componente de intercambio y correlación en el enlace de halógeno viene del índice de deslocalización. El DI es una generalización del concepto de orden de enlace que cuenta el número de electrones compartidos entre dos átomos. Los valores de la tabla 3.6 muestran valores tan grandes como 0.16 u.a., muy lejos del valor para un enlace covalente simple, pero de magnitud comparable al DI encontrado para un enlace de hidrógeno tradicional. Esto es una prueba más de la existencia del intercambio de densidad electrónica entre la jaula y la molécula de halógeno.

Así, distintos análisis de la QCT de la naturaleza de la interacción entre las moléculas de halógeno y el agua en los clatratos 5^{12} y $5^{12}6^2$ muestran que los sistemas estudiados presentan enlaces de halógeno. Los resultados IQA para estos complejos son comparables a aquellos correspondientes a los sistemas de referencia $H_2O\cdots Cl_2$ y $H_2O\cdots Br_2$, donde no hay duda alguna de la presencia de enlace de halógeno.

3.2. Interacciones en compuestos inorgánicos

Los tres artículos que conforman esta sección de la tesis fueron producidos como una colaboración teórico-experimental en conjunto con el grupo del doctor Hugo Torrens del departamento de química inorgánica la Universidad Nacional Autónoma de México. Este trabajo ha sido para mi una de las partes más gratificantes de la tesis, no solamente por los buenos resultados obtenidos, sino porque muestra por un lado la complementareidad de teoría y práctica en el tratamiento de problemas complejos, y por otro la capacidad de la QCT para escudriñar las entrañas de una molécula y ofrecernos nueva información.

En este trabajo, estudiamos diferentes complejos organometálicos de oro. La cantidad de estudios sistemáticos respecto a este tipo de compuestos ha sido mínima [95], esto a pesar de que estos poseen un amplio rango de aplicaciones, entre las que destacan su versatilidad y selectividad como catalizador [96; 97; 98], y sus poco comunes propiedades fisicoquímicas [99; 100].

Las herramientas de la QCT permiten analizar por separado distintas interacciones. Utilizando QTAIM podemos analizar los cambios en la interacción entre dos átomos al cambiar un sustituyente en uno de estos de una manera cuantitativa. NCI permite discernir interacciones que al no ser propiamente enlaces, como puentes de hidrógeno intramoleculares débiles o interacciones $\pi - \pi$ [101], muchas veces son pasadas por alto. Esto, a pesar de que en ocasiones un conjunto de interacciones débiles es determinante en la forma que adoptan las moléculas [102].

Para esta serie de artículos, debido a las similitudes entre los sistemas y con el objetivo de ser consistentes en la investigación, se utilizó una misma metodología. Primeramente, a partir de estructuras obtenidas mediante cristalografía de rayos X se realizaron cálculos de estructura electrónica a nivel DFT usando el funcional BP86 [103; 104] en conjunto con la base TZV [105], usando la aproximación regular de orden cero [106; 107] al Hamiltoniano relativista (ZORA por sus iniciales en inglés). Estos cálculos se llevaron a cabo tal como están implementados en el programa ORCA[78]. Posteriormente, se realizó análisis QTAIM utilizando el programa AIMAll [65] así como un un estudio de las interacciones no covalentes usando el paquete NCIPlot [41].

3.2.1. π-Backbonding and non-covalent interactions in the JohnPhos and polyfluorothiolate complexes of gold(I)

JohnPhos es una fosfina de Buchwald que se carateriza por su vasta estericidad, la cual generalmente impide la formación de contactos entre átomos de oro de moléculas adyacentes. De esta manera, el oro acomplejado con la fosfina JohnPhos normalmente forma otro tipo de interacciones no covalentes, como Au-π_{phenyl}, Au-F o Au-H.

En este artículo [45] se exploró el comportamiento de diferentes complejos formados por oro, la fosfina JohnPhos, y diferentes tiolatos polifluorinados con la intención de observar como diferencias en el grado de fluorinación afectan, por un lado el acomplejamiento oro-fosfina y oro-tiolato, y por otro la formación de otros contactos entre el oro y los sustituyentes circundantes. Para ello se sintetizó una serie de complejos organometálicos con fórmula [Au(SR_F)(JPhos)], donde JPhos=P($C_6H_4-C_6H_5$)(t−But)$_2$ y R_F=C_6F_5 (**1**), C_6HF_4-4 (**2**), $C_6H_3F_2-3,5$ (**3**), $C_6H_3F_2-2,4$ (**4**), C_6H_4F-2 (**5**), C_6H_4F-3 (**6**), C_6H_4F-4 (**7**) y CF_3 (**8**), los cuales se muestran en la Figura 3.13. En el artículo original se detalla la síntesis de estos compuestos.

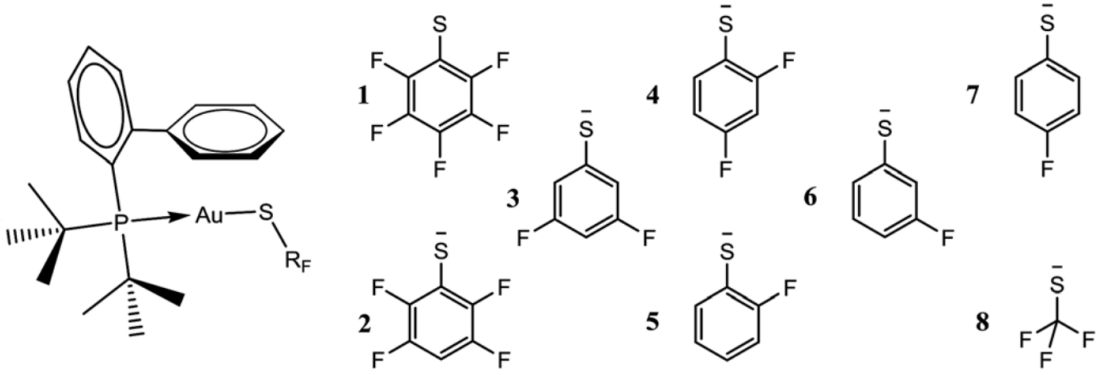

Figura 3.13: Sintetized compounds. R_F represents the thiolates 1 to 8.

En la tabla 3.7 se muestran las distancias azufre-oro y oro-fósforo asó como el ángulo azufre-oro-fósforo para compuestos estudiados. Para todos estos, la distancia azufre oro es de alrededor de 2.30 Å, mientras que aquella entre oro y fósforo es ligeramente más pequeña, de aproximadamente 2.27 Å. Lo primero que podemos apreciar es que el grado de fluorinación tiene una influencia mínima en las características geométricas de los enlaces:

En la tabla 3.8 se muestran la densidad en en $\rho(\mathbf{r}_{bcp})$, un descriptor cualitativo de la fuerza de enlace, y el DI, una medida del número de electrones compartidos entre dos átomos, para los enlaces Au-S y Au-P. Como podemos apreciar, no hay diferencias significativas de los valores de

Tabla 3.7: Distancias, en angstrom, para los enlaces oro-azufre y oro-fósforo, así como el ángulo azufre-oro-fósforo para los compuestos estudiados. Los valores de las distancias están en Ånstrongs.

Compound	d(S-Au)	d(Au-P)	Angle (S-Au-P)
[Au(SC_6F_5)(JPhos)] 1	2.30	2.27	173.6
[Au(SC_6HF_4)(JPhos)] 2	2.30	2.27	173.7
[Au($SC_6H_3F_2-3,5$)(JPhos)] 3	2.31	2.28	175.6
[Au($SC_6H_3F_2-2,4$)(JPhos)] 4	2.30	2.28	174.6
[Au(SC_6H_4F-2)(JPhos)] 5	2.30	2.27	173.6
[Au(SC_6H_4F-3)(JPhos)] 6	2.30	2.28	176.3
[Au(SC_6H_4F-4)(JPhos)] 7	2.30	2.28	174.6
[Au(SCF_3)(JPhos)] 8	2.31	2.27	175.7

$\rho(\mathbf{r}_{bcp})$ y DI entre los compuestos estudiados. Hasta este punto todo apunta a que las diferencias en el grado de fluorinación del tiolato no tienen efectos significativos sobre los enlaces químicos que forma el átomo de oro.

Tabla 3.8: Densidad de carga en el punto críticos de enlace ($\rho(\mathbf{r}_{bcp})$), elipticidad (ϵ), e índice de deslocalización (DI) para los enlaces Au-S y Au-P así como las cargas atómicas de azufre, oro, y fósforo. Todo lo anterior en unidades atḿicas.

	S-Au			Au-P			Charges		
Compound	ρ(rbcp)	ϵ	DI	ρ(rbcp)	ϵ	DI	S	Au	P
1	0.1099	0.0584	1.0487	0.1200	0.0350	0.98645	-0.1210	-0.0177	1.3811
2	0.1102	0.0580	1.0514	0.1212	0.0346	0.99249	-0.1254	-0.0195	1.3918
3	0.1110	0.0697	1.0801	0.1191	0.0416	0.97962	-0.1799	-0.0476	1.3880
4	0.1088	0.0602	1.0768	0.1174	0.0362	0.97583	-0.2137	-0.0449	1.3679
5	0.1088	0.0686	1.0726	0.1183	0.0409	0.98350	-0.1862	-0.0473	1.3986
6	0.1108	0.0650	1.1038	0.1191	0.0379	0.98318	-0.2392	-0.0561	1.3751
7	0.1108	0.0631	1.0936	0.1182	0.0349	0.97691	-0.2300	-0.0512	1.3560
8	0.1089	0.0491	1.0457	0.1210	0.0355	0.99085	-0.1226	-0.0272	1.3834

Sin embargo, cuando observamos el valor correspondiente a la elipticidad del enlace, un reflejo de la acumulación de densidad a lo largo de un plano y por tanto un predictor del caracter π de una interacción, notamos que para todos los casos el valor de ϵ es diferente de cero y distinto entre sí. Lo primero es muestra de la presencia de retrodonación de densidad electrónica por

parte del oro hacia los ligantes, y lo segundo indica que el grado de ésta es diferente para cada compuesto.

El término retrodonación es un concepto de química inorgánica que se apoya en la idea de orbitales atómicos y enlace dativo. En algunos casos la formación de un enlace entre ligante y metal en un complejo está dada por la donación de densidad del ligante al metal y posterior retrodonación de densidad del metal al ligante. Esto está representado en la figura 3.14 en términos de orbitales atómicos: el primer paso sería descrito como el paso de electrones de un par a un orbital vacío del metal y el segundo como la descarga de una parte de esa densidad desde un orbital d del metal hacia el orbital de antienlace π del ligante.

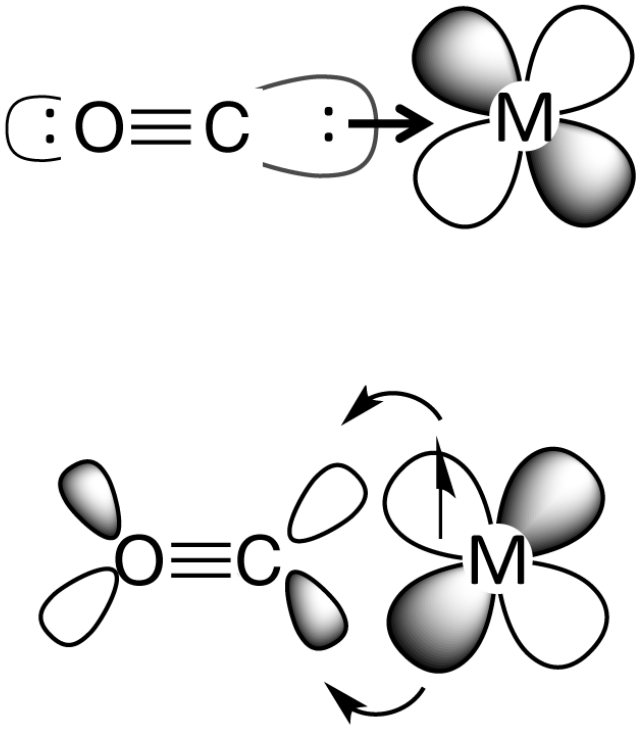

Figura 3.14: Esquema del concepto de retrodonación. Arriba, el carbono del carbonilo dona densidad electrónica a un metal. Abajo, el metal "regresa" parte de esa densidad.

Otra cosa que podemos ver en la tabla 3.8 es que el compuesto **8**, donde el sustituyente no es un tiolato sino (SCF_3), tiene menos caracter π. Esto es, la presencia del grupo fenil aumenta la capacidad del azufre para recibir retrodonación. En términos del caracter creciente de elipticidad podemos ordenar a los compuestos estudiados como 8 <2 <1 <4 <7 <6 <5 <3. Esto indica que el grado de retrodonación depende tanto del número de sustituyentes fluoruro como de la

posición relativa de los mismos.

A pesar de la complejidad de los enlaces que establece el oro en los sistemas estudiades, es posible observar una relación entre la carga presente en el átomo de oro y la cantidad de retrodonación presente en cada sistema. En la figura 3.15 podemos ver que a medida que la elipticidad del enlace Au-S se incrementa la carga del átomo de oro se hace más negativa. Así, es posible controlar, dentro de ciertos parámetros, la forma del enlace Au-S mediante la modulación de la cantidad de densidad electrónica en el átomo de oro.

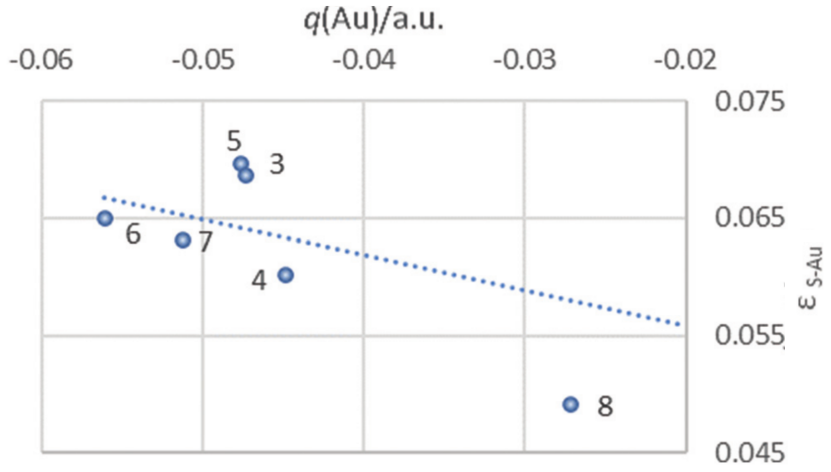

Figura 3.15: Relación entre la carga QTAIM del átomo de oro y la elipticidad del enlae Au-S.

Los cambios observados en el carácter π del enlace Au-S no están acompañados por modificaciones ni en el orden ni en la distancia de enlace correspondiente. Es decir, no hay cambio en el número total de electrones compartidos, sino únicamente una reorganización de la distribución de densidad electrónica entre enlaces σ y π. Dicha reorganización está dada por las diferencias en los diferentes tiolatos provocadas por los grados de fluorinación de cada compuesto.

Otra relación interesante que observamos es aquella entre las cargas de los átomos de azufre y oro. Como podemos ver en la parte izquierda de la figura 3.16 la correlación entre ambas cantidades es muy buena. En la parte derecha de la misma figura tenemos la relación entre la suma de las cargas de azufre y oro con el grado de fluorinación. Para los compuestos con menos fluor, como (6) y (7), la suma de cargas es más negativa. La combinación de estos resultados indica que por un lado los fluoruros adicionales están atrayendo hacia si densidad de carga y por otro que dicha densidad proviene prácticamente a partes iguales del azufre y el oro.

La interacción entre el anillo π de la fosfina también es importante. En la figura 3.17 podemos ver la extensión de esta interacción en la isosuperficie verde entre el átomo de oro y en anillo.

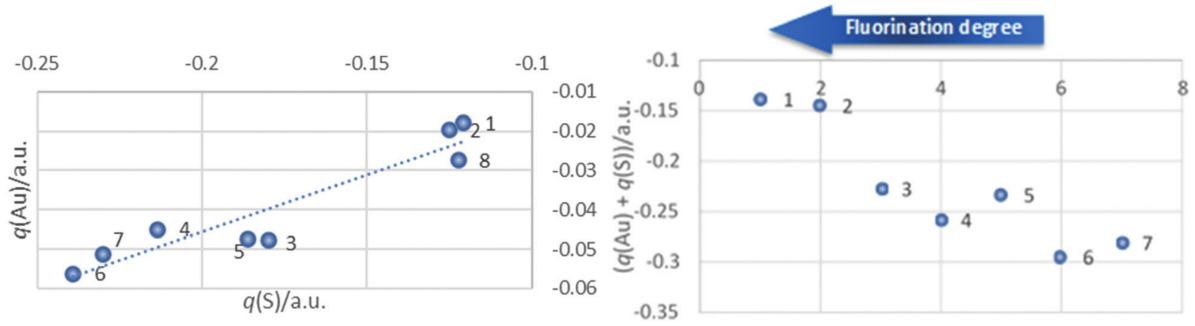

Figura 3.16: Arriba: Correlación entre las cargas QTAIM de los átomos de oro y azufre. $R^2 = 0{,}88$. Abajo: la relación entre q(Au) + q(S) y el grado de fluoración del grupo feniltiolato.

Para todos los compuestos estudiados la distancia $Au - C_\pi$ es particularmente corta debido a la interacción $Au - \pi$. Usamos la hapticidad de Kochi como criterio para poder caracterizar estas interacciones, aunque cabe recordar que este parámetro no es indicativo de la fuerza de las mismas. En la tabla 3.9 se muestran los resultados correspondientes. Para todos los casos la distancia $Au - C_{ipso}$ es menor que la suma de radios de van der Waals de oro y carbono, 3.36 Å.

Tabla 3.9: Hapticidad, densidad en el punto crítico e índice de deslocalización entre el oro y el carbono ipso.

Compound	Hapticidad	ρ(rbcp) Au-C_{ipso}	DI Au-C_{ipso}
[Au(SC_6F_5)(JPhos)] 1	1.294	0.0175	0.0984
[Au(SC_6HF_4)(JPhos)] 2	1.585	0.0174	0.0966
[Au($SC_6H_3F_2$−3,5)(JPhos)] 3	1.444	0.0177	0.0903
[Au($SC_6H_3F_2$−2,4)(JPhos)] 4	1.680	0.0169	0.0907
[Au(SC_6H_4F−2)(JPhos)] 5	1.762	0.0178	0.0977
[Au(SC_6H_4F−3)(JPhos)] 6	1.582	0.0196	0.1180
[Au(SC_6H_4F−4)(JPhos)] 7	1.729	0.0179	0.0991
[Au(SCF_3)(JPhos)] 8	1.651	0.0183	0.0985

La tabla 3.9 contiene los datos de la densidad en el BCP entre Au y C_{ipso} así como el índice de deslocalización entre ambos átomos. Ahí podemos apreciar que existe una deslocalización electrónica substancial entre el carbono ipso y el oro. Esta estabilización se encuentra reforzada por la presencia de hidrógenos alrededor del átomo de oro.

Utilizamos la metodología NCI para poder observar los las diferentes interacciones no covalen-

tes que se presentan en los compuestos estudiados. Todos ellos presentan interacciones atractivas entre el átomo de oro y los hidrógenos circundates. En la figura 3.17 se pueden apreciar estos contactos en el compuesto [Au($SC_6H_3F_2$−3, 5)(JPhos)].

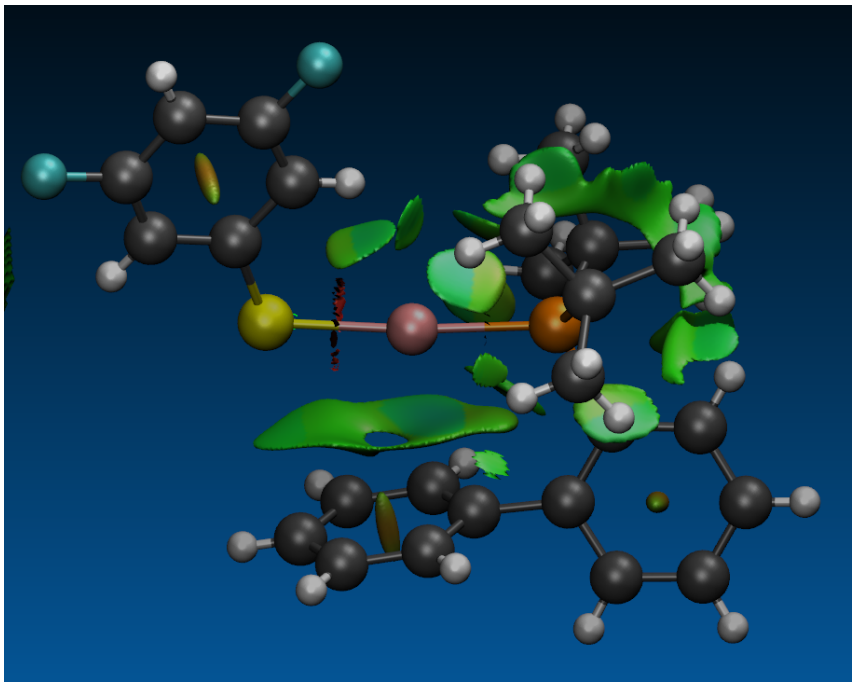

Figura 3.17: Interacciones no covalentes en el compuesto [Au($SC_6H_3F_2$−3, 5)(JPhos)] como se muestran usando el programa NCIPlot. El código de color es azufre = amarillo, oro = rosa y fósforo = naranja.

3.2.2. Structural effects of trifluoromethylation and fluorination in gold(I) BIPHEP fluorothiolates

La naturaleza de los contactos entre átomos es muchas veces cuestión de debate entre los químicos inorgánicos. Son especialmente controvertidas aquellas interacciones que están condicionadas, o soportadas, por el resto de la estructura del compuesto. Este artículo estudia dos compuestos que presentan un contacto oro-oro soportado por un puente de difosfina. Los resultados muestran que la interacción contiene elementos que pueden considerarse como covalentes.

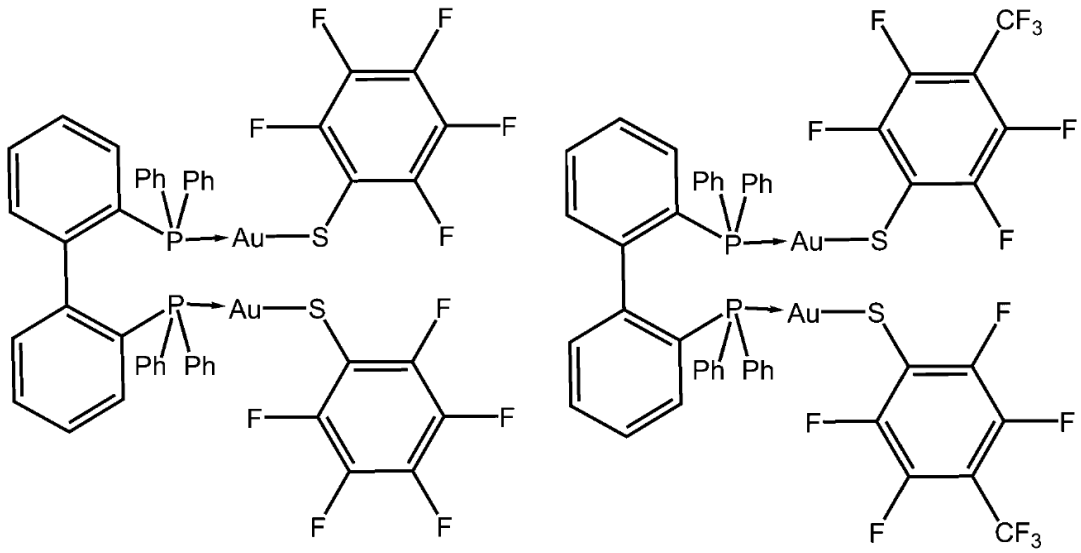

Figura 3.18: Estructuras de los sistemas estudiados de oro (I).

Para el presente trabajo se sintetizaron y caracterizaron dos complejos diáuricos que contienen un puente formado por la fosfina BIPHEP[4] y con perflurorotiolatos como ligantes con fórmula $[Au_2(SR_F)_2(\mu\text{−BIPHEP})]$ com $SR_F = SC_6F_5$ (1) y $SC_6F_4(CF_3)$−4 (2), tal como se muestra en la figura 3.18.

Las estructuras atómicas de los compuestos (1) y (2) son muy similares en tanto que muestran conectividades casi idénticas. Sin embargo, el cambio de sustituyente $-F$ por $-CF_3$ modifica al resto de la molécula, provocando diferencias en las longitudes de enlace en interacciones que no son próximas. Así nos encontramos con que el enlace oro-oro, la distancia entre el fluoruro en posición orto del anillo del tiolato y uno de los oros, y la separación entre el azufre y el anillo del

[4] 2,20-bis(difenilfosfino)-1,10-bifenil

tiolato adyacente son más pequeños en el compuesto (2) que en el compuesto (1). Los parámetros anteriores se pueden observar en la figura 3.19. Es notable que al pasar de $-F$ a $-CF_3$ en la posición para del anillo se ha producido un compactamiento general en la estructura.

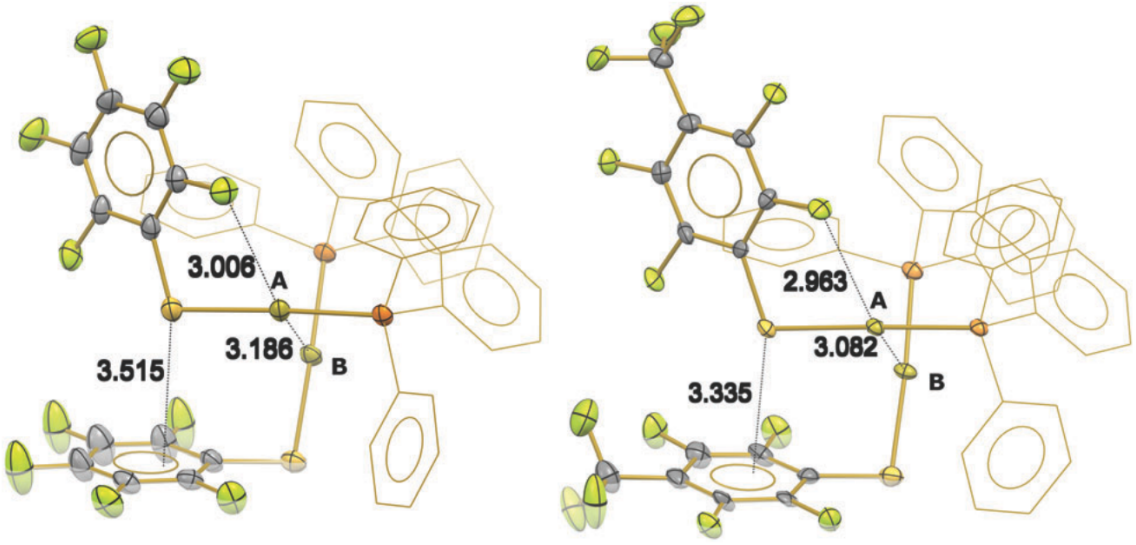

Figura 3.19: Representación de los resultados del análisis de rayos X para las estructuras de los compuestos 1 (izquierda) y 2 (derecha). Los anillos fenilo del BIPHEP se muestran como esqueletos y los átomos de hidrógeno se han omitido por claridad. El esquema de colores es el siguiente: Au, oro; F, verde; S, amarillo; P, naranja y C, gris.

Otra propiedad de los compuestos estudiados es que los dos átomos de oro en cada molécula no son equivalentes. Uno de ellos, señalado en la figura 3.19 como A, es mucho más cercano a un fluoruro en posición orto del tiofenil, mientras que el otro, señalado como B, no tiene contacto alguno con ningún átomo de flúor. Adicionalmente, podemos designar como P_x y S_x al fósforo y al azufre más cercanos al átomo X, donde X puede ser el átomo A o B.

En la tabla 3.10 se muestran las distancias entre pares seleccionados. Ahí podemos apreciar que las distancias de enlace entre interacciones covalentes son casi idénticas para ambos compuestos. En contraste, para las interacciones no covalentes dichas diferencias son apreciables.

En ambas moléculas, la distancia $S - \pi_{\text{fenil}}$ es menor que la suma del radio de van der Waals de azufre y carbono ($\sum r_{vdW} = 3{,}66$ Å), lo que indica una interacción cuando menos débil. Esta interacción puede llegar a jugar un papel importante en la estructura final de las moléculas estudiadas aquí puesto que es un motivo que se repite con relativa regularidad en las estructuras del CSD [108].

Tabla 3.10: Distancias (Å) entre pares seleccionados de átomos de las moléculas (1) y (2).

Distances	Compound 1	Compound 2
Au_A–P_A	2.2566	2.2559
Au_B–P_B	2.2607	2.2601
Au_A–S_A	2.3054	2.3033
Au_B–S_B	2.3183	2.3205
Au_A–Au_B	3.1862	3.0823
Au_A–F	3.0060	2.9630

Otro contacto cuya distancia es menor que la suma de los radios de van der Waals correspondientes es aquel entre el fluor en la posición orto del anillo del tiolato y el átomo de oro A ($\sum r_{rvW}$ = 3,13 Å). La presencia de esta interacción es contraria a la teoría de ácidos y bases duras y blandas. De acuerdo a esta teoría, un átomo pequeño que soporta una carga grande es considerado como duro, mientras que un átomo de mayor tamaño y poca carga es denominado como blando. Los átomos duros se identifican como poco polarizables mientras que los blandos son susceptibles a la polarización. Según esta teoría los ácidos blandos serían atraídos por bases blandas, mientras que los ácidos duros interaccionarían más con bases duras. De esta forma, la interacción observada en estos compuestos entre un ácido blando como el oro y una base dura como lo es el fluor es inesperada.

Usamos indicadores de QTAIM para estudiar el contacto F-Au. los valores para la densidad y el Laplaciano en el BCP son pequeños para ambos compuestos. Esto es comúm en interacciones con metales de transición debido a la naturaleza difusa de los enlaces que forman estos. Por otra parte, el que la energía cinética sea mayor que la potencial en el BCP y que el DI entre átomos sea menor a 0.01 u.a. indican que la interacción es mayormente de capa cerrada.

Otra manera de estudiar la naturaleza del contacto F-Au es comparando los oros A y B dado que este se presenta únicamente para Au_A. Así encontramos que el oro A no presenta carga, mientras que el oro B tiene una carga ligeramente negativa (-0.03 y -0.02 u.a para los compuestos 1 y 2, respectivamente). Además, los fluoruros que tienen contacto con el oro son ligeramente más negativos que sus contrapartes no interactuante (-0.62 and -0.63 u.a. en los sistemas 1 y 2 contra -0.60 u.a.). Esto señala hacia una transferencia de densidad electrónica desde el oro hacia el fluor a través de la interacción observada.

De manera similar a los contactos anteriores, para la interacción oro-oro la distancia interató-

mica también es más pequeña que los correspondientes radios de van der Waals. Los resultados QTAIM respecto a este contacto se encuentran resumidos en la tabla 3.11. Ahí podemos apreciar que la densidad y el Laplaciano en el BCP tienen valores bajos. El valor de $H(r_{BCP})$, negativo para ambos compuestos y el valor del DI indican que la interacción tiene cierto grado de covalencia.

Tabla 3.11: Varios indicadores derivados de QTAIM que caracterizan la naturaleza de la interacción entre los átomos de oro en los compuestos 1 y 2. Valores en unidades atómicas.

Descriptor	Compound 1	Compound 2
$\rho(r_{BCP})$	0.0236	0.0284
$\nabla^2\rho(r_{BCP})$	0.0583	0.0721
$H(r_{BCP})$	-0.0002	-0.0011
$G(r_{BCP})/\rho(r_{BCP})$	0.6271	0.6760
DI	0.2755	0.3172

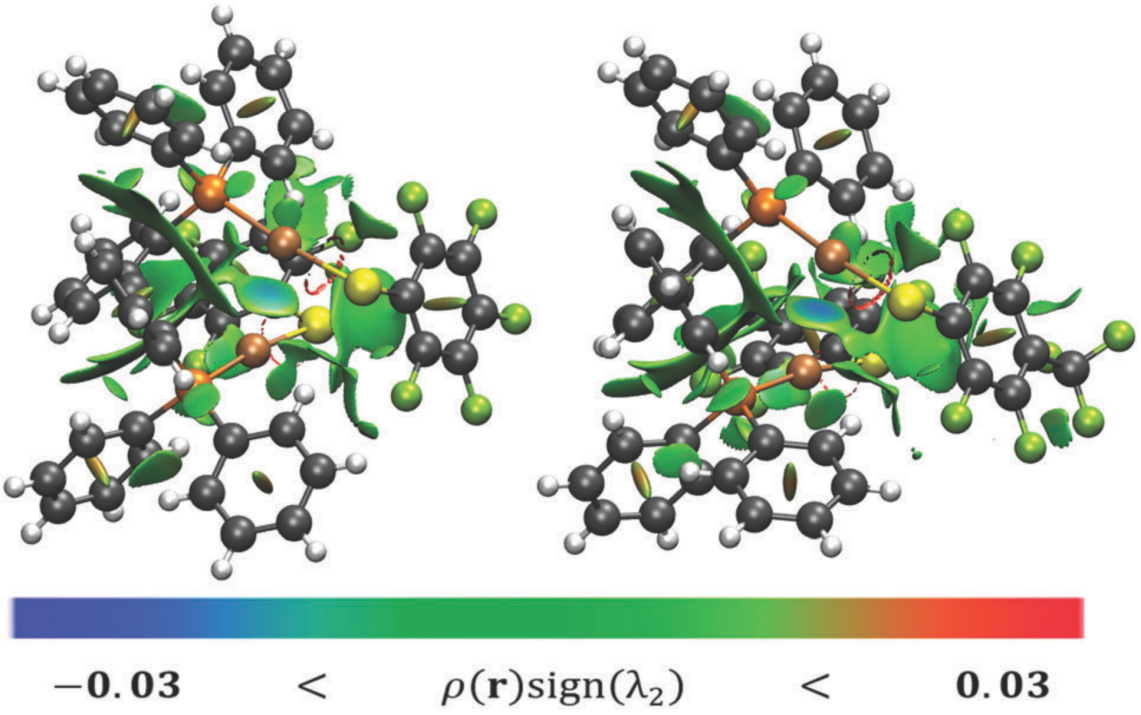

Figura 3.20: Isosuperficies de NCI que muestran interacciones no covalentes en compuestos los compuestos 1 (izquierda) y 2 (derecha). La superficie de interacciones débiles se muestra en color verde mientras que en azul están señaladas las interacciones más covalentes.

La figura 3.20 muestra las isosuperficies del gradiente reducido de la densidad para los compuestos 1 y 2. Aquí podemos apreciar en el color azul más pronunciado en la isosuperficie interatómica que la interacción Au-Au es más fuerte en 2 que en 1. Lo anterior concuerda con los resultados QTAIM, donde tanto $\rho(r_{BCP})$ como DI son mayores para 2 que para 1.

Evidencias experimentales y resultados del análisis QTAIM sugieren que el $-CF_3$ produce un efecto inductivo mayor que el -F. Estas observaciones están de acuerdo con lo reportado por True y colaboradores [109], quienes senálan que el efecto inductivo del fluor es mayor para átomos adyacentes pero menor para grupos que no se encuentran en su vecindad inmediata, mientras que para el caso del $-CF_3$ pasa lo contrario, sus fuerza inductiva de largo alcance es mayor que en proximidad.

En este artículo encontramos evidencias sustanciales de interacción aurofílica en ambos compuestos. Además, pudimos estudiar la manera en que el oro y el fluor interaccionan utilizando QTAIM. Sin embargo, personalmente el resultado más significativo para mi fue el del efecto inductivo de largo alcance. Este podría constituir una herramienta para el ajuste fino de propiedades de ciertas propiedades en una parte de la molécula sin alterar su ambiente químico inmediatamente adyacente. Esto podría ser de particular importancia para el diseño de nuevos fármacos.

3.2.3. Stability and trans Influence in Fluorinated Gold(I) Coordination Compounds

Cambios, a veces mínimos, de ligante pueden alterar diferentes propiedades de un compuesto de coordinación. Investigar la manera en cómo dichos cambios modifican un complejo de manera sistemática permite la modulación de sus propiedades y proporciona herramientas adicionales a los químicos a la hora de diseñar nuevos compuestos.

En este trabajo estudiamos la forma en que un ligante afecta el enlace metal-ligante que se encuentra en posición *trans* respecto a este, es decir, el efecto *trans*. Para ello aprovechamos por un lado que los complejos de oro usualmente presentan una geometría lineal, lo que los hace idóneos para estudiar este efecto sin interferencia de otros ligantes. Por otro lado, el ligante escogido para esta investigación fue una fosfina debido a que el fósforo es activo en la resonancia magnética nuclear (RMN), par poder usar esta técnica.

De esta manera, se sintetizaron y caracterizaron tres complejos derivados de fluorofosfinas de oro (I) de fórmula [AuCl(PPhF)] donde PPhF = $P(C_6H_5)_2(C_6F_5)$ (**1**), $P(C_6H_5)(C_6F_5)_2$ (2) y $P(C_6F_5)_3$ (3). La estructura de estos compuestos se puede observar en la figura 3.21. Adicionalmente, se prepararon 8 compuestos derivados a través de la sustitución de cloruro en los compuestos 1 y 2 con tiolatos fluorinados, obteniendo compuestos de fórmula [Au(SRF)(PPhF)] (donde SRF = SCF_3 (a), SCH_2CF_3 (b), SC_6F_5 (c), $SC_6F_4(CF_3)$–4 (d)).

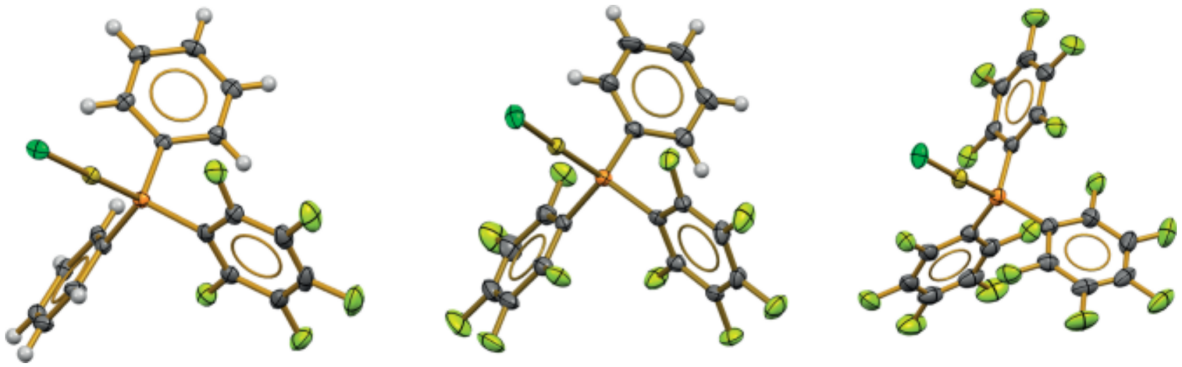

Figura 3.21: Diagramas de ORTEP con 50 % de probabilidad de las estructuras de rayos X de los compuestos 1, 2, y 3. El código de color es: naranja, P, oro, Au; verde, Cl; gris, C; blanco, H.

Para estudiar la estabilidad relativa de los tres compuestos se llevaron a cabo reacciones de sustitución de ligantes comenzando desde el compuesto 3. Estas reacciones fueron seguidas utilizando espectroscopía RMN de ^{31}P. Estos experimentos indican que la reacción procede de

manera tal que las fosfinas fluoradas son sustituidas por fenilos. Esto se puede apreciar de manera esquemática en la figura 3.21.

Para entender el origen de la mayor afinidad del fósforo por el anillo no fluorado se calculó el ΔG de estas reacciones utilizando la metodología mencionada anteriormente pero esta vez incluyendo el uso del modelo de polarización continuo [110]. Los valores de ΔG para cada reacción se encuentran en la parte derecha de la figura 3.22. En todos los casos la energía libre de Gibbs es negativa, es decir que se trata de una reacción termodinámicamente favorecida.

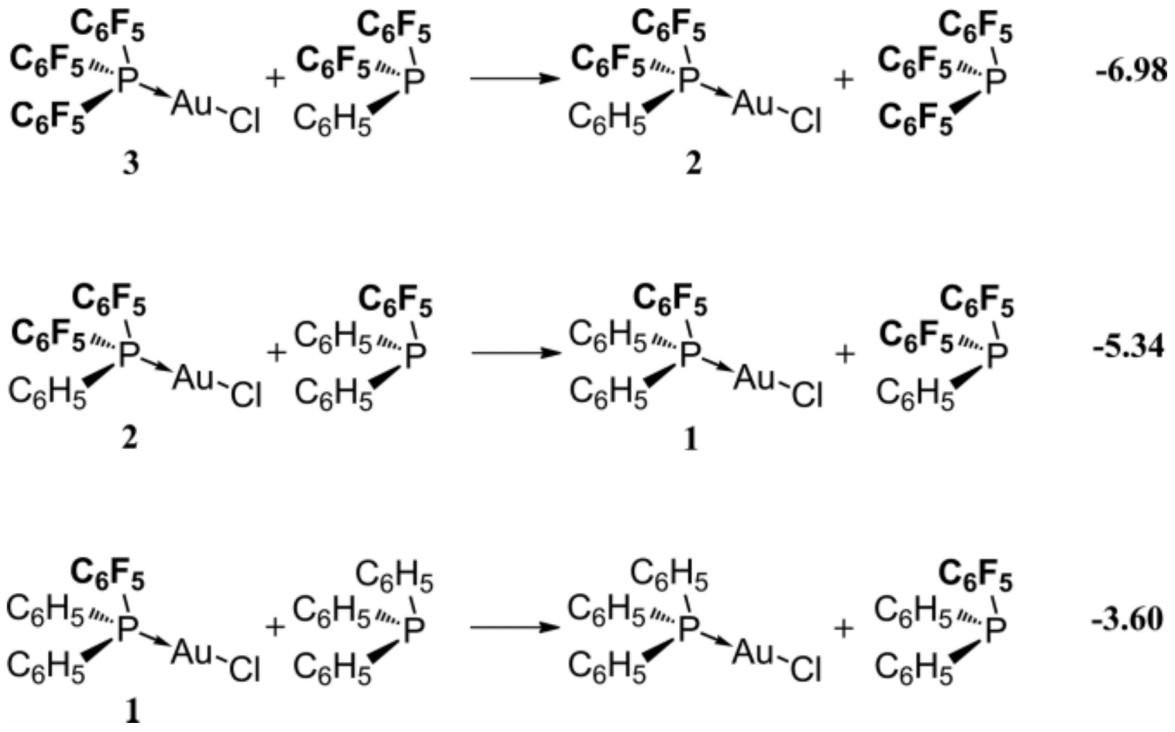

Figura 3.22: Valores calculados (kcal/mol) para las reacciones de sustitución de fosfinas.

Conjuntamente la evidencia experimental y las simulaciones sugieren que el enlace fósforo-oro es mucho más débil cuando la fosfina contiene sustituyentes fluor. El análisis QTAIM de estos compuestos explica parcialmente este resultado. Los valores de carga para los compuestos [AuCl(PPh_3)], 1, 2, y 3 son 0.02, 0.05, 0.09, y 0.13 a.u., respectivamente. Como podemos apreciar, el oro pierde densidad electrónica conforme aumenta el número de fluoruros en la fosfina.

Una relación que se encontró y nos pareció interesante fue aquella entre la carga del oro y el desplazamiento químico. Como podemos ver en la figura 3.23, un incremento en la carga del átomo de oro es directamente proporcional a un incremento en el desplazamiento químico de

^{31}P. Esta tendencia se mantiene cuando cambiamos el cloruro por sustituyentes tiolatos, de tal manera que podemos inferir que cuando el fósforo se encuentra ligado al oro (I), como en este caso, la desprotección del primero en RMN indica indirectamente que el oro ha perdido densidad electrónica.

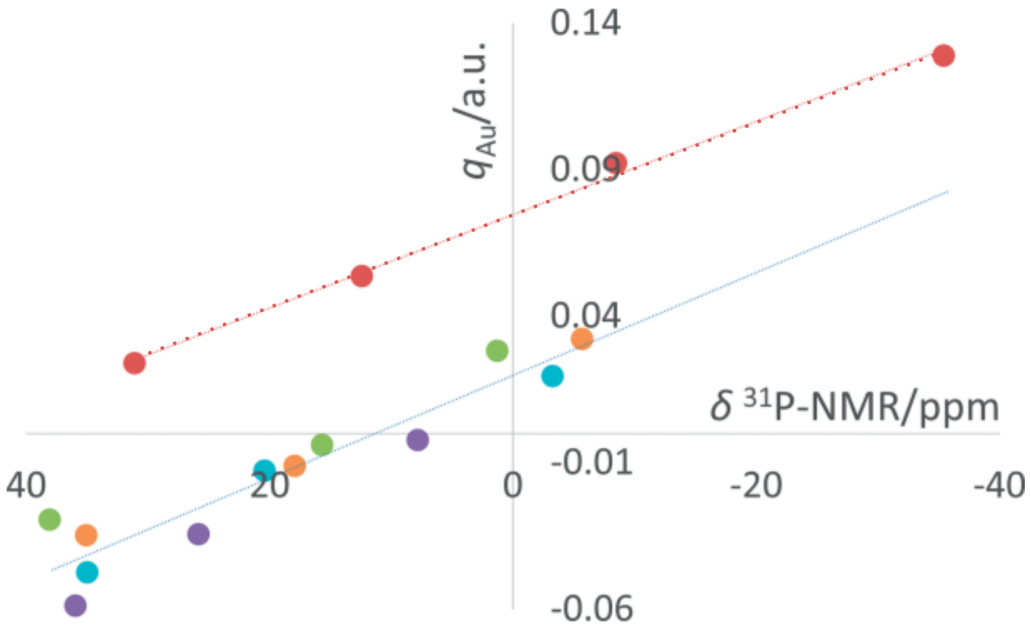

Figura 3.23: Relación entre la carga QTAIM en el átomo de oro y el desplazamiento químico de ^{31}P en RMN. Código de color: rojo, cloruro; verde, $-SCF_3$, púrpura, $-SCH_2F_3$, naranja, $-SC_6F_4(CF_3)-4$; azul, $-SC_6F_5$.

Con respecto al mecanismo que siguen las reacciones de sustitución de la fosfinas, este puede ser asociativo o disociativo. Ambas alternativas se muestra de manera esquemática en la figura 3.24. La principal evidencia contra el mecanismo asociativo es la alta barrera de disociación de este, calculada en 45 kcal/mol para el compuesto 3, que es difícilmente salvable en las condiciones de laboratorio. En contra del mecanismo disociativo está que no encontramos evidencia de la producción de la especie tricoordinada (aunque tampoco de la fosfina libre) en los experimentos de RMN. Sin embargo, es posible que la concentración de la especie intermedia sea muy baja, que la fosfina libre se produzca en cantidades muy pequeñas, o que se de un equilibrio entre la especie tricoordinada y la fosfina libre. En cualquiera de estos casos una detección con RMN no sería posible. Considerando todo esto, nuestro análisis sugiere un mecanismo asociativo, pero el mecanismo disociativo no puede ser completamente descartado sin más.

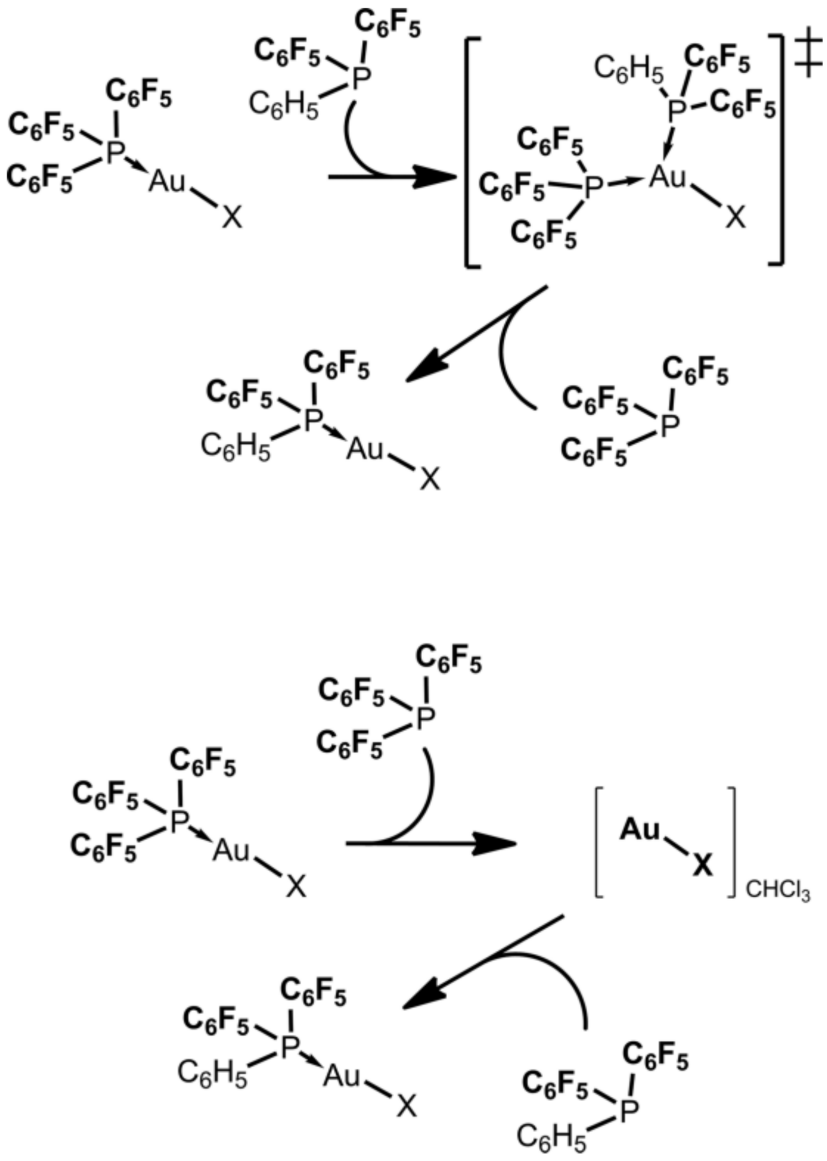

Figura 3.24: Mexanismos propuestos para la reacción de sustitución de las fosfinas. Mecanismos disociativo (arriba) y disociativo (abajo).

Nuestros resultados muestran que el aumento en el grado de fluorinación de la fosfina disminuye la fuerza del enlace Au-P. Además, en una demostración del efecto *trans*, el cambio del ligante cloro por un tiolato fluorado genera una disminución en la covalencia del enlace Au-P.

3.3. Performance of the RI and RIJCOSX approximations in the topological analysis of the electron density

La calidad del análisis QTAIM depende fuertemente de la calidad de la densidad electrónica sobre la que se realice. Esta densidad puede ser obtenida tanto experimentalmente como a partir de cálculos de química computacional, como HF, DFT, or post-HF. En el estudio de sistemas grandes la dispersión se vuelve un factor importante en la forma de los mismos. Como es sabido, HF no toma en cuenta la dispersión. En DFT, las correcciones introducidas en los funcionales híbridos para considerar la dispersión no se ven reflejadas en la densidad electrónica resultante. Finalmente, la mayoría de los métodos post-HF más sofisticados tienen un costo computacional asociado demasiado elevado como para calcular moléculas y cúmulos moleculares de manera efectiva.

En este contexto, la teoría de perturbaciones a segundo orden, en la implementación de Møller-Plesset (MP2) [62], se ha convertido en la metodología más usada para el estudio de complejos debilmente enlazados debido a que es el método más sencillo que es autoconsistente en tamaño, que incluye correlación electrónica, y que ofrece una descripción cualitativamente correcta de interacciones de largo alcance. Desafortunadamente, el escalado de MP2 es de $\mathcal{O}(N^5)$, donde N es el número de bases en el sistemas lo hace inadecuado para el modelado de sistemas grandes, como el mostrado en la figura 3.25.

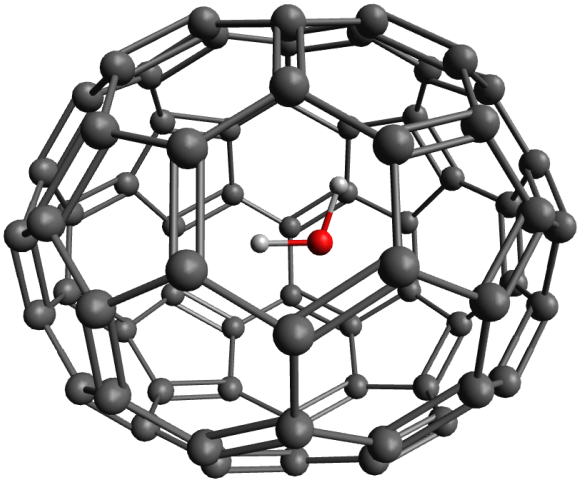

Figura 3.25: El complejo $H_2O@C_{70}$.

Una aproximación a MP2 que disminuyera el orden de escalado desarrollada por Vahtras, Almløf, and Feyereisen [111] propuso transformar las integrales de repulsión de cuatro centros

de MP2 en integrales de tres centros usando para ello una base auxiliar. Este procedimiento se conoce como resolución de la identidad (RI por sus iniciales en inglés). Posteriormente, esta idea fue retomada por Neese [112] en lo que se denomina como método split-RI-J. Con la misma idea de reducir el tiempo de computo Neese[113] propuso el algoritmo conocido como "chain of spheres", o cadena de esferas, para el cálculo de las integrales de intercambio. En este, se reduce el costo computacional únicamente considerando aquellas integrales donde dos funciones de base se superponen por encima de cierto límite. De esta manera se evita el cálculo de multitud de integrales cuya contribución es despreciable.

A la combinación de la metodología de la cadena de esferas con la aproximación RI se le conoce como el método RIJCOSX-MP2. Esta implementación tiene un escalado notablemente mejor que el MP2 tradicional, lo que permite su uso en el estudio de sistemas de mayor tamaño. En varias ocasiones se ha comprobado la aceleración en tiempo de computo y la exactitud en la reproducción de la energía que ofrece este método [114; 115; 77]. Sin embargo, hasta el momento no se ha producido ningún análisis sistemático de la calidad de RI-MP2 o RIJCOSX-MP2 usando descriptores de la densidad electrónica.

La necesidad de este análisis se justifica en el hecho que las equaciones que definen a los métodos de estructura electrónica MP2, RI-MP2, RIJCOSX-MP2 son diferentes y por tanto el uso del Lagrangiano para la construcción de las densidades relajadas que cumplen con el teorema de Hellman-Feynman pueden conducir a resultados distintos. De esta manera, en este artículo se ha calculado una serie de indicadores de QTAIM, incluyendo $\varrho(\mathbf{r})$, $\nabla^2\varrho(\mathbf{r})$ y la energía cinética en el BCP, junto con algunas cantidades integradas en los átomos, como cargas atómicas, momento dipolar, y los índices de localización y deslocalización entre átomos de acuerdo con la aproximación de Müller [66]. Las moléculas utilizadas como ejemplo fueron cúmulos pequeños de agua $(H_2O)_n$, $n = 2 - 10$, así como $CH_3{-}CH_3$, $CH_2{=}CH_2$, C_6H_6, H_2O, y LiF. Los conjuntos de propiedades y de moléculas estudiadas fueron elegidos para representar cálculos de QTAIM estándar [116].

En cuanto a los cálculos en sí mismos, las estructuras de los cúmulos de agua fueron tomadas del trabajo de Segarra y colaboradores [117] mientras que para el resto de los sistemas, sus geometrías fueron optimizadas con el nivel de teoría CCSD/aug-cc-pVDZ [63] en el programa GAUSSIAN-09 [64]. Funciones de ona de referencia a niveles HF/cc-pVTZ y MP2/cc-pVTZ fueron calculados también con GAUSSIAN-09. La optimización de geometría del complejo $H_2O@C_{70}$ (Figura 3.25) fue llevada a cabo en el nivel de teoría PBE/Def2-TZVP [118]. Todos los cálculos hechos con las aproximaciones RI y RIJCOSX se hicieron utilizando el programa ORCA [78].

La tabla 3.12 muestra la desviación promedio con respecto a los valores de referencia de algunos descriptores QTAIM para los cúmulos de agua estudiados. Es destacable lo pequeñas que son las diferencias observadas en general. Aún así es posible notar que las cantidades basadas en $\varrho(\mathbf{r})$ se comportan ligeramente mejor que aquellas que dependen de sus derivadas, como el Laplaciano. Esto concuerda con la idea que ligeros cambios en la densidad se aprecian más fácilmente a través de las derivadas de esta. Este es el caso la estructura de capas del átomo que es revelada mediante el análisis de $\nabla^2\varrho(\mathbf{r})$. Los errores más grandes se dan para las propiedades integradas, y son especialmente pronunciadas para los momentos dipolo de los átomos. Sin embargo, en todos los casos los errores se mantienen por abajo del 1 %.

Tabla 3.12: Desviaciones promedio (expresadas como porcentaje) de algunos descriptores de QTAIM in el conjunto de cúmulos de agua estudiados con respecto a la referencia correspondiente.

Method	ϱ	$\nabla^2\varrho$	G	LI	DI	Vol(Ω)	$\mu(\Omega)$
RIJCOSX-HF	0.06	0.11	0.07	0.02	0.08	0.20	0.76
RI-MP2	0.03	0.06	0.02	0.01	0.03	0.11	0.04
RIJCOSX-MP2	0.03	0.06	0.05	0.00	0.04	0.18	0.55

Cuando comparamos el uso de RIJCOSX para HF y MP2 notamos que los resultados de aproximación de la cadena de esteras son mucho mejores en el caso del último. Esto se debe a que las densidades promedio, como las de HF, son mucho más deslocalizadas que las correlacionadas, como las MP2. Cualquier esquema de truncamiento debe por tanto comportarse ligeramente mejor cuando se incluye la correlación.

La tabla 3.13 ilustra la evolución de las cargas QTAIM con la inclusión de correlación y la consideración de la aproximación RI. Los datos indican que la sensibilidad de esos descriptores decrece conforme aumenta la polaridad de la molécula. Las desviaciones para H_2O LiF son menores de 0,25 % pero mucho mayores para etano, para el cual la inclusión de correlación electrónica cambia el signo de la carga de los átomos de carbono. No obstante, las aproximaciones RI reproduce los signos en concordancia con la referencia original. El caso del benceno,, donde hay más deslocalización electrónica, la carga del carbono usando el método RIJCOSX-HF difiere tanto como 5 % del valor de referencia.

A manera de prueba, usamos la metodología RIJCOSX-MP2 para obtener la función de onda correspondiente al complejo endohédrico de una molécula de agua dentro del fullereno C_{70}, que se muestra en la figura 3.25. Lo primero que notamos es que la geometría de la molécula de agua

Tabla 3.13: Cargas QTAIM para átomos seleccionados en moléculas aisladas. Valores en unidades atómica.

Method	O@H_2O	F@LiF	C@C_2H_6	C@C_2H_4	C@Benzene
HF	−1.24122	−0.94475	0.13363	−0.02775	−0.01261
RIJCOSX−HF	−1.24102	−0.94472	0.13735	−0.02749	−0.01198
MP2	−1.17925	−0.93352	−0.01120	−0.08681	−0.04643
RI−MP2	−1.17933	−0.93352	−0.01140	−0.08701	−0.04648
RIJCOSX−MP2	−1.17897	−0.93351	−0.00844	−0.08668	−0.04605

apenas cambia al ser introducida en la cavidad del fullereno; la distancia hidrógeno-oxígeno pasa de 0.977 a 0.978 Åy el ángulo hidrógeno-oxígeno-hidrógeno se mueve de 101.8 a 101.9 grados. Coincidentemente, el análisis topológico de la densidad electrónica revela que practicamente no existe transferencia de carga (0.002 u.a., por debaje de la presición de la metodología utilizada) entre la molécula de agua y el fullereno. Las cargas tanto de la molécula de agua como de el C_{70} se mantienen constantes. Sin embargo, dentro de la molécula de agua se da un ligero reajuste de la densidad. La carga del oxígeno pasa de −1.17 a −1.20 u.a. al pasar de la molécula aislada a dentro del C_{70}. La densidad que gana el oxígeno se desplaza de manera equitativa desde cada uno de los hidrógenos, que pasan de 0.586 a 0.601 u.a. al formar el complejo. Este cambio en la densidad electrónica es resultado de su interacción con el fullereno C_{70}. La transferencia de carga de 0.015 u.a. está asociada con un cambio de energía de 0.15 u.a., o alrededor de 9 kcal/mol, una cantidad no despreciable en el contexto de interacciones no covalentes.

Entre el fullereno C_{70} y la molécula de agua se establecen únicamente cuatro trayectorias de enlace las cuales son mostradas en la figura 3.26. La tabla 3.14 contiene los valores de algunos descriptores QTAIM para esas interacciones. Como podemos observar a través de los valores de DI y ϱ, la interacción más fuerte corresponde al par H73$\cdots$C14, sin embargo, todas las interacciones, incluyendo esta, son muy débiles. Además, el valor de $\nabla^2\varrho$ es pequeño y positivo para todos los pares de átomos conectados por las trayectorias, por lo que podemos caracterizar a estas interacciones como contactos de capa cerrada. La naturaleza de estas interacciones también se ve reflejada en la densidad energética total, $H(\mathbf{r})$, que es positiva para todos los casos.

Finalmente, un resultado notable es que las tres interacciones carbono-oxígeno son muy similares, lo cual contrasta con la idea química que el átomo de oxígeno interactua a través de sus pares libres. Adicionalmente, si se diera el caso de una interacción entre los pares libres del agua

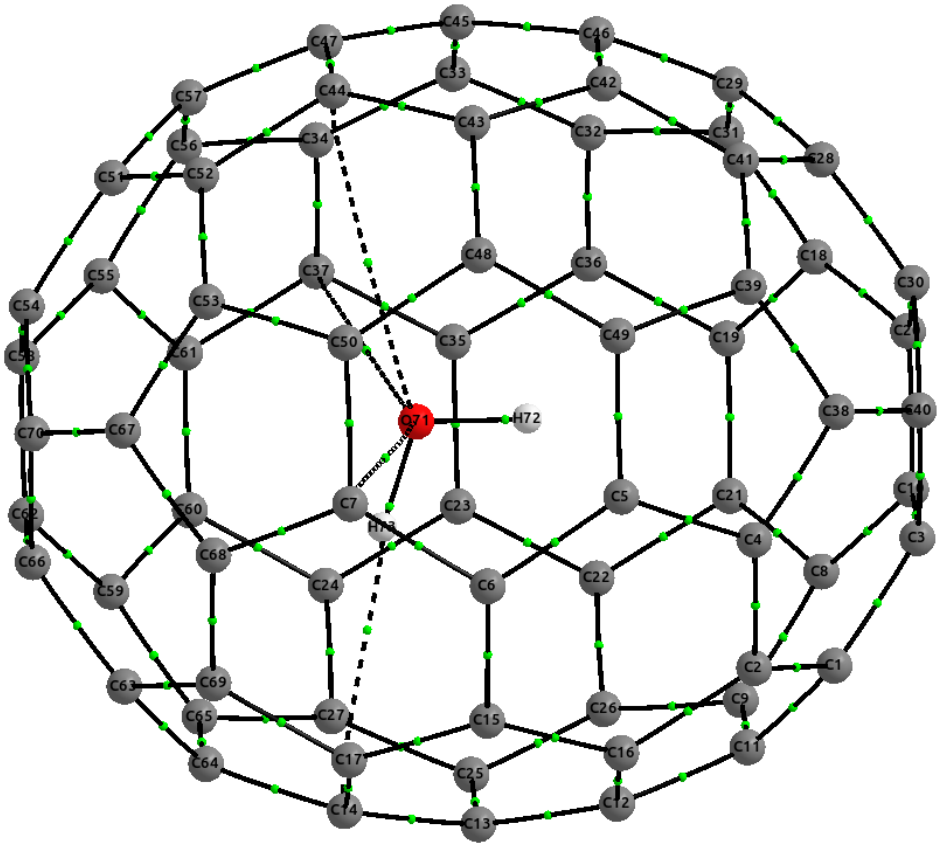

Figura 3.26: Trayectorias de enlace en H_2O dentro de C_{70}.

y el C_{70}, debería haber una transferencia de densidad a los carbonos y ese no es el caso. Las cargas de los carbonos que se conectan con el oxógeno mediante las trayectorias de enlace son -0.005, 0.002, and 0.001, en concordancia con los valores del resto de los carbonos. Por tanto, la naturaleza de la interacción entre H_2O y C_{70} es dispersiva.

Tabla 3.14: Descriptores QTAIM en los BCP entre átomos en la moĺecula de agua y el C_{70}. Los valores están en u.a.

Pair	ϱ	DI	$\nabla^2\varrho$	V	G	H	$\lvert V\rvert/G$
O71-C7	0.0049	0.0108	0.0172	-0.0031	0.0037	0.0006	0.84
O71-C37	0.0053	0.0113	0.0198	-0.0035	0.0042	0.0007	0.83
O71-C44	0.0047	0.0097	0.0176	-0.0031	0.0037	0.0006	0.83
H73-C14	0.0097	0.0137	0.0308	-0.0064	0.0071	0.0006	0.91

Podemos concluir que los resultados obtenidos utilizando la metodología RIJCOSX son muy buenos para las propiedades tanto topológicas como integradas de la distribución de carga, especialmente cuando la correlación es incluida.

3.4. Where Does Electron Correlation Lie? Some Answers from a Real Space Partition

En este artículo se realizó la partición en la energía de correlación en términos intra e interatómicos bajo la metodología IQA. Esto se hizo con la intención de entender la localización en el espacio de esta energía. Los resultados muestran que la mayor parte de la energía de correlación se encuentra concentrada en la parte intratómica (o intrafragmento).

Con el constante aumento en el poder de computo que se ha venido dando durante las últimas décadas, la química computacional ha podido abocarse al estudio de sistemas más grandes y de mayor complejidad. Sin embargo, al día de hoy aún quedan territorios más allá de lo que es asequible para nuestra tecnología. Uno de esos territorios es el tratamiento adecuado de la correlación electrónica (CE), un elemento muy importante en la descripción de muchos procesos fisicoquímicos como el enlace metal-metal [119] o el plegamiento de proteinas [120].

Más allá de la descripción puramente teórica o del cálculo computacional asociado a obtener energías de correlación precisa, es importante entender donde espacialmente dentro de la molécula o cúmulo molecular se localiza esta energía. En 1988 Gatti y colaboradores ofrecieron una primera approximación a este problema bajo la óptica de QTAIM [121]. Más recientemente Popelier et al. [122] particionaron la energía de correlación MP2 en intra e interatómica dentro del método IQA. Sin embargo, la expansión de MP para la energía de correlación que usaron únicamente contiene elementos bielectrónicos. En esta aproximación, todas las contribuciones son iguales a las de HF con excepción de las energías de intercambio y correlación.

Lo anterior constituye un problema debido a que la distribución de carga se ve afectada en sí misma por la inclusión de la CE. Una adecuada descripción requiere entonces el uso de matrices de densidad relajadas en lugar de matrices efectivas, que reproducen la energía de correlación pero subestiman el efecto de la CE en la partición IQA.

Dentro de la metodología podemos dividir a la energía total de un sistema como

$$E = \sum_{\mathrm{A}} E^{\mathrm{A}}_{\mathrm{self}} + \sum_{\mathrm{A>B}} E^{\mathrm{AB}}_{\mathrm{int}}. \tag{3.5}$$

donde el término $E^{\mathrm{A}}_{\mathrm{self}}$ se refiere a la autoenergía del átomo A, que es la suma de términos que dependen únicamente de los núcleos y electrones contenidos en el átomo A, y el término $E^{\mathrm{AB}}_{\mathrm{int}}$ es la energía interatómica que agrupa a las contribuciones de partículas en los átomos A y B. De tal manera que $E^{\mathrm{A}}_{\mathrm{self}} = T^{\mathrm{A}} + V^{\mathrm{AA}}_{\mathrm{ne}} + V^{\mathrm{AA}}_{\mathrm{ee}}$ y $E^{\mathrm{AB}}_{\mathrm{int}} = V^{\mathrm{AB}}_{\mathrm{nn}} + V^{\mathrm{AB}}_{\mathrm{ee}} + V^{\mathrm{AB}}_{\mathrm{ne}} + V^{\mathrm{BA}}_{\mathrm{ne}}$.

Una forma práctica de definir la energía de correlación es aquella propuesta por Löwdin, que usa como referencia la energía HF y define E_{corr} como:

$$\begin{aligned} E_{\mathrm{corr}}^{\mathrm{Löwdin}} &= \sum_{\mathrm{A}} (E_{\mathrm{self}}^{\mathrm{correlacionada}} - E_{\mathrm{self}}^{\mathrm{HF}})^{\mathrm{A}} + \sum_{\mathrm{A>B}} (E_{\mathrm{int}}^{\mathrm{correlacionada}} - E_{\mathrm{int}}^{\mathrm{HF}})^{\mathrm{AB}} \\ &= \sum_{\mathrm{A}} E_{\mathrm{corr}}^{\mathrm{self,A}} + \sum_{\mathrm{A>B}} E_{\mathrm{corr}}^{\mathrm{int,AB}} = E_{\mathrm{corr}}^{\mathrm{self}} + E_{\mathrm{corr}}^{\mathrm{int}}, \end{aligned} \tag{3.6}$$

donde $E^{\mathrm{self,A}}$ es la autoenergía del átomo A y $E^{\mathrm{int,AB}}$ es la energía de interacción entre átomos A y B. La energía de correlación de Löwdin es la diferencia entre las cantidades calculadas a nivel HF y sus contrapartes correlacionadas. Al igual que la energía de interacción misma, $E_{\mathrm{corr}}^{\mathrm{int}}$ puede ser dividida entre sus contribuciones clásica y de intercambio y correlación, $E_{\mathrm{corr}}^{\mathrm{int}} = E_{\mathrm{corr}}^{\mathrm{int,cl}} + E_{\mathrm{corr}}^{\mathrm{int,xc}}$.

Para este estudio se calculó la partición energética de 43 sistemas (tabla 3.15) en múltiples niveles de teoría. Este conjunto de sistemas incluye moléculas cuyas geometrías fueron tomadas de la base de datos del NIST [123] y dímeros moleculares de los conjuntos S22 y KB49 [124; 125; 126]. Algunos ejemplos (señalados en la tabla 3.15) fueron optimizados usando la aproximación CCSD/aug-cc-pvdz con el programa GAMESS-US [127]. Los cálculos para obtener las matrices de densidad HF, CISD, CCSD y CCSD(T) se hicieron con la base cc-pVDZ utilizando para ello el programa PySCF suite [128]. Las funciones de onda DMRG [129] fueron obtenidas con el código BLOCK [130; 131; 132; 133; 134] considerando todos los electrones y orbitales. Todos los cálculos IQA se llevaron a cabo usando el programa PROMOLDEN [79].

La tabla 3.16 recoge los valores para las contribuciones $E_{\mathrm{corr}}^{\mathrm{self}}$ y $E_{\mathrm{corr}}^{\mathrm{int}}$, mientras que las tablas 3.17 y 3.18 contienen descomposiciones más finas de estos términos. Para simplificar la discusión se considerará que A y B en la ecuación (3.6) se refieren a átomos para moléculas aisladas mientras que para los dímeros señalan monómeros.

Una primera inspección de la tabla 3.16 revela que para la gran mayoría de las moléculas que contienen enlaces covalentes, $E_{\mathrm{corr}}^{\mathrm{int}}$ es positivo, es decir, la inclusión de CE disminuye la magnitud de $E_{\mathrm{int}}^{\mathrm{AB}}$. Además, los valores de $E_{\mathrm{corr}}^{\mathrm{int,xc}}$ son también desestabilizantes para muchas de las interacciones mostradas en la tabla 3.18. Aunque estos resultados pudieran parecer contraintuitivos, tienen un origen físico muy preciso. Cuando consideramos únicamente la correlación de Fermi, los electrones de espín opuesto se comportan como entidades estadísticamente independientes y se deslocalizan libremente a lo largo de regiones del espacio más grandes que cuando se ven afectados por la correlación de Coulomb [135; 136; 137]. Debido a que $V_{\mathrm{xc}}^{\mathrm{AB}}$ es una energía que mide la deslocalización electrónica entre dos átomos, la inclusión de CE disminuye el valor de esta.

Tabla 3.15: Lista de las moléculas estudiadas en este artículo. Las geometrías fueron tomadas de los conjuntos de datos NIST, S22, y KB49 [124; 125; 126], excepto en los casos donde estas se optimizaron como se especifica en el texto.

Molecule	Geometry	Molecule	Geometry
C_2H_2	NIST	HCN···HF	KB49
Ar_2	NIST	HCN	NIST
Be_2	NIST	HF···ClF	Optimizada
BH_3	NIST	HF···CO	Optimizada
C_2	NIST	HF···F_2	Optimizada
CF^+	Optimizada	HF···H_2O	Optimizada
$(CH_3F)_2$	KB49	$(HF)_2$	KB49
$(CH_4)_2$	S22	HF···N_2	Optimizada
CH_4···HF	KB49	HF	NIST
CH_4···NH_3	KB49	HNC	NIST
CN^-	NIST	LIF	NIST
CO	NIST	CH_3OH	NIST
C_2H_4	NIST	CH_4	NIST
F_2	NIST	N_2	NIST
FCN	NIST	Ne_2	NIST
$(H_2CO)_2$	Optimizada	NH_3···F_2	Optimizada
H_2CO	NIST	$(NH_3)_2$	S22
CH_2O_2	NIST	NH_3	NIST
H_2CF^+	Optimizada	NO^+	NIST
$(H_2O)_2$	Optimizada	$(NO)_2$	NIST
H_2O	Optimizada	OC···BH_3	Optimizada
HCl	NIST		

Por otro lado, tenemos a las interacciones interatómicas (o interfragmento) de larga distancia de correlación o dispersión, y que tradicionalmente se han considerado como contribuciones estabilizantes. En el caso de Ar···Ar and Ne···Ne, por ejemplo, $E_{\text{corr}}^{\text{int}}$ es débilmente negativo, por lo que resulta tentador asociar a $E_{\text{corr}}^{\text{int}}$ a la dispersión. Esto debido a que este término toma en cuenta excitaciones dobles en las cuales un electrón se localiza en el fragmento A mientras que el otro está en el monómero B. Sin embargo, es necesario ser cuidadoso a este respecto: las correcciones dispersivas únicamente están definidas en la teoría de perturbaciones estándar

dentro de la aproximación de polarización [50], además de que dentro de teoría de perturbaciones adaptada por simetría (SAPT por sus iniciales en inglés) existen varias expresiones posibles para la energía de dispersión. En cualquier caso, es razonble asociar $E_{\text{corr}}^{\text{int}}$ con la dispersión en el espacio real siempre que las regiones involucradas en la interacción se encuentren separadas. Conforme dichas regiones se aproximan entre sí, contribuciones a la correlación de corto alcance aparecen, y $E_{\text{corr}}^{\text{int}}$ se transforma de una interacción similar a la dispersión a una energía intraatómica. Para procedimientos invariantes ante el cambio de orbitales, como este, no es posible separar inequívocamente dispersión y correlación de corto alcance.

En los enlaces altamente iónicos la inclusión de CE no tiene efectos tan claros como es el caso de enlaces covalentes típicos. Aquí, la trasferencia de carga a nivel HF son un poco demasiado largas, lo que es contrarrestado en parte por la CE, de manera que la deslocalización aumenta ligeramente ante la inclusión de esta. Dicha circunstancia provoca que $E_{\text{corr}}^{\text{int}}$ sea apenas positivo para sistemas como LiF or BH_3. En esto casos, $E_{\text{corr}}^{\text{int}}$ se vuelve más importante para determinar el valor total de $E_{\text{corr}}^{\text{CCSD(T)}}$ conforme la fuerza del enlace aumenta.

Es notable lo bien que el signo de $E_{\text{corr}}^{\text{int}}$ diferencía entre interacciones fuertes y débiles. Así, la tabla 3.16 prácticamente está divida en dos, por un lado las moléculas fuertemente enlazadas y por el otro los dímeros. Usando este descriptor, se puede clasificar a $(NO)_2$ como un sistema fuertemente enlazado, en concordancia con el consenso actual.

Las tablas 3.17 y 3.18 contienen una partición de $E_{\text{corr}}^{\text{self}}$ y $E_{\text{corr}}^{\text{int}}$ en sus componentes cinético (únicamente para $E_{\text{corr}}^{\text{self}}$), clásico y de intercambio y correlación. Con respecto a los términos de autoenergía, el cambio en la energía cinética cuando se incluye energía de correlación es casi siempre positivo. Esto no se cumple únicamente en el caso de los dímeros de los gases nobles donde el cambio en $E_{\text{corr}}^{\text{self}}$ es negativo. Esto se debe a que a nivel HF estos sistemas se encuentran muy lejos del equilibrio.

La contribución de intercambio y correlación intraatómica es estabilizante en todos los casos, siendo el único componente que cumple con esta característica. Esto es un indicador de la importancia de la energía de intercambio y correlación para determinar si E_{corr} es positiva o negativa. El cambio en la energía de repulsión electrón-electrón, medida como la suma de J y xc reportados en la tabla 3.18, provocado por la inclusión de CE es siempre negativo. Sin embargo, este resultado es generado de dos formas diferentes. En sistemas covalentes no polares, como C_2, N_2 o C_2H_2, los electrones estan más localizados por efecto de la correlación electrónica. Esto a su vez provoca que la interacción electrón-núcleo sea más negativa (atractiva), un aumento en la energía cinética de los electrones, y se incremente la respulsión electrón-electrón, resultando en

Tabla 3.16: Partición de las energías de correlación de Löwdin a nivel CCSD(T) de acuerdo con la ecuación (3.6). Aquí, "self" se refiere a $E_{\text{corr}}^{\text{self}}$, la suma de todos los valores no equivalentes de $E_{\text{corr}}^{\text{self,A}} = E_{\text{self}}^{\text{CCSD(T),A}} - E_{\text{self}}^{\text{HF,A}}$, donde A se refiere a átomos para moléculas aisladas y a monómeros en el caso de dímeros. De igual manera, "int" se refiere a $E_{\text{corr}}^{\text{int}}$, y corresponde la suma de todos los valores no equivalentes de los términos interatómicos o intermoleculares, $E_{\text{corr}}^{\text{int,AB}} = E_{\text{int}}^{\text{CCSD(T),AB}} - E_{\text{int}}^{\text{HF,AB}}$. Datos reportados en u.a.

Sistema	self	int	Total	Sistema	self	int	Total
C_2	−0.498809	0.155563	−0.343246	$HF\cdots H_2O$	−0.424186	−0.003399	−0.427586
CF^+	−0.361418	0.057722	−0.303696	$(HF)_2$	−0.420501	−0.002719	−0.423220
CN^-	−0.448912	0.151339	−0.297573	$HF\cdots N_2$	−0.528874	−0.002779	−0.531653
CO	−0.437109	0.128281	−0.308828	Ne_2	−0.383820	−0.000050	−0.383870
F_2	−0.499545	0.084036	−0.415509	$NH_3\cdots F_2$	−0.626559	−0.001640	−0.628199
HCl	−0.191449	0.020562	−0.170887	$(NH_3)_2$	−0.417352	−0.002932	−0.420284
HF	−0.221964	0.011302	−0.210662	$(NO)_2$	−0.885738	0.088935	−0.796803
LiF	−0.217534	0.005486	−0.212048	$OC\cdots BH_3$	−0.426038	−0.020936	−0.446974
N_2	−0.553463	0.228442	−0.325021	BH_3	−0.125914	0.006540	−0.119373
NO^+	−0.603477	0.251072	−0.352405	C_2H_2	−0.523356	0.235412	−0.287944
Ar_2	−0.315209	−0.000350	−0.315559	C_2H_4	−0.531402	0.211851	−0.319551
Be_2	−0.091713	−0.010124	−0.101838	CH_2O_2	−0.742443	0.209378	−0.533065
$(CH_3F)_2$	−0.732845	−0.001978	−0.734823	CH_3OH	−0.524479	0.148977	−0.375502
$(CH_4)_2$	−0.381721	−0.001667	−0.383388	CH_4	−0.301611	0.110678	−0.190933
$CH_4\cdots HF$	−0.400637	−0.003070	−0.403707	FCN	−0.740873	0.247006	−0.493867
$CH_4\cdots NH_3$	−0.399239	−0.001442	−0.400681	H_2CF^+	−0.423656	0.094291	−0.329365
$(H_2CO)_2$	−0.687735	−0.001271	−0.689006	H_2CO	−0.520161	0.173249	−0.346912
$(H_2O)_2$	−0.429695	−0.002489	−0.432184	H_2O	−0.261064	0.044648	−0.216415
$HCN\cdots HF$	−0.518226	−0.003211	−0.521437	HCN	−0.524103	0.214406	−0.309697
$HF\cdots ClF$	−0.565216	−0.000817	−0.566033	HNC	−0.470410	0.168882	−0.301528
$HF\cdots CO$	−0.515506	−0.000964	−0.516470	NH_3	−0.290928	0.082119	−0.208809
$HF\cdots F_2$	−0.616486	−0.001723	−0.618209				

una J positiva. En el caso de las moléculas polares, como CO y LiF, y de cúmulos moleculares unidos por fuerzas dispersivas, como Ar_2 o Ne_2, J es negativa. Esto se debe a que el método HF comprime las densidades electrónicas más de la cuenta, ya sea debido a una excesiva transferencia de carga, en el primer caso, o por la incapacidad de HF para deslocalizar electrones correctamente en la descripción de los segundos.

Pasamos a las contribuciones interatómicas o interfragmento en la tabla 3.18. Para sistemas covalentes, el término de intercambio y correlación usualmente determina el signo de $E_{\text{corr}}^{\text{int}}$. En el caso de interacciones homopolares, como en CH_4, C_2H_2, N_2, o F_2, la redistribución de la densidad genera diferentes contribuciones clásicas que se cancelan entre sí, por lo que $E_{\text{corr}}^{\text{int,cl}}$ resulta ser mucho menor que $E_{\text{corr}}^{\text{int,xc}}$. Una excepción interesante lo constituye C_2, donde la correlación contiene una contribución electrostática estabilizante que suge de los considerablemente más negativs términos $V_{\text{ne}}^{\text{AB}}$, que no se ven compensados por el incremento en repulsión entre electrones.

Para sistemas covalentes muy polares, la inclusión de la correlación tiende a disminuir la polaridad resultante de HF, provocando una desestabilización no despreciable en los componentes de $E_{\text{corr}}^{\text{int,cl}}$. Este es el caso de CF^+, CO, HF, BH_3, H_2O, y HCN entre otros. Como se dijo antes, esto está generalmente acompañado de una desestabilización de $E_{\text{corr}}^{\text{int,xc}}$, aunque existen algunas excepciones notables de este hecho, como CF^+ y BH_3. Una inspección detallada de BH_3, por ejemplo, muestra que el origen de la estabilización del componente de intercambio y correlación es la pobre descripción de los átomos de hidrógeno, cuya forma es similar a la de un hidruro. Finalmente, la gran mayoría de los sistemas débilmente enlazados se caracterizan por tener valores pequeños de $E_{\text{corr}}^{\text{int,cl}}$ y porque $E_{\text{corr}}^{\text{int,xc}}$ es una contribución estabilizadora dominante.

Los dímeros son un excelente ejemplo para entender como se divide E_{corr}. Como se muestra claramente en la tabla 3.16, la mayor parte de la energía de correlación de un sistema se encuentra siempre en el término intramonómero (intratómico para el caso de las moléculas). Esto recuerda a la conjetura de Feynman acerca del rol de las distorsiones intratómicas de la densidad como la fuerza generadora de la dispersión [138]. El valor absoluto de $E_{\text{corr}}^{\text{Löwdin}}$ es proporcional al número total de electrones, y las excepciones a esta regla se explican por la naturaleza multiconfiguracional de estos sistemas, como es el caso de los dímeros de NO o Be. Por tanto, la partición de la energía de correlación siempre está dominada por términos intratómicos o intrafragmento.

Estos términos están asociados a una disminución de la energía mediante la localización electrónica y a un detrimento de la energía de enlace en el caso de enlaces covalentes. Sin embargo, desde un punto de vista químico, los componentes interfragmento son más importantes. Esto se debe a que a través de estos es posible estudiar la energía de dispersión y la conversión de esta en correlación de corto alcance conforme la distancia entre fragmentos disminuye. Este cambio de la CE, desde una estabilización de largo alcance a una desestabilización a corta distancia puede estar relacionada con la existencia de varios mínimos en el agujero de Coulomb, como revelan los cálculos de posición intracular en átomos [139; 140].

Tabla 3.17: Partición de las energías de correlación CCSD(T) intraatómicas o intrafragmento, $E_{\mathrm{corr}}^{\mathrm{self}}$, en sus componentes cinético (T), núcleo-electrón (NE), Coulómbico (J), y de intercambio y correlación (xc). Los datos están en u.a.

Sistema	T	NE	J	xc	Sistema	T	NE	J	xc
C_2	0.3528	−0.5025	0.4014	−0.7506	$HF\cdots H_2O$	0.2825	0.3462	−0.2391	−0.7097
CF^+	0.1956	0.2933	−0.3905	−0.4598	$(HF)_2$	0.2147	0.4715	−0.3028	−0.6982
CN^-	0.3985	−0.3564	0.0749	−0.5659	$HF\cdots N_2$	0.5510	−0.2149	0.0559	−0.9036
CO	0.3363	−0.0652	−0.1923	−0.5159	Ne_2	−0.0154	0.6177	−0.3462	−0.6399
F_2	0.4061	−0.1352	0.0118	−0.7822	$NH_3\cdots F_2$	0.6241	−0.1738	0.0014	−1.0613
HCl	0.0556	0.1788	−0.1175	−0.3084	$(NH_3)_2$	0.4148	−0.0089	−0.0599	−0.7157
HF	0.1117	0.2228	−0.2105	−0.3459	$(NO)_2$	1.2592	−1.2795	0.6895	−1.4455
LiF	0.0634	0.4239	−0.3916	−0.3133	$OC\cdots BH_3$	0.4018	−0.1116	−0.0056	−0.7242
N_2	0.4694	−0.4859	0.2556	−0.7926	BH_3	0.0939	−0.0541	0.0120	−0.1777
NO^+	0.5050	−0.4334	0.0786	−0.7537	C_2H_2	0.3745	−0.3286	0.1658	−0.7351
Ar_2	−0.0149	0.3727	−0.1404	−0.5326	C_2H_4	0.3590	−0.2915	0.1650	−0.7638
Be_2	0.0462	−0.0561	0.0790	−0.1608	CH_2O_2	0.5256	0.0764	−0.4312	−0.9132
$(CH_3F)_2$	0.5050	0.3991	−0.3762	−1.2195	CH_3OH	0.3457	−0.0169	−0.1204	−0.7329
$(CH_4)_2$	0.3498	−0.2561	0.0283	−0.6641	CH_4	0.1747	−0.1284	0.0883	−0.4362
$CH_4\cdots HF$	0.2807	0.1169	−0.1404	−0.6812	FCN	0.5272	−0.2003	−0.1463	−0.9214
$CH_4\cdots NH_3$	0.3774	−0.1260	−0.0189	−0.6889	H_2CF^+	0.1876	0.4111	−0.4627	−0.5596
$(H_2CO)_2$	0.6937	0.0245	−0.1770	−1.1414	H_2CO	0.3668	−0.0283	−0.2037	−0.6549
$(H_2O)_2$	0.3602	0.2231	−0.1770	−0.7241	H_2O	0.1897	0.0982	−0.1738	−0.3751
$HCN\cdots HF$	0.5239	−0.1105	−0.0155	−0.8771	HCN	0.4247	−0.3619	0.0696	−0.6565
$HF\cdots ClF$	0.3336	0.1491	−0.1668	−0.9368	HNC	0.3746	−0.2096	−0.0923	−0.5431
$HF\cdots CO$	0.4256	0.1952	−0.1606	−0.8536	NH_3	0.2099	−0.0169	−0.0685	−0.4154
$HF\cdots F_2$	0.4613	0.1892	−0.1994	−1.0326					

3.4.1. La correlación electrónica en diferentes metodologías

Un resultado secundario de nuestra investigación es la comparación de los efectos de la CE en diferentes componentes de la energía para distintos niveles de teoría. Para ello, comparamos los resultados de la partición IQA para HF, MP2, interacción de configuraciones simples y dobles (CISD), CCSD, CCSD(T), y casi interacción de configuraciones completa (FCI como resultado de usar DMRG). Estos datos son de utilidad a la hora de calibrar la sensibilidad de los diferentes componentes de la energía a la CE.

Con esto en mente, dividimos el total de los sistemas estudiados en moléculas y dímeros. En el caso de las primeras, reportamos estadísticas de los resultados IQA usando como refencia los

Tabla 3.18: Partición de las energías correlación CCSD(T) de interacción $E_{\text{corr}}^{\text{int}}$ en sus componentes electrón-núcleo (EN, donde los electrones están en el fragmento A y los núcleos en el fragmento B), núcleo-electrón (NE, con los núcleos en el fragmento A y los electrones en el B), Coulómbica (J), clásica (cl), y de intercambio y correlación (xc). Todos los valores están en u.a.

Sistema	EN	NE	J	cl	xc	Sistema	EN	NE	J	cl	xc
C_2	−0.0620	−0.0620	0.0943	−0.0297	0.1852	$HF\cdots H_2O$	−0.0279	0.0164	0.0129	0.0014	−0.0048
CF^+	−0.2959	0.1481	0.2281	0.0803	−0.0226	$(HF)_2$	0.0092	−0.0280	0.0197	0.0009	−0.0036
CN^-	−0.1954	0.1945	0.0990	0.0981	0.0532	$HF\cdots N_2$	−0.0226	−0.0049	0.0273	−0.0002	−0.0026
CO	−0.2914	0.2206	0.1946	0.1238	0.0045	Ne_2	0.0000	0.0000	−0.0000	0.0000	−0.0001
F_2	0.0046	0.0046	−0.0082	0.0010	0.0829	$NH_3\cdots F_2$	0.0279	−0.0110	−0.0168	0.0001	−0.0018
HCl	−0.0827	0.0072	0.0777	0.0022	0.0184	$(NH_3)_2$	0.0460	−0.0446	−0.0009	0.0005	−0.0034
HF	−0.0655	0.0130	0.0689	0.0164	−0.0051	$(NO)_2$	−0.1972	0.1991	−0.0020	0.0000	0.0891
LiF	−0.0293	0.0164	0.0213	0.0084	−0.0028	$OC\cdots BH_3$	−0.1985	0.1379	0.0543	−0.0063	−0.0146
N_2	0.0128	0.0128	−0.0257	−0.0001	0.2285	BH_3	−0.0173	0.0677	−0.0140	0.0364	−0.0299
NO^+	−0.3154	0.3083	0.1033	0.0962	0.1549	C_2H_2	0.0309	−0.0114	−0.0196	−0.0001	0.2356
Ar_2	−0.0000	−0.0000	0.0001	0.0001	−0.0004	C_2H_4	−0.0045	0.0779	−0.0690	0.0043	0.2074
Be_2	−0.0167	−0.0167	0.0317	−0.0017	−0.0084	CH_2O_2	−0.4705	0.2909	0.3533	0.1737	0.0356
$(CH_3F)_2$	−0.1050	0.1136	−0.0075	0.0011	−0.0030	CH_3OH	−0.0941	0.1065	0.0396	0.0520	0.0969
$(CH_4)_2$	−0.0246	0.0250	−0.0006	−0.0002	−0.0016	CH_4	−0.0197	0.0990	−0.0728	0.0065	0.1041
$CH_4\cdots HF$	−0.0002	−0.0172	0.0174	0.0000	−0.0031	FCN	−0.5645	0.4376	0.2765	0.1496	0.0974
$CH_4\cdots NH_3$	−0.0056	0.0066	−0.0008	0.0002	−0.0016	H_2CF^+	−0.2435	0.1278	0.1768	0.0611	0.0331
$(H_2CO)_2$	−0.1828	0.1974	−0.0120	0.0026	−0.0038	H_2CO	0.2190	−0.2626	0.1409	0.0973	0.0760
$(H_2O)_2$	−0.0149	0.0119	0.0038	0.0008	−0.0033	H_2O	0.0356	−0.0953	0.0949	0.0352	0.0095
$HCN\cdots HF$	0.0291	−0.0290	0.0012	0.0013	−0.0044	HCN	−0.2020	0.2149	0.0763	0.0892	0.1252
$HF\cdots ClF$	−0.0328	0.0200	0.0137	0.0009	−0.0016	HNC	0.1695	−0.2053	0.1746	0.1388	0.0300
$HF\cdots CO$	−0.0253	0.0417	−0.0149	0.0015	−0.0024	NH_3	0.0389	−0.0612	0.0483	0.0260	0.0562
$HF\cdots F_2$	−0.0313	0.0002	0.0310	−0.0001	−0.0017						

resultados de DMRG, mientras que para los segundos utilizamos los resultados CCSD(T) como punto de comparación.

La figura 3.27 muestra el error medio absoluto (MAE por sus iniciales en inglés) junto con el error porcentual medio absoluto (MAPE por sus iniciales en inglés para el conjunto de moléculas estudiadas. Es notable la poca diferencia que existe entre los valores CCSD(T) y aquellos correspondientes a DMRG. Como era de esperarse, la calidad de los términos IQA mejora de acuerdo a la serie HF, MP2, CISD, CCSD, y CCSD(T). Las autoenergías a nivel HF presentan el error absoluto más grande, aunque en porcentaje este error sea pequeño. Debido a que HF y MP2 comparten la matriz de densidad reducida de primer orden, las propiedades que depende

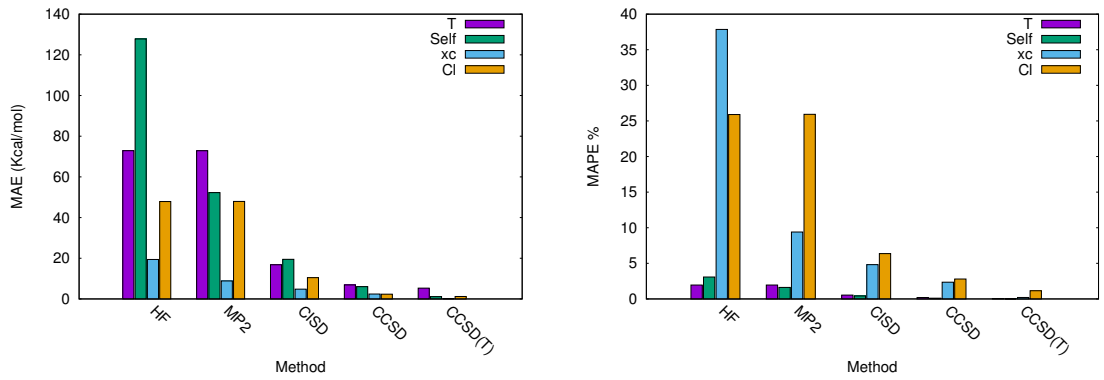

Figura 3.27: Errores MAE y MAPE para descriptores IQA seleccionados del conjunto de moléculas estudiadas usando DMRG como referencia.

de esta, como T^{A} o $V_{\mathrm{cl}}^{\mathrm{AB}}$, son iguales para ambos métodos. La descripción de estas propiedades mejora notablementente cuando se utilizan matrices reducidas de primer orden relajadas, como en los niveles CISD o CCSD.

El comportamiento de $V_{\mathrm{xc}}^{\mathrm{AB}}$ es interesante: su MAE, aún a nivel HF, es mucho menor que aquel asociado a $V_{\mathrm{cl}}^{\mathrm{AB}}$. Esta diferencia se acentúa a nivel MP2. Esta tendencia se mantiene para el resto de niveles de teoría que incluyen correlación, aún CCSD(T). Esta peculiaridad tiene su origen en la gran magnitud the la iteracción clásica en la metodología IQA.

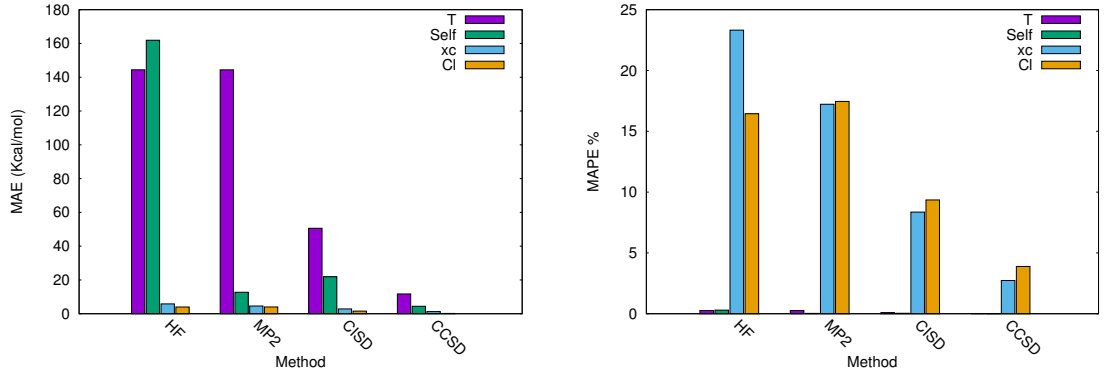

Figura 3.28: Errores MAE y MAPE para descriptores IQA seleccionados del conjunto de dímeros estudiados usando datos CCSD(T) como referencia.

La figura 3.28 reporta los datos correspondientes a los dímeros estudiados, esta vez con referencia a los resultados CCSD(T). Para estos sistemas hay una gran disparidad entre las autoenergías y las energías de interacción entre monómeros. Es interesante notar que para los dímeros los errores asociados a las contribuciones clásica y de intercambio y correlación evolucionan de manera similar cuando mejora la calidad del método utilizado. Sin embargo, una vez más surge

la tendencia de tener una mejor descripción para el término de intercambio y correlación que para el clásico.

Estos resultados indican que a pesar de que las densidades sin relajar pueden proveer una estimación conveniente de la energía de correlación, la descripción de sus componentes cinético y electrostático son necesarios si una imagen completa de la CE es necesaria. En el caso de los dímeros, por ejemplo, el porcentaje de error de los componentes IQA no es menor de 10 % con respecto a CCSD(T) a menos que se utilicen métodos como CISD.

Capítulo 4

Conclusiones

Las distintas metodologías de la QCT constituyen cada una en sí misma poderosas herramientas de análisis en química computacional. Sin embargo, a lo largo de este trabajo de tesis he aprendido que su verdadera fuerza está en su combinación, en como la visión, parcial, de una metodología se complementa con la perspectiva de otra y se retroalimentan para obtener una mejor descripción del fenómeno estudiado.

Además de este aspecto metodológico, me gustaría señalar algunos aprendizajes particulares de cada uno de los artículos publicados. En el trabajo de la lluvia ácida, logramos aplicar lo aprendido en trabajos anteriores sobre cooperatividad y anticooperatividad en cúmulos pequeños de agua para dar sentido a un proceso químico muy importante. Actualmente, estamos usando esta metodología para estudiar otras reacciones orgánicas y arrojar luz sobre el papel del disolvente en la reactividad.

Durante nuestro trabajo con RAHB encontramos que ciertos compuestos se comportaban de manera muy diferente a lo esperado a pesar de ser también sistemas π conjugados con enlaces de hidrógeno intramoleculares. La exploración de este concepto, llamado RIHB, mostró que a pesar de las similitudes externas, internamente RAHB y RIHB se comportaban diferente respecto a la homogeneización de órdenes de enlace. Esto sirvió también como confirmación de que las estructuras mesoméricas no son el origen de la (des)estabilización en este tipo de compuestos.

En el artículo sobre el enlace de halógeno, el uso del la metodología QCT dejó muy claro que primero, existe un enlace entre una de las moéculas de agua de la caja y el átomo de halógeno, y que ese enlace corresponde con el modelo de enlace de halógeno. Aquí, la QCT demostró su utilidad para esclarecer sin ambigüedad la naturaleza de un enlace que había sido controversial.

El estudio de complejos de oro fue realmente productivo y nos permitió revelar diversas

características los sistemas con los que trabajamos. En el estudio del complejo de oro con fosfinas JohnPhos y diferentes tiolatos aprendimos que las interacciones Au-P y Au-S es que el cambio del grado de fluorinación del tiolato provoca un cambio en el balance $\sigma - \pi$ presente en los enlaces, y que este es modulable.

La investigación sobre las los enlaces oro-oro en las fosfinas BIPHEP indicó que la interacción entre estos es al menos en parte covalente. Esta covalencia está en parte dada por la concentración de densidad electrónica en los átomos de oro, que a pesar de tener una carga formal de uno, su carga calculada por QTAIM es prácticamente cero, como en el oro metálico. Esto podría indicar que el camino hacia enlaces metal-metal más fuertes pasa por incrementar la cantidad de carga en cada átomo de oro.

El trabajo sobre fosfinas fluoradas confirma esta intuición sobre los enlaces químicos que forma el oro. Aquí encontramos que los compuestos más estables son aquellos donde el oro tiene un exceso de densidad electrónica. Esta idea puede servir para modular la fuerza de la interacción oro-ligante de manera que sea idónea para una aplicación específica. También durante esta investigación confirmamos que los parámetros de densidad e índice de deslocalización no son descriptores adecuados para predecir la estabilidad cinética de un enlace.

El artículo en el que indagamos sobre el desempeño de aproximaciones RI y RIJCOSX a MP2 en el análisis QTAIM surgió de una desconfianza de mi parte respecto a la calidad de la densidad resultante. La conclusión obtenida fue que la reproducción de la densidad por parte de RI y RIJCOSX es excelente. Es completamente adecuado utilizar estas metodologías para acceder al estudio de la función de onda de sistemas de gran tamaño.

Finalmente, análisis de distribución espacial de la correlación electrónica confirmó mediante una investigación sistemática la intuición de que la energía de correlación está concentrada en el término intraómico de la partición IQA. Sin embargo, por encima de esto el resultado más importante es que el signo de la correlación interatómica distingue entre interacciones mayormente covalentes e interacciones iónicas o no enlazantes.

Más allá de lo aprendido durante la producción de cada uno de los artículos contenidos en este trabajo, la realización de esta tesis me ha enseñado dos cosas. La primera es que hacer las preguntas correctas es el primer paso para conocer la respuesta. En un problema que está correctamente planteado ya está implicita parte de su solución. Con esto no quiero decir que no debemos lanzarnos hacia lo desconocido, dado que ese es el principal quehacer científico, sino que debemos hacerlo de la manera más consciente posible.

Las palabras de Donald Rumsfeld, secretario de Defensa de los Estados Unidos durante la

administración de George W. Bush me parecen particularmente esclarecedoras a este respecto:

> "Reports that say that something hasn't happened are always interesting to me, because as we know, there are known knowns; there are things we know we know. We also know there are known unknowns; that is to say we know there are some things we do not know. But there are also unknown unknowns-the ones we don't know we don't know [141]."

Esta frase, vilipendiada por la prensa y parodiada hasta el hartazgo, es un excelente resumen del trabajo científico. Los *known knowns*, lo que sabemos que sabemos, son los pilares sobre los que descansa nuestro entendimiento del mundo. Cuando hacemos una síntesis no dudamos de la existencia del átomo. Investigar los *known unknowns*, lo que sabemos que no sabemos, constituye el quehacer diario de los científicos. Es decir, desarrollar una hipótesis para ser probada a través de experimentos diseñados para ello, normalmente esperando que el resultado que se obtendrá se encontraá dentro de un rango de posibilidades conocidas. Sin embargo, en algunas ocasiones el resultado de dicho experimento es completamente inesperado: se ha encontrado un *unknown unknown*, algo que se desconocía que se desconocía.

El científico que participa de la continua tarea de construcción del edificio que afectuosamente llamamos ciencia debe ser consciente de estas cosas. Debe entender lo que sabe que sabe. Debe usar esta base para intentar conocer lo que sabe que no sabe. Finalmente, debe estar preparado para reconocer aquellos resultados, los más extraordinarios, aquellos que desafían su entendimiento del mundo, si se llegaran a presentar.

Lo segundo que he aprendido en la realización de esta tesis es tal vez más prosaico, pero lo considero igualmente importante. En el pasado se pensaba que el propósito de la educación era llenarnos de conocimiento. La modernidad en cambio nos dice, en lo que tal vez sea el cliché más cansino para cualquiera que haya padecido algún curso de pedagogía, que la educación debe enseñarnos a pensar. Yo creo que la función de la educación en general y de un doctorado en ciencia en particular, es aprender a elegir sobre qué pensar.

Yo creo que aprender a elegir a qué dedicamos nuestros pensamientos quiere decir algo muy específico. Quiere decir ser un poco menos arrogante. Quiere decir ser un poco más crítico acerca de mi mismo, mis certezas, y mis suposiciones. Esto es porque resulta que una gran parte de las cosas que damos por hecho son erróneas. Esto, que parece sencillo es extremadamente complicado. Es muy difícil mantenerse alerta y atento en lugar de dejarnos llevar por el monólogo interno de nuestra mente.

Quiero pensar que esto lo he aprendido bien. Quiero pensar que he conseguido ser suficientemente consciente para elegir a qué prestar atención. Quiero pensar que estoy aprendiendo a construir ciencia.

Capítulo 5

Artículos publicados

A continuación se presentan los artículos que conforman esta tesis:

- Romero-Montalvo, E., Guevara-Vela, J.M., Vallejo Narváez, W.E., Costales, A.,Martín Pendás, Á, Hernández-Rodríguez, M., and Rocha-Rinza, T. **Bifunctional catalytic role of water clusters in the formation of acid rain**.*Chem. Commun.*, 53 (25),3516–3519, 2017.

- Jara-Cortés, J., Guevara-Vela, J. M., Martín Pendás, Á., Hernández-Trujillo, J. **Chemical bonding in excited states: Energy transfer and charge redistribution from a real space perspective**. *J. Comp. Chem.*, 38, 957–970, 2017.

- Guevara-Vela, J.M., Rocha-Rinza, T., Martín Pendás, Á. **Performance of the RI and RIJCOSX approximations in the topological analysis of the electron density**. *Theor. Chem. Acc.*, 136, 57, 2017.

- Moreno-Alcántar, G., Hess, K., Guevara-Vela, J.M., Rocha-Rinza, T., Martín Pendás, Á., Flores-Álamo, M., Torrens, H. **π-Backbonding and non-covalent interactions in the JohnPhos and polyfluorothiolate complexes of gold(I)**. *Dalton Trans.* 46 (37), 12456–12465, 2017.

- Moreno-Alcántar, G., Guevara-Vela, J.M., Delgadillo-RuÃz, R., Rocha-Rinza, T., Martín Pendás, Á., Flores-Álamo, M., and Torrens, H. **Structural effects of trifluoromethylation and fluorination in gold(I) BIPHEP fluorothiolates**. *New J. Chem*, 41 (19), 10537–10541, 2017.

- Guevara-Vela, J.M., Romero-Montalvo, E., del Río-Lima, A., Martín Pendás, Á., Hernández-Rodríguez, M., Rocha-Rinza, T. **Hydrogen-Bond Weakening through π Systems: Resonance-Impaired Hydrogen Bonds (RIHB)**. *Chem. Eur. J.* 23 (65), 16605–16611. 2017.

- Casalz-Sainz, J.L., Guevara-Vela, J.M., Francisco, E., Rocha-Rinza, T., Martín-Pendás, Á. **Where Does Electron Correlation Lie? Some Answers from a Real Space Partition** *ChemPhysChem*, 18 (24), 3553–3561, 2017.

- Guevara-Vela, J.M., Ochoa-Reséndiz, D., Costales, A., Hernández-Lamoneda, R., Martín Pendás, Á. **Halogen bonds in clathrate cages: A real space perspective** *ChemPhysChem*, 19 (19), 2512–2517, 2018.

- Moreno-Alcántar, G. , Hernández-Toledo, H., Guevara-Vela, J.M., Rocha-Rinza, T. , Martín Pendás, Á. , Flores-Álamo, M. and Torrens, H. **Stability and trans Influence in Fluorinated Gold(I) Coordination Compounds.** *Eur. J. Inorg. Chem.*, 2018: 4413–4420, 2018.

ChemComm

COMMUNICATION

View Article Online
View Journal | View Issue

Published on 07 February 2017. Downloaded by Universidad de Oviedo on 4/29/2019 7:29:27 PM.

Cite this: *Chem. Commun.*, 2017, 53, 3516

Received 3rd December 2016,
Accepted 7th February 2017

DOI: 10.1039/c6cc09616f

rsc.li/chemcomm

The bifunctional catalytic role of water clusters in the formation of acid rain†

Eduardo Romero-Montalvo,[a] José Manuel Guevara-Vela,[b] Wilmer Esteban Vallejo Narváez,[a] Aurora Costales,[b] Ángel Martín Pendás,[b] Marcos Hernández-Rodríguez[a] and Tomás Rocha-Rinza*[a]

State-of-the-art chemical bonding analyses show that water clusters have a bifunctional catalytic role in the formation of H_2SO_4 in acid rain. The embedded H_2O monomers mitigate the change in the chemical bonding scenario of the rate-limiting step, reducing thereby the corresponding activation energy in accordance with Hammond's postulate. We expect that the insights given herein will prove useful in the elucidation of the catalytic mechanisms of water in inorganic and organic aqueous chemistry.

Hydrogen bonds (HBs) can exert a strong effect on the structure and energetics of molecular clusters,[1] and hence they might also affect the chemical properties of these systems. An example of this is the importance of surrounding water molecules in the production of acid rain,[2,3] which can be examined by comparing the processes:

$$\mathrm{SO_3} + (\mathrm{H_2O})_n \xrightarrow{(1)} \mathrm{SO_3}\cdots(\mathrm{H_2O})_n \xrightarrow{(2)} \left[\mathrm{SO_3}\cdots(\mathrm{H_2O})_n\right]^{\ddagger} \quad (1)$$
$$\left[\mathrm{SO_3}\cdots(\mathrm{H_2O})_n\right]^{\ddagger} \xrightarrow{(3)} \mathrm{H_2SO_4}\cdots(\mathrm{H_2O})_{n-1}$$

for n = 1–3 as shown in Fig. 1. This communication considers a detailed account of the changes in the reactivity of the H_2O and SO_3 molecules in the formation of H_2SO_4 because of H-bond cooperativity (*i.e.* the mutual strengthening of two or more HBs) related to the apparently unreactive water molecules. The aim of this paper is therefore twofold: first, to illustrate how HB cooperativity can modify the nucleophilic and electrophilic character of species in a chemical reaction and second, to provide insights into the generation of sulphuric acid in the atmosphere, which is a very relevant phenomenon in environmental science. We considered only the reaction of SO_3 with $(H_2O)_n$ (n = 1–3) because the formation of H_2SO_4 is of second order and, in some circumstances, of third order with respect to water vapour.[3,4] Moreover, theoretical calculations indicate that the water dimer and trimer and their corresponding adducts with SO_3 are considerably more abundant than their counterparts with larger water clusters.[5,6]

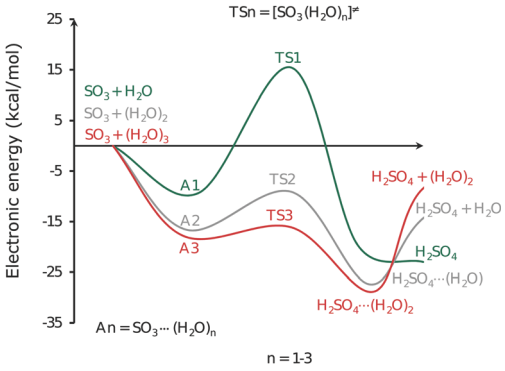

Fig. 1 MP2/aug-cc-pVTZ potential energy curves for the formation of H_2SO_4 from the reaction of SO_3 with the water clusters $(H_2O)_n$ (n = 1, 2, 3). The corresponding profile of the Gibbs free energy is shown in Fig. S1 (ESI†). All energies are referred to the corresponding value for the sum $E(SO_3) + E((H_2O)_n)$.

The production of sulphuric acid in acid rain involves the occurrence of supramolecular complexes $(H_2O)_n\cdots SO_3$ and thereafter the nucleophilic attack of water on sulphur trioxide in order to yield sulphuric acid.[2,3] In other words, the generation of H_2SO_4 from H_2O and SO_3 entails the formation and rupture of covalent bonds as well as HBs throughout the reaction process. We need, therefore, to make use of methods able to properly describe long and short range interactions on the same rigorous basis. The Quantum Theory of Atoms in Molecules (QTAIM)[7] and the Interacting Quantum Atoms (IQA)[8] energy partition are methodologies for wave function analyses within the field of quantum chemical topology with this desirable feature. The QTAIM is based on the topological properties of the electron

[a] *Institute of Chemistry, National Autonomous University of Mexico, Ciudad Universitaria, Coyoacán, 04510, Mexico City, Mexico. E-mail: tomasrocharinza@gmail.com*
[b] *Department of Analytical and Physical Chemistry, University of Oviedo, Oviedo, Asturias, Spain*

† Electronic supplementary information (ESI) available: Methods, computational details, additional QTAIM and IQA data (V_{xc}^{AB} and delocalization indices), equilibrium geometries, harmonic frequencies of the addressed transition states, thermodynamic data of all systems and information relative to the formation of carbonic acid. See DOI: 10.1039/c6cc09616f

This journal is © The Royal Society of Chemistry 2017

Published on 07 February 2017. Downloaded by Universidad de Oviedo on 4/29/2019 7:29:27 PM.

density $\rho_1(\mathbf{r}_1)$ while the IQA approach is built on the one and two electron density functions which are scalar fields invariant under orbital rotations completely determined by the wave function. This characteristic enables the QTAIM and IQA approaches to address covalent and non-covalent bonds on the same consistent basis. Most importantly, previous studies using QTAIM and IQA have been able to elucidate the nature of H-bond non-additive effects,[9] *i.e.*, where different HBs strengthen or weaken each other, as is the case for the systems under consideration in this research. Overall, the results herein give insights about (i) the manner in which cooperative effects in non-covalent interactions might alter reactivity within molecular clusters and (ii) the formation of H_2SO_4 from the interaction of sulphur trioxide with water oligomers in terms of mechanistic ideas conceived in bifunctional catalysis.[10]

As previously reported,[2,3] and indicated in step (1) of eqn (1) and the left of Fig. 1, the first step of the reaction is the formation of the molecular adducts $H_2O\cdots SO_3$ (A1), $(H_2O)_2\cdots SO_3$ (A2) and $(H_2O)_3\cdots SO_3$ (A3), whose structures are shown in Fig. 2. We also note that the molecular complexes $(H_2O)_n\cdots SO_3$ are more energetically stable *i.e.* their formation processes are more exothermic and exergonic despite the negative contribution of ΔS (Fig. S1 and Table S1, ESI†) as additional water molecules are included in the system. The ESI† presents a detailed discussion of the kinetics and the thermodynamics of the reactions in eqn (1). This increase in the stability of the molecular clusters can be understood in similar terms to those used to explain hydrogen-bond cooperative effects within H_2O clusters. Indeed, the structure of the systems $(H_2O)_2\cdots SO_3$ and $(H_2O)_3\cdots SO_3$ are evocative of the homodromic cycles of the water trimer and tetramer.[9]

Fig. 2(d) shows the formation of the water dimer with its concomitant flow of electron density from the H-bond acceptor to the HB donor. This makes the oxygen of the latter monomer richer in electrons and therefore more susceptible to interact with electron-deficient species, *i.e.* it increases its nucleophilicity. The same process increases the acidity of the hydrogens of the

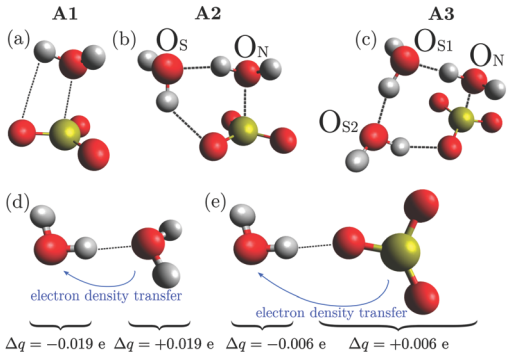

Fig. 2 Top: Equilibrium structures of (a–c) the supramolecular complexes $(H_2O)_n\cdots SO_3$ with n = 1, 2, 3. The labels O_N on the one hand and O_{S1} and O_{S2} on the other refer respectively to the nucleophilic and spectator character of the H_2O molecules in the Lewis acid/base addition. Bottom: Charge transfer in the hydrogen bonds (d) $H_2O\cdots H_2O$ and (e) $O_2S{=}O\cdots H_2O$. The braces indicate the change in the total charge of a given molecule within the corresponding adduct.

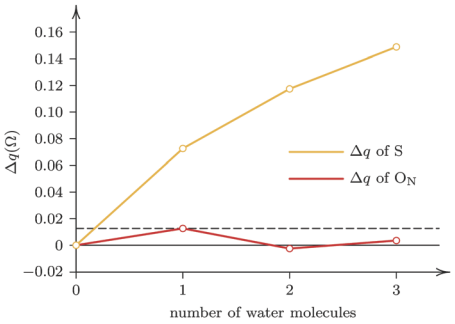

Fig. 3 Changes in QTAIM charges of the nucleophilic oxygen and sulphur atoms within the molecular clusters $(H_2O)_n\cdots SO_3$ with n = 1, 2, 3. The points at n = 0 represent the isolated H_2O and SO_3 species. The values of $\Delta q(\Omega)$ are reported in atomic units.

HB acceptor. Similarly, a hydrogen-bonded sulphur trioxide molecule, displayed in Fig. 2(e), loses electron density with respect to an isolated SO_3 molecule. Sulphur is the atom which decreases its number of electrons the most, a fact that makes it more liable for interplay with an electron-rich species. That is to say, H-bonds in which sulphur trioxide is the HB acceptor, like HO_S–H$\cdots$O=SO_2 and HO_{S2}–H$\cdots$O=SO_2 in Fig. 2(b) and (c) respectively, make the sulphur atom a better electrophile. To illustrate this idea better, Fig. 3 shows the change in $q(\Omega)$ for the sulphur and the nucleophilic oxygen (O_N) atom as a function of the number of H_2O molecules within the supramolecular complex. We observe that the charge of the sulphur atom increases monotonically as the molecular adduct comprises more water monomers, *i.e.*, S becomes more electronic deficient with the number of embedded H_2O molecules. The charge of the nucleophilic oxygen also changes with the interaction of water and sulphur trioxide species. When a water molecule interacts with SO_3, the nucleophilic O atom loses charge density, which remains in the oxygen atoms of the sulphur trioxide. The second water molecule increases the number of electrons of O_N as depicted in Fig. 2(d). Notwithstanding the small loss of electrons of O_N after the inclusion of a third H_2O monomer, the number of electrons of the nucleophilic oxygen is still larger than it is in the system A1 as pointed out by the horizontal dashed line in Fig. 3. The plots in the figure indicate that the change in the electrophilicity of S is considerably larger than the corresponding effect on O_N.

The flows of charge considered so far are indeed reminiscent of strategies followed in organic bifunctional catalysis[10] to promote nucleophilic additions to a given substrate by the formation of H-bonds involving Ñu–H and E=Y: as schematized in Fig. 4(a). In other words, the design followed recently in synthetic organic chemistry by activating nucleophiles and electrophiles through hydrogen bonds[11–13] becomes useful in the explanation of the formation of acid rain presented herein. The so-called spectator H_2O molecules displayed in green in Fig. 4(b) and (c) perform a bifunctional catalytic role. More specifically, these molecules activate an electrophile and a nucleophile through hydrogen bonds in which a transport of protons occurs by means of the Grotthuss mechanism.[14] Conversely, the comparison of water with bifunctional organocatalysts might give important insights

Published on 07 February 2017. Downloaded by Universidad de Oviedo on 4/29/2019 7:29:27 PM.

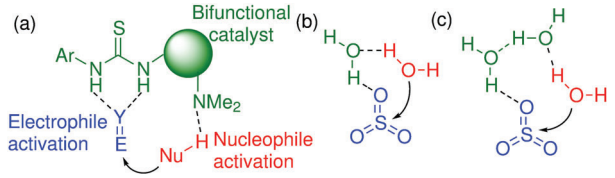

Fig. 4 Comparison between (a) a typical bifunctional catalyst in synthetic organic chemistry and the embedded water molecules in the supramolecular complexes (b) $(H_2O)_2\cdots SO_3$ and (c) $(H_2O)_3\cdots SO_3$. The nucleophiles, electrophiles and the catalysts are displayed in red, blue and green respectively.

into the role of water in inorganic and organic aqueous chemistry, *e.g.*, *the "on water" method for the nucleophilic opening of an epoxide*.[15]

In order to quantitatively assess the effect of the surrounding water molecules on the interaction of the reacting H_2O and SO_3 species, we determined the values of $E_{int}^{\mathscr{F}\mathscr{G}}$, defined in eqn (S6) in the ESI† as a pairwise energy decomposition of the processes described in step (1) of eqn (1). Table 1 shows that the presence of the second H_2O molecule increases the magnitude of the interaction of the nucleophilic water monomer and the sulphur trioxide by $|-20.16 - (-8.65)|$ kcal mol^{-1} = 11.51 kcal mol^{-1}. The inclusion of an extra molecule into the system A2 favours the formation of the supramolecular complex A3 even more as observed in Fig. 1. The absolute value of $E_{int}^{\mathscr{F}\mathscr{G}'}$ for the interaction between the nucleophilic H_2O molecule and the SO_3 species is incremented by $|-31.11 - (-20.16)|$ kcal mol^{-1} = 10.95 kcal mol^{-1} (Table 1). The strengthening of the interaction between monomers can also be accounted by the QTAIM Delocalization Indices (DIs) on the left side of Fig. 5. DIs, usually denoted as δ(A,B) are chemical bonding descriptors which measure the number of electrons shared by two species (atoms, functional groups or molecules) in an electronic system and hence indicate the degree of covalency between them: the larger the value of δ(A,B), the stronger is the covalent character of the interaction of A and B.‡

Table 1 Decomposition of (a) the formation energy of the molecular complexes A1, A2 and A3 shown in Fig. 2 (step (1) in eqn (1)) as well as (b) the activation energy of the rate-limiting steps in Fig. 1 (step (2) in eqn (1)) in pairwise IQA interaction energies $E_{int}^{\mathscr{F}\mathscr{G}'}$ (eqn (S6), ESI). Monomers $\mathscr{F}$ and $\mathscr{G}$ are indicated in the first row and column respectively of every chart and the labels, N, S, S1 and S2 are defined in Fig. 2. The values are reported in kcal mol^{-1}

(a) Molecular cluster

	A1	A2		A3		
$\mathscr{G}\backslash\mathscr{F}$	H_2O(N)	H_2O(N)	H_2O(S)	H_2O(N)	H_2O(S1)	H_2O(S2)
SO_3	−8.65	−20.16	−8.98	−31.11	−3.70	−15.27
H_2O(N)	—	—	13.43	—	8.20	23.25
H_2O(S1)	—	—	—	—	—	0.88
Total	−8.65	−15.71		−17.75		

(b) Transition state

	TS1	TS2		TS3		
$\mathscr{G}\backslash\mathscr{F}$	H_2O(N)	H_2O(N)	H_2O(S)	H_2O(N)	H_2O(S1)	H_2O(S2)
SO_3	20.89	13.10	−7.18	4.63	−6.24	0.69
H_2O(N)	—	—	2.28	—	−1.73	−0.91
H_2O(S1)	—	—	—	—	—	4.96
Total	20.89	8.20		1.40		

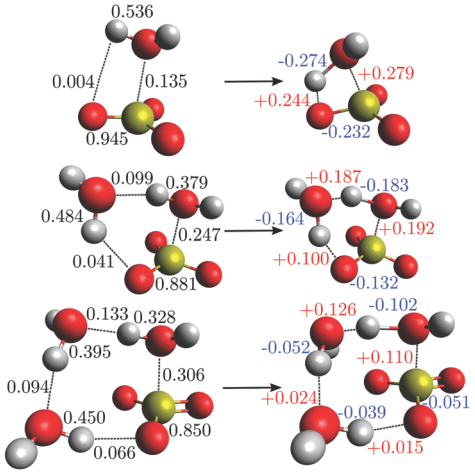

Fig. 5 Left: QTAIM delocalization indices within the considered molecular clusters (Fig. 2(a)–(c)) for the pairs of atoms involved in the formation and rupture of chemical bonds in the considered rate-limiting steps of the formation of acid rain in step (2) of eqn (1). Right: Changes in these indices after the formation of the corresponding transition states. The increments/reductions in δ(A,B) are indicated with red/blue colour. Atomic units are used throughout.

Concerning the rate-limiting steps of the investigated reactions, *i.e.*, step (2) in eqn (1), we note that the activation energies for these processes diminish with the number of water molecules in the system, in agreement with previous reports.[2,3] The pairwise decomposition of the activation energies (part (b) of Table 1) points out that the absolute values of $E_{int}^{\mathscr{F}\mathscr{G}'}$ are considerably smaller as more neighboring water molecules surround the reaction, a condition which leads to the stabilization of the corresponding transition state. This implies that the chemical bonding scenario in the formation of acid rain changes less drastically as more water molecules are included in the system. The right sides of Fig. 5 and Fig. S2 (ESI†) show respectively the variations in the QTAIM delocalization indices and the exchange component V_{xc}^{AB} for the pairs of atoms of reactants and products directly involved in the formation and breaking of chemical bonds in step (2) of eqn (1). Indeed, the alteration in the DIs and V_{xc}^{AB} for the interaction of $(H_2O)_2$ and $(H_2O)_3$ with SO_3 are milder than for the H_2O + SO_3 system as shown in Fig. 5. In this regard, the Hammond postulate[16] indicates that *structures close in energy that transform directly into each other are also similar in structure*.[17] We see therefore that the accompanying water molecules in the SO_3 + H_2O Lewis acid/base addition not only increase the magnitude of the interaction of the oxygen and sulphur atoms in the molecular cluster at the beginning of the reaction, but also relieve the changes in chemical bonding which lead to the formation of the transition state. This reduction in the modification of the involved covalent and non-covalent interactions abates greatly the activation energy of the rate-limiting step for the formation of H_2SO_4.

We considered the changes in the delocalization indices and V_{xc}^{AB} values for the bonds broken and formed around the SO_3 to yield H_2SO_4 as shown in Fig. S3 and S4 in the ESI† to test whether there is a dominant interaction for the trends observed in Fig. 1. The electronic and energetic tendencies for the set of

 This journal is © The Royal Society of Chemistry 2017

Published on 07 February 2017. Downloaded by Universidad de Oviedo on 4/29/2019 7:29:27 PM.

bonds formed and broken evolve almost linearly with the number of surrounding water molecules, another indication of cooperativity, and that there is not a single chemical interaction dominating the activation energy of the different rate-limiting steps for the formation of acid rain. Instead, hydrogen bond cooperativity alleviates the energetic cost of this process by affecting different chemical bonds simultaneously.

Finally, we point out that the analysis presented up to this point can be extended to the formation of other oxyacids, *e.g.* H_2CO_3 as shown in Fig. S5–S8 and Table S2 (ESI†). This illustrates that the bifunctional catalytic role of water discussed in this communication can be observed in other phenomena different from the formation of acid rain.

In summary, the catalytic activity of water oligomers in the production of H_2SO_4 in acid rain occurs *via* the same mechanisms as organic bifunctional catalysts in a way that compensates the low acidity and basicity of water itself. The embedded H_2O monomers reduce the activation energy of the rate-limiting step of the reaction by means of the attenuation of the changes in the chemical bonding scenario in this elementary step. All in all, the results of this investigation give valuable insights into the formation of acid rain and we expect them to be useful in the understanding of the catalytic properties of water to promote reactions in organic aqueous chemistry.

We acknowledge financial support from CONACyT (grant 253776 as well as scholarships 273438, 308773 and 381483) and the Spanish government (project CTQ-2015-65790-P). We are also thankful for computer time DGTIC/(grants SC16-1-IG-99 and SC16-1-IR-109) along with technical support from Magdalena Aguilar Araiza, Gladys Cortés Romero, David Vázquez Cuevas and Víctor Duarte Alaniz.

References

‡ The exchange–correlation component of the IQA interaction energy ($V_{xc}^{A,B}$) is consistent with the augmentation of DIs (left part of Fig. S2 in the ESI†). The delocalization index δ(A,B) and V_{xc}^{AB} represent two independent measurements of the covalence between the fragments A and B within a molecule or a supramolecular adduct. The section Methods in the ESI† has a brief discussion on the QTAIM delocalization indices and the exchange–correlation contribution of the IQA interaction energy.

1 T. Steiner, *Angew. Chem., Int. Ed.*, 2002, **41**, 48–76.
2 K. Morokuma and K. Muguruma, *J. Am. Chem. Soc.*, 1994, **116**, 10316–10317.
3 L. J. Larson, M. Kuno and F.-M. Tao, *J. Chem. Phys.*, 2000, **112**, 8830–8838.
4 C. E. Kolb, J. T. Jayne, D. R. Worsnop, M. J. Molina, R. F. Meads and A. A. Viggiano, *J. Am. Chem. Soc.*, 1994, **116**, 10314–10315.
5 T. Loerting and K. R. Liedl, *Proc. Natl. Acad. Sci. U. S. A.*, 2000, **97**, 8874–8878.
6 B. J. Mhin, S. J. Lee and K. S. Kim, *Phys. Rev. A: At., Mol., Opt. Phys.*, 1993, **48**, 3764–3770.
7 R. F. W. Bader, *Atoms in molecules: A Quantum Theory*, Oxford University Press, 1990.
8 M. A. Blanco, Á. Martín Pendás and E. Francisco, *J. Chem. Theory Comput.*, 2005, **1**, 1096–1109.
9 J. M. Guevara-Vela, R. Chávez-Calvillo, M. García-Revilla, J. Hernández-Trujillo, O. Christiansen, E. Francisco, A. Martín Pendás and T. Rocha-Rinza, *Chem. – Eur. J.*, 2013, **19**, 14304–14315.
10 T. Okino, Y. Hoashi and Y. Takemoto, *J. Am. Chem. Soc.*, 2003, **125**, 12672–12673.
11 W.-Y. Siau and J. Wang, *Catal. Sci. Technol.*, 2011, **1**, 1298–1310.
12 X. Fang and C.-J. Wang, *Chem. Commun.*, 2015, **51**, 1185–1197.
13 Y. Wang, H. Lu and P.-F. Xu, *Acc. Chem. Res.*, 2015, **48**, 1832–1844.
14 C. J. D. von Grotthuss, *Ann. Chim.*, 1806, **58**, 54–73.
15 S. Narayan, J. Muldoon, M. G. Finn, V. V. Fokin, H. C. Kolb and K. B. Sharpless, *Angew. Chem., Int. Ed.*, 2005, **44**, 3275–3279.
16 G. S. Hammond, *J. Am. Chem. Soc.*, 1955, **77**, 334–338.
17 J. Clayden, N. Greeves, S. Warren and P. Wothers, *Organic Chemistry*, Oxford University Press, 2000.

Chemical Bonding in Excited States: Energy Transfer and Charge Redistribution from a Real Space Perspective

Jesús Jara-Cortés,[a] José Manuel Guevara-Vela,[b] Ángel Martín Pendás,[b] and Jesús Hernández-Trujillo*[a]

This work provides a novel interpretation of elementary processes of photophysical relevance from the standpoint of the electron density using simple model reactions. These include excited states of H_2 taken as a prototype for a covalent bond, excimer formation of He_2 to analyze non-covalent interactions, charge transfer by an avoided crossing of electronic states in LiF and conical interesections involved in the intramolecular scrambling in C_2H_4. The changes of the atomic and interaction energy components along the potential energy profiles are described by the interacting quantum atoms approach and the quantum theory of atoms in molecules. Additionally, the topological analysis of one- and two-electron density functions is used to explore basic reaction mechanisms involving excited and degenerate states in connection with the virial theorem. This real space approach allows to describe these processes in a unified way, showing its versatility and utility in the study of chemical systems in excited states. © 2017 Wiley Periodicals, Inc.

DOI: 10.1002/jcc.24769

Introduction

The last 15 years have witnessed the progress in the understanding of many chemical processes taking place in excited states.[1] From the theoretical point of view, this has been possible thanks to developments in hardware, electronic structure methods and efficient computational codes that enable together to perform calculations for a variety of systems[2]; however, the connection between the calculations and chemical intuitive concepts (bond, functional groups, electron delocalization, etc.) is not straightforward but often controversial. In the present theoretical work, simple systems in the ground and lowest excited states are studied at the molecular level as archetypes of some general fundamental chemical processes. The H_2 molecule is used as a model for the making or breaking of single bonds in photophysical processes involving singlet or triplet electronic states.[3] The He_2 excimer is chosen to describe some fundamental processes of complexes in excited states. LiF is taken as representative for charge transfer processes and because of its close relationship with NaI, a historical molecule in the development of femtochemistry.[4] Finally, the internal rotation and the incipient proton transfer in C_2H_4 are analyzed for the description of conical intersections of potential energy surfaces (PES), regions of high transition probabilities between electronic states of vital importance in photochemistry.[5] For these systems, we assess the question as to how the molecular energy is locally redistributed into the reactant molecules and what are the changes on the electron distribution involved in the processes. In this respect, the methods introduced by the quantum theory of atoms in molecules (QTAIM) have contributed to the understanding of a wide range of chemical transformations of ground state molecules.[6,7] In addition, the energy partitioning provided by the interacting quantum atoms approach (IQA)[8] allows to carry out the energetic analysis beyond equilibrium geometries in terms of molecular fragment contributions. Although these tools have recently been applied in the study of molecules in excited states,[9–17] they are used here to describe basic reaction mechanisms of photophysical interest.

Theoretical Aspects

The study of reaction mechanisms in terms of the PES can be complemented by the interpretative descriptors provided by the QTAIM. An important aspect of this analysis is oriented to the understanding of the energetic changes taking place along a reaction path. Whereas the usual topological partitioning of the molecular energy in terms of scaled kinetic energy contributions can only be used at stationary points of the PES, the IQA approach provides physically sound contributions to the molecular energy during a chemical process.

A brief description of the IQA approach is provided next and further details can be found in Ref. [8]. Under the Born-Oppenheimer approximation, in the non-relativistic case and the absence of

[a] J. Jara-Cortés, J. Hernández-Trujillo
Departamento de Física y Química Teórica, Facultad de Química, UNAM, México City 04510, México
E-mail: jesusht@unam.mx
[b] J. Manuel Guevara-Vela, Á. M. Pendás
Departamento de Química Física y Analítica, Facultad de Química, Universidad de Oviedo, 33006 Oviedo, Spain
Contract grant sponsor: DGTIC-UNAM for supercomputer resources (project SC16-1-IR-71), UNAM-DGAPA-PAPIIT (project IN115215) (to J.H.-T. and J.J.-C.); Contract grant sponsor: Spanish MINECO/FEDER (to A.M.P.); Contract grant number: CTQ2015-65790-P; Contract grant sponsor: PAIP Facultad de Química UNAM (to J.H.-T.); Contract grant number: 5000-9004; Contract grant sponsor: CONACyT-México (to J.J.-C. and J.M.G.-V.); Contract grant numbers: 270166 and 381483
© 2017 Wiley Periodicals, Inc.

external fields, the system energy can be written as the sum of atomic energies plus interaction terms:

$$E=\sum_{\Omega}E^{\Omega}+\frac{1}{2}\sum_{\Omega}\sum_{\Omega'\neq\Omega}E_{\mathrm{int}}^{\Omega,\Omega'} \quad (1)$$

The self-energy of an atom Ω is defined as

$$E^{\Omega}=T^{\Omega}+V_{\mathrm{ne}}^{\Omega}+V_{\mathrm{ee}}^{\Omega} \quad (2)$$

with T^{Ω}, V_{ee}^{Ω}, and V_{en}^{Ω} being, respectively, the kinetic energy, the electron-electron Coulomb repulsion and the nucleus-electron attraction between the nucleus and electrons associated with Ω. In addition, the interaction energy between the basins Ω and $\Omega\prime$ is given by

$$E_{\mathrm{int}}^{\Omega,\Omega'}=V_{\mathrm{nn}}^{\Omega,\Omega'}+V_{\mathrm{en}}^{\Omega,\Omega'}+V_{\mathrm{ne}}^{\Omega,\Omega'}+V_{\mathrm{ee}}^{\Omega,\Omega'} \quad (3)$$

where $V_{\mathrm{nn}}^{\Omega,\Omega'}$, $V_{\mathrm{en}}^{\Omega,\Omega'}$, $V_{\mathrm{ne}}^{\Omega,\Omega'}$, and $V_{\mathrm{ee}}^{\Omega,\Omega'}$ account, respectively, for the internuclear repulsion, the electron-nucleus attractive contributions and the electron repulsion involving the two atomic basins.

It is also useful to express the atomic energies in terms of a reference value, usually the dissociation limit. In the case of a diatomic molecule with an inter-nuclear distance R, the atomic deformation energy is defined as

$$E_{\mathrm{def}}^{\Omega}=E_{R}^{\Omega}-E_{R=\infty}^{\Omega} \quad (4)$$

Moreover, separating the electronic repulsion term into Coulombic and exchange-correlation parts ($V_{\mathrm{ee}}^{\Omega,\Omega'}=V_{\mathrm{coul}}^{\Omega,\Omega'}+V_{\mathrm{xc}}^{\Omega,\Omega'}$), the interaction energies can be further divided into electrostatic and covalent components

$$E_{\mathrm{int}}^{\Omega,\Omega'}=V_{\mathrm{elec}}^{\Omega,\Omega'}+V_{\mathrm{xc}}^{\Omega,\Omega'} \quad (5)$$

where

$$V_{\mathrm{elec}}^{\Omega,\Omega'}=V_{\mathrm{nn}}^{\Omega,\Omega'}+V_{\mathrm{en}}^{\Omega,\Omega'}+V_{\mathrm{ne}}^{\Omega,\Omega'}+V_{\mathrm{coul}}^{\Omega,\Omega'} \quad (6)$$

Energy transfer accompanying the charge redistribution on the transition between electronic states will be analyzed using these expressions in selected test molecules.

Computational Methods

The electronic structure calculations were performed at the MRCI-SD level of theory, using as reference state averaged SA-CASSCF wave functions and the d-aug-cc-pVDZ basis set[18–21] which is suitable for the description of Rydberg states. In all cases, equal weights were used in the SA-CASSCF calculations, constraining the symmetry to abelian point groups. The active spaces comprise 2 electrons and 10 orbitals—designated as (2,10)—in the case of H_2, (4,4) for He_2, (6,6) for LiF, and (2,6) for C_2H_4. Inclusion of dynamic electron correlation is mandatory for the proper description of the He_2 excimer and of the position of the avoided crossing of states of LiF. The following potential energy curves were obtained. H_2: $X^1\Sigma_g^+$, $B^1\Sigma_u^+$, E, $F^1\Sigma_g^+$, and $b^3\Sigma_u^+$; He_2: $X^1\Sigma_g^+$, $A^1\Sigma_u^+$, $C^1\Sigma_g^+$, and $A^3\Sigma_u^+$; LiF: $1^1\Sigma^+$ and $2^1\Sigma^+$. In addition, the PES of C_2H_4 for some valence (S_0 and the lowest $\pi-\pi^*$) and Rydberg (3s, $3p_x$, $3p_y$, $3p_z$) states along the twist and pyramidalization coordinates were obtained; in the latter, the minimum energy conical intersection points between the states S_0 and $\pi-\pi^*$ associated with the twisted-pyramidalized and proton migration geometries were also calculated. The SA-CASSCF states were calculated as follows: For H_2 and He_2 (D_{2h} symmetry), two of the singlet states belong in the A_g representation, the remaining one and the triplet are B_{1u} states. For LiF (C_{2V} point group), the two are A_1 states. In the case of C_2H_4 along the twist coordinate (C_2 symmetry), five A and three B states were averaged, respectively; for the pyramidalization coordinate and the conical intersection, no symmetry constraints were imposed and three singlet states were averaged. All the electronic structure calculations were performed using Columbus and Molpro,[22,23] and subsequently the partitioning of the total energy by the IQA method was carried out using Promolden.[8] The total energies obtained with Promolden using eq. (1) differ at most in 0.5 kcal/mol relative to the energies calculated with Molpro; errors of 1.5 kcal/mol are found in some isolated points that do not affect the individual or global trends of the energy components. The multi-configurational one- and two-electron density matrices, necessary for the IQA energy partition, were obtained from wave functions computed with Molpro. The Appendix describes the procedure to generate the input files with this information for the Promolden program and a Perl script was written to carry out this task. The Promolden code and the Perl script are available to interested readers on request.

Results

Excited states of H_2

Figure 1 shows the calculated PES for the $X^1\Sigma_g^+$, $B^1\Sigma_u^+$, E, $F^1\Sigma_g^+$, and $b^3\Sigma_u^+$ states of H_2. The $X^1\Sigma_g^+$ and $b^3\Sigma_u^+$ pose no major interpretation problems. Much more interesting are the next two singlets, $B^1\Sigma_u^+$ and E, $F^1\Sigma_g^+$, which dissociate to H(1s)+H(2l). Standard correlation diagrams show that $B^1\Sigma_u^+$ connects the 1s2pσ configuration of the united He atom with the $H^+ + H^-$ dissociation limit. Similarly, the E state links He-1s2s to H(1s)+H(2l), and the F state He-$2p^2$ to $H^+ + H^-$

Both the B and F states should therefore show a clear ionic character. However, as the $H^+ + H^-$ dissociation falls between the H(1s)+H(4l) and the H(1s)+H(5l) levels, several avoided crossings occur as the internuclear separation increases that preclude dissociation to the ionic state. This also explains the double minimum of the E,F state, as found by Davidson.[24] According to Herzberg,[25] the inner minimum is largely covalent, while the outer is mainly ionic. The nature of the E, $F^1\Sigma_g^+$ state has also been analyzed by Wang et al.[26] in terms of the pair density and the contributions to the molecular energy. The ground state H_2 molecule is characterized by the shortest equilibrium distance, R_e, and largest binding energy with

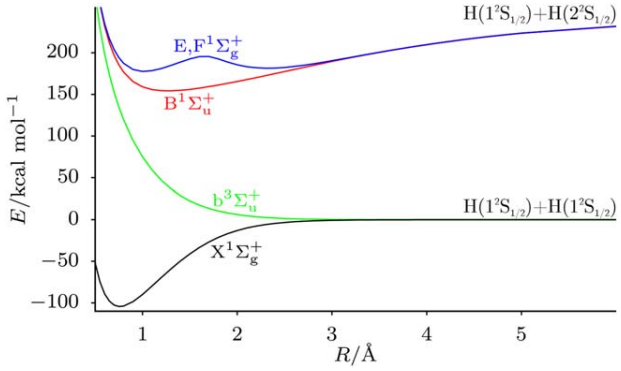

Figure 1. Potential energy curves for the ground and the lowest excited states of H_2. [Color figure can be viewed at wileyonlinelibrary.com]

respect to the singlet excited states. These results are in keeping with previous reports on the molecule.[27,28]

We now proceed to the analysis of the atomic energy contributions along the PES of the lowest electronic states of the H_2 molecule using the IQA approach. From these, the $X^1\Sigma_g^+$ and $b^3\Sigma_u^+$ states have been reported before at the CAS level[29,30]; they are included here to establish trends with the other states. According to Figures 2a and 2b, the ground state E_{def}^H and the contributions to the interaction energy have little variation with internuclear separation for R values greater than ca. 3 Å. At long distances, $E_{int}^{H,H'}$ is small because the exchange-correlation term, V_{xc}, is not relevant yet and the classical interactions cancel each other yielding a negligible V_{elec} contribution, as detailed in Fig. S1 of the Supporting Information; at short R values, E_{def}^H rises due to a buildup of $V_{ee}^{H,H'}$, although its magnitude remains small even at equilibrium. This intra-atomic destabilization is more than compensated by a large stabilizing $E_{int}^{H,H'}$, clearly dominated by the covalent exchange-correlation component. At distances smaller than R_e, the increase in the classical repulsion between the atomic charge densities, due to the $V_{coul}^{H,H'}$ and $V_{nn}^{H,H'}$ terms, is responsible for the repulsive behaviour of the total energy curve.

Regarding the $b^3\Sigma_u^+$ state, a very steep increase in E_{def}^H for $R < 3$ Å is responsible for the repulsive character of the PES, in agreement with the standard Pauli repulsion explanation, that is not offset by a deeper $E_{int}^{H,H'}$ stabilization. The latter may be traced to the small value of $E_{xc}^{H,H'}$ shown in Figure 2b that reveals inefficient interatomic delocalization.

In the case of the singlet excited states, all the energy components start differing from each other at distances smaller than 3.5 Å, Figure 2. A first interesting point is that the atomic self-energies of both H atoms are always equal to each other, tending at large distances to half the energy of a 1s and a 2s H atoms. In our opinion, this is a very nice demonstration of the entangled character of the states, which is clearly unveiled by IQA. The deformation energies of the $B^1\Sigma_u^+$ and $E,F^1\Sigma_g^+$ states rise very quickly as the inter-nuclear distance is shortened, being at $R \approx 6.3$ Å as large as E_{def}^H for the X singlet at its equilibrium geometry. This implies a very long-range interaction. At shorter distances, these deformation energies reach a plateau and then decrease significantly for $R < 2$ Å, becoming negative as the united atom limit approaches. The origin of all these changes may be beautifully traced back by examining Figure 2c. The initial increase in E_{def}^H is caused by the prompt rise in V_{ee}^H. Notice that this seems to occur at about $R \approx 7$ Å, which points to a state crossing. Taking into account that the electron repulsion in a hydride ion (192.6 kcal/mol at the Full-CI/d-aug-cc-pVDZ level) is about twice V_{ee}^H of the B and E,F singlets between 2 and 5 Å, this fact is a clear demonstration that during the plateau these states are clearly ionic. We can thus follow the transition from the covalent-like H(1s)+H(2s)

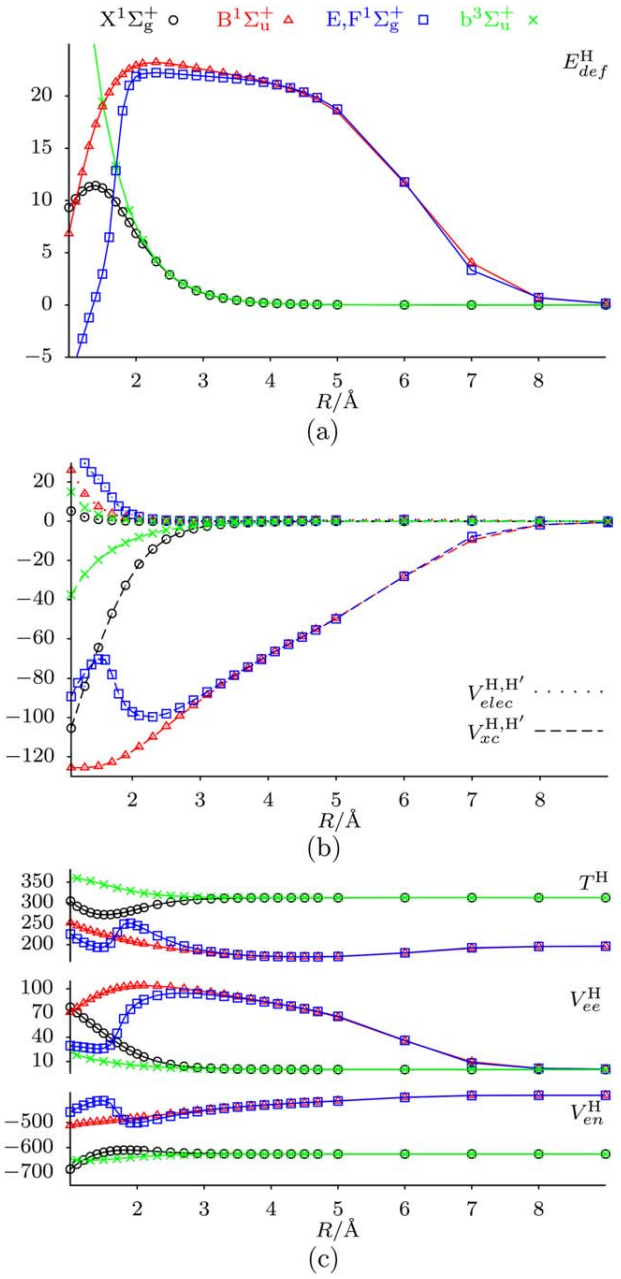

Figure 2. IQA electronic energy partition for the $X^1\Sigma_g^+$, $B^1\Sigma_u^+$, $E,F^1\Sigma_g^+$, and $b^3\Sigma_u^+$ states of H_2. a) Deformation energies, b) electrostatic and exchange-correlation contributions to $E_{int}^{H,H'}$, and c) components of the atomic energy. The values are given in kcal/mol. [Color figure can be viewed at wileyonlinelibrary.com]

Table 1. IQA energy contributionas and Θ_{RR} at the equilibrium geometry for the electronic states of H_2.

	$X^1\Sigma_g^+$	$B^1\Sigma_u^+$	$E^1\Sigma_g^+$	$F^1\Sigma_g^+$
R_e	0.7616	1.2660	1.0157	2.3222
T^H	350.4826	234.8151	222.7575	219.8020
V_{ee}^H	94.1671	85.1762	28.5899	92.1792
V_{en}^H	−749.5200	−501.2498	−453.9896	−485.3776
E^H	−304.8702	−181.2585	−202.6421	−173.3964
E_{def}^H	8.4664	13.8102	−7.5728	21.6729
$V_{nn}^{H,H'}$	436.0077	262.2724	326.9303	142.9949
$V_{en}^{H,H'}$	−367.6851	−209.8528	−212.3572	−136.6388
$V_{ee}^{H,H'}$	178.1065	47.4070	56.0610	31.8492
$E_{int}^{H,H'}$	−121.2561	−110.0268	−41.7231	−98.4336
$V_{elec}^{H,H'}$	24.8631	15.4461	49.4220	1.0323
$V_{xc}^{H,H'}$	−146.1192	−125.4729	−91.1451	−99.4658
Θ_{RR}	−4.1556	−18.2900	−52.0768	−13.2905

The distances are in Å, the energies in kcal/mol and Θ_{RR} in a.u.

dissociation limit toward the ionic state. Turning to the H, H′ interaction in Figure 2b we see the very large, almost linear stabilization due to the V_{xc} component. In terms of the resonant structures $H^- + H^+ \leftrightarrow H^+ + H^-$, this adds to the ionic interpretation, as ionic resonance implies an important enhancement in the exchange energy, in contrast to charge transfer where V_{elec} should dominate. The maximum shown by V_{xc} in the E, F state also allows to identify very clearly the avoided crossing with the He-1s2s covalent limit as the origin of the double well in the PES. We will find a similar situation again in the LiF molecule. The crossing is also recognized in the behavior of T^H, V_{ne}^H, and V_{ee}^H, the latter decreasing steeply at $R \approx 1.7$ Å as we pass from an ionic to a covalent resonance. V_{ne}^H is also revealing the smaller electron-nucleus attraction coming from a 2s component in the E minimum as opposed to the main 1s term in the F one. In this sense, all traditional insights about the nature of the electronic states may be immediately read from the IQA decomposition: The inner and outer minima are mainly covalent and ionic, respectively.

Table 1 shows the equilibrium geometry energy contributions of the lowest singlet electronic states of H_2. As a consequence of having the smallest R_{eq} value, the ground state molecule has the largest magnitude intra- and inter-basin nucleus-electron attraction and internuclear repulsion energies. Although the magnitudes of V_{ne}^H and $V_{ne}^{H,H'}$ for the excited states are smaller, the intra- and inter-basin repulsions also decrease. Regarding the two minima on the E, $F^1\Sigma_g^+$ PES, the $F^1\Sigma_g^+$ state is characterized by a large 21 kcal/mol deformation energy and a very stabilizing −98 kcal/mol interatomic interaction fully dominated by its covalent part. In this sense, it is a very delocalized, strongly deformed ionic version of the ground state. In contrast, the $E^1\Sigma_g^+$ minimum displays a much smaller $E_{int} \approx -41$ kcal/mol resulting from a similar V_{xc} covalent component and a considerably more destabilizing V_{elec} term, significantly more positive than V_{elec} for the B state at the same distance. This is easily understood if we notice the diffuse character of its 1s2s limit. E_{def}^H at the E minimum is negative, close to −7 kcal/mol, as expected for the covalent state. Overall, the binding energy of E is not very different from that of F, although with very different interpretation. Similar arguments explain why the binding energy of $B^1\Sigma_g^+$ is greater than for $E^1\Sigma_g^+$ and $F^1\Sigma_g^+$.

The trace of the matrix of electric second moments, $\Theta_{RR} = \langle xx \rangle + \langle yy \rangle + \langle zz \rangle$, allows to quantify the spatial extent of a charge distribution.[31] The values of this property at the minima in the PES of H_2 are given in Table 1. From the values for the E and F states, one can easily read the extraordinary transition to the covalent 1s2s Rydberg state as one traverses from the F to the E minimum.

Figure 3 displays contour plots of $\rho(\vec{r})$ for the singlet states of H_2 at $R = 1$ Å, which is nearly the average of the R_e values

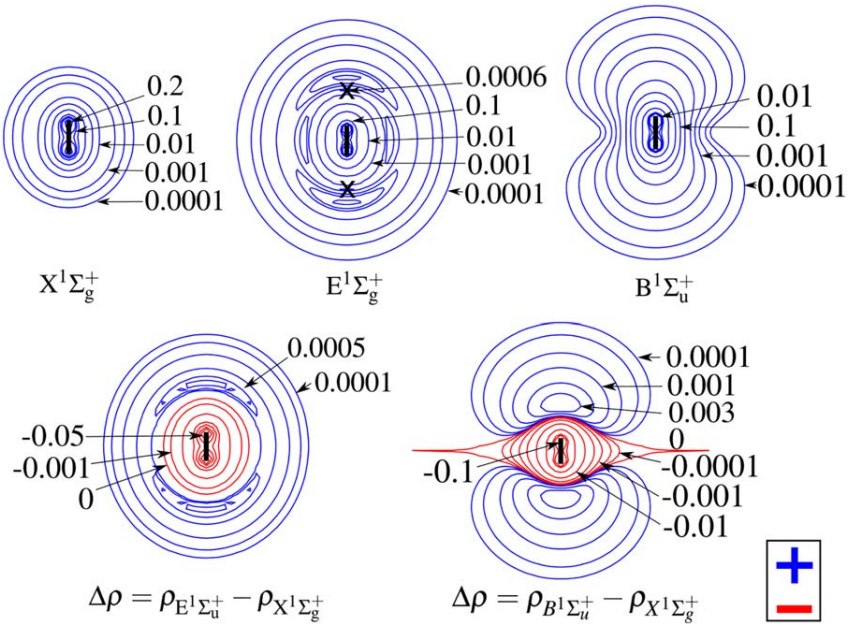

Figure 3. Contour plots of $\rho(\vec{r})$ and $\Delta\rho(\vec{r})$ for the lowest singlet electronic states of H_2 at $R = 1$ Å. The crosses on E, $F^1\Sigma_g^+$ denote the non-nuclear maxima; the red areas in the lower contour plots represent negative values of $\Delta\rho(\vec{r})$. [Color figure can be viewed at wileyonlinelibrary.com]

Table 2. Energy values for the ground (1^1S_0) and excited singlet (2^1S_0) and triplet (1^3S_1) states of the helium atom; energies are given in kcal/mol.

	1^1S_0	2^1S_0	1^3S_1
$\langle E \rangle$	−1813.2465	−1341.9016	−1360.4904
$\langle T \rangle$	1792.0999	1346.6076	1370.9250
$\langle V_{ne} \rangle$	−4201.8359	−2841.6530	−2898.5517
$\langle V_{ee} \rangle$	596.4895	153.1438	167.1363
Θ_{RR}	−2.4332	−36.5478	−24.8502

The values of Θ_{RR} (in a.u.) are also shown.

for the X, E and B singlet states given in Table 1. It shows that the electronic distribution of $X^1\Sigma_g^+$ is compact, in contrast to the diffuse character of $B^1\Sigma_u^+$ and $E^1\Sigma_g^+$. This can be further illustrated by the electron density differences between an excited and the ground state. For example, from the contour plots of $\Delta\rho = \rho_{B^1\Sigma_u^+} - \rho_{X^1\Sigma_g^+}$, also shown in Figure 3, it is seen that there is an electron density decrease in the bonding region and near the attraction basins, and an increase in the non-bonded regions for the excited state. These characteristics are the origin of the Θ_{RR} values discussed before. Furthermore, a striking feature of the contour plots of $E^1\Sigma_g^+$ is the density accumulation toward the non-bonded regions of the atomic basins that results in the appearance of two non-nuclear maxima (NNM) in $\rho(\vec{r})$ for internuclear distances less than 1.4 Å, whose presence was confirmed by a series of calculations using basis sets as large as d-aug-cc-pVQZ with and without symmetry constraints. The appearance of NNM at short internuclear distances is an anticipated feature for many molecules,[32] being also expected in excited states. In this work, we have always used the ground state H – H interatomic surface to avoid any problem with NNMs, as our aim is comparing different electronic states in as similar as possible conditions. A final comment on the overall appearance of the ρ contours is due: they also allow for a simple mapping to the united atom states they correlate to. For instance, it is easily seen that the B state is 2p-like, and that the E state is 2s-like, although the cylindrical symmetry distorts the He-2s spherical node. Actually the two NNMs are nothing but the symmetry broken remnants of the second radial maximum of that 2*s* orbital.

Excimers of He_2

Because of their importance in low-temperature physics, the electronic states of He_2 are among the most studied systems from the theoretical and experimental points of view.[33,34] The first step leading to the formation of the lowest energy excimers is the excitation of a helium atom either to the lowest triplet (1^3S_1) or first excited singlet (2^1S_0) state. According to Table 2, as a consequence of this excitation the kinetic and potential electron-electron energies of the helium atom decrease and the nucleus-electron attraction increases with respect to the ground state. These changes are lower in magnitude for the 1^3S_1 state, with an overall stabilizing effect due to the greater nucleus-electron attraction.[35] In addition, $|\Theta_{RR}|$ increases from 2.43 a.u. in the ground state, Table 2, to 36.55 and 24.85 a.u. in the 2^1S_0 and 1^3S_1 states, respectively. That the spatial extent of the helium atom is smaller in the triplet than in the first singlet excited state together with the more attractive electron-nucleus contribution to the atomic energy provides a physical basis for Hund's rule.[36]

Once a helium atom is excited to the 2^1S_0 state, its interaction with another He atom in the ground state leads to the excimer formation in two possible singlet states associated with the ungerade and gerade combinations of the monomer wavefunctions yielding the $A^1\Sigma_u^+$ and $C^1\Sigma_g^+$ states, respectively. Similarly, the interaction of a helium atom in the 1^3S_1 state with another in the ground state yields two triplet excimer states, $A^3\Sigma_u^+$ and $C^3\Sigma_g^+$. The potential energy curves for the ground state He_2 dimer and its lowest singlet and triplet excimers are shown in Figure 4. Note that the dissociation energy of the ground state dimer is three orders of magnitude smaller than for the $A^1\Sigma_u^+$, $C^1\Sigma_g^+$, and $A^3\Sigma_u^+$ states, and that the binding energies of the lowest excimer states are typical of standard covalent links.

At large internuclear distances, as in the case of H_2, the He atoms in the excited states are in a spatially entangled state, corresponding to a 50/50 superposition of a ground state and a singlet/triplet 1s2s He atom.

Table 3 shows the IQA energy contributions for the electronic states of He_2 at R_e. A simple back of the envelope calculation from the data of Table 2 shows how close the magnitude of each quantity to the 50/50 entangled mixture is. Overall, the atomic deformation energies are very small, only a few kcal/mol larger than those for the H_2 molecule in the ground state. This is a particularly satisfactory feature of the IQA procedure. As the interactions are regarded, it is the very large exchange-correlation energies, $V_{xc}^{He,He'}$, which account for binding. These display values in line with a perfectly delocalized covalent interaction. The diffuse nature of the 1s2s states leads to a considerably destabilizing $V_{elec}^{He,He'}$, coming from incomplete nuclear shield in Rydberg states, as the V_{nn}, V_{en}, and V_{ee} interaction values reveal. This is behind the smaller binding energies of the excimers with respect to the ground state H_2, for instance. As for the relative stabilities of the excited states, Table 3 shows that the sum of exchange-correlation

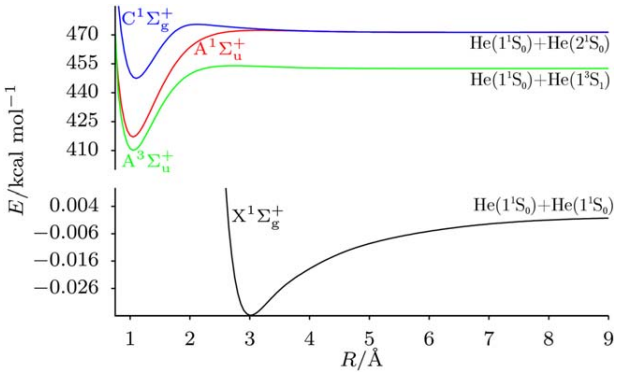

Figure 4. Potential energy curves for the ground and lowest excited electronic states of He_2. [Color figure can be viewed at wileyonlinelibrary.com]

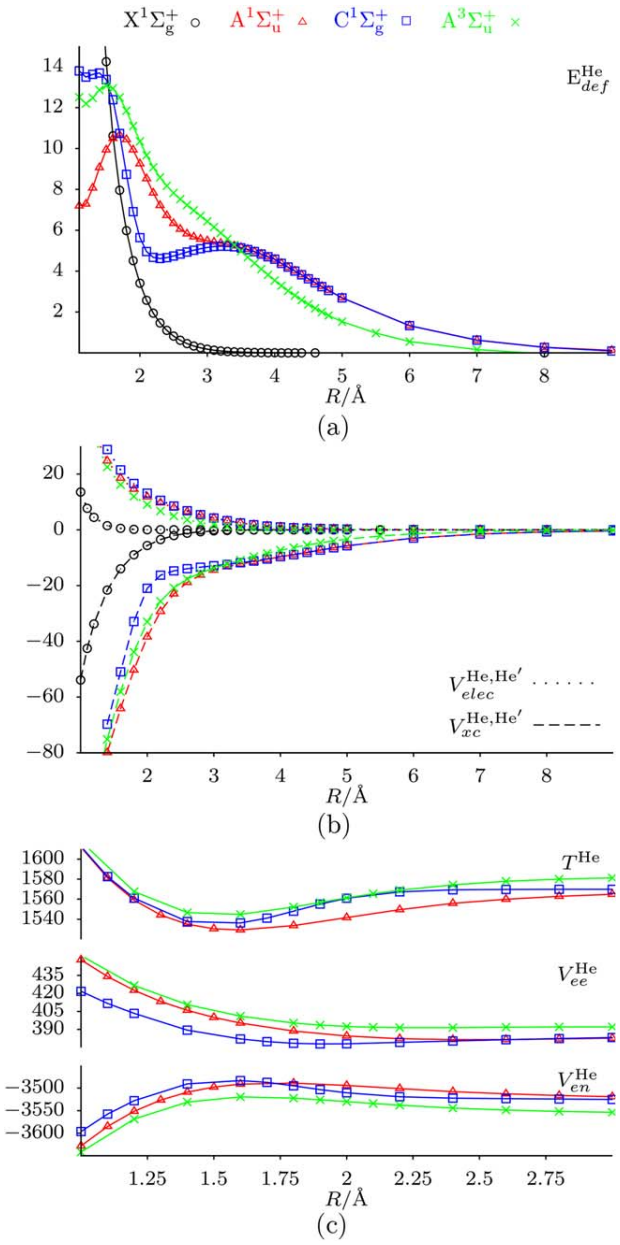

Figure 5. IQA electronic energy contributions for the $X^1\Sigma_g^+$, $A^1\Sigma_u^+$, $C^1\Sigma_g^+$, and $A^3\Sigma_u^+$ states of He_2. a) Deformation energies, b) electrostatic and correlation-exchange energies, c) components of atomic energy; the values are given in kcal/mol. [Color figure can be viewed at wileyonlinelibrary.com]

interaction plus atomic deformation energy is more stabilizing in the A ungerade state. Figure 5a shows that the A and C states undergo two consecutive changes at about 3.5 and 2 Å. At the equilibrium geometry, the C state has gained a considerable united atoms p character, a fact that considerably increases its self-energy and weakens the exchange-correlation interaction.

Now we follow the evolution of the IQA quantities as the internuclear distance changes. In the case of the ground state He_2 complex, Figures 5a and 5b show that the atomic and interaction energies remain virtually constant for a wide range of R values that includes R_e. At the equilibrium geometry, the slight deformation of the interacting electronic distributions is accompanied by a small increase of atomic energies and an increase in the magnitude of the interaction energy which leads to complex formation.[29] These energy contributions show important changes only when R becomes less than 2 Å, yielding the repulsive part of the total energy curve for shorter internuclear separations; except at the shortest distances, V_{elec} is very small, and the repulsive nature of the PES may be understood as due to an overall positive sum of the atomic deformations and the exchange-correlation stabilization. We have shown[37] that in the perturbation regime for the interaction of two closed-shell systems, that combination, usually called the exchange-repulsion, is positive.

The features described above change significantly in an electronic excited state. Consider the $A^3\Sigma_u^+$ excimer and Figure 5. At large distance, the deformation energy grows relatively smoothly, as in any spatial delocalization process. Concomitantly, the exchange-correlation interaction stabilizes the system. As the distance decreases, a shoulder in E_{def} is developed at about 3.5 Å, followed by a maximum at $R \approx 2$ Å. Similar anomalies can also be seen in all the other states, and may be also distinguished in V_{xc}, very clearly in the C singlet. We will not analyze the nature of these changes in detail. At small distances, the V_{elec} repulsion dominates, and the inner repulsive wall develops. A comparison with the ground state of the H_2 molecule should convince us that this triplet He_2 excimer is developing a standard covalent bond.

The evolution of the $A^1\Sigma_u^+$ and $C^1\Sigma_g^+$ states is more interesting. Both evolve in unison until the first $R \approx 3.5$ Å anomaly, where they start separating, both from the atomic (E_{def}) and interatomic (V_{xc}) points of view. This reveals a change in their electronic nature, which is maintained when R is between c.a. 1.8 and 3.5 Å. At smaller distances, another change occurs, and the self-energy of the C state abruptly increases to become stable again around its equilibrium distance. Notice that these changes are reflected neither in V_{xc} nor in V_{elec}, thus pointing to intra-atomic redistributions.

Figure 6 displays some contour plots of $\rho(\vec{r})$ for the singlet state He_2 excimers at $R = 1$ Å. This value is very close to R_e of

Table 3. IQA energy contributions and Θ_{RR} values at the equilibrium geometry for the lowest electronic states of He_2.

	$X^1\Sigma_g^+$	$A^1\Sigma_u^+$	$C^1\Sigma_g^+$	$A^3\Sigma_u^+$
R_e	3.0150	1.0476	1.0996	1.0522
T^{He}	1794.4913	1596.0453	1581.5906	1601.2298
V_{ee}^{He}	598.1642	440.9117	409.1930	443.9563
V_{en}^{He}	−4205.5044	−3606.5032	−3554.2932	−3618.7164
E^{He}	−1812.8490	−1569.5462	−1563.5096	−1573.5303
E_{def}^{He}	0.1701	7.6311	13.6615	13.0509
$V_{nn}^{He,He'}$	440.5483	1267.9014	1207.9423	1262.3580
$V_{en}^{He,He'}$	−440.4812	−1054.5954	−982.8316	−1058.0687
$V_{ee}^{He,He'}$	440.0338	771.4251	706.4515	784.9165
$E_{int}^{He,He'}$	−0.3803	−69.8650	−51.2694	−68.8628
$V_{elec}^{He,He'}$	0.0006	48.4374	49.8292	46.0246
$V_{xc}^{He,He'}$	−0.3809	−118.3024	−101.0986	−114.8875
Θ_{RR}	−4.8566	−37.5720	−58.0397	−33.3678

The distances are given in Angstroms, the energies in kcal/mol and Θ_{RR} in a.u.

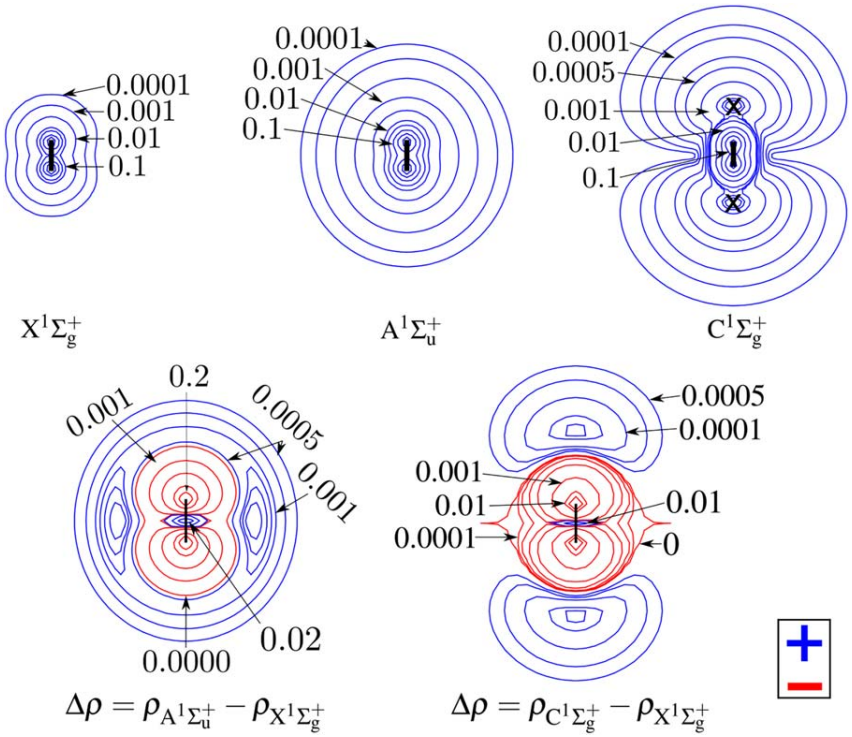

Figure 6. Contour plots of $\rho(\vec{r})$ and $\Delta\rho(\vec{r})$ for the lowest singlet electronic states of He_2 at $R = 1$ Å. The $\times$ marks in $C^1\Sigma_g^+$ denote the non-nuclear maxima. [Color figure can be viewed at wileyonlinelibrary.com]

the singlet excited states. The charge distribution of the triplet is very similar to that of the $A^1\Sigma_u^+$ state and therefore is not analyzed. This figure shows that the electronic distributions of the excimers have a diffuse character, which can be expressed in terms of Θ_{RR}. The values of this property are given in Table 3 for the equilibrium geometries and only have small variations at 1 Å. In addition, the electron density differences with respect to the ground state show that, in the excited state, $\rho(\vec{r})$ decreases near the nuclear positions, and increases at distances in the bonding and non-bonding regions. Notice how the A and C states develop marked united atom 2*s* and 2*p* character, respectively, in line with the correlation diagram[38] of the molecule. Notice also that the electron density of the C state has two NNM whenever $R < 1.4$ Å. This latter characteristic was already described in previous studies[39,40] of the triplet He_2 excimers.

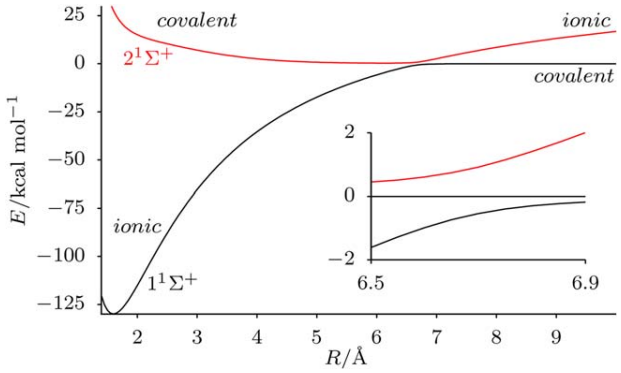

Figure 7. Potential energy curves for the $1^1\Sigma^+$ and $2^1\Sigma^+$ states of LiF. [Color figure can be viewed at wileyonlinelibrary.com]

Avoided crossing of states in LiF

Figure 7 shows the potential energy curves of the $1^1\Sigma^+$ and $2^1\Sigma^+$ states of LiF. The evolution of the electron density in this process has been discussed before[12,41,42] and is complemented here with an analysis of the energy contributions within the IQA approach. The formation of the LiF molecule from the neutral atoms involves an avoided crossing of electronic states within a range of ±0.3 Å around R_c=6.64 Å and an electron transfer of 0.94 e to the F atom at the equilibrium ionic molecule. At infinite separation, the $1^1\Sigma^+$ and $2^1\Sigma^+$ states are respectively the so-called covalent and ionic states, while at short distances the trends are inverted, so that $1^1\Sigma^+$ becomes the ionic and $2^1\Sigma^+$ the covalent state.

The components of the atomic and interaction energies in terms of R for the $1^1\Sigma^+$ and $2^1\Sigma^+$ states of LiF are displayed in Figure 8. We will concentrate in the region surrounding the avoided crossing, where a nice story is told. A first point regards all the intra-atomic IQA energy components, for the Li and the F atoms. Figures 8a and 8b show how amazingly constant T^X, V^X_{ee}, and V^X_{en} (X=Li,F) would be on approaching the two moieties from infinity up to $R \approx 4$ Å should the crossing not exist. This means that, due to quantum mechanical interference, the Li-F and Li^+ F^- pairs transform extremely quickly into each other, leaving almost no scars after this process ends. For instance, if we deleted in the figure a narrow region around the crossing, let us say between 7 and 6 Å, the neutral

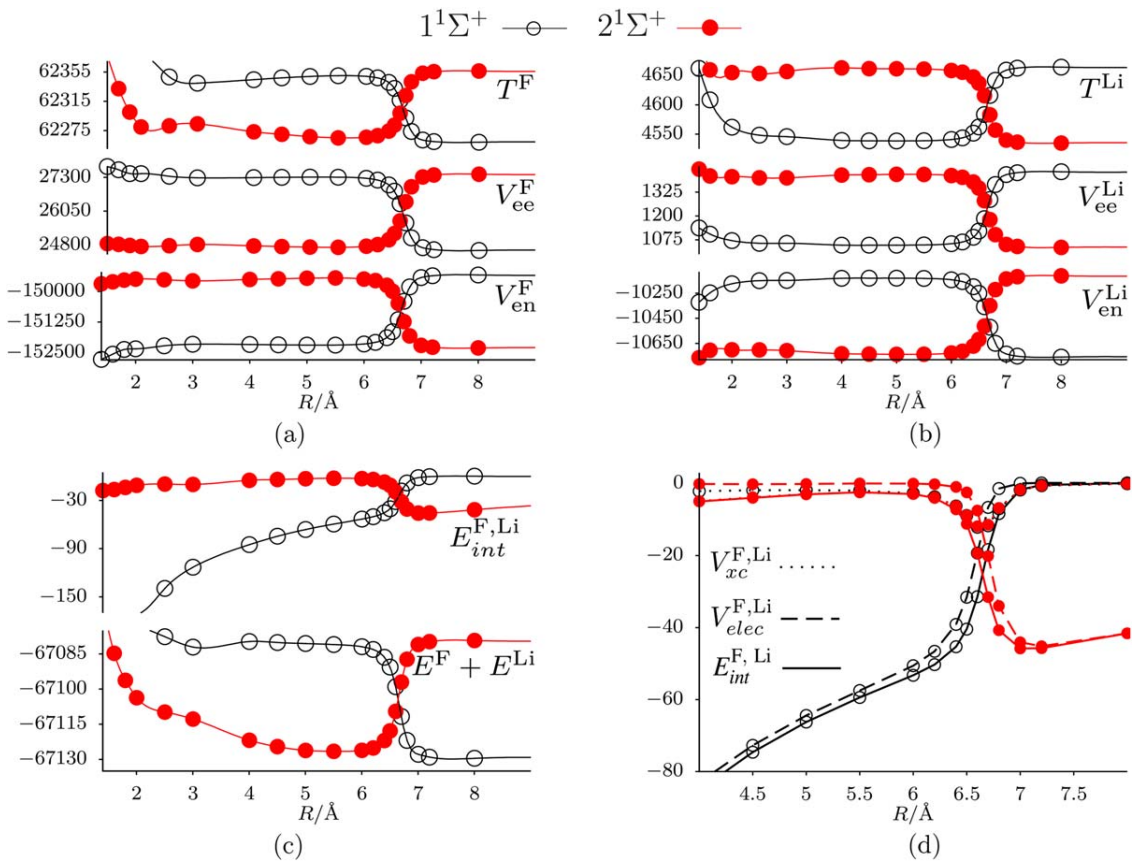

Figure 8. IQA electronic energy partition for the $1^1\Sigma^+$ and $2^1\Sigma^+$ states of LiF. a) F and b) Li atomic energy components, c) sum of self-energies and interaction energy, and d) exchange-correlation and electrostatic interaction components. The values are given in kcal/mol. [Color figure can be viewed at wileyonlinelibrary.com]

Li-F or ionic Li^+ F^- species would still be perceived as non-interacting, aside from their Coulombic attraction in the latter case, until their distance falls below $R \approx 4$ Å. Figures 8c–8d reinforce this image. Notice that the exchange-correlation contribution is very small from dissociation up to $R \approx 4$ Å except in the surroundings of the crossing, where quantum effects cannot be neglected. In fact, Figure 8d can be nicely read as: (i) a very flat, small covalent interaction between the two charged species in the ionic state (the $2^1\Sigma^+$ red line with closed circles curve at large distance and the black line with open circles $1^1\Sigma^+$ state after the crossing) that is accompanied by a $-1/R$ electrostatic attraction envelope formed by the dashed lines with closed and open circles, respectively; (ii) a normal covalent interaction that grows as distance decreases, with a small electrostatic component in the covalent state. Only close to the crossing we can see further structure.

Another relevant point is associated to the relative weight of V_{elec} and V_{xc} in the interaction energy, E_{int}, eq. (5), of LiF. Before the crossing, that is, when $R > R_c$, the interaction in the $1^1\Sigma^+$ state is dominated by V_{xc}, much as in the early stages of formation of any standard covalent link. The contrary is true for the $2^1\Sigma^+$ state. As we approach the crossover, the absolute values of V_{elec} and V_{xc} resemble more and more each other. Interestingly, V_{elec} and V_{xc} in both states become almost identical in magnitude at the very crossing. Once the crossing is passed, V_{elec} dominates the interaction in the $1^1\Sigma^+$, and vice-versa. V_{xc} is still very small in the ground (ionic) state, but becomes larger in the covalent one, as one would expect. The processes described in Figure 8 are tightly coupled to interatomic charge transfer. The atomic charges jump from nearly zero to about ± 1 in the same narrow window associated to the crossing; at R_c, their absolute values are very close to 0.5 a.u.

Finally, a non-trivial result emerges from our data. In a very large distance range ($R > 5.5$ Å), our calculated interatomic V_{xc} values for both singlets are indistinguishable. This is not necessarily expected, and points toward a deep duality in both states. We think that further work is needed to clarify to what extend this result may be extended to other systems.

Although clear from the above statements, at their respective equilibrium geometries the 1,2 $^1\Sigma^+$ states are ionic and covalent, with atomic self-energies close to the ions and neutral atoms, respectively, and with interactions dominated by classical and *xc* terms. The broad minimum in the $2^1\Sigma^+$ PES is obviously due to the flat landscape offered by the E_{self} and E_{int} values. This justifies that its equilibrium distance occurs close to where V_{xc} acquires its most negative value, that is, close to the crossing.

Figure 9a shows $\Delta\rho$ contour plots for the $1^1\Sigma^+ \rightarrow 2^1\Sigma^+$ Franck-Condon transition of the LiF molecule at the ground

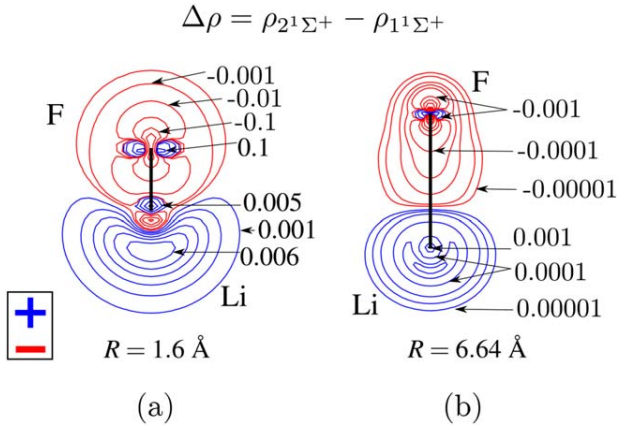

Figure 9. Electron density difference contour plots between the $2^1\Sigma^+$ and $1^1\Sigma^+$ states of LiF at a) the ground state geometry and b) the avoided crossing of states. [Color figure can be viewed at wileyonlinelibrary.com]

state equilibrium geometry. In the process, the electron density is increased within a small torus centered at the F nucleus and decreases in the rest of the atomic basin, shown as a shadowed region in Figure 9; in regard to the Li atom, $\rho(\vec{r})$ increases considerably in a small region centered at the nuclear maximum, with a minor decrease in the rest of the atom. The net result is the transfer of one electron toward Li, an increase of its atomic volume and the interatomic surface changing its concavity toward the F atom in the covalent state.

Excited states of C_2H_4

The absorption spectrum of ethylene involves excitation energies less than 230 kcal/mol dominated by a progression of vibronic bands between the ground and the lowest $\pi-\pi^*$ valence state in which several peaks of Rydberg transitions are superimposed. The energy gap between the $3p_x$ and the $\pi-\pi^*$ states is 27 kcal/mol at the SA-CASSCF level of theory, decreasing to only 0.47 kcal/mol after inclusion of dynamic electron correlation at the MRCI-SD level, in agreement with previous[43] reports. Because of limitations found in the Promolden code, we were unable to perform the IQA energy partition at the MRCI-SD level. Nevertheless, the SA-CASSCF results provide an adequate qualitative description of the PES of C_2H_4, allowing to analyze the minimum energy conical intersections associated with the twisted-pyramidalized and H-migration geometries. The Rydberg states were considered in the calculations of their strong configurational mixing with the $\pi-\pi^*$ valence state but their electron densities were not analyzed.

Potential energy curves along the twist and pyramidalization coordinates (freezing all other internal coordinates at their S_0 values) for the electronic states calculated are shown in Figure 10. It can be seen that whereas the Rydberg states are destabilized along the twist θ coordinate, the $\pi-\pi^*$ valence state decreases in energy to become the lowest excited state. Although pyramidalization of the molecule further destabilizes the Rydberg and the S_0 states, S_1 still decreases in energy. At the molecular geometry for θ=90° and β=100° the S_0 and S_1 states are nearly degenerate so that optimizations from geometries close to this configuration lead to several minimum energy conical intersection points. Some portions of this S_1/S_0 conical intersection seam are involved in the intramolecular proton transfer process, $CH_2CH_2 \rightarrow CHCH_3$, whereas others are involved in the $S_0 \rightarrow S_1$ non-radiative transition of C_2H_4.[44]

The energetic components are analyzed in the neighborhood of the conical intersection point of C_2H_4, particularly in the g – h branching plane where the energy degeneracy of states is linearly lifted; the $\vec{g}$ vector is the energy gradient difference between the two states and $\vec{h}$ is the non-adiabatic coupling vector.[45] Fig. S3 of the Supporting Information shows these vectors expressed in terms of internal coordinates at the C_2H_4 conical intersection point analyzed. Displacements along $\vec{g}$ and $\vec{h}$ are dominated by the R_{C-C} distance and the twisting angle α measured with respect to the non piramidalized methylene fragment F_2 at the conical intersection point, respectively. The angle α is defined in Supporting Information Fig. S3 and the molecular fragments in Figure 11f. These coordinates have the values R_{C-C}=1.395 and α=0° at the conical intersection point. The potential energy curves of the S_0 and S_1 states of C_2H_4 along $\vec{g}$ and $\vec{h}$ in the vicinity of the conical intersection point and their kinetic energy contributions are shown in Figures 11a and 11b, respectively. The kinetic energy contributions are discontinuous at the crossing because the ground and excited states change in nature after passing this point along the R_{C-C} and α coordinates. Figures 11c–11f show that the functional group energies and the interaction energy contributions are also discontinuous at the conical intersection. Notice how the intra- and inter-fragment energy decomposition offers a very detailed picture of the reaction mechanism around the intersection point. Figure 11c shows that each fragment's self-energy in the S_0 state (shown as open circles and squares for F1 and F2, respectively) becomes higher than in the S_1 state in a narrow interval around the conical intersection along $\vec{h}$. This is because, following the nature of the states, the self-energies (and also the interaction energies) cross, the $F_1(F_2)$ E_{self} crossings being delayed/

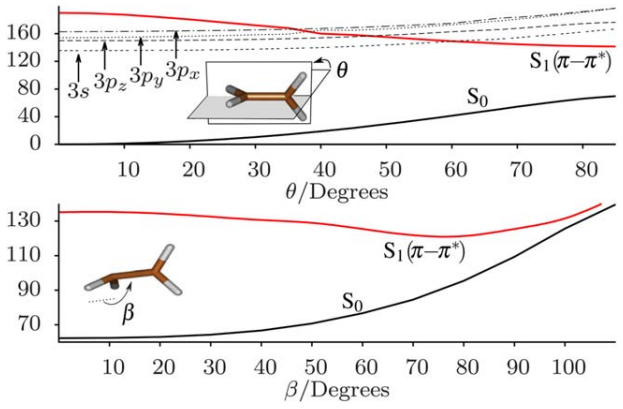

Figure 10. SA-CASSCF potential energies curves along the twist (θ) and pyramidalization (β) coordinates for the valence (S_0, S_1) and Rydberg states ($3s$, $3p_x$, $3p_y$, $3p_z$) of C_2H_4. The energies are given in kcal/mol. [Color figure can be viewed at wileyonlinelibrary.com]

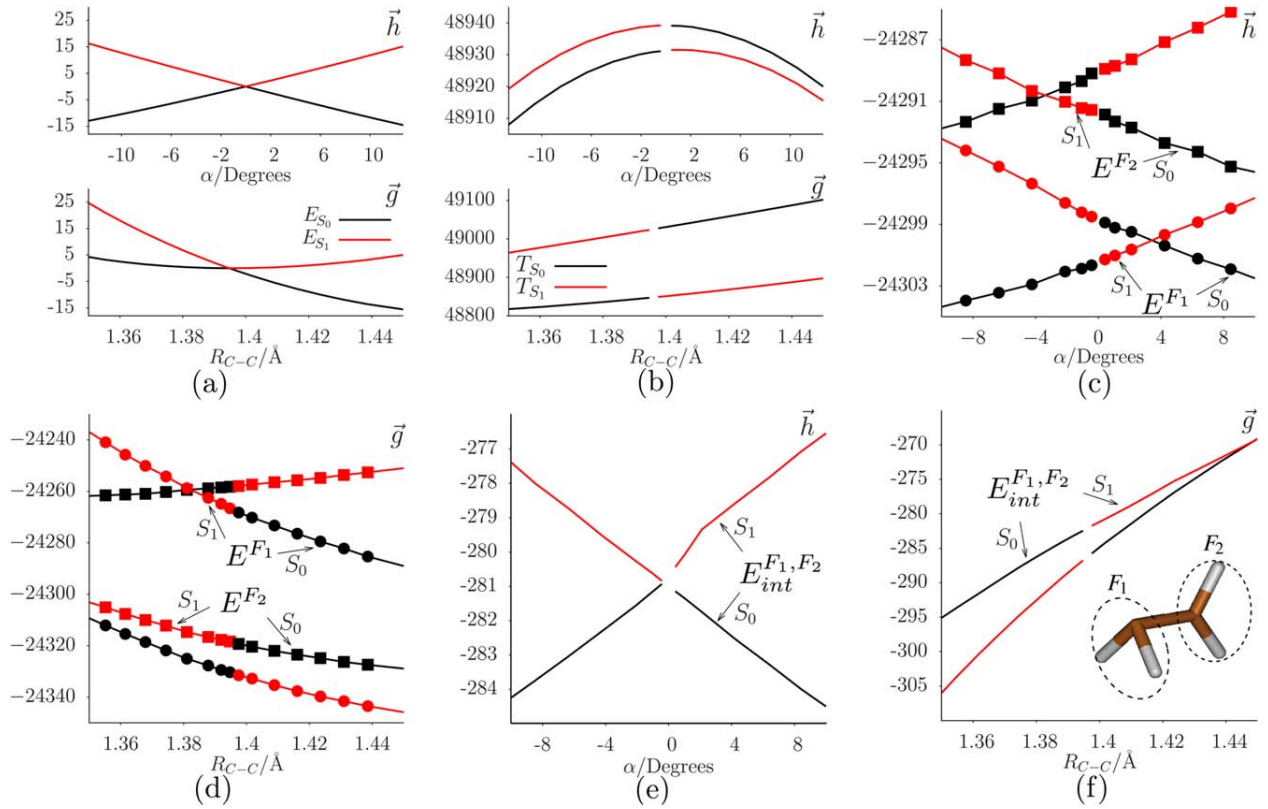

Figure 11. IQA energy contributions for the S_0 and S_1 states of C_2H_4 in the neighborhood of the conical intersection of the twisted-pyramidalized geometry. a) and b): total and kinetic energies; c) and d): self-energies of the methylene fragments along $\vec{h}$ and $\vec{g}$; e) and f) inter-fragment interaction energies along $\vec{h}$ and $\vec{g}$. [Color figure can be viewed at wileyonlinelibrary.com]

advanced with respect to the conical intersection. A few kcal/mol separate the self-energies of the fragments at the intersection, but their mutual E_{int} values cross at almost exactly $\alpha = 0$ degrees. Interestingly, the behavior of E_{self} and E_{int} along $\vec{g}$ is different, and $E_{self}^{F_1}$ develops a crossing while $E_{self}^{F_2}$ and $E_{int}^{F_1,F_2}$ do not. Moreover, along this coordinate the energetic changes are considerably larger than along $\vec{h}$. We think that this type of analyses may be very useful to isolate the relevant molecular regions/fragments involved in more complex excited states landscapes.

Figures 12a and 12b display $\Delta\rho$ isosurfaces for the $S_0 \rightarrow \pi{-}\pi^*$ vertical transition and the twisted pyramidalized conical intersection point of C_2H_4. They show, for example, how the electron density decreases above and below the C—C bond and increases on the top and below CH_2 fragments on the vertical excitation from the ground state equilibrium geometry. Another interesting feature is the gain of electron density by the pyramidalized methylene fragment F1 in the S_1 state when the conical intersection point is reached. In addition, the charge redistribution of the methylene groups is reversed when leaving the conical intersection along $+\vec{g}$ (Figs. 12b and 12c). The same behavior is observed when passing the conical intersection along $\vec{h}$ (Figs. 12b, 12d, and 12e), in line with the atomic contributions to the molecular energy.

We also analyzed the minimum energy conical intersection associated to the H-migration to yield $CHCH_3$. Tables S3 and S4 of the Supporting Information show the IQA self-energy contributions and interatomic components, respectively, of the S_0 y S_1 states at the corresponding conical intersection point; $\Delta\rho$ envelopes at the Franck-Condon and conical intersection regions are shown in Fig. S6 of the Supporting Information. As in the case of the pyramidalization process, the two electronic states change in nature and the IQA energy components of the methylene fragments are discontinuous at the conical intersection. In addition, the $\Delta\rho$ envelopes also show a reverse of charge redistribution along the $\vec{g}$ and $\vec{h}$ vectors. However, there are some differences in the energy components of the incipient proton transfer with respect to the pyramidalization process analyzed before because of the differing topographies of the PES for these processes.

Electron distribution at avoided crossing of states and conical intersections

One question of interest concerns the points of degeneracy or near degeneracy on the PES because of their relevance in the avoided crossing of electronic states and conical intersections. In particular, we explore the question of whether the electron distribution functions—the electron density and the pair density—are the same at a point ***R*** of the nuclear configuration space where the PES of the electronic states *i* and *j* intersect each other,

$$\langle i|H|i\rangle = \langle j|H|j\rangle \; . \tag{7}$$

Introducing the explicit definition of the Hamiltonian, $H = T + V_{nn} + V_{en} + V_{ee}$, one finds that $T^i - T^i = (V_{en}^i + V_{ee}^i) - (V_{en}^i +$

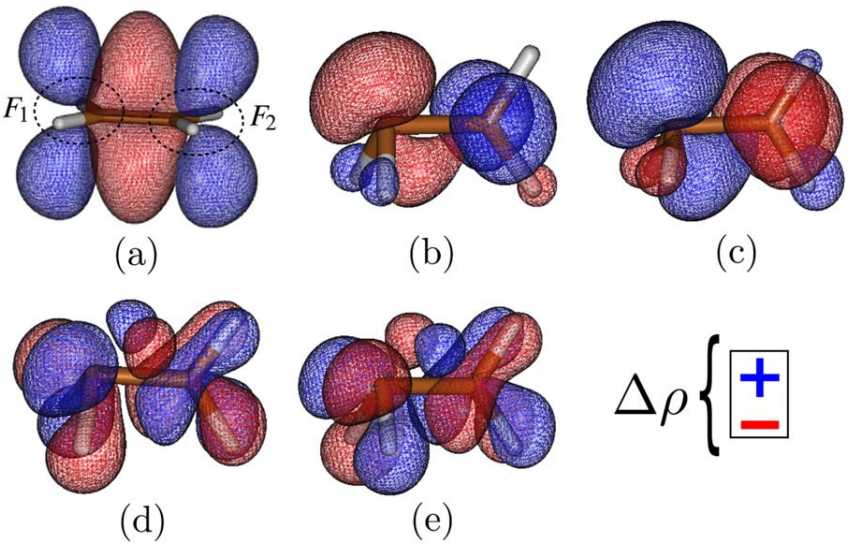

Figure 12. $\Delta\rho=\rho_{S_1}(\vec{r})-\rho_{S_0}(\vec{r})=0.005$ isosurfaces for relevant conformations of C_2H_4. a) Franck-Condon region and b) twisted-pyramidalized minimun energy conical intersection. Starting from this point, displacements along c) $+\vec{g}$ (R_{C-C}=1.39197), d) $+\vec{h}$ (α=0.212) and e) $-\vec{h}$ (α=−0.212). [Color figure can be viewed at wileyonlinelibrary.com]

V^j_{ee}) or $\Delta T=-\Delta V$. In terms of the one and two-electron density matrices, ρ_1 and ρ_2, respectively, of the states *i* and *j*, this result implies[46]:

$$\int_{\vec{r}'\to\vec{r}_1}\frac{1}{2}\nabla^2\left(\rho_1^j(\vec{r}_1,\vec{r}')-\rho_1^i(\vec{r}_1,\vec{r}')\right)d\vec{r}_1 = \int\int\left(\frac{1}{r_{12}}-\sum_a\frac{Z_a}{r_{a1}}\right)\left(\rho_2^i(\vec{r}_1,\vec{r}_2)-\rho_2^j(\vec{r}_1,\vec{r}_2)\right)d\vec{r}_1 d\vec{r}_2 \quad (8)$$

The conditions that the density matrices must comply to satisfy eq. (8) can be analyzed in terms of the virial theorem,[47] which for state *i* is

$$V^i=-2T^i-\sum_k\vec{R}_k\cdot\vec{F}^i_k \quad (9)$$

where $\vec{R}_k$ and $\vec{F}^i_k$ denote the position vector of the *k*-th nucleus and the Hellmann-Feynman force exerted on it, respectively. In the case of diatomic molecules, eq. (9) for state *i* reduces to $V^i=-2T^i-RdE^i/dR$, being *R* the internuclear distance. Except accidentally, this means that the density functions will be either equal, or that they will transform among themselves as components of a multidimensional spatial irreducible representation of the molecular point group. Also in general, this will lead to equal energy components in the IQA approach, eqs. (2) and (3). The second case occurs for a non-stationary point on the PES of near degeneracy, such as an avoided crossing of states, or at a conical intersection, in which the Hellmann-Feynman forces acting on the nuclei are not zero. In these situations, the states *i* and *j* might be associated with different ρ_1 and ρ_2 functions but still satisfying eq. (8). It should be pointed out that although the wave functions used in this work do not fulfill the virial theorem, it is observed that $\Delta T\simeq-\Delta V$ at the degenerate or near degenerate points analyzed.

Consider the $B^1\Sigma_g^+$ and $E,F^1\Sigma_g^+$ states of H_2 which have the same dissociation limit (energy degeneracy) and virtually zero forces at long inter-nuclear separation. The electron densities and pair densities of these states should tend to the same values; such is the observed behavior according to the E^H and $E^{H,H'}_{int}$ discussed in the previous section. The same applies to the He_2 excimers: the 1 and 2 electron probability distributions of the $A^1\Sigma_g^+$ and $C^1\Sigma_g^+$ states are the same at infinite separation. Although we do not show them, hints of their convergence can be seen in Figure 13a.

In the case of LiF, even though the total energy curves of the $1^1\Sigma^+$ and $2^1\Sigma^+$ states do not touch each other because of the non-crossing rule,[45] the energy difference between these states has a minimum value of 1.48 kcal/mol at R_c. Moreover, at this point the forces acting on the nuclei are nearly zero, and ΔT and ΔV are closest with negligible values, as Figure 13b corroborates. Therefore, eqs. (7) and (8) are approximately fulfilled. Interestingly, the results obtained suggest that the electron distributions of the $1^1\Sigma^+$ and $2^1\Sigma^+$ states are similar to each other at R_c: the electron density differences are small, Figure 9b; the Li and F atomic charges are essentially the same; and the atomic and interaction energy curves of the two states intersect within a narrow range around R_c, Figure 8.

The conical intersections of C_2H_4 differ significantly with respect to the avoided crossing of states in LiF. Figure 11a shows that the Hellmann-Feynman force is not defined at the intersection point for either state and renders eq. (9) inapplicable at this molecular geometry. Such mathematical complicacy would not occur if the nature of the electronic states was followed instead. As a consequence, ΔT and ΔV are discontinuous at the crossing point along both $\vec{g}$ and $\vec{h}$ as shown in Figure 13c, although eq. (7) is satisfied. In this case, the charge distributions and the atomic and interaction energies differ between the S_0 and S_1 states, as shown in Figure 11 and

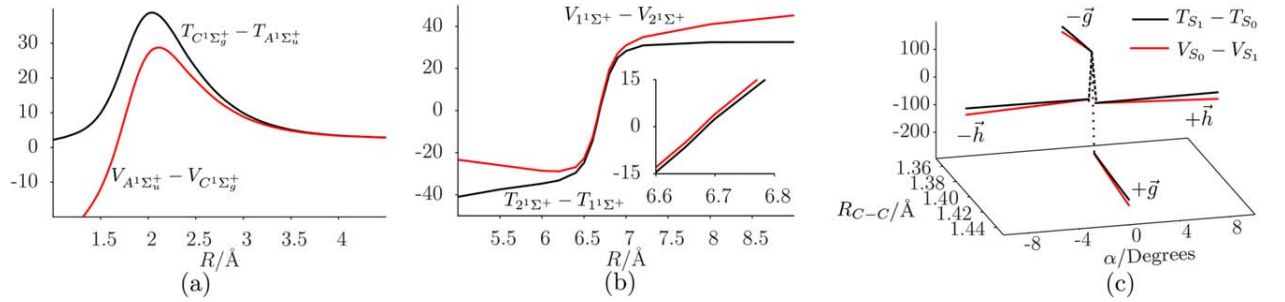

Figure 13. Kinetic ($T_{2^1\Sigma^+} - T_{1^1\Sigma^+}$) and potential ($V_{1^1\Sigma^+} - V_{2^1\Sigma^+}$) energies differences in terms of the internuclear distance for a) the $A^1\Sigma_g^+$ and $C^1\Sigma_g^+$ states of the He excimer, b) the $1^1\Sigma^+$ and $2^1\Sigma^+$ states of LiF, and c) along the $\vec{g}$ and $\vec{h}$ main contributions around the twisted-pyramidalized conical intersection of C_2H_4. [Color figure can be viewed at wileyonlinelibrary.com]

tables S1 and S2 of the Supporting Information. In addition, the electron density differences at the conical intersection, displayed in Figure 12b, agree with a charge transfer of c.a. 0.4 e toward the pyramidalized methylene fragment. These results show that, in this portion of the PES, the photophysics of C_2H_4 involves a conical intersection in which an intramolecular energy transfer from the planar to the pyramidalized methylene takes place, a process accompanied by intramolecular electron transfer to the latter functional group.

Conclusions

Basic reaction mechanisms involving electronic excited states were investigated in terms of atomic or functional group energy contributions using the interacting quantum atoms method. The analysis shows how the energetic variations at the atomic level yield a clear picture of the covalent, ionic, or non-covalent nature of photophysical processes. The atomic entanglement of states was clearly revealed from the atomic and interaction energy contributions along the reaction mechanisms. It was also found that energy transfer can involve a sudden intramolecular charge transfer at avoided crossing of states and conical intersection points. Therefore, this approach provides physical information on a quantitative level that complements the common orbital interpretations of reaction mechanisms in excited states. The ideas explored in this work comprise a new description of photophysical processes that can be extended to the study larger systems.

Appendix

A MRCI-SD/IQA partition

In the implementation of MRCI-SD in Molpro, the configurations generated from the double excitations are contracted, thereby decreasing the number of variational parameters to be optimized but increasing the complexity of the wavefunction[19,20,48,49]:

$$\Psi = \sum_I c^I \,|\, \Psi_I\rangle + \sum_S \sum_a c_a^S |\Psi_S^a\rangle + \sum_{ij} \sum_p \sum_{ab} c_{ab}^{ijp} \,|\, \Psi_{ijp}^{ab}\rangle \qquad \text{(A.1)}$$

where $|\Psi_I\rangle$ and $|\Psi_S^a\rangle$ are CSF that respectively correspond to the basis functions of the internal space and those generated by single excitations. In addition, $|\Psi_{ijp}^{ab}\rangle$ are contracted bi-electronic functions. From $a_P^\dagger$ and a_P is possible to define the *n* particle excitation operators:

$$\hat{E}_{ij} = \sum_\rho a_{i,\rho}^\dagger a_{j,\rho} \qquad \rho \in [\alpha, \beta] \qquad \text{(A.2)}$$

$$\hat{E}_{ij,kl} = \hat{E}_{ij}\hat{E}_{kl} - \delta_{jk}\hat{E}_{ij} \qquad \text{(A.3)}$$

of which the definition of the bi-electronic functions is obtained

$$|\Psi_{ijp}^{ab}\rangle = \frac{1}{2}\left(\hat{E}_{ai,bj} + p\hat{E}_{bi,aj}\right)|\Psi_0\rangle \qquad \text{(A.4)}$$

p can be 1 or −1, depending on the coupling of the electron pair (singlet or triplet). In this equation, $|\Psi_0\rangle$ is the zero order wavefunction, which is expressed as a linear combination of CSFs:

$$|\Psi_0\rangle = \sum_i a_i |\Psi_i^0\rangle \qquad \text{(A.5)}$$

$$|\Psi_i^0\rangle = \sum_j c_{i,j} |\phi_{i,j}\rangle \qquad \text{(A.6)}$$

where $|\phi_{j,i}\rangle$ is an occupation number vector expressed in the determinants basis. The Ψ_{ijp}^{ab} functions are in general not orthonormal

$$\langle \Psi_{ijp}^{ab} | \Psi_{klq}^{cd} \rangle = \frac{1}{2}\delta_{pq}(\delta_{ac}\delta_{bd} + p\delta_{ad}\delta_{bc}) S_{ij,kl}^{(p)} \qquad \text{(A.7)}$$

$$S_{ij,kl}^{(p)} = \langle \Psi_0 | \hat{E}_{ik,jl} + p\hat{E}_{il,jk} | \Psi_0 \rangle \qquad \text{(A.8)}$$

$$N = \delta_{pq} \frac{1 - \delta_{ab} + \sqrt{2}\delta_{ab}}{\sqrt{\langle \Psi_{ijp}^{ab} | \Psi_{ijp}^{ab} \rangle}} \qquad \text{(A.9)}$$

In the latter expression, *N* is the normalization factor of $|\Psi_{ijp}^{ab}\rangle$.

To write an input file for Promolden with the data from a MRCI-SD calculation, the CI vector is required on the determinants basis, as well as the information of the molecular orbitals used to express them; this information is used to obtain the first and second order density matrices and for the evaluation of one and two-electron integrals. The data of the molecular orbitals can be obtained directly from the output file of

Molpro, however, this is not the case of the CI vector. In the output file of a MRCI-SD calculation, the information of the $|\Psi_I\rangle$ and $|\Psi_S^a\rangle$ functions is provided in terms of occupation number vector of each CSF, as well as the respective coefficients. The transformation from CSF to determinants can be accomplished by the genealogical coupling scheme, where the coefficients $c_{i,j}$ [eq. (A.6)] are expressed as products of Clebsch-Gordan coefficients.[50] The occupation number vector on the basis of determinants can be obtained from the CSF ocupation vector through a series of permutations and a format change (orbital occupations 0 or 2 are ignored); the change of basis involves products of c^I or c_a^S with $c_{i,j}$ and subsequent summation over unique determinants.

The process is more elaborate in the case of $|\Psi_{ijp}^{ab}\rangle$. In the output file of a MRCI-SD calculation, the coefficients of the bielectronic functions $|\Psi_{ijp}^{ab}\rangle$ are listed by specifying the associated orbital indexes i, j, a and b and the spin coupling. In this case, it is necessary to first express Ψ_0 in terms of determinants in a analogous way as for $|\Psi_I\rangle$ y $|\Psi_S^a\rangle$; subsequently, applying the excitation operators indicated in eq. (A.4), the bielectronic functions are obtained as a linear combination of determinants; there are eight explicit forms of the operator given in (A.4) (some which are zero) in terms of creation and annihilation operators, which depend on the possible values of i, j, a and *b* and the respective spin coupling (*p* value); then it is necessary to multiply each coefficient of the linear combination by the respective coefficient of $|\Psi_{ijp}^{ab}\rangle$ in the wave function, and subsequently by the normalization factor given in eq. (A.9); according to the values of i, j, a and *b*, there are 8 explicit forms of normalization factor. The final step is a summation over unique determinants.

To carry out the above procedure, a Perl program was written, which consists of a series of routines that allow to obtain the input file for Promolden from the output of a MRCI-SD calculation with Molpro.

Acknowledgment

Prof. Gerald Knizia is acknowledged for his assistance for writting the MRCI-SD wavefunction in terms of determinants.

Keywords: excited states · electron density analysis · interacting quantum atoms · energy transfer · conical intersections

How to cite this article: J. Jara-Cortés, J. Manuel Guevara-Vela, Á. Martín Pendás, J. Hernández-Trujillo. *J. Comput. Chem.* **2017**, *38*, 957–970. DOI: 10.1002/jcc.24769

Additional Supporting Information may be found in the online version of this article.

[1] J. J. W. McDouall, *Computational Quantum Chemistry: Molecular Structure and Properties In Silico*, (RSC Theoretical and Computational Chemistry Series); Royal Society of Chemistry, Cambridge, **2013**.
[2] L. González, D. Escudero, L. Serrano-Andrés, *ChemPhysChem* **2012**, *13*, 28.
[3] M. Klessinger, J. Michl, *Excited States and Photochemistry of Organic Molecules*; VCH Publishers, Inc., New York, **1995**.
[4] A. H. Zewail, *J. Phys. Chem. A* **2000**, *104*, 5660.
[5] W. Domcke, D. R. Yarkony, H. Köppel, *Conical Intersections: Theory, Computation and Experiment;* World Scientific Publishing Company, Toh Tuck Link, Singapore, **2011**.
[6] R. F. W. Bader, *Atoms in Molecules: A Quantum Theory;* Clarendon Press: Oxford, **1990**.
[7] C. F. Matta, R. J. Boyd, *The Quantum Theory of Atoms in Molecules: From Solid State to DNA and Drug Design;* Wiley, Darmstadt, **2007**.
[8] M. A. Blanco, A. Martín Pendás, E. Francisco, *J. Chem. Theory Comput.* **2005**, *1*, 1096.
[9] L. Gutiérrez-Arzaluz, T. Rocha-Rinza, F. Cortés-Guzmán, *Comput. Theor. Chem.* **2015**, *1053*, 214.
[10] L. Gutierrez-Arzaluz, F. Cortes-Guzman, T. Rocha-Rinza, J. Peon, *Phys. Chem. Chem. Phys.* **2015**, *17*, 31608.
[11] D. Ferro-Costas, A. Martín Pendás, L. Gonzalez, R. A. Mosquera, *Phys. Chem. Chem. Phys.* **2014**, *16*, 9249.
[12] R. Chávez-Calvillo, J. Hernández-Trujillo, *J. Phys. Chem. A* **2011**, *115*, 13036.
[13] J. Jara-Cortés, T. Rocha-Rinza, J. Hernández-Trujillo, *Comput. Theor. Chem.* **2015**, *1053*, 220.
[14] F. Feixas, E. Matito, J. Poater, M. Sola, *Chem. Soc. Rev.* **2015**, *44*, 6434.
[15] L. Bertini, P. Fantucci, L. De Gioia, *Organometallics* **2011**, *30*, 487.
[16] V. Tognetti, L. Joubert, *Chem. Phys. Lett.* **2013**, *557*, 150.
[17] M. Estevez-Fregoso, J. Hernandez-Trujillo, *Phys. Chem. Chem. Phys.* **2016**, *18*, 11792.
[18] H. J. Werner, W. Meyer, *J. Chem. Phys.* **1980**, *73*, 2342.
[19] H. J. Werner, P. J. Knowles, *J. Chem. Phys.* **1988**, *89*, 5803.
[20] P. J. Knowles, H. J. Werner, *Theor. Chim. Acta* **1992**, *84*, 95.
[21] D. E. Woon, T. H. Dunning, *J. Chem. Phys.* **1994**, *100*, 2975.
[22] H. J. Werner, P. J. Knowles, G. Knizia, F. R. Manby, M. Schû¥tz, P. Celani, T. Korona, R. Lindh, A. Mitrushenkov, G. Rauhut, K. R. Shamasundar, T. B. Adler, R. D. Amos, A. Bernhardsson, A. Berning, D. L. Cooper, M. J. O. Deegan, A. J. Dobbyn, F. Eckert, E. Goll, C. Hampel, A. Hesselmann, G. Hetzer, T. Hrenar, G. Jansen, C. Köppl, Y. Liu, A. W. Lloyd, R. A. Mata, A. J. May, S. J. McNicholas, W. Meyer, M. E. Mura, A. Nicklass, D. P. O'Neill, P. Palmieri, K. Pflüger, R. Pitzer, M. Reiher, T. Shiozaki, H. Stoll, A. J. Stone, R. Tarroni, T. Thorsteinsson, M. Wang, A. Wolf, *MOLPRO (versión 2010.26): A package of Ab Initio Programs*; **2010**. Available at: www.molpro.net
[23] H. Lischka, R. Shepard, I. Shavitt, R. M. Pitzer, M. Dallos, T. Müller, P. G. Szalay, F. B. Brown, R. Ahlrichs, H. J. Böhm, A. Chang, D. C. Comeau, R. Gdanitz, H. Dachsel, C. Ehrhardt, M. Ernzerhof, P. Höchtl, S. Irle, G. Kedziora, T. Kovar, V. Parasuk, M. J. M. Pepper, P. Scharf, H. Schiffer, M. Schindler, M. Schüler, M. Seth, E. A. Stahlberg, J.-G. Zhao, S. Yabushita, Z. Zhang, M. Barbatti, S. Matsika, M. Schuurmann, D. R. Yarkony, S. R. Brozell, E. V. Beck, J.-P. Blaudeau, M. Ruckenbauer, B. Sellner, F. Plasser, J. J. Szymczak, *COLUMBUS, an Ab Initio Electronic Structure Program*;2015. Available at: https://www.univie.ac.at/columbus/
[24] E. R. Davidson, *J. Chem. Phys.* **1960**, *33*, 1577.
[25] G. Herzberg, *Molecular Spectra and Molecular Structure. I. Spectra of Diatomic Molecules*; Van Nostrand Reinhold: Princeton, **1950**.
[26] J. Wang, J. M. Mercero, I. Silanes, J. M. Ugalde, *EPL (Europhysics Letters)* **2006**, *76*, 808.
[27] T. Sharp, *At. Data Nucl. Data Tables* **1970**, *2*, 119.
[28] C. W. Lee, Y. Gim, T. H. Choi, *Bull. Korean Chem. Soc.* **2013**, *34*, 1771.
[29] A. M. Pendás, E. Francisco, M. A. Blanco, *J. Phys. Chem. A* **2006**, *110*, 12864.
[30] A. Martín Pendás, E. Francisco, M. A. Blanco, *Chem. Phys. Lett.* **2007**, *437*, 0009.
[31] M. Olivucci, *Computational Photochemistry, Theoretical and Computational Chemistry;* Elsevier Science, Amsterdam, **2005**.
[32] A. Martín Pendás, M. A. Blanco, A. Costales, P. Sánchez Mori, V. Luaña, *Phys. Rev. Lett.* **1999**, *83*, 1930.
[33] S. Yang, A. M. Ellis, *Chem. Soc. Rev.* **2013**, *42*, 472. URLhttps://doi.org/10.1039/C2CS35277J.
[34] S. E. Huber, A. Mauracher, *J. Phys. Chem. A* **2014**, *118*, 6642. URLhttps://doi.org/10.1021/jp503643r.
[35] F. Rioux, *J. Chem. Educ.* **2007**, *84*, 358.
[36] N. Shenkuan, *J. Chem. Educ.* **1992**, *69*, 800.
[37] A. Martín Pendás, M. A. Blanco, E. Francisco, *J. Comput. Chem.* **2009**, *30*, 98.

[38] D. R. Yarkony, H. F. Schaefer, *J. Chem. Phys.* **1974**, *61*, 4921.
[39] M. Pavanello, M. Cafiero, S. Bubin, L. Adamowicz, *Int. J. Quantum Chem.* **2008**, *108*, 2291.
[40] J. Eloranta, V. A. Apkarian, *J. Chem. Phys.* **2001**, *115*, 752.
[41] J. Hernández-Trujillo, R. F. W. Bader, *J. Phys. Chem. A* **2000**, *104*, 1779.
[42] M. Rodríguez-Mayorga, E. Ramos-Cordoba, P. Salvador, M. Solà, E. Matito, *Mol. Phys.* **2016**, *114*, 1345.
[43] M. Barbatti, J. Paier, H. Lischka, *J. Chem. Phys.* **2004**, *121*, 11614.
[44] M. Ben-Nun, J. Quenneville, T. J. Martínez, *J. Phys. Chem. A* **2000**, *104*, 5161.
[45] D. R. Yarkony, *J. Phys. Chem. A* **2001**, *105*, 6277.
[46] R. McWeeny, *Rev. Mod. Phys.* **1960**, *32*, 335.
[47] C. Cohen-Tannoudji, B. Diu, F. Laloe, *Quantum Mechanics*, Vol. *2*; Wiley, New York, **1991**.
[48] H. J. Werner, E. A. Reinsch, *J. Chem. Phys.* **1982**, *76*, 3144.
[49] H.-J. Werner, In *Advances in Chemical Physics*; Wiley, Chichester, **2007**; pp. 1–62.
[50] T. Helgaker, P. Jorgensen, J. Olsen, *Molecular Electronic-Structure Theory*; Wiley, West Sussex, **2014**.

Received: 28 December 2016
Revised: 25 January 2017
Accepted: 27 January 2017
Published online on 7 March 2017

Theor Chem Acc (2017) 136:57
DOI 10.1007/s00214-017-2084-0

REGULAR ARTICLE

Performance of the RI and RIJCOSX approximations in the topological analysis of the electron density

José Manuel Guevara-Vela[1] · **Tomás Rocha-Rinza**[2] · **Ángel Martín Pendás**[1]

Received: 11 January 2017 / Accepted: 29 March 2017
© Springer-Verlag Berlin Heidelberg 2017

Abstract The performance of the Møller–Plesset (MP2) method in its resolution of the identity (RI-MP2), and the chain of spheres exchange (RIJCOSX-MP2) variants within the Quantum Theory of Atoms in Molecules (QTAIM) wavefunction analyses is examined. We have obtained QTAIM descriptors at bond critical points for a series of small molecules and water clusters of different sizes. We also considered integrated properties, like QTAIM atomic charges or localization and delocalization indices. The performance of RI methods with respect to the plain MP2 benchmark results is excellent, with mean deviations for all the properties considered below 0.15%. However, in systems where electron delocalization plays a more important role, we found differences up to 5% (e.g. C_6H_6) from a suitable reference. The account of RIJCOSX-HF results shows that the RIJCOSX approximation works better when electron correlation is included. Finally, a topological analysis of the electron density on the endofullerene complex $H_2O@C_{70}$ is reported. Overall, herein we suggest the possibility to carry out the QTAIM topological analysis using correlated wavefunctions in large molecules and molecular clusters, thereby extending the applicability of this important methodology.

Keywords QTAIM · Fullerene · Endofullerene · Water clusters

1 Introduction

The Quantum Theory of Atoms in Molecules (QTAIM) [1] provides a quantum mechanical route to partition exhaustively the real space of a molecule or molecular cluster into disjoint regions through the analysis of the topology of the electron density distribution $\varrho(\mathbf{r})$, which is the average value of a Dirac observable, i.e. $\varrho(\mathbf{r}) = \left\langle \sum_{i=1}^{N} \delta(\mathbf{r} - \mathbf{r}_i) \right\rangle$ [2, 3], wherein N is the number of electrons in the system. In this way, the expectation value of any quantum mechanical operator $\widehat{A}$ may be written as a one-basin (if $\widehat{A}$ is monoelectronic) or two-basin (if $\widehat{A}$ is bielectronic) sum of contributions, which are usually called atomic or interaction properties, respectively. By using techniques borrowed from the theory of dynamical systems, the topology induced by the electron density scalar field is used to identify and classify critical points (CP) of $\varrho(\mathbf{r})$.

The topological features of $\varrho(\mathbf{r})$ are endorsed with different chemical and physical meanings that recover fundamental concepts of molecular structure such as atoms, bonds and functional groups [1]. QTAIM-based chemical bonding indices are of wide use in computational chemistry, and correlations between these indicators and all kinds of chemical properties are popular among the QSAR communities [4]. Several generalizations introducing density matrices of higher order in the theory, like the interacting quantum atoms energy partition [5] or the multicentre

Published as part of the special collection of articles derived from the 10th Congress on Electronic Structure: Principles and Applications (ESPA-2016).

✉ José Manuel Guevara-Vela
jmguevarav@gmail.com

✉ Ángel Martín Pendás
angel@fluor.quimica.uniovi.es

[1] Department of Physical and Analytical Chemistry, University of Oviedo, 33006 Oviedo, Spain

[2] Institute of Chemistry, National Autonomous University of Mexico, Circuito Exterior, Ciudad Universitaria, Delegación Coyoacán, C.P. 04510, Mexico City, Mexico

Published online: 12 April 2017

extension of several descriptors [6], have provided sound physical roots for chemical concepts (e.g. aromaticity) that were originally outside the scope of the QTAIM.

Indeed, as an important tool in theoretical chemistry, the QTAIM has been used to study such diverse range of phenomena like metal–ligand bonding [7–10], molecular recognition [11], intramolecular [12–15] and intermolecular [16, 17] hydrogen bonding, halogen bonding [18] or chemical shifts of agostic protons [19]. Furthermore, the availability of increasingly accurate experimental charge densities from X-ray diffraction experiments [7, 20] has permitted the merging of QTAIM and crystallography [21].

The reliability of the QTAIM theoretical analysis depends heavily on the quality of the input $\varrho(\mathbf{r})$ which can be obtained by either experiment or quantum chemical calculations using density functional theory (DFT), the Hartree–Fock approximation (HF) or post-HF wavefunction methods. Despite the widespread use of density functional theory in the study of large systems and the importance of the dispersion corrections introduced in DFT hybrid functionals, these rectifications of the energy are not usually reflected in the resulting electron density. On the other hand, it is not viable to use the most sophisticated correlated methods for large molecular clusters and molecules.

In this regard, second-order perturbation theory, as implemented in the Møller–Plesset (MP2) methodology [22], has become a *de facto* standard in the study of weakly bound complexes because it is the simplest size-consistent, correlated, wavefunction-based method which yields reasonable energetics and a qualitatively correct description of long-range interactions. Unfortunately, its $\mathcal{O}(N^5)$ computational cost makes it unsuitable for large systems. An amelioration to this scaling behaviour was reported by Vahtras, Almlølf and Feyereisen [23], who proposed to transform four centre repulsion integrals into three centre ones by means of an auxiliary basis set. This procedure is known as the resolution of the identity (RI) approximation that was further improved by Neese [24] in what it is called the split-RI-J method. Similar ideas have also been used to speed up the computation of exchange integrals. For instance, in the "chain of spheres" procedure [25] the intent is to efficiently compute the exchange-type matrix elements. This is done by considering that two basis functions overlap only with their closest neighbours, and thus a small "chain of shells", containing only those functions which contribute in a non-negligible way to the matrix is built. A combination of these methodologies known as the RIJCOSX-MP2 procedure shows a particularly low scaling exponent and has allowed the study of much larger molecules than those usually addressed with the MP2 approximation. Several tests [26–28] have demonstrated the overall excellent accuracy of these techniques, coupled to speed-up ratios that may reach values up to 300 in favourable cases [24]. For this reason, the RI, split-RI-J and RIJCOSX variants of electronic structure methods have become quite attractive, and they have found applications in organometallics [29, 30], fullerene science [31, 32], bioinorganic chemistry [33, 34] and biochemistry [35].

Although the global accuracy for energy calculation of these methods has been proved, no systematic analysis of the performance of RI-MP2 or RIJCOSX-MP2 density-based descriptors beyond some isolated calculations [36] has been carried out. This analysis is justified because the sets of equations defining the electronic structure methods MP2, RI-MP2, RIJCOSX-MP2 are different and therefore the Lagrangian technique for the construction of relaxed densities that comply with the Hellman–Feynman theorem may lead to different results. We have thus computed a simple set of local QTAIM indicators, including $\varrho(\mathbf{r})$, $\nabla^2\varrho(\mathbf{r})$ and the positive definite kinetic energy density $G(\mathbf{r})$ at bond critical points (BCPs), together with some representative basin-integrated quantities like atomic charges, volumes, electronic dipole moments, and the localization (LI) and delocalization (DI) indices between quantum atoms under the Müller approximation [37], which provides a reasonable approximation to the 2-RDM in weakly correlated systems [38]. Both the set of properties and the computed model molecules that have been chosen in this work are representative of standard QTAIM calculations [10, 39, 40]. Overall, the RIJCOSX procedure gives very good results for the topological and integrated properties of the charge distribution, especially when electron correlation is included, that is, when this approach is most useful.

2 Computational details

Small water clusters $(H_2O)_n$, $n = 2$–10, as well as CH_3-CH_3, $CH_2=CH_2$, C_6H_6, H_2O and LiF, were used as model systems. These molecules and molecular clusters are particularly well suited for our purposes because we may simultaneously gauge the behaviour of the approximations on strong covalent bonds and on intermolecular interactions which are well represented at the MP2 level. The structures of the water clusters were taken from the work of Segarra et al. [41]. In the rest of the systems, geometries were optimized with the CCSD/aug-cc-pVDZ [42] approximation, as implemented in the Gaussian-09 [43] suite of programs. The geometry optimization of the $H_2O@C_{70}$ complex (Fig. 1) was carried out with the PBE/Def2-TZVP [44] method. Reference wavefunctions at the HF/cc-pVTZ and MP2/cc-pVTZ levels of theory were obtained with the Gaussian-09 package as well. Calculations within the RI and RIJCOSX approximations were performed with the program Orca [45], using the corresponding auxiliary

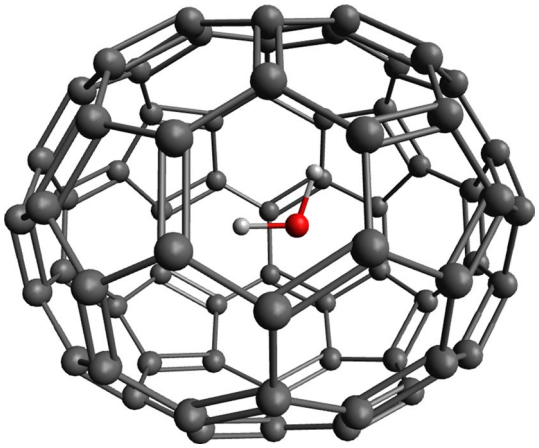

Fig. 1 The $H_2O@C_{70}$ complex

basis sets, cc-pVTZ/C and cc-pVTZ/J. Finally, all the QTAIM properties were computed using the AIMAll [46] code.

3 Results

Since RI-based total energies and optimized geometries have been repeatedly contrasted against full MP2 calculations in the literature [24, 27, 28], we will concentrate here only on QTAIM-based indicators. Table 1 shows the average deviations with respect to reference values of some QTAIM descriptors for the considered water clusters. Note the excellent agreement of the approximated descriptors. Nevertheless, a simple visual inspection shows that quantities based on $\varrho(\mathbf{r})$ perform slightly better than those that depend on its derivatives, like the Laplacian or the kinetic energy density. This is in agreement with the idea that subtle changes in the density can be better appreciated through its derivatives, e.g. the observation of the shell structure of atoms by means of the analysis of $\nabla^2\varrho(\mathbf{r})$. On the whole, however, errors are larger for the integrated properties of atoms in molecules, and specially pronounced for the atomic dipole moments. In every case, nonetheless, errors stay below 1%.

As we compare the RIJCOSX variants of the HF and MP2 methods, we note that the chain of spheres approximation performs substantially better with the latter level of theory. This occurs since mean field densities are considerably more delocalized than correlated ones. Any real space truncation scheme should therefore perform slightly better as correlation is included. Table 2 illustrates the evolution of QTAIM charges upon the inclusion of correlation and the consideration of the RI approximations. The data indicate that the sensitivity of these descriptors to the level of calculation decreases as polarity increases. Deviations are smaller than 0.25% in H_2O and LiF but much larger in ethane, in which the inclusion of electron correlation changes the sign of the net charge of the carbon atoms. Nevertheless, the RI approximations reproduce very clearly the signs according to the original reference used. Our previous warning still applies here: for benzene at the HF level, where electron delocalization is enhanced, the RIJCOSX-HF carbon charge differs by as much as 5% from the reference HF value.

As a proof of concept, we used the RIJCOSX-MP2 method to obtain the electron density of the endohedral complex of a water molecule within the C_{70} fullerene, as shown in Fig. 1. We note that the structure of the water molecule hardly changes when it is introduced in the C_{70} cavity, the oxygen–hydrogen distance changes from 0.977 to 0.978 Å and the hydrogen–oxygen–hydrogen angle moves from 101.8° to 101.9°. Likewise, the corresponding topological analysis of $\varrho(\mathbf{r})$ reveals that there is virtually no charge transfer (0.002 a.u., below the precision

Table 1 Average deviations (expressed as percentages) of some QTAIM descriptors in the whole set of studied water clusters with respect to the appropriate reference

Method	ϱ	$\nabla^2\varrho$	G	LI	DI	Vol (Ω)	μ(Ω)
RIJCOSX-HF	0.06	0.11	0.07	0.02	0.08	0.20	0.76
RI-MP2	0.03	0.06	0.02	0.01	0.03	0.11	0.04
RIJCOSX-MP2	0.03	0.06	0.05	0.00	0.04	0.18	0.55

Table 2 QTAIM charges for selected atoms in isolated molecules

Method	$O@H_2O$	F@LiF	$C@C_2H_6$	$C@C_2H_4$	$C@C_6H_6$
HF	−1.24122	−0.94475	0.13363	−0.02775	−0.01261
RIJCOSX−HF	−1.24102	−0.94472	0.13735	−0.02749	−0.01198
MP2	−1.17925	−0.93352	−0.01120	−0.08681	−0.04643
RI−MP2	−1.17933	−0.93352	−0.01140	−0.08701	−0.04648
RIJCOSX−MP2	−1.17897	−0.93351	−0.00844	−0.08668	−0.04605

Atomic units are used throughout

of the methodology used) between the C_{70} host fullerene and the water molecule. The QTAIM charges of neither the water molecule nor the carbon cage change appreciably on account of the inclusion of H_2O within C_{70}. The charge of the oxygen atom becomes slightly more negative within the fullerene, −1.20 as compared with −1.17 a.u., the extra electrons being extracted from both hydrogen atoms. Each hydrogen loses 0.015 electrons approximately, with their charge changing from 0.586 a.u. in the isolated molecule to 0.601 a.u. within the complex. This small alteration of the electron density within the water molecule is a result of its interaction with the C_{70} cage.

The few bond paths established between the atoms in the water molecule and the carbons in the fullerene are shown in Fig. 2. Table 3 summarizes the value of some QTAIM descriptors for these interactions. We observe, as reflected by the DI and ϱ values, that all interactions are very weak, albeit the H73···C14 non-covalent bond is slightly stronger. Additionally, $\nabla^2\varrho$ is small and positive for all the intermolecular bond critical points in the system $H_2O@C_{70}$. This condition allows us to characterize these contacts as closed-shell interactions. This is also echoed in the total energy density, $H(\mathbf{r})$, the difference between the potential energy density $V(\mathbf{r})$ and the kinetic energy density $G(\mathbf{r})$ at BCPs whose values if negative signal covalency [47]. $H(\mathbf{r})$ is positive for all the interactions between H_2O and C_{70}. Moreover, the relationship $|V| / G$ is lower than one in all cases, which is another indicator of closed-shell interactions [48].

A surprising result is that all three oxygen–carbon interactions are very similar. Indeed, the most chemically intuitive idea regarding oxygen in the water molecule is that it mostly interacts by means of its two lone pairs. In our case, the existence of three almost identical bond paths is in disagreement with this simple expectation. Additionally, if the lone pairs were indeed participating in the host–guest interaction, we should observe a change in the atomic charge of the involved atoms with respect to that of the rest of the guest carbons, and this is not the case. The charges for C7, C37 and C44 are −0.005, 0.002 and 0.001, respectively, in line with the values corresponding to the rest of atoms. Another hint about the nature of the interactions is the bond ellipticity of the carbon–carbon contacts; being around 0.15 it is midway between a typical σ bond (0.00) and an aromatic C–C bond, such as in benzene with an ellipticity value equal to 0.23. Thus, the host–guest interaction for the case of $H_2O@C_{70}$ is mostly dispersive in nature.

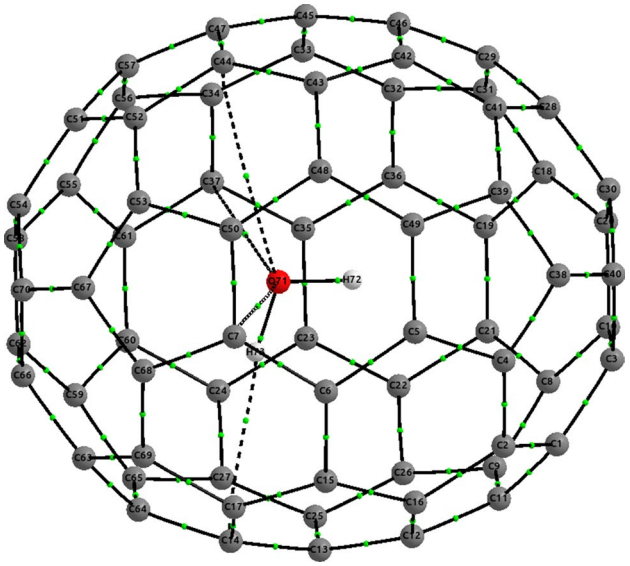

Fig. 2 Bond paths in the (H_2O) at C_{70} complex

4 Concluding remarks

We have examined the performance of resolution of the identity techniques and their generalization, as implemented in the MP2 methodology, in the computation of standard descriptors of bonding and stability under the formalism of QTAIM. We determined that the errors introduced by the RI techniques with respect to standard MP2 computations are negligible. Results on a set of model systems reproduce the reference MP2 data to a very high accuracy. QTAIM descriptors at bond critical points show average deviations below 0.15%, with peaks around 0.5%. There is a close agreement for integrated properties of the electron density throughout the QTAIM basins. We also offered an explanation for some of the largest deviations observed for the RI variants as compared with the reference values. In order to illustrate the type of systems which can be studied with QTAIM in conjunction with the RIJCOSX approximations, we have used this methodology to examine the topology of $\varrho(\mathbf{r})$ within the $H_2O@C_{70}$ complex and

Table 3 QTAIM descriptors at the bond critical points between atoms in the water molecule and the C_{70} cage

Pair	ϱ	DI	$\nabla^2\varrho$	V	G	H	$\lvert V\rvert / G$
O71–C7	0.0049	0.0108	0.0172	−0.0031	0.0037	0.0006	0.84
O71–C37	0.0053	0.0113	0.0198	−0.0035	0.0042	0.0007	0.83
O71–C44	0.0047	0.0097	0.0176	−0.0031	0.0037	0.0006	0.83
H73–C14	0.0097	0.0137	0.0308	−0.0064	0.0071	0.0006	0.91

The values are given in a.u

concluded that the interactions between the water molecule and the C_{70} cage are mostly closed-shell in nature. Overall, we show that QTAIM properties computed from wavefunctions obtained using the RI- and RIJCOSX-MP2 approximations are reliable, thereby encouraging the study of large electronic systems and the applicability of this important method of wavefunction analysis.

Acknowledgements The authors gratefully acknowledge DGTIC/UNAM (project LANCAD-UNAM-DGTIC-250) for computer time, the Spanish government (grants CTQ-2015-65790-P, FC-15-GRUPIN14-049) and J.M.G.V. is also grateful to CONACyT/Mexico for financial support (grant 381483).

References

1. Bader RFW (1994) Atoms in molecules: a quantum theory (International series of monographs on chemistry). Oxford University Press, New York
2. Matta RJ, Boyd Chérif F (2007) The quantum theory of atoms in molecules: from solid state to DNA and drug design. Wiley-VCH, Weinheim
3. Helgaker T, Jørgensen P, Olsen J (2004) Molecular electronic structure theory. Wiley, Sussex
4. Platts JA, Butina D, Abraham MH, Hersey A (1999) J Chem Inf Comput Sci 39:835–845
5. Blanco MA, Martín Pendás A, Francisco E (2005) J Chem Theory Comput 1:1096–1109
6. Bultinck P, Ponec R, Van Damme S (2005) J Phys Org Chem 18:706–718
7. Farrugia LJ, Evans C, Tegel M (2006) J Phys Chem B 110:7952–7961 PMID: 16789785
8. Corral I, Mó O, Yáñez M (2003) J Phys Chem A 107:1370–1376
9. Cukrowski I, de Lange JH, Mitoraj M (2014) J Phys Chem A 118:623–637
10. Cortés-Guzmán F, Bader RF (2005) Coord Chem Rev 249:633–662
11. Galindo-Murillo R, Ruíz-Azuara L, Moreno-Esparza R, Cortés-Guzmán F (2012) Phys Chem Chem Phys 14:15539
12. Lapointe SM, Farrag S, Bohórquez HJ, Boyd RJ (2009) J Phys Chem B 113:10957–10964
13. Fuster F, Grabowski SJ (2011) J Phys Chem A 115:10078–10086
14. Guevara-Vela JM, Romero-Montalvo E, Costales A, Pendas AM, Rocha-Rinza T (2016) Phys Chem Chem Phys 18:26383–26390
15. Romero-Montalvo E, Guevara-Vela JM, Costales A, Pendas AM, Rocha-Rinza T (2016) Phys Chem Chem Phys 19:97–107
16. Guevara-Vela JM, Chávez-Calvillo R, García-Revilla M, Hernández-Trujillo J, Christiansen O, Francisco E, Martín Pendás A, Rocha-Rinza T (2013) CEJ 19:14304–14315
17. Guevara-Vela JM, Romero-Montalvo E, Mora-Gómez VA, Chávez-Calvillo R, García-Revilla M, Francisco E, Pendás Á Martín, Rocha-Rinza T (2016) Phys Chem Chem Phys 18:19557–19566
18. Grabowski SJ (2012) J Phys Chem A 116:1838–1845
19. Barquera-Lozada JE, Obenhuber A, Hauf C, Scherer W (2013) J Phys Chem A 117:4304–4315
20. Terlan B, Akselrud L, Baranov AI, Borrmann H, Grin Y (2013) Z Anorg Allg Chem 639:2065–2070
21. Gatti C (2005) Zeitschrift fur Kristallographie 220:399–457
22. Møller C, Plesset MS (1934) Phys Rev 46:618–622
23. Vahtras O, Almløf J, Feyereisen M (1993) Chem Phys Lett 213:514–518
24. Neese F (2003) J Comput Chem 24:1740–1747
25. Neese F, Wennmohs F, Hansen A, Becker U (2009) Chem Phys 356:98–109
26. Weigend F, KoÌĹhn A, HaÌĹttig C (2002) J Chem Phys 116:3175
27. Kossmann S, Neese F (2009) Chem Phys Lett 481:240–243
28. Kossmann S, Neese F (2010) J Chem Theory Comput 6:2325–2338
29. Zabula A, Rogachev A, Guzei I, West R (2013) Organomet 32:3760–3768
30. Romero T, Orenes RA, Espinosa A, Tárraga A, Molina P (2011) IO 50:8214–8224
31. Popov A, Schiemenz S (2011) J Phys Chem C 115:15257–15265
32. Kuvychko IV, Shustova NB, Avdoshenko SM, Popov AA, Strauss SH, Boltalina OV (2011) Chem Eur J 17:8799–8802
33. Ames W, Pantazis DA, Krewald V, Cox N, Messinger J, Lubitz W, Neese F (2011) J Am Chem Soc 133:19743–19757
34. Ye S, Neese F (2011) Proc Nat Acad Sci 108:1228–1233
35. Riplinger C, Neese F (2011) ChemPhysChem 12:3192–203
36. Yamasaki H, Nakamura H (2012) Chem Phys Lett 536:129–135
37. Müller A (1984) Phys Lett A 105:446
38. García-Revilla M, Francisco E, Costales A, Martín Pendás A (2012) J Phys Chem A 116:1237–1250
39. Rocha-Rinza T, Hernández-Trujillo J (2006) Chem Phys Lett 422:36–40
40. Matta CF (2009) J Comput Chem 31:1297–1311
41. Segarra-Martí J, Merchán M, Roca-Sanjuán D (2012) J Chem Phys 136:244306
42. Dunning TH (1007) J Chem Phys 1989:90
43. Frisch MJ, Trucks GW, Schlegel HB, Scuseria GE, Robb MA, Cheeseman JR, Scalmani G, Barone V, Mennucci B, Petersson GA, Nakatsuji H, Caricato M, Li X, Hratchian HP, Izmaylov AF, Bloino J, Zheng G, Sonnenberg JL, Hada M, Ehara M, Toyota K, Fukuda R, Hasegawa J, Ishida M, Nakajima T, Honda Y, Kitao O, Nakai H, Vreven T, Montgomery JA, Peralta JE Jr, Ogliaro F, Bearpark M, Heyd JJ, Brothers E, Kudin KN, Staroverov VN, Kobayashi R, Normand J, Raghavachari K, Rendell A, Burant JC, Iyengar SS, Tomasi J, Cossi M, Rega N, Millam JM, Klene M, Knox JE, Cross JB, Bakken V, Adamo C, Jaramillo J, Gomperts R, Stratmann RE, Yazyev O, Austin AJ, Cammi R, Pomelli C, Ochterski JW, Martin RL, Morokuma K, Zakrzewski VG, Voth GA, Salvador P, Dannenberg JJ, Dapprich S, Daniels AD, Farkas Ö, Foresman JB, Ortiz JV, Cioslowski J, Fox DJ (2009) Gaussian 09 Revision C.1. Gaussian Inc, Wallingford
44. Weigend F, Ahlrichs R (2005) Phys Chem Chem Phys 7:3297–3305
45. Neese F (2012) WIREs Comput Mol Sci 2:73–78
46. Keith TA (2012) AIMAll (Version 12.06.03), TK Gristmill Software, Overland Park KS, USA, 2012 (aim.tkgristmill.com)
47. Cremer D, Kraka E (1984) Angewandte Chemie Int Ed Engl 23:627–628
48. Espinosa E, Alkorta I, Elguero J, Molins E (2002) J Chem Phys 117:5529–5542

Dalton Transactions

PAPER

Check for updates

Cite this: *Dalton Trans.*, 2017, **46**, 12456

π-Backbonding and non-covalent interactions in the JohnPhos and polyfluorothiolate complexes of gold(I)†

Guillermo Moreno-Alcántar,*[a] Kristopher Hess,‡[a] José Manuel Guevara-Vela,‡[b] Tomás Rocha-Rinza,[c] Ángel Martín Pendás,[b] Marcos Flores-Álamo[a] and Hugo Torrens*[a]

Received 16th March 2017,
Accepted 22nd June 2017

DOI: 10.1039/c7dt00961e

rsc.li/dalton

We studied the influence of changing the degree of fluorination in eight new gold(I) derivatives containing both JohnPhos phosphine and polyfluorinated thiolates: [Au(SR_F)(JPhos)], JPhos = P(C_6H_4-C_6H_5)(*t*-But)$_2$ and R_F = C_6F_5 (**1**), C_6HF_4 (**2**), $C_6H_3F_2$-3,5 (**3**), $C_6H_3F_2$-2,4 (**4**), C_6H_4F-2 (**5**), C_6H_4F-3 (**6**), C_6H_4F-4 (**7**) and CF_3 (**8**). We determined the molecular and crystal structures of all new compounds by single crystal X-ray diffraction. Later, we characterised the chemical bonding scenario with quantum chemical topology tools, specifically the Quantum Theory of Atoms in Molecules (QTAIM) and the analysis of the NCI-index. Our QTAIM results indicate that while the linear S–Au–P moiety is unaffected by the variation of the fluorine content on the thiolates and that Au–S and Au–P bond strengths are mostly constant for all compounds in the series, the π character of gold bonds seems to be modified by the fluorination of the substituents at the thiolate ligand. Besides, the examination of the NCI-index reveals the presence of weak Au–π_{Phenyl} non-covalent interactions in all compounds. Overall, this study shows the relevance of (i) the π-backbonding properties of the metal centre and (ii) different non-covalent interactions in the stability of JohnPhos gold(I) compounds.

Introduction

Gold complexes bearing the Buchwald ligands[1] have a broad range of applications in catalysis, generally showing a good selectivity due to both steric and electronic factors.[2,3] Despite the interest in this type of system, most of the efforts to modulate their properties rely on empirical knowledge while the theoretical descriptions of these molecules are still scarce.[4]

Much of the attention paid to gold(I) compounds comes from the possibility of the occurrence of metallophilic interactions among them.[5–10] Previously, gold(I) Buchwald-type phosphine compounds showed notable Au–π_{Phenyl} interactions particularly in cationic species.[11–13] JohnPhos is an emblematic Buchwald phosphine, whose steric demands exclude the possibility that gold atoms in neighbouring molecules exhibit any aurophilic contacts and therefore these centres establish other kinds of weak interactions. For example, Au–π_{Phenyl} contacts are stronger and more recurrent than one could expect in this series of compounds. This interaction along with incipient anagostic Au–H interactions[14] and Au–F contacts could indeed influence the chemical bonding between the JohnPhos ligand and gold(I) centres.

We have long-standing interest in transition metal derivatives bearing both phosphines and polyfluorinated thiolate ligands.[15–18] In particular, our focus is on the modulation of molecular properties by variations in the fluorination degree of thiolate ligands attached to the metal centre. This tuning has at least two major components. First, the electronic aspects derived from a variable number of electronegative fluorine atoms in different positions of the aliphatic or aromatic substituents at the thiolate ligands, extending along the sulphur–metal–phosphorus fragment. Second, the steric aspects related to the volume change on going from hydrogen (vdW radii 120 pm (ref. 19 and 20)) to fluorine (vdW radii 146 pm (ref. 19 and 20)) atoms. This second issue involves not only a change in the molecular volume but also other struc-

[a]*Department of Inorganic and Nuclear Chemistry, School of Chemistry, UNAM, Ciudad Universitaria, 04510 CDMX, Mexico. E-mail: lgma@comunidad.unam.mx, torrens@unam.mx*
[b]*Department of Physical and Analytical Chemistry, University of Oviedo, Julián Clavería 8, Oviedo, E-33006, Spain*
[c]*Department of Physical Chemistry, Institute of Chemistry, UNAM, Ciudad Universitaria, 04510 CDMX, Mexico*

†Electronic supplementary information (ESI) available: Crystallographic details, complete other theoretical results and NMR spectra. CCDC 1532190–1532197. For ESI and crystallographic data in CIF or other electronic format see DOI: 10.1039/c7dt00961e

‡These authors contributed equally.

This journal is © The Royal Society of Chemistry 2017

tural consequences on the examined compounds. These two factors have an important role in the molecular and supramolecular properties of the adducts of interest.

We aim to achieve a rational modulation of molecular and supramolecular properties by assessing the influence that ligands exert over coordination compounds.[21] For this reason, we have previously examined the *cis* and *trans* influence of a series of fluorinated thiolate ligands (SR_F) in cationic complexes with the general formula $[Pt(SR_F)(triphos)]^+$.[22] More specifically, we found that the most fluorinated ligands unshielded the phosphorus atom in the *trans* position the most presumably due to inductive effects through the S–Pt–P fragment. Likewise, we expected that the presence of thiolate ligands with a different degree of fluorination would affect the structural or electronic parameters related to the S–Au–P fragment.

The purpose of this work is to understand how the substitution of hydrogen with fluorine in thiolate ligands influences the electronic environment of JohnPhos gold(I) complexes. For this purpose, we synthesised a series of eight new compounds with the general formula $[Au(SR_F)(JPhos)]$, where JPhos = $P(C_6H_4\text{-}C_6H_5)(t\text{-But})_2$ and R_F = C_6F_5 (**1**), C_6HF_4-4 (**2**), $C_6H_3F_2$-3,5 (**3**), $C_6H_3F_2$-2,4 (**4**), C_6H_4F-2 (**5**), C_6H_4F-3 (**6**), C_6H_4F-4 (**7**) and CF_3 (**8**). Our results altogether provide valuable insights into the chemical bonding scenario in this type of compound which might be useful in the understanding of its stability and catalytic properties.

Experimental

Material and methods

Solvents were dried using established procedures and distilled under nitrogen gas immediately before use.[23] Thin layer chromatography (TLC) (Sigma-Aldrich, silica gel 60 F_{254} or neutral aluminium oxide 60 F_{254}) was used to follow the progress of the reactions under examination employing hexane/ethyl acetate (9 : 1) as the eluent.

Instrumentation: melting points were obtained using a Fisher-Johns apparatus. Infrared spectra were recorded on a PerkinElmer FTIR/FIR Spectrum 400 spectrometer in the range of 4000 to 400 cm^{-1} using Attenuated Total Reflectance (ATR). Elemental analyses were conducted utilising a Thermo Scientific Flash 2000 Analyser at 950 °C. ^1H and ^{13}C NMR spectra were obtained on a 9.4 T Varian VNMRS spectrometer while ^{19}F and $^{31}P\{^1H\}$ NMR spectra were obtained on a 7.0 T Oxford Spectrometer. Chemical shifts are in ppm relative to internal TMS δ = 0 (^1H, ^{13}C) and to external references of $CFCl_3$ (for ^{19}F) and H_3PO_4 (for ^{31}P) at 0 ppm. *J* values are given in Hz. Positive-ion fast atom bombardment mass spectra (FAB + MS) were obtained on an MStation JMS-700 mass spectrometer operated at an acceleration voltage of 10 kV. Samples were desorbed from a 3-nitrobenzyl alcohol matrix by 3 keV xenon atoms employing the matrix ions as the reference material.

CS_2, AgF, $Pb(OOCCH_3)_2$, chloro[(1,1′-biphenyl-2-yl)di-*tert*-butylphosphine]gold(I) $[AuCl(PC_{20}H_{27})]$, and all seven aromatic thiols (R_FSH) were purchased from Sigma-Aldrich Co. and used without further purification. Lead thiolates ($Pb(SR_F)_2$ where R_F = C_6F_5, C_6HF_4-4, $C_6H_3F_2$-2,4, $C_6H_3F_2$-3,5, C_6H_4F-2, C_6H_4F-3, C_6H_4F-4) and $Ag(SCF_3)$ were prepared as previously reported.[24,25]

Caution: Pb(II) salts are known to be extremely toxic. All procedures were conducted in a fume cupboard.

Synthesis

For the preparation of compounds **1–8** all the synthetic procedures were similar, thus only one is described below (Scheme 1). One equivalent of the corresponding lead thiolate, $Pb(SR_F)_2$ (60.1 mg, 0.1 mmol for R_F = C_6F_5) in 10 mL of CH_2Cl_2 and a solution of two equivalents of [AuCl(JPhos)] (59.7 mg, 0.2 mmol) in 25 mL of dichloromethane were mixed under continuous stirring in a 50 mL round bottom flask. After 24 h, the yellow solution became a colourless suspension that was filtered off to obtain solid white $PbCl_2$ and a clear solution that was evaporated over a period of around 24 h giving a colourless crystalline solid formulated as $[Au(SC_6F_5)(JPhos)]$ **1**.

Compound 1 $[Au(SC_6F_5)(PC_{20}H_{27})]$. Colourless crystalline solid; 83% yield; mp: 110–113 °C; elemental analysis found C, 45.1; H, 4.1. Calc. for $C_{26}H_{27}AuF_5PS$: C, 45.0; H, 3.9%; IR(ATR) $\nu_{max}(cm^{-1})$ 3057w, 2922s, 1504vs, 1471vs, 1083, 967s, 855s, 755s. NMR δH (400 MHz; acetone-d_6; Me_4Si) 8.0–7.1 (9 H, m, 1,1′-biphenyl-2-yl), 1.29 (18 H, d, $^3J_{P-H}$ = 15.34, *tert*-butyl). $\delta P\{^1H\}$ (121.3 MHz; acetone-d_6; H_3PO_4) 62.9 (1 P, s). δF (282 MHz; acetone-d_6; $CFCl_3$) −133.8 (2F, m, F_o), −166.8 (1 F, m, F_p), −167.22 (2 F, m, F_m). MS-FAB$^+$ *m*/*z* 694 (M^+, 10%), 495 (M-SC_6F_5, 100), 1189 (M_2-SC_6F_5, 77).[26,27]

Compound 2 $[Au(SC_6HF_4\text{-}4)(PC_{20}H_{27})]$. Colourless crystalline solid; 85% yield; mp: 182–184 °C; elemental analysis found C, 45.9; H, 4.3. Calc. for $C_{26}H_{28}AuF_4PS$: C, 46.2; H, 4.2%; IR(ATR) $\nu_{max}(cm^{-1})$ 3079w, 3061w, 2963s, 2901, 1623s, 1482vs, 1425vs, 1164s, 909s, 885s, 755s, 698. NMR δH (400 MHz; acetone-d_6; Me_4Si) 8.0–7.1 (9 H, m, 1,1′-biphenyl-2-yl), 6.95 (1H, m, C_6F_4H-4) 1.42 (18H, d, $^3J_{P-H}$ = 15.33 Hz, *tert*-butyl). $\delta P\{^1H\}$ (121.3 MHz; acetone-d_6; H_3PO_4) 62.8 (1P, s). δF (282 MHz; acetone-d_6; $CFCl_3$) −134.1 (2F, m, F_o), −143.4 (2F, m, F_m).

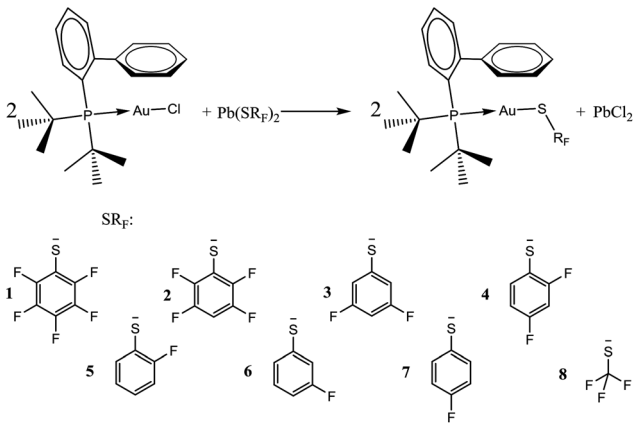

Scheme 1 Synthesis of compounds **1–8**.

MS-FAB$^+$ *m*/*z* 676 (M^+, 15%), 495 (M-SC_6F_4H, 100), 1171 (M_2-SC_6F_4H, 50).[26,27]

Compound 3 [Au($SC_6H_3F_2$-3,5)($PC_{20}H_{27}$)]. Colourless crystalline solid; 75% yield; mp: 155–156 °C; elemental analysis found C, 48.6; H, 4.8. Calc. for $C_{26}H_{30}AuF_2PS$: C, 48.75; H, 4.7%; IR(ATR) ν_{max}(cm^{-1}) 3199w, 3062w, 2957s, 1599vs, 1570vs, 1421vs, 1171, 1105s, 947, 873s, 838s, 755s. NMR δH (400 MHz; acetone-d_6; Me_4Si) 8.0–7.1 (9 H, m, 1,1′-biphenyl-2-yl), 6.49 (1H, m, $C_6H_2F_2H$-4), 6.91 (2H, m, $C_6HF_2H_2$-2,6), 1.52 (18H, d, $^3J_{P-H}$ = 15.25 Hz, *tert*-butyl). δP{^{1}H} (121.3 MHz; acetone-d_6; H_3PO_4) 63.48 (1P, s), δF (282 MHz; acetone-d_6; $CFCl_3$) −114.4 (2F, m). MS-FAB$^+$ *m*/*z* 640 (M^+, 25%), 495 (M-$SC_6H_3F_2$, 65), 1135 (M_2-$SC_6H_3F_2$, 100).[26,27]

Compound 4 [Au($SC_6H_3F_2$-2,4)($PC_{20}H_{27}$)]. Colourless crystalline solid; 78% yield; mp: 140–143 °C; elemental analysis found C, 48.35; H, 4.8. Calc. for $C_{26}H_{30}AuF_2PS$: C, 48.75; H, 4.7%; IR(ATR) ν_{max}(cm^{-1}) 3051w, 2960s, 1586, 1471s, 1365, 1252, 1110, 956, 840, 753s. NMR δH (400 MHz; acetone-d_6; Me_4Si) 8.2–7.1 (10 H, m, 1,1′-biphenyl-2-yl and $C_6H_2F_2H$-6), 6.67 (2H, m, $C_6HF_2H_2$-3,5), 1.43 (18H, d, $^3J_{P-H}$ = 15.20 Hz, *tert*-butyl). δP{^{1}H} (121.3 MHz; acetone-d_6; H_3PO_4) 63.08 (1P, s), δF (282 MHz; acetone-d_6; $CFCl_3$) −102.4 (1F, m, F-2), −120.34(1F, m, F-4). MS-FAB$^+$ *m*/*z* 640 (M^+, 25%), 495 (M-$SC_6H_3F_2$, 100), 1135 (M_2-$SC_6H_3F_2$, 80).[26,27]

Compound 5 [Au(SC_6H_4F-2)($PC_{20}H_{27}$)]. Colourless crystalline solid; 81% yield; mp: 130–133 °C; elemental analysis found C, 49.9; H, 5.1. Calc. for $C_{26}H_{31}AuFPS$: C, 50.2; H, 5.0%; IR(ATR) ν_{max}(cm^{-1}) 3059w, 2953s, 1561w, 1462vs, 1439s, 1364, 1214s, 1172s, 1067, 747vs, 698. NMR δH (400 MHz; acetone-d_6; Me_4Si) 8.0–7.1 (9H, m, 1,1′-biphenyl-2-yl), 6.87 (4H, m, C_6H_4F-2), 1.50 (18H, d, $^3J_{P-H}$ = 15.17 Hz, *tert*-butyl). δP{^{1}H} (121.3 MHz; acetone-d_6; H_3PO_4) 63.16 (1P, s), δF (282 MHz; acetone-d_6; $CFCl_3$) −107.67 (1F, m). MS-FAB$^+$ *m*/*z* 622 (M^+, 85%), 495 (M-SC_6H_4F, 100), 1117 (M_2-SC_6H_4F, 80).[26,27]

Compound 6 [Au(SC_6H_4F-3)($PC_{20}H_{27}$)]. Colourless crystalline solid; 84% yield; mp: 143–145 °C; elemental analysis found C, 50.4; H, 5.0. Calc. for $C_{26}H_{31}AuFPS$: C, 50.2; H, 5.0%; IR(ATR) ν_{max}(cm^{-1}) 2947s, 1592w, 1461vs, 1425vs, 1254s, 1168s, 875vs. NMR δH (400 MHz; acetone-d_6; Me_4Si) 8.0–7.1 (9H, m, 1,1′-biphenyl-2-yl), 7.10–6.56 (4H, m, C_6H_4F-3), 1.46 (18H, d, $^3J_{P-H}$ = 15.22 Hz, *tert*-butyl). δP{^{1}H} (121.3 MHz; acetone-d_6; H_3PO_4) 68.81 (1P, s), δF (282 MHz; acetone-d_6; $CFCl_3$) −111.69 (1F, m). MS-FAB$^+$ *m*/*z* 622 (M^+, 85%), 495 (M-SC_6H_4F, 100), 1117 (M_2-SC_6H_4F, 80).[26,27]

Compound 7 [Au(SC_6H_4F-4)($PC_{20}H_{27}$)]. Colourless crystalline solid; 85% yield; mp: 115–117 °C; elemental analysis found C, 50.0; H, 5.1. Calc. for $C_{26}H_{31}AuFPS$: C, 50.2; H, 5.0%; IR(ATR) ν_{max}(cm^{-1}) 3048w, 2956s, 1477vs, 1441, 1218, 1085, 751, 697. NMR δH (400 MHz; acetone-d_6; Me_4Si) 8.0–7.1 (9H, m, 1,1′-biphenyl-2-yl), 7.17 (m, 2H, $C_6H_2FH_2$-3,5), 6.72 (m, 2H, $C_6H_2FH_2$-2,4), 1.44 (18H, d, $^3J_{P-H}$ = 15.09 Hz, *tert*-butyl). δP{^{1}H} (121.3 MHz; acetone-d_6; H_3PO_4) 68.59 (1P, s), δF (282 MHz; acetone-d_6; $CFCl_3$) −119.84 (1F, m). MS-FAB$^+$ *m*/*z* 622 (M^+, 50%), 495 (M-SC_6H_4F, 80), 1117 (M_2-SC_6H_4F, 100).[26,27]

Compound 8 [Au(SCF_3)($PC_{20}H_{27}$)]. Colourless crystalline solid; 80% yield; mp: 204–207 °C; elemental analysis found C, 42.1; H, 5.2. Calc. for $C_{21}H_{27}AuF_3PS$: C, 42.3; H, 5.4%; IR(ATR) ν_{max} (cm^{-1}) 3059w, 2963, 1463, 1173w, 1072vs, 755, 700, 528. NMR δH (400 MHz; acetone-d_6; Me_4Si) 8.2–7.1 (9H, m, 1,1′-biphenyl-2-yl), 1.45 (18H, d, $^3J_{P-H}$ = 15.45 Hz, *tert*-butyl,), δP {^{1}H} (121.3 MHz; acetone-d_6; H_3PO_4) 61.75 (1P, s), δF (282 MHz; acetone-d_6; $CFCl_3$) −19.71 (3F, s). MS-FAB$^+$ *m*/*z* 596 (M^+, 8%), 495 (M-SC_6F_5, 100).

Suitable crystals for X-ray diffraction analyses of compounds **1** to **8** were grown by slow multi-day solvent evaporation of a concentrated acetone solution at room temperature (293–298 K). The crystals of compounds **1–8** were studied with an Oxford Diffraction Gemini "A" diffractometer with a CCD area detector and a radiation source of $\lambda_{MoK\alpha}$ = 0.71073 Å using graphite-monochromatized radiation at 130 K for compounds **3**, **5–8** and at 298 K for **1**, **2** and **4**. CrysAlisPro and CrysAlis RED software packages[28,29] were used for data collection and integration. The double pass method of scanning was employed to exclude any noise. The collected frames were integrated *via* an orientation matrix determined from the narrow frame scans. Final cell constants were determined by a global refinement. Collected data were corrected for absorbance by using analytical/numerical absorption corrections[30] through a multifaceted crystal model based on expressions upon the Laue symmetry. Structure solution and refinement were carried out with SHELXS-2014 and SHELXL-2014 packages.[31] The WinGX v. 2014.1 software was utilised to prepare material for publication.[32] Full-matrix least-squares refinement was carried out by minimising $(F_o^2 - F_c^2)^2$. All non-hydrogen atoms were refined anisotropically. On the other hand, H atoms attached to C atoms were placed in geometrically idealised positions and refined as riding on their parent atoms, with C–H = 0.95–0.98 Å and with U_{iso}(H) = 1.2U_{eq}(C) or U_{iso}(H) = 1.5U_{eq}(C) for aromatic and methyl groups, respectively.

Computational details

Single point calculations of the structures obtained with X-ray refinement/diffraction measurements were performed using Density Functional Theory (DFT) under the Zeroth Order Regular Approximation (ZORA).[33,34] We considered the BP86 exchange–correlation functional[35,36] along with the TVZ-ZORA basis set,[37] as implemented in the ORCA program.[38] This methodology has been successfully used to describe metal–metal and metal–ligand bonding in organometallic compounds.[39,40]

The Quantum Theory of Atoms in Molecules (QTAIM) is a method of wave function analysis based on a partition of space into disjoint regions, identified with the atoms in chemistry.[41–43] The QTAIM is founded on the topology of the charge distribution $\rho(\mathbf{r})$ which is invariant under orbital rotations. This approach is a powerful tool that has proven to be useful in the study of bonding in donor–acceptor complexes.[44] The QTAIM analysis was performed by dint of the AIMAll program.[45]

Given the important role that non-covalent interactions could play in the investigated systems, we further examined this kind of contact through the NCI index,[46] a descriptor

 This journal is © The Royal Society of Chemistry 2017

derived from the electron density and its reduced gradient. We used the NCIPlot program[47] to examine the properties of the NCI indicator, and the corresponding results were visualised with the VMD software.[48]

Results and discussion

X-ray structures

Compound 1: [Au(SC$_6$F$_5$)(JPhos)]. Isolated crystals belong to the orthorhombic space group P_{bca}, with only one molecule of [Au(SC$_6$F$_5$)(JPhos)] in the asymmetric unit (Fig. 1). The P–Au–S angle is almost linear (173.60(6)°), and the conformation around the phosphorous is slightly distorted from a tetrahedral arrangement due to the sterical demands of the substituent. As expected, the C–S–Au angle (106.7(2)°) is faintly smaller than that of an sp^3 sulphur atom. The angle seems to be modified by the observed Au–F interaction. There is an angle of 80.93° between the biphenyl group ring planes.

The second coordination sphere of compound **1** exhibits several non-covalent intramolecular interactions. For example, there is an Au–F contact with an unusually short distance (d_{Au-F} = 3.002(4) Å), which is shorter than the sum of the van der Waals radii of gold and fluorine atoms ($\sum r_{vdW}$ = 3.06 Å, r_F = 1.40 Å, and r_{Au} = 1.66 Å).[19,20] There is also a metal–π interaction with the phosphine capping the phenyl ring (*i.e.* the phenyl parallel to the P–Au–S axis) and the gold centre (Au–C$_{ipso}$ = 3.068(5) Å). The system also presents interactions between the hydrogens from the *tert*-butyl groups of the phosphine and the gold centres, with Au–H distances ranging from 2.7 to 3.1 Å. Several Au–H interactions as those found in this work have been previously described.[14] The crystalline packing arrangement of this compound is directed mainly by the various F···H intermolecular interactions among neighbouring molecules.

Compound 2: [Au(SC$_6$HF$_4$-4)(JPhos)]. The analysed crystal belongs to the orthorhombic space group P_{bca} in which the asymmetric unit comprises only one molecule of [Au(SC$_6$HF$_4$-4)(JPhos)] as displayed in Fig. 2. The geometry around the gold centres is nearly linear (S–Au–P angle 173.60(6)°), and the distribution of ligands is very similar to that observed in compound **1**. There is one relatively short Au–F contact (Au–F = 2.994(3) Å) which is also less than the sum of the van der Waals radii of Au and F ($\sum r_{vdW}$ = 3.06 Å, r_F = 1.40 Å, and r_{Au} = 1.66 Å).[19,20] There is an additional Au–π contact with an associated distance Au–C$_{ipso}$ = 3.082(4) Å. Similar to compound **1**, the aromatic fluorinated ring in system **2** is nearly parallel to the capping phenyl ring. One fluorine atom at position 2 of the thiolate interacts with a hydrogen of the biphenyl group of a neighbouring molecule (C–F = 3.238(6) Å). There are Au–H contacts in the second coordination sphere of the metal centres as well.

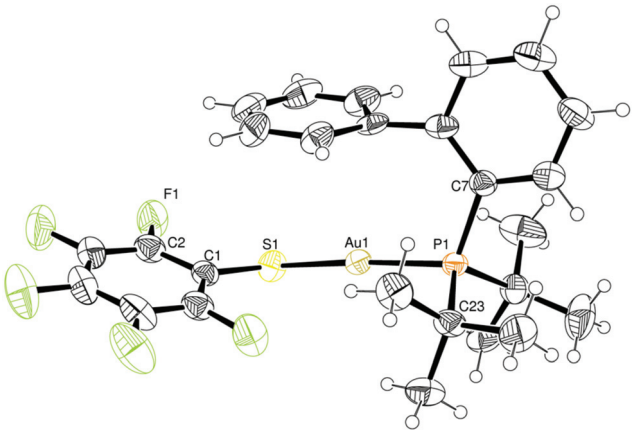

Fig. 1 ORTEP diagram for compound [Au(SC$_6$F$_5$)(JPhos)] **1**, ellipsoids at 40% of probability level. Selected distances and angles: P1–Au1 2.2674(15) Å, S1–Au1 2.3007(16) Å, C1–S1–Au1 106.7(2)°, S1–Au1–P1 173.60(6)°.

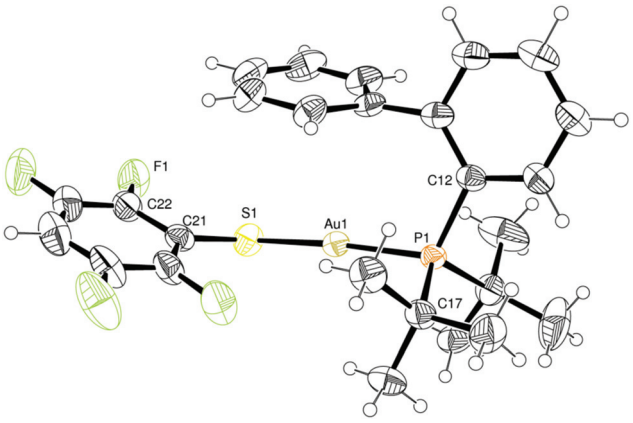

Fig. 2 ORTEP diagram for compound [Au(SC$_6$HF$_4$-4)(JPhos)] **2**, ellipsoids at 40% of probability level. Selected distances and angles: P1–Au1 2.2728(9) Å, S1–Au1 2.3024(11) Å, C1–S1–Au1 107.24(13)°, S1–Au1–P1 173.69(4)°.

Compound 3: [Au(SC$_6$H$_3$F$_2$-3,5)(JPhos)]. The molecular structure of this compound is shown in Fig. 3 and the isolated crystals belong to the triclinic space group $P\bar{1}$. The discrete unit consists of two molecules having almost the same conformation. The nearly linear gold(I) centre (S–Au–P angle 174.83(4)°) interacts with the capping phenyl ring (Au–C$_{ipso}$ = 3.049(5) Å). As expected, all other weak interactions of gold in this compound are structurally limited to Au–H contacts including one of the *ortho* hydrogens of the fluorinated ring which directs towards the gold centre.

Compound **3** does not exhibit π interactions between the fluorinated phenyl ring and the capping C$_6$H$_5$ group. In this case, the aromatic rings are not oriented parallel to each other. The supramolecular arrangement in the crystal is mainly directed by different F···H interactions with the *tert*-butyl hydrogens of vicinal molecules.

Compound 4: [Au(SC$_6$H$_3$F$_2$-2,4)(JPhos)]. Fig. 4 shows the structure of this adduct whose crystals belong to the monoclinic space group $P2_1/c$ and, the corresponding asymmetric unit is made up of one molecule of [Au(SC$_6$H$_3$F$_2$-2,4)(JPhos)].

The molecular structure of **4** is similar to those found in compounds **1** and **2** with an almost linear S–Au–P moiety

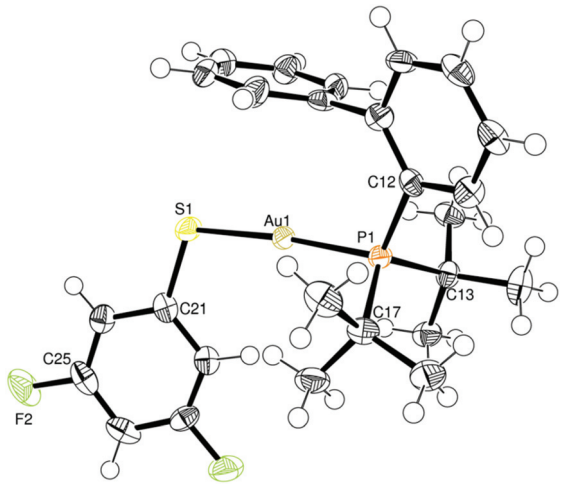

Fig. 3 ORTEP diagram for compound [Au($SC_6H_3F_2$-3.5)(JPhos)] **3**, ellipsoids at 70% of probability level. Selected distances and angles: P1–Au1 2.2784(11) Å, P2–Au2 2.2847(12) Å, S1–Au1 2.3093(11) Å, S2–Au2 2.3115(12), Au1–Au2 11.120 Å, C21–S1–Au1 104.75(15)°, S1–Au1–P1 174.83(4)°, C47–S2–Au2 106.40(16)°, S2–Au2–P2 175.56(4)°.

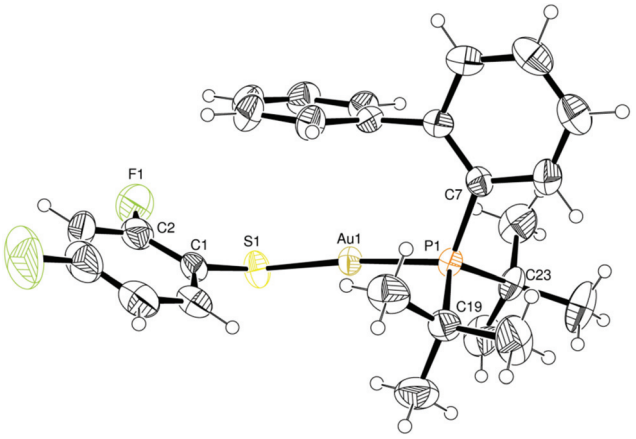

Fig. 4 ORTEP diagram for compound [Au($SC_6H_3F_2$-2,4)(JPhos)] **4**, ellipsoids at 70% of probability level. Selected distances and angles: P1–Au1 2.2755(11) Å, S1–Au1 2.2994(13) Å, C1–S1–Au1 103.43(16)°, S1–Au1–P1 174.63(5)°.

(S1–Au1–P1 174.63(5)°) interacting with the capping biphenyl π system (Au–C_{ipso} = 3.103(4) Å) and with the fluorinated thiolate ring parallel to the biphenyl aromatic ring. Secondary contacts of the gold centre are of Au–H type. There are several F···H and S···H intermolecular interactions that determine the observed supramolecular arrangement.

Compound 5: [Au(SC_6H_4F-2)(JPhos)]. The crystal of this system corresponds to the monoclinic space group $P2_1/c$, and its asymmetric unit is constituted by only one molecule. The structure of this compound (Fig. 5) also displays a thiolate ring interacting weakly with the capping phenyl ring. Linear gold(I) presents an S–Au–P angle of 175.91(4)°. Interestingly, this compound exhibits no F–Au contacts, although there is a fluorine in a suitable position to interact with the gold atom and an

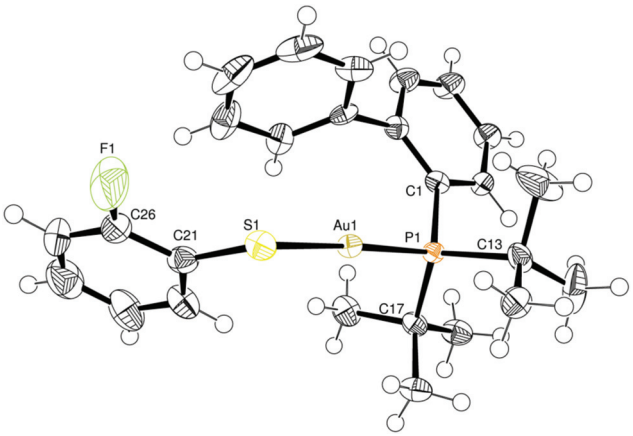

Fig. 5 ORTEP diagram for compound [Au(SC_6H_4F-2)(JPhos)] **5**, ellipsoids at 60% of probability level. Selected distances and angles: P1–Au1 2.2790(10) Å, S1–Au1 2.3113(11) Å, C21–S1–Au1 103.46(15)°, S1–Au1–P1 175.91(4)°.

unexpected H–Au contact is favoured. The Au–π interaction is also found in this compound with an Au–C_{ipso} distance of 3.082(4) Å. The molecular arrangement in the crystal structure seems to result from the F···H interactions between the *tert*-butyl units and the thiolate moieties.

Compound 6: [Au(SC_6H_4F-3)(JPhos)]. Fig. 6 displays the structure of this compound. The crystal corresponds to the triclinic space group $P\bar{1}$. The asymmetric unit consists of two molecules of [Au(SC_6H_4F-3)(JPhos)]. Two different conformers were found in the crystal although the variations in distances and angles are relatively small. The quasi-linear gold centres have angles of 176.35(3)° and 178.40(4)°, while the Au–C shortest distances are also slightly different: 2.990(5) Å and 3.071(4) Å, respectively. These variations seem to be mutually related,

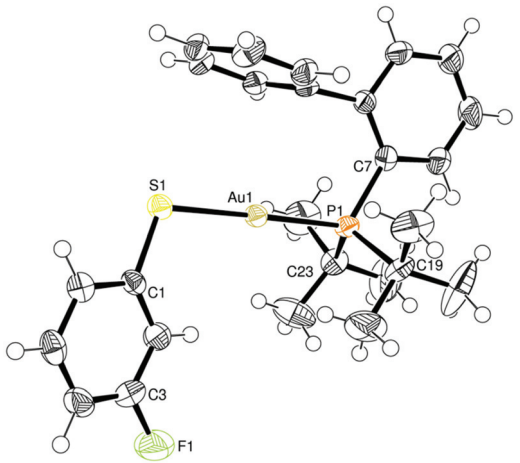

Fig. 6 ORTEP diagram for compound [Au(SC_6H_4F-3)(JPhos)] **6**, ellipsoids at 60% of probability level. Selected distances and angles: P1–Au1 2.2792(12) Å, P2–Au2 2.2299(11) Å, S1–Au1 2.3051(12) Å, S2–Au2 2.3017(11) Å, C1–S1–Au1 108.35(15)°, S1–Au1–P1 178.40(4)°, C27–S2–Au2 106.36(16)°, S2–Au2–P2 176.35(3)°.

This journal is © The Royal Society of Chemistry 2017

i.e. the shortening of the Au-phenyl distance is associated with a larger deviation of the linearity of the S–Au–P moiety. Weak interactions between fluorine and nearby *tert*-butyl hydrogens seem to be responsible for the crystalline packing.

Compound 7: [Au(SC$_6$H$_4$F-4)(JPhos)]. The structure of this system is presented in Fig. 7. The examined crystal belongs to the triclinic space group $P\bar{1}$. The asymmetric unit is composed of two molecules of [Au(SC$_6$H$_4$F-4)(JPhos)] with two very similar conformations. The corresponding S–Au–P angles are in the expected range for Au(I) linear compounds: 178.20(3)° and 175.90(3)°. The gold atoms interact with the capping phenyl ring with Au–C$_{ipso}$ distances of 3.061(3) Å and 3.122(4) Å, respectively. In the former, the nearest C to the gold atom is the α carbon rather than the usual C$_{ipso}$ with a corresponding distance Au–Cα 3.030(4) Å. The supramolecular adduct contains a peculiar F-C$_6$H$_5$ η^1 contact which involves a neighbouring biphenyl (F–C 3.092(4) Å).

Compound 8: [Au(SCF$_3$)(JPhos)]. Fig. 8 displays the structure of this complex. The studied crystal belongs to the monoclinic space group $P2_1/c$ and the asymmetric unit consists of merely one molecule. The S–Au–P angle is in the expected range for Au(I) linear compounds: 175.72(5)°. The gold atom interacts with the capping phenyl ring with an Au–C$_{ipso}$ distance of 3.046(5) Å. The supramolecular adduct has multiple F···H contacts between the trifluoromethyl and *tert*-butyl groups of nearby molecules.

π-Backbonding

Gold π-backbonding capabilities have been scarcely studied, and most of the work on this topic have focused on organometallic Au compounds.[49–55] This situation occurs perhaps because many metal centres are better π donors than gold. At first, we were baffled by the fact that all the Au–S and Au–P distances are very similar regardless of the fluorination degree of thiolate ligands. We, therefore, carried out QTAIM analyses to address this issue. We determined the value of $\rho(\mathbf{r})$ at the bond critical point (bcp) that is a qualitative estimate of the bond strength. We also evaluated delocalization indices (DI), which measure the number of electrons shared between atoms. As we can see in Table 1, neither $\rho(\mathbf{r}_{bcp})$ nor the corresponding DI for the Au–S and Au–P interaction shows appreciable differences among the examined compounds. In other words, the fluorination of the thiolate ligand does not substantially affect the amount of electron density or the number of shared electrons for these chemical bonds.

We considered another useful chemical bonding descriptor in QTAIM, *i.e.*, the ellipticity, ε, which determines the preferential accumulation of electron density in a given plane and hence the π character of a particular bond.[41–43] For instance, the ellipticity for a characteristic σ bond, *e.g.* in ethane is close to 0.0, while the corresponding value for the double bond in ethylene equals 0.45. The ellipticities for the S–Au and Au–P bcps in all the studied systems are different from zero, an indication of the π character in the associated chemical bonding. We note that the absence of a phenyl ring in compound **8** decreases substantially the ellipticity of the examined bonds, a condition that suggests the reduced π acidity of the thiolate.

Bond ellipticities indicate that the fluorination of the thiolate ligands affects the π-backbonding capabilities of gold in both Au–S and Au–P contacts. The result is more noticeable for the former chemical bonds. The following series shows the order of increasing bonding ellipticity for the fluorophenylthiolate compounds: [Au(SCF$_3$)(JPhos)] **8** < [Au(SC$_6$HF$_4$)(JPhos)] **2** < [Au(SC$_6$F$_5$)(JPhos)] **1** < [Au(SC$_6$H$_3$F$_2$-2,4)(JPhos)] **4** < [Au(SC$_6$H$_4$F-4)(JPhos)] **7** < [Au(SC$_6$H$_4$F-3)(JPhos)] **6** < [Au(SC$_6$H$_4$F-2)(JPhos)] **5** < [Au(SC$_6$H$_3$F$_2$-3,5)(JPhos)] **3**

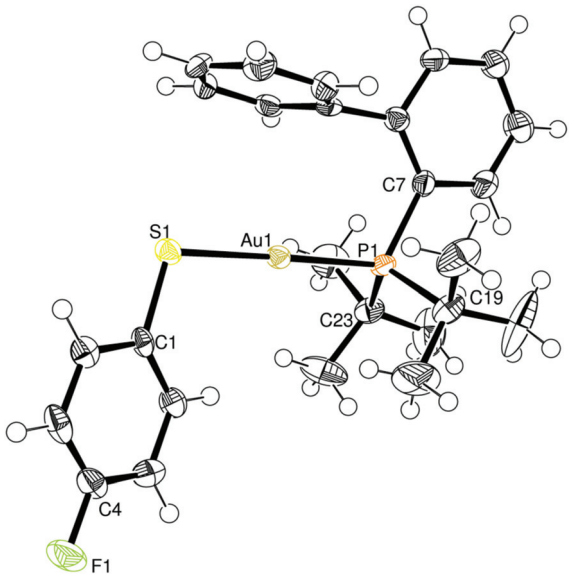

Fig. 7 ORTEP diagram for compound [Au(SC$_6$H$_4$F-4)(JPhos)] **7**, ellipsoids at 60% of probability level. Selected distances and angles: P1–Au1 2.2752(10) Å, P2–Au2 2.2791(9) Å, S1–Au1 2.3020(9) Å, S2–Au2 2.3016(9) Å, C1–S1–Au1 107.55(13)°, S1–Au1–P1 178.20(3)°, C27–S2–Au2 105.46(11)°, S2–Au2–P2 175.90(3)°.

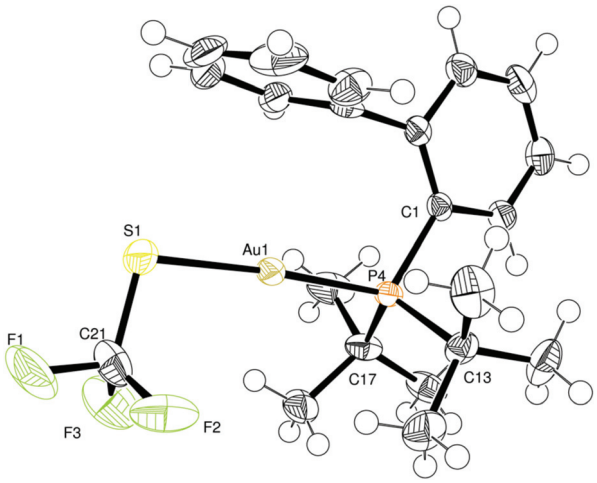

Fig. 8 ORTEP diagram for compound [Au(SCF$_3$)(JPhos)] **8**, ellipsoids at 60% of probability level. Selected distances and angles: P1–Au1 2.2675(13) Å, S1–Au1 2.3082(14) Å, C21–S1–Au1 99.8(2)°, S1–Au1–P1 175.72(5)°.

Table 1 Density at the bond critical point ($\rho(\mathbf{r}_{bcp})$), ellipticity (ε), and delocalization index (DI) for the Au–S and Au–P bonds as well as QTAIM charges for sulphur, gold, and phosphorus atoms. Atomic units are used throughout

	S–Au			Au–P			Charges		
Compound	$\rho(\mathbf{r}_{bcp})$	ε	DI	$\rho(\mathbf{r}_{bcp})$	ε	DI	S	Au	P
[Au(SC_6F_5)(JPhos)] **1**	0.1099	0.0584	1.0487	0.1200	0.0350	0.98645	−0.1210	−0.0177	1.3811
[Au(SC_6HF_4)(JPhos)] **2**	0.1102	0.0580	1.0514	0.1212	0.0346	0.99249	−0.1254	−0.0195	1.3918
[Au($SC_6H_3F_2$-3,5)(JPhos)] **3**	0.1110	0.0697	1.0801	0.1191	0.0416	0.97962	−0.1799	−0.0476	1.3880
[Au($SC_6H_3F_2$-2,4)(JPhos)] **4**	0.1088	0.0602	1.0768	0.1174	0.0362	0.97583	−0.2137	−0.0449	1.3679
[Au(SC_6H_4F-2)(JPhos)] **5**	0.1088	0.0686	1.0726	0.1183	0.0409	0.98350	−0.1862	−0.0473	1.3986
[Au(SC_6H_4F-3)(JPhos)] **6**	0.1108	0.0650	1.1038	0.1191	0.0379	0.98318	−0.2392	−0.0561	1.3751
[Au(SC_6H_4F-4)(JPhos)] **7**	0.1108	0.0631	1.0936	0.1182	0.0349	0.97691	−0.2300	−0.0512	1.3560
[Au(SCF_3)(JPhos)] **8**	0.1089	0.0491	1.0457	0.1210	0.0355	0.99085	−0.1226	−0.0272	1.3834

These results indicate that the number of F atoms along with their positioning is critical for the observed effect. *Meta* substitution (compounds **5** and **7**) increases the π character of the Au–S and Au–P bonds. On the other hand, fluorination at *ortho* and *para* positions decreases bond ellipticities, with the influence on ε being larger for the former substitution pattern. Accordingly, the double substitution in positions 3 and 5 greatly enhances the π-backbonding character of the gold atom.

Despite the complexity of gold bonding in the studied systems, it is possible to observe a relationship between the charge of the gold atom and its π-backbonding donor capabilities. Fig. 9 indicates that the ellipticity of the Au–S bond increases with the negative charge of the Au atom. In other words, as the negative charge on the gold centre increases, this atom has a more noticeable tendency to establish π-backbonding interactions with the thiolate system.

The observed changes in the π character evidenced by ε do not entail a significant modification of the corresponding bond orders. The number of electrons shared between gold and sulphur or phosphorus, characterised by DI, remains in the range of a single bond. Indeed, this condition of the DIs explains the observed marginal variations of bond lengths in the examined crystal structures. The total densities in the Au–S and Au–P chemical bonds are differently distributed between the σ bond and π-backbonding on account of the π acidity and σ basicity of the thiolate ligands which are being modified by the fluorination. We stress that the sum of σ and π electronic densities which participate in the bond is almost constant in all the studied compounds and therefore the strength of the chemical bonds under examination remains unaffected.

On the other hand, there is a good correlation between the charges of sulphur and gold along the series of the analysed compounds (top of Fig. 10). Both atoms lose electron density when more fluorine atoms are included in the molecule. Indeed, the value of the total charge of the S–Au fragment is related to the fluorination degree of the phenyl ring on the thiolate: when this group becomes more fluorinated, the negative charge on the Au–S moiety decreases as observed in the bottom of Fig. 10.

Au weak interactions

Every compound under consideration shows remarkably short Au–C_π distances due to a dative Au–π interaction.[12] We used

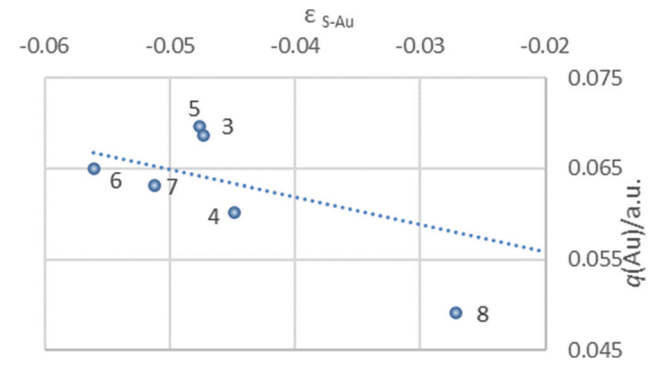

Fig. 9 Relation between the QTAIM charge of the gold centre and the ellipticity of the Au–S bond.

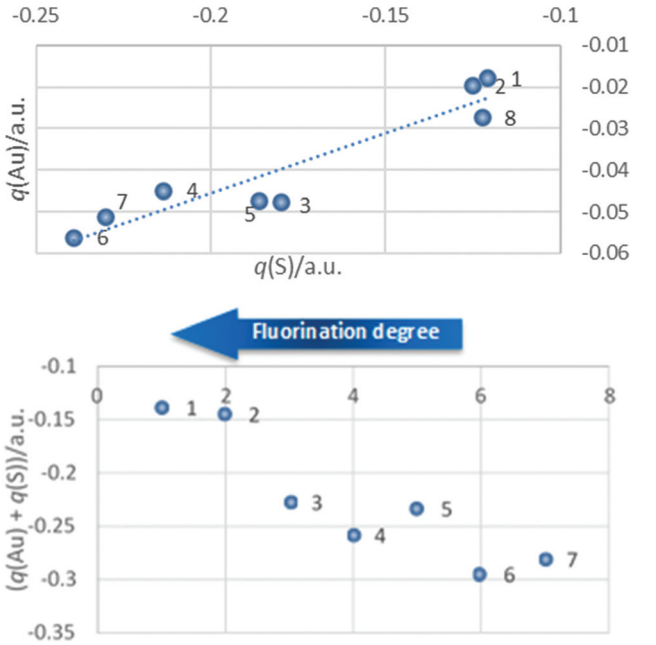

Fig. 10 Top: Linear correlation between QTAIM charges of the gold and sulphur atoms (R^2 = 0.88). Bottom: Relationship between q(Au) + q(S) and the fluorination degree of the phenylthiolate group.

This journal is © The Royal Society of Chemistry 2017

the Kochi's structural hapticity[56] parameter as a criterion for the characterisation of these contacts. Table 2 shows the calculated hapticity for the family of compounds considered in this investigation. We point out that this parameter is not indicative of the strength of the interaction. Au–C_{ipso} distances in all compounds are significantly smaller than the sum of the van der Waals radii of Au and C (3.36 Å[19,20]).

We used the NCI index[46,47] to examine the interactions around the metallic centre, in particular the Au–π interactions. Fig. 11 shows the different non-covalent contacts in the investigated compounds. This analysis indicates that there are indeed weak attractive interactions between the π system and the gold atom. These interactions are stronger in the region corresponding to the *ipso* and α carbons as indicated in dark green in Fig. 10 in agreement with the calculated Kochi's hapticities between η^1 and η^2 (Table 2). There are interactions between sulphur and the biphenyl π system in all the examined systems. The molecules with at least an *ortho*-fluorine in the thiolate ligand (**1**, **2**, **4** and **5**) present C_6H_5-$C_6F_nH_{5-n}$ π–π contacts as well. All these interactions expand all over the Au-thiolate system with the capping phenyl ring.

Table 2 shows a few selected quantum chemical topology parameters to characterise the Au–C_{ipso} contact. We note that compound **6** has the highest values of density at the bcp and DIs in agreement with the previously stated evidence that indicates the significant π-backbonding character of this system. In other words, a powerful back donor nature of gold promotes its acceptance of π density from the biphenyl ring giving place to a stronger interaction. The topological analyses for the S–C_{para} interaction reported in Table S1 in the ESI† indicate that these bonds are weaker than those associated with Au–C_{ipso} interactions.

The NCI analysis also reveals that all compounds present attractive interactions which involve the Au atom and the surrounding hydrogens including those of the fluorophenylthiolate moiety for compounds **3**–**7**. Anagostic Au–H interactions are supported by the ligand in a similar fashion to other cases reported in the literature.[57,58] On the other hand, compounds **4** and **5** have fluorine atoms only in one of the *ortho* carbons while the other position preserves the hydrogen atom. This feature gives us the opportunity to observe the preference of gold for either Au–H or Au–F interactions. We only detect the former one in these compounds.

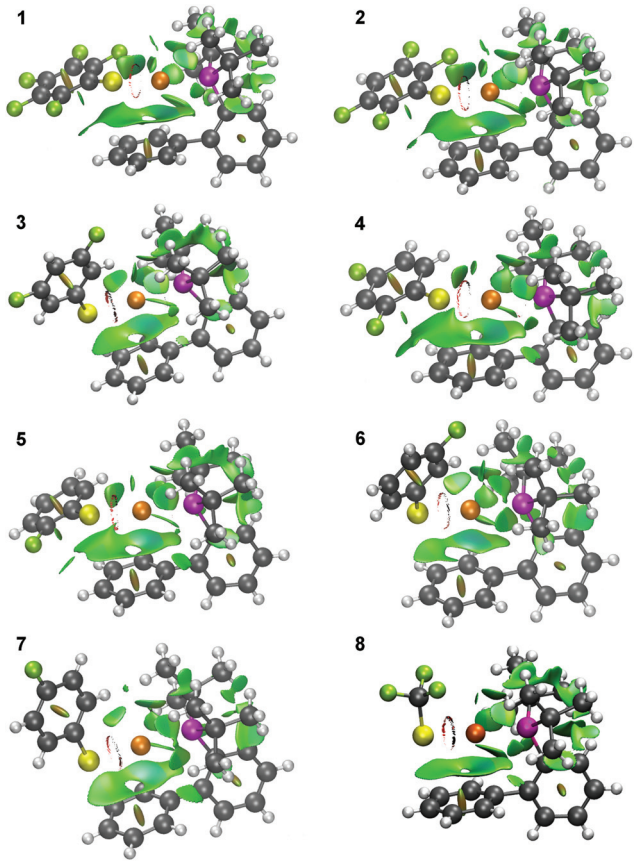

Fig. 11 NCI index plots for the 8 compounds addressed herein. The attractive/repulsive interactions are indicated in green/red. Colour code: P: pink, Au: orange, S: yellow, F: green, C: grey and H: white.

Table 2 Calculated Kochi hapticity parameter for the studied compounds and QTAIM analysis results for the observed Au–C_{ipso} interactions. The eight compounds showed a bond path Au–C_{ipso}. The density at the corresponding bond critical point and the delocalization between these atoms are reported in atomic units

Compound	Hapticity	$\rho(\mathbf{r}_{bcp})$ Au–C_{ipso}	DI Au–C_{ipso}
[Au(SC_6F_5)(JPhos)] **1**	1.294	0.0175	0.0984
[Au(SC_6HF_4)(JPhos)] **2**	1.585	0.0174	0.0966
[Au($SC_6H_3F_2$-3,5)(JPhos)] **3**	1.444	0.0177	0.0903
[Au($SC_6H_3F_2$-2,4)(JPhos)] **4**	1.680	0.0169	0.0907
[Au(SC_6H_4F-2)(JPhos)] **5**	1.762	0.0178	0.0977
[Au(SC_6H_4F-3)(JPhos)] **6**	1.582	0.0196	0.1180
[Au(SC_6H_4F-4)(JPhos)] **7**	1.729	0.0179	0.0991
[Au(SCF_3)(JPhos)] **8**	1.651	0.0183	0.0985

Conclusions

The structural and theoretical analyses of eight new fluorinated thiolate gold(I) derivatives: [Au(SR_F)(JPhos)] JPhos = $P(C_6H_4$–$C_6H_5)(t$-But$)_2$ and R_F = C_6F_5 (**1**), C_6HF_4-4 (**2**), $C_6H_3F_2$-3,5 (**3**), $C_6H_3F_2$-2,4 (**4**), C_6H_4F-2 (**5**), C_6H_4F-3 (**6**) C_6H_4F-4 (**7**) and CF_3 (**8**) show the influence of structural modifications in the thiolate ligands over the donor character of the gold centre. The examination of QTAIM bond ellipticities indicates that fluorination in the *meta* position of the R_F group increases the gold(I) centre π-backbonding to the ligands while fluorine atoms in *ortho* and *para* have the opposite effect.

Au–S distances do not show clear tendencies regarding the fluorination of the thiolate ligand. We explain these results by considering the fact that fluorination has two effects over this chemical bond. F atoms, on the one hand, promote the π acceptor character of the ligand and hence backdonation, and on the other hand, decrease the σ donor character of the sulphur atom by inductive effects. These two conditions

oppose each other, and the observed distances are the final result of the balance between both.

According to the NCI study of these JohnPhos gold complexes, phosphine ligand substituents interact with the gold centre *via* an Au–π interaction that can extend to an (Au–S)–π contact. Theoretical analyses of the systems show a substantial electron delocalization between the gold atom and the *ipso* carbon of the biphenyl ring. The stabilisation of the metal centre in this complex of the Buchwald ligand is further reinforced by the hydrogen basket of attractive Au–H anagostic closed-shell interactions.

The wavefunction analysis of the compounds by QTAIM allowed us to study how the chemical bonding scenario changes within these complexes on account of the considered thiolate ligands. Gold–Buchwald complexes present significant weak interactions which together with steric restrictions must have an effect on the modulation of the gold centre that could be exploited in several fields, for example in catalyst design.

Acknowledgements

We acknowledge the technical support of USAII at the School of Chemistry, UNAM. We are also thankful to DGAPA-UNAM, CONACYT-Mexico and the Spanish Government for funding through the projects IN202314, CB-2012/177498 and CTQ-2015-65790-P, respectively, along with Ph.D. Scholarships 270993 (G. M-A.) and 381483 (J. M. G-V). We also express our gratitude to DGTIC/UNAM for supercomputer resources (project LANCAD-UNAM-DGTIC-250) together with Luis Turcio-García for experimental assistance, Matthew Asay and Magdalena Quezada for Elemental Analysis and to Alberto Fernández for his valuable review of the manuscript.

Notes and references

1 K. Billingsley and S. L. Buchwald, *J. Am. Chem. Soc.*, 2007, **129**, 3358–3366.
2 P. Calleja, M. Muratore, T. Jiménez and A. Echavarren, *Synthesis*, 2016, 3183–3198.
3 A. M. Echavarren, A. S. K. Hashmi and F. D. Toste, *Adv. Synth. Catal.*, 2016, **358**, 1347–1347.
4 C. A. Gaggioli, G. Ciancaleoni, D. Zuccaccia, G. Bistoni, L. Belpassi, F. Tarantelli and P. Belanzoni, *Organometallics*, 2016, **35**, 2275–2285.
5 A. Laguna, *Modern Supramolecular Gold Chemistry*, Wiley-VCH Verlag GmbH & Co. KGaA, Weinheim, Germany, 2008.
6 H. Schmidbaur and A. Schier, *Chem. Soc. Rev.*, 2012, **41**, 370–412.
7 J. Muñiz, C. Wang and P. Pyykkö, *Chem. – Eur. J.*, 2011, **17**, 368–377.
8 C.-K. Li, X.-X. Lu, K. M.-C. Wong, C.-L. Chan, N. Zhu and V. W.-W. Yam, *Inorg. Chem.*, 2004, **43**, 7421–7430.
9 V. W.-W. Yam and K. K.-W. Lo, *Chem. Soc. Rev.*, 1999, **28**, 323–334.
10 P. Ai, M. Mauro, L. De Cola, A. A. Danopoulos and P. Braunstein, *Angew. Chem., Int. Ed.*, 2016, **55**, 3338–3341.
11 P. Pérez-Galán, N. Delpont, E. Herrero-Gómez, F. Maseras and A. M. Echavarren, *Chem. – Eur. J.*, 2010, **16**, 5324–5332.
12 D. V. Partyka, T. J. Robilotto, M. Zeller, A. D. Hunter and T. G. Gray, *Organometallics*, 2008, **27**, 28–32.
13 E. Herrero-Gómez, C. Nieto-Oberhuber, S. López, J. Benet-Buchholz and A. M. Echavarren, *Angew. Chem., Int. Ed.*, 2006, **45**, 5455–5459.
14 H. Schmidbaur, H. G. Raubenheimer and L. Dobrzańska, *Chem. Soc. Rev.*, 2014, **43**, 345–380.
15 G. Moreno-Alcántar, A. Nácar-Anaya, M. Flores-Álamo and H. Torrens, *New J. Chem.*, 2016, **40**, 6577–6579.
16 S. E. Castillo-Blum, M. Flores-Alamo, D. Franco-Bodek, G. Hernandez and H. Torrens, *Inorg. Chem. Commun.*, 2014, **45**, 44–47.
17 G. Rivera, S. Bernès, C. R. de Barbarín and H. Torrens, *Inorg. Chim. Acta*, 2009, **362**, 5122–5125.
18 L. Villanueva, M. Arroyo, S. Bernès and H. Torrens, *Chem. Commun.*, 2004, 1942–1943.
19 S. Alvarez, *Dalton Trans.*, 2013, **42**, 8617.
20 A. Bondi, *J. Phys. Chem.*, 1964, **68**, 441–451.
21 T. Simler, P. Braunstein and A. A. Danopoulos, *Dalton Trans.*, 2016, **45**, 5122–5139.
22 R. Cervantes, J. Tiburcio and H. Torrens, *New J. Chem.*, 2015, **39**, 631–638.
23 J. A. Riddick, W. B. Bunger, T. Sakano and A. Weissberger, *Organic solvents: physical properties and methods of purification*, Wiley, 1986.
24 M. E. Peach, *Can. J. Chem.*, 1968, **46**, 2699–2706.
25 H. F. Emeleus and D. E. MacDuffie, *J. Chem. Soc.*, 1961, 2595–2597.
26 A. L. Bandini, G. Banditelli, D. Favretto and P. Traldi, *Rapid Commun. Mass Spectrom.*, 2000, **14**, 1499–1506.
27 M. I. Bruce and M. J. Liddell, *J. Organomet. Chem.*, 1992, **427**, 263–274.
28 *CrysAlisPro*, Agilent, 2014.
29 *CrusAlis RED*, Oxford Diffraction, 2006.
30 R. C. Clark and J. S. Reid, *Acta Crystallogr., Sect. A: Found. Crystallogr.*, 1995, **51**, 887–897.
31 G. M. Sheldrick, *Acta Crystallogr., Sect. A: Found. Crystallogr.*, 2008, **64**, 112–122.
32 L. J. Farrugia, *J. Appl. Crystallogr.*, 1999, **32**, 837–838.
33 E. Van Lenthe, E. J. Baerends and J. G. Snijders, *J. Chem. Phys.*, 1993, **99**, 4597.
34 C. van Wüllen, *J. Chem. Phys.*, 1998, **109**, 392–399.
35 M. Levy and J. P. Perdew, *J. Chem. Phys.*, 1986, **84**, 4519.
36 A. D. Becke, *Phys. Rev. A*, 1988, **38**, 3098–3100.
37 D. A. Pantazis, X.-Y. Chen, C. R. Landis and F. Neese, *J. Chem. Theory Comput.*, 2008, **4**, 908–919.
38 F. Neese, *Wiley Interdiscip. Rev.: Comput. Mol. Sci.*, 2012, **2**, 73–78.
39 L. J. Farrugia and H. M. Senn, *J. Phys. Chem. A*, 2010, **114**, 13418–13433.

 This journal is © The Royal Society of Chemistry 2017

40 L. J. Farrugia, C. Evans, H. M. Senn, M. M. Hänninen and R. Sillanpää, *Organometallics*, 2012, **31**, 2559–2570.
41 R. F. W. Bader, *Acc. Chem. Res.*, 1985, **18**, 9–15.
42 R. F. W. Bader, *Atoms in molecules: a quantum theory*, Clarendon Press, 1990.
43 C. F. Matta, R. J. Boyd and Wiley InterScience (Online service), *The quantum theory of atoms in molecules: from solid state to DNA and drug design*, Wiley-VCH, 2007.
44 L. J. Farrugia, C. Evans, D. Lentz and M. Roemer, *J. Am. Chem. Soc.*, 2009, **131**, 1251–1268.
45 T. A. Keith, *AIMAll (version 12.06.03) 2016*, 2016.
46 E. R. Johnson, S. Keinan, P. Mori-Sánchez, J. Contreras-García, A. J. Cohen and W. Yang, *J. Am. Chem. Soc.*, 2010, **132**, 6498–6506.
47 J. Contreras-García, E. R. Johnson, S. Keinan, R. Chaudret, J. P. Piquemal, D. N. Beratan and W. Yang, *J. Chem. Theory Comput.*, 2011, **7**, 625–632.
48 W. Humphrey, A. Dalke and K. Schulten, *J. Mol. Graphics*, 1996, **14**, 33–38.
49 D. Marchione, L. Belpassi, G. Bistoni, A. Macchioni, F. Tarantelli and D. Zuccaccia, *Organometallics*, 2014, **33**, 4200–4208.
50 G. Bistoni, L. Belpassi and F. Tarantelli, *Angew. Chem., Int. Ed.*, 2013, **52**, 11599–11602.
51 D. Zuccaccia, L. Belpassi, A. Macchioni and F. Tarantelli, *Eur. J. Inorg. Chem.*, 2013, **2013**, 4121–4135.
52 G. Ciancaleoni, L. Biasiolo, G. Bistoni, A. Macchioni, F. Tarantelli, D. Zuccaccia and L. Belpassi, *Chem. – Eur. J.*, 2015, **21**, 2467–2473.
53 G. Seidel, R. Mynott and A. Fürstner, *Angew. Chem., Int. Ed.*, 2009, **48**, 2510–2513.
54 A. S. K. Hashmi, *Angew. Chem., Int. Ed.*, 2008, **47**, 6754–6756.
55 D. Marchione, M. A. Izquierdo, G. Bistoni, R. W. A. Havenith, A. Macchioni, D. Zuccaccia, F. Tarantelli and L. Belpassi, *Chem. – Eur. J.*, 2017, **23**, 2722–2728.
56 A. V. Vasilyev, S. V. Lindeman and J. K. Kochi, *Chem. Commun.*, 2001, 909–910.
57 F. Groenewald, J. Dillen, H. G. Raubenheimer and C. Esterhuysen, *Angew. Chem., Int. Ed.*, 2016, **55**, 1694–1698.
58 F. Rekhroukh, L. Estévez, C. Bijani, K. Miqueu, A. Amgoune and D. Bourissou, *Angew. Chem., Int. Ed.*, 2016, **55**, 3414–3418.

This journal is © The Royal Society of Chemistry 2017

View publication stats

NJC

LETTER

View Article Online
View Journal | View Issue

Cite this: *New J. Chem.*, 2017, **41**, 10537

Received 20th June 2017,
Accepted 31st August 2017

DOI: 10.1039/c7nj02202f

rsc.li/njc

Published on 01 September 2017. Downloaded by FAC DE QUIMICA on 25/09/2017 17:15:14.

Structural effects of trifluoromethylation and fluorination in gold(I) BIPHEP fluorothiolates†

Guillermo Moreno-Alcántar, *[a] José Manuel Guevara-Vela, [b] Rafael Delgadillo-Ruíz,[a] Tomás Rocha-Rinza, [c] Ángel Martín Pendás, [b] Marcos Flores-Álamo[a] and Hugo Torrens*[a]

We synthesised and characterised two new BIPHEP-bridged digold(I) perfluorothiolates. Experimental and theoretical analyses through the Quantum Theory of Atoms in Molecules revealed that the long-range inductive effects are larger for CF_3 than they are for F. Moreover, the aurophilic interaction and F–Au contacts were qualified mostly as covalent and closed-shell type respectively.

Gold(I) coordination compounds are versatile and selective catalysts for a growing number of synthetic transformations.[1–4] Gold complexes have also drawn considerable attention due to their unique photophysical properties.[5–7] These characteristics of gold derivatives are closely related to the electronic environment surrounding the Au centre(s).[1,8,9] The prevailing assumption in organometallic chemistry is that the interaction of a substrate with a catalytic centre is a combination of electrostatic, inductive, resonance and steric contributions. On the other hand, stereospecific selectivity is a considerable challenge in modern catalysis. One strategy frequently used to bestow chirality upon reacting systems is to choose ligands with axial chirality such as tropos ligands. For example, BIPHEP (2,2′-bis(diphenylphosphino)-1,1′-biphenyl) is one of the most commonly used chiral diphosphines.[10,11] In addition, fluorination of organic moieties is an extended strategy that modifies the molecular electronic distribution and therefore the reactivity of molecules.[12–14] A better understanding about how the inductive effect of fluorine propagates in Au complexes would be a significant contribution to the set of tools available in the design of new luminescent or catalytic materials based on gold.

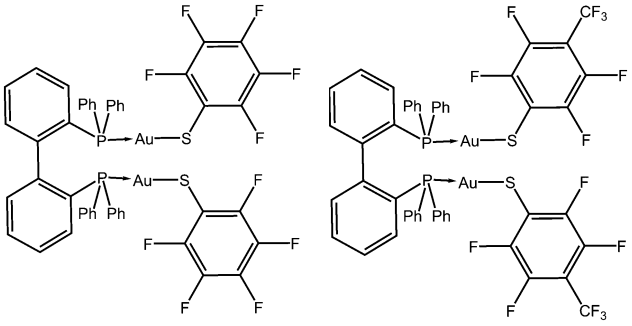

Scheme 1 Structures of the studied gold(I) compounds.

We studied herein the changes in the electronic environment around gold centres on account of the replacement of a fluorine atom in a perfluorinated thiolate ligand $-CF_3$ group *via* the difference in their corresponding inductive effects. For this purpose, we synthesised the coordination compounds $[Au_2(SR_F)_2(\mu\text{-BIPHEP})]$ with $SR_F = SC_6F_5$ (**1**) and $SC_6F_4(CF_3)$-4 (**2**) as shown in Scheme 1. Fluorination changes in the fluorothiolate ligands can potentially distort the molecular electronic environment of gold centres by altering the electron density flow to the metal. In other words, the amount and position of the fluorine substituents can influence their overall inductive effect on the Au atoms.[15] To examine these effects on the gold centres, we performed electronic structure calculations of the studied systems to later carry out the topological analysis of the electron density in agreement with the Quantum Theory of Atoms in Molecules (QTAIM)[16] and the Non-Covalent Interaction (NCI) Index.[17,18]

Crystals appropriate for X-ray diffraction analysis for systems **1** and **2** were obtained by slow evaporation of concentrated CH_2Cl_2/CH_3CN 1:1 solutions at room temperature (293–298 K). The corresponding experimental molecular structures are shown in Fig. 1. The geometries of the two compounds are very similar, with the observed gold coordination being almost linear in both compounds. There are, however, noticeable differences between compounds **1** and **2**: for example, (i) the length of the Au–Au bond, (ii) the distance between the fluorine in the *ortho* position

---

[a] *School of Chemistry, National Autonomous University of Mexico, Circuito Escolar, Ciudad Universitaria, Delegación Coyoacán, 04510, Mexico City, Mexico. E-mail: lgma@comunidad.unam.mx, torrens@unam.mx*

[b] *Department of Analytical and Physical Chemistry, University of Oviedo, E-33006, Julián Clavería, 8, 33006, Oviedo, Spain*

[c] *Institute of Chemistry, National Autonomous University of Mexico, Circuito Exterior, Ciudad Universitaria, Delegación Coyoacán, 04510, Mexico City, Mexico*

† Electronic supplementary information (ESI) available: Experimental and computational details. CCDC 1545829 and 1545830. For ESI and crystallographic data in CIF or other electronic format see DOI: 10.1039/c7nj02202f

Published on 01 September 2017. Downloaded by FAC DE QUIMICA on 25/09/2017 17:15:14.

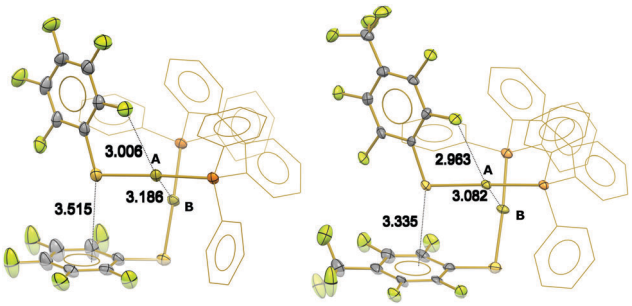

Fig. 1 ORTEP representation of the X-ray diffraction structures for **1** (left) and **2** (right) along with some selected intramolecular distances. BIPHEP phenyl rings are displayed as wireframes and H atoms are omitted for clarity. The colour scheme used is as follows: Au, golden; F, green; S, yellow; P, orange and C, grey.

of the thiolate ring and one of the Au atoms and (iii) the separation between the sulphur atom and the nearby thiolate ring. All of these geometrical parameters are smaller in **2** as compared with those in **1**. In a sense, compound **2** is appreciably more ''compact'' than complex **1**.

Another feature of the experimental structures of **1** and **2** is the inequivalence between the two Au atoms in the same molecule. One of them, labelled A in Fig. 1, is closer to an *ortho*-fluorine from the thiophenyl group, while the other (B) has no contact with any F atom. From now on, we denote by S_X and P_X the sulphur and phosphorus atoms bonded directly to atom X, with X being equal to A or B. Table 1 shows some selected bond lengths in compounds **1** and **2**. The differences in Au–P and Au–S bond distances are rather small. Overall, bond lengths are almost identical for covalent interactions in both compounds.

In contrast, the differences between these two complexes become more pronounced when we consider their weak intramolecular contacts. The Au–Au, Au–F and S–π_{phenyl} interactions are similarly affected by the substitution of –F by $-CF_3$ in the thiolate ring. In every case, the observed distances are smaller in the *p*-CF_3 substituted thiolate. These interactions in adducts **1** and **2** are examined below.

In both molecules, the S–π_{phenyl} distances (Fig. 1) are shorter than the sum of the van der Waals radii of C and S (Σr_{vdW} = 3.66 Å[19,20]), a condition which indicates the occurrence of a weak interaction. These contacts might have an important influence in the form of the examined molecules as they occur in many structures of the CSD,[21] of which five are gold compounds.[22–26] The hapticity of these contacts is close to three. S–π_{phenyl} interactions have an important effect on the conformation of the investigated molecules but it is hard to estimate their importance because they are cooperative with the aurophilic interaction. We also noted that the distances associated with these contacts are reduced as a consequence of the *p*-F to *p*-CF_3 substitution.

The distance between the fluorine in the *ortho* position of the thiolate ring and the A gold atom is short as well, and it is smaller than the sum of the van der Waals radii of Au and F (Σr_{vdW} = 3.13 Å) in molecules **1** and **2** (3.006 Å and 2.963 Å respectively). Although fluorine is a hard base and gold is a soft acid, and therefore, its interaction is in principle unexpected, there are hundreds of Au–F vdW interactions in Au complexes with C–F bonds.[21] This recurrent interaction has not been theoretically examined until now. Additionally, compound **2** presents also intermolecular Au–F contacts which can be found at larger separation distances (3.558 Å). Fig. 2 displays a lateral view of the NCI isosurfaces surrounding the S_A–Au_A–P_A region for compound **1**. Green surfaces reveal weak interactions among A with its surrounding fluorine and hydrogen atoms. There is an interaction between gold A and one of the hydrogens in the phosphine group which might be characterised as an anagostic interaction on account of its geometrical and electronic parameters, *i.e.* an electronic rich metal centre interacting with a hydrogen atom.[27] We found no bond path between the involved H and Au atoms. This result suggests that the existence of a bond path is not a necessary condition for the attainment of an anagostic interaction in the same sense in which it is not a requirement for the existense of an H-bond;[28] this is a new finding that could be helpful in the characterization of Au–H interactions, which is consistent with the previously stated existence of bond paths for agostic Au–H contacts.[29] We checked the availability of conformations in which the sterical hindrance of the Au–F and Au–H is noticeably decreased. The results indicate that neither the Au–F nor the Au–H interactions occur due to geometrical constraints, but instead they are indeed favoured in the observed structures.

The Au–F interactions in these types of compounds have barely been studied. QTAIM analyses provide valuable insights into these contacts. The values of (i) the electron density at the

Table 1 Distances (Å) between selected pairs of atoms for molecules **1** and **2**

Distance	Compound **1**	Compound **2**
Au_A–P_A	2.2566(17)	2.2559(17)
Au_B–P_B	2.2607(17)	2.2601(16)
Au_A–S_A	2.3054(18)	2.3033(17)
Au_B–S_B	2.3183(17)	2.3205(17)
Au_A–Au_B	3.1862(5)	3.0823(5)
Au_A–F	3.006(4)	2.963(4)

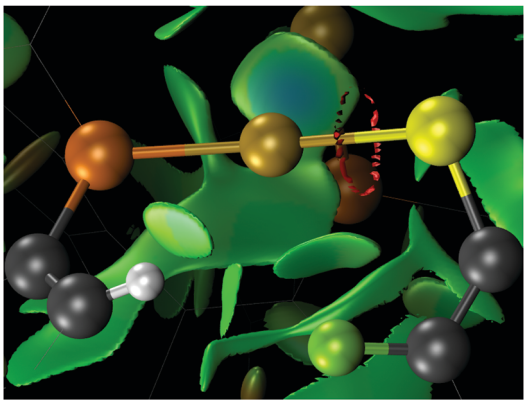

Fig. 2 NCI isosurfaces showing the Au–F, Au–H, and F–H non-covalent interactions in $[Au_2(SC_6F_5)_2(\mu\text{-BIPHEP})]$ **1**. The isosurface value is s = 0.5 a.u. with $\rho \leq 0.015$ a.u. Only the relevant atoms for these contacts are shown. The colour scheme is the same as that used in Fig. 1.

 This journal is © The Royal Society of Chemistry and the Centre National de la Recherche Scientifique 2017

Published on 01 September 2017. Downloaded by FAC DE QUIMICA on 25/09/2017 17:15:14.

corresponding Bond Critical Point (BCP), $\rho(\mathbf{r}_{BCP})$,[16] a qualitative descriptor of bond strength, and (ii) the Laplacian of the charge distribution ($\nabla^2\rho(\mathbf{r}_{BCP})$)[16] are small. On the other hand, the energy density at the BCP is predominantly kinetic. These features of the electronic density distribution are indicative of a closed shell contact. The associated delocalisation index (DI), which is a measure of the number of electrons shared between two atoms, is small (<0.1 a.u.) corresponding to a weak interaction.[30] The Au–F contacts are only observed for atom A in both compounds. Thus, we can evaluate the influence of the fluorine contact on gold by comparing the interactions held by centres A and B. Indeed, the gold atom that interacts with fluorine, A, shows no charge, while that with no interaction, B, is slightly negative (−0.03 and −0.02 a.u. for systems **1** and **2** respectively). Moreover, the fluorine atom bonded to Au is moderately more negative (−0.62 a.u. in adduct **1** and −0.63 a.u. in complex **2**) than their non-interacting counterparts at the *ortho* position of the thiolate rings (−0.60 a.u. in both compounds) The Au and F charges could indicate certain charge transfer from gold to fluorine through the observed interaction. Although these charge donations might seem small, the transfer of centesimals of atomic units of charge can have significant consequences. For example, there is a transfer of 0.01 to 0.03 a.u. from the Hydrogen Bond (HB) acceptor to the HB donor. This transference of charge is related to HB cooperative effects in small water clusters.[31] Finally, we indicate that a charge transfer of 0.01 a.u. is associated with a change of roughly 0.1 atomic unit of energy, *i.e.*, 6 kcal mol^{-1}, which is by no means negligible in the context of non-covalent interactions.[32]

Similarly to the C–S and Au–F interactions discussed above, Au–Au distances in the studied compounds are smaller than the sum of their van der Waals radii. This feature has repeatedly been used as an indicator of aurophilic contacts.[33,34] Notwithstanding the occurrence of several van der Waals interactions in the examined complexes, those between the gold centres are the most important as indicated in the scale shown in the NCI analysis of Fig. 3. The NCI surfaces indicate that the aurophilic interactions are attractive in nature. This attraction seems to be stronger in compound **2** than it is in system **1** since the associated NCI blue surface is larger in the former system than in the latter.[35]

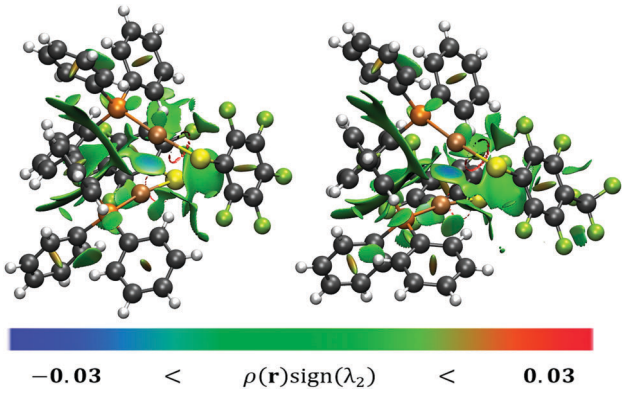

Fig. 3 NCI isosurfaces showing non-covalent interactions in compounds **1** (left) and **2** (right). Aurophilic attractive interactions are indicated with blue-coloured surfaces. The isosurface value is s = 0.5 a.u. with $\rho \leq$ 0.015 a.u. The colour code is the same as that in Fig. 1 and 2 and the hydrogen atoms are shown in white.

Table 2 Different QTAIM indicators characterising the nature of the interaction between Au atoms in compounds **1** and **2**. All local properties are reported at the Au–Au bond critical point. Atomic units are used throughout

Descriptor	Compound **1**	Compound **2**
$\rho(\mathbf{r}_{BCP})$	0.0236	0.0284
$\nabla^2\rho(\mathbf{r}_{BCP})$	0.0583	0.0721
$H(\mathbf{r}_{BCP})$	−0.0002	−0.0011
$G(\mathbf{r}_{BCP})/\rho(\mathbf{r}_{BCP})$	0.6271	0.6760
DI	0.2755	0.3172

Table 2 shows a summary of some QTAIM properties used in the characterisation of this aurophilic contact. Related to the Au–Au interaction, $\rho(\mathbf{r}_{BCP})$ is quite small and it is very similar in both systems. $\nabla^2\rho(\mathbf{r}_{BCP})$ is small and positive, indicating a closed shell interaction. The negative value of the energy density $H(\mathbf{r}_{BCP})$, on the other hand, suggests a contact with some degree of covalency.[36] Likewise, the $G(\mathbf{r}_{BCP})/\rho(\mathbf{r}_{BCP})$ ratio is smaller than 1.0, as it is in many other covalent bonds involving transition metals.[30] Thus, the examined aurophilic contact has a substantial covalent character.

Our analyses also reveal significant differences in the Au–Au interactions in compounds **1** and **2**. The values of all the local indices, $\rho(\mathbf{r}_{BCP})$, $H(\mathbf{r}_{BCP})$ and $G(\mathbf{r}_{BCP})/\rho(\mathbf{r}_{BCP})$, indicate that the Au–Au bond is stronger in compound **2** than in complex **1**. The delocalisation index between the gold atoms is also larger for compound **2**. These results point that the Au–Au bond has a greater interaction energy and it is more covalent in complex **2** as compared with adduct **1**.

The results discussed above were obtained by considering the experimental distances in the crystals of systems **1** and **2**. We optimised the structures of these molecules in the gas phase to investigate how the crystal packing of the compounds affects the covalency of the Au–Au interactions. In the optimised geometries, which are shown in the ESI,† the Au–Au distance becomes slightly shorter as compared with the crystalline structures (2.986 and 2.973 Å for molecules **1** and **2**, respectively). Since the short distances between atoms in the molecule are not strongly influenced by crystal packing, the increase in covalency is not generated by the steric effects of the substituents but rather by their different inductive patterns.

Another relevant aspect is the different inductive effects on the sulphur atoms of systems **1** and **2**. The atomic charge of S_A in compound **1** is −0.14 a.u., while in compound **2** it is −0.11 a.u. Hence, S_A is a poorer σ-donor and a better π-acceptor in the latter compound, which allows the A centre to strengthen the aurophilic contact.

As a way to study the inductive effect of the substituents separately from other phenomena, we performed gas phase calculations of fluorobenzene and trifluoromethyl-benzene molecules. We found that the positive charge of the *ipso* carbon is larger for C_6H_5–F (0.49 a.u.) than for C_6H_5–CF_3 (0.01 a.u.). In contrast, the net charge of the CH group in the *para* position for

Published on 01 September 2017. Downloaded by FAC DE QUIMICA on 25/09/2017 17:15:14.

Ph-CF_3 (0.02 a.u.) is twice the value for Ph–F (0.01 a.u.). Thus, in the control systems (C_6H_5–X, X = F, CF_3), the long-range inductive effect of the trifluoromethyl group is larger than that of the fluorine. These observations are in agreement with the findings of True and coworkers,[37] who concluded that the inductive effect of fluorine is large on adjacent atoms but small for groups which are further away as opposed to the behaviour of CF_3 whose long range inductive effects are more evident.

In conclusion, we analysed the effect on an Au–Au contact caused by changing the *ortho*-fluorine substituent of a perfluorinated thiolate ligand to a trifluoromethyl group. We characterised the Au–F interaction theoretically as a closed shell weak interaction. Besides, our results show how the aurophilic interaction has a considerable covalent character. The analysis of QTAIM charges and the use of model systems indicate that the inductive effect all over the S–Au fragment is larger due to the trifluoromethyl moiety than it is on account of the fluorine group. These differences in the inductive effect are reflected in the length of the aurophilic interactions under examination. The calculated quantum topological indicators show that the Au–Au interaction is stronger for the compound with the trifluoromethyl substituent. The same trend is observed in other weak intramolecular interactions. Overall, we expect that this new perspective on the impact of the inductive effects of different substituents on aurophilic interactions will prove valuable in the understanding of these important contacts in gold chemistry.

Conflicts of interest

There are no conflicts to declare.

Acknowledgements

We acknowledge the technical support of USAII at the School of Chemistry, UNAM. We are also thankful to DGAPA-UNAM, CONACYT-Mexico and the Spanish Government for funding through projects IN202314, CB-2012/177498 and CTQ-2015-65790-P, respectively, along with PhD scholarships 270993 (G.M.A.) and 381483 (J.M.G.V.). We also express our gratitude to DGTIC/UNAM for supercomputer resources (project LANCAD-UNAM-DGTIC-250).

Notes and references

1 A. M. Echavarren, A. S. K. Hashmi and F. D. Toste, *Adv. Synth. Catal.*, 2016, **358**, 1347.
2 D. J. Gorin and F. D. Toste, *Nature*, 2007, **446**, 395–403.
3 A. M. Echavarren, *Nat. Chem.*, 2009, **1**, 431–433.
4 R. L. LaLonde, Z. J. Wang, M. Mba, A. D. Lackner and F. D. Toste, *Angew. Chem., Int. Ed.*, 2010, **49**, 598–601.
5 X. He and V. W.-W. Yam, *Coord. Chem. Rev.*, 2011, **255**, 2111–2123.
6 V. W.-W. Yam and E. C.-C. Cheng, *Chem. Soc. Rev.*, 2008, **37**, 1806–1813.
7 M. C. Blanco, J. Cámara, M. C. Gimeno, A. Laguna, S. L. James, M. C. Lagunas and M. D. Villacampa, *Angew. Chem., Int. Ed.*, 2012, **51**, 9777–9779.
8 Z. Li, C. Brouwer and C. He, *Chem. Rev.*, 2008, **108**, 3239–3265.
9 D. J. Gorin, B. D. Sherry and F. D. Toste, *Chem. Rev.*, 2008, **108**, 3351–3378.
10 K. Aikawa, K. Mikami, C. H. Kim, S. R. Choi, M. J. Jun, K. Hirotsu, D. P. Curran, S. Kawakami, M. Konishi, K. Yamamoto, M. Kumada, C. H. Senanayake, C.-K. Shih, L. Zuvela-Jelaska, G. Nabozny and D. S. Thomson, *Chem. Commun.*, 2012, **48**, 11050.
11 K. Mikami, K. Aikawa, Y. Yusa, J. J. Jodry and M. Yamanaka, *Synlett*, 2002, 1561–1578.
12 R. Berger, G. Resnati, P. Metrangolo, E. Weber and J. Hulliger, *Chem. Soc. Rev.*, 2011, **40**, 3496.
13 M. N. Pillay and W. E. van Zyl, *Comments Inorg. Chem.*, 2012, **33**, 122–160.
14 G. Moreno-Alcántar, A. Nácar-Anaya, M. Flores-Álamo and H. Torrens, *New J. Chem.*, 2016, **40**, 6577–6579.
15 V. I. Galkin, *J. Phys. Org. Chem.*, 1999, **12**, 283–288.
16 R. F. W. Bader, *Atoms in molecules: a quantum theory*, Clarendon Press, 1990.
17 J. Contreras-García, E. R. Johnson, S. Keinan, R. Chaudret, J. P. Piquemal, D. N. Beratan and W. Yang, *J. Chem. Theory Comput.*, 2011, **7**, 625–632.
18 E. R. Johnson, S. Keinan, P. Mori-Sánchez, J. Contreras-García, A. J. Cohen and W. Yang, *J. Am. Chem. Soc.*, 2010, **132**, 6498–6506.
19 A. Bondi, *J. Phys. Chem.*, 1964, **68**, 441–451.
20 S. Alvarez, *Dalton Trans.*, 2013, **42**, 8617.
21 C. R. Groom, I. J. Bruno, M. P. Lightfoot and S. C. Ward, *Acta Crystallogr., Sect. B: Struct. Sci., Cryst. Eng. Mater.*, 2016, **72**, 171–179.
22 E. C.-C. Cheng, W.-Y. Lo, T. K.-M. Lee, N. Zhu and V. W.-W. Yam, *Inorg. Chem.*, 2014, **53**, 3854–3863.
23 H. Hiraga, H. Miyasaka, R. Clérac, M. Fourmigue and M. Yamashita, *Inorg. Chem.*, 2009, **48**, 2887–2898.
24 C. E. Strasser, S. Cronje, H. Schmidbaur and H. G. Raubenheimer, *J. Organomet. Chem.*, 2006, **691**, 4788–4796.
25 Q.-F. Sun, T. K.-M. Lee, P.-Z. Li, L.-Y. Yao, J.-J. Huang, J. Huang, S.-Y. Yu, Y.-Z. Li, E. C.-C. Cheng and V. W.-W. Yam, *Chem. Commun.*, 2008, 5514.
26 N. Oberbeckmann-Winter, P. Braunstein and R. Welter, *Organometallics*, 2005, **24**, 3149–3157.
27 W. I. Sundquist, D. P. Bancroft and S. J. Lippard, *J. Am. Chem. Soc.*, 1990, **112**, 1590–1596.
28 J. R. Lane, J. Contreras-García, J.-P. Piquemal, B. J. Miller and H. G. Kjaergaard, *J. Chem. Theory Comput.*, 2013, **9**, 3263–3266.
29 H. Schmidbaur, H. G. Raubenheimer and L. Dobrzańska, *Chem. Soc. Rev.*, 2014, **43**, 345–380.
30 P. Macchi and A. Sironi, *Coord. Chem. Rev.*, 2003, **238**, 383–412.
31 J. M. Guevara-Vela, R. Chávez-Calvillo, M. García-Revilla, J. Hernández-Trujillo, O. Christiansen, E. Francisco,

 This journal is © The Royal Society of Chemistry and the Centre National de la Recherche Scientifique 2017

Á. Martín Pendás and T. Rocha-Rinza, *Chem. – Eur. J.*, 2013, **19**, 14304–14315.
32 A. M. Pendás, M. A. Blanco and E. Francisco, *J. Comput. Chem.*, 2009, **30**, 98–109.
33 H. Schmidbaur and A. Schier, *Chem. Soc. Rev.*, 2012, **41**, 370–412.
34 H. Schmidbaur, *Nature*, 2001, **413**, 31–33.
35 V. Duarte Alaniz, T. Rocha-Rinza and G. Cuevas, *J. Comput. Chem.*, 2015, **36**, 361–375.
36 D. Cremer and E. Kraka, *Angew. Chem., Int. Ed.*, 1984, **23**, 627–628.
37 J. E. True, T. D. Thomas, R. W. Winter and G. L. Gard, *Inorg. Chem.*, 2003, **42**, 4437–4441.

Published on 01 September 2017. Downloaded by FAC DE QUIMICA on 25/09/2017 17:15:14.

View publication stats

ChemPubSoc Europe

DOI: 10.1002/chem.201703436

CHEMISTRY
A European Journal
Full Paper

Noncovalent Interactions

Hydrogen-Bond Weakening through π Systems: Resonance-Impaired Hydrogen Bonds (RIHB)

José Manuel Guevara-Vela,[a] Eduardo Romero-Montalvo,[b] Alejandra del Río-Lima,[b] Ángel Martín Pendás,[a] Marcos Hernández-Rodríguez,[b] and Tomás Rocha Rinza*[b]

The concept of resonance-impaired hydrogen bonds (RIHBs) is introduced to describe interactions in which a network of conjugated bonds strongly hinders a hydrogen bond (HB). For this purpose, the intramolecular RIHB between the extremes of the conjugated base 3-aminoacrylaldehyde, namely, H–N=CH–CH=CH–O$^-$, which has a formation energy considerably lower (at least 8 kcal mol^{-1}) than that of typical σ-HBs involving charged species, is examined. The interacting quantum atoms (IQA) energy partition indicates that, despite the non-zero net charge of the fragments involved in these RIHBs, these interactions present smaller total IQA classical interactions (comprising the sum of electrostatic attractions, charge transfer, and charge and polarisation) than that of other neutral resonance-assisted hydrogen bonds (RAHBs) and σ-HBs. As opposed to typical RAHBs, the occurrence of an RIHB involves an increase in the covalent-bond order of double bonds, whereas single bonds exhibit the opposite behaviour, as revealed by electron delocalisation. Nevertheless, a lack of aromaticity is not a source of destabilisation for RIHBs. This research is expected to contribute to understanding the intricate interplay between HBs and conjugated π systems.

Introduction

Hydrogen bond (HB) cooperative/anticooperative effects, that is, the mutual strengthening/weakening of two or more HBs, are crucial in the structure and stability of molecules and supramolecular clusters that present these interactions.[1,2] For example, the oxygen–oxygen distance in small water clusters is reduced due to HB cooperativity,[3] and the relative energy of the isomers of the H_2O hexamer is determined by a balance between the number of HBs in the system and their non-additive properties.[4] The HB cooperative effects in O–H···O–H motifs were recently used to explain the bifunctional catalytic role of $(H_2O)_2$ and $(H_2O)_3$ in the formation of H_2SO_4 in acid rain and the hydrolysis of CO_2 in the generation of H_2CO_3.[5] Such HB non-additivity has been related to the flow of charge density from the HB acceptor to the HB donor that occurs throughout σ bonds, for instance, in hydrogen cyanide chains,[6] H–C≡N···H–C≡N···H–C≡N···H–C≡N, which display a significantly enhanced HCN dipole moment, compared with that of the value in vacuo. This contributes to the large dielectric constant of this compound in the liquid phase.[7] Other examples of the redistribution of charge density that lead to HB non-additivity are those occurring in double HB donors and acceptors, which lead to HB anticooperativity in antidromic cycles.[4]

Charge transfer, leading to HB cooperative and anticooperative effects, can also occur across networks of π bonds. For instance, Wu and co-workers associated HB strengthening and weakening with the occurrence of aromaticity and antiaromaticity in dimers of π-conjugated heterocycles, as well as acyclic amides and amidines.[8,9] Resonance-assisted hydrogen bonds (RAHB)[10–12] constitute other relevant systems, in which the interplay between a conjugated π network and an HB strengthen the latter interaction. The simple classical resonance structures of malondialdehyde (**1**) and 3-aminoacrylaldehyde (**2**) shown in Figure 1 suggest 1) a strengthening of the H···O bond in the HB acceptor, and 2) a weakening of the X–H linkage (X = O, N in **1** and **2**, respectively).

Both conditions contribute to strenthening of the intramolecular HB in **1** and **2**, compared with those of σ-OH···O and NH···O HBs. Two HBs can also be connected throughout RAHBs to exert cooperative and anticooperative effects on each other.[13,14]

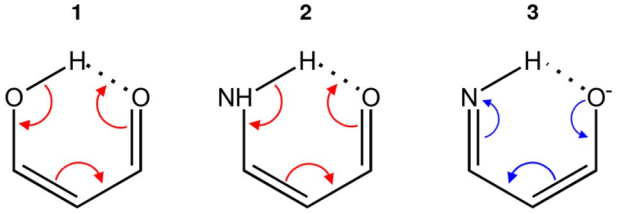

Figure 1. RAHBs in malondialdehyde (**1**) and 3-aminoacrylaldehyde (**2**). The resonance-impaired hydrogen bonds (RIHBs) in the conjugated base of **2**, that is, compound **3** is shown as well. The arrow pushing shown in red/blue strengthens/weakens the schematised HBs.

[a] J. M. Guevara-Vela, Prof. Dr. Á. Martín Pendás
Department of Analytical and Physical Chemistry
University of Oviedo, 33006, Oviedo (Spain)

[b] E. Romero-Montalvo, A. del Río-Lima, Prof. Dr. M. Hernández-Rodríguez, Prof. Dr. T. Rocha Rinza
Institute of Chemistry, National Autonomous University of Mexico
Circuito Exterior, Ciudad Universitaria, Delegación Coyoacán C.P. 04510, Mexico City (Mexico)
E-mail: tomasrocharinza@gmail.com

Supporting information and the ORCID identification number(s) for the author(s) of this article can be found under https://doi.org/10.1002/chem.201703436.

© 2017 Wiley-VCH Verlag GmbH & Co. KGaA, Weinheim

On the other hand, Figure 1 shows the intramolecular HB in the conjugated base of **2**, namely, anion **3**. This species is generated by the loss of an N–H hydrogen and subsequent tautomerisation to the enolate, by virtue that an enol is more acidic than an enamine. The resonance structure shown in Figure 1 suggests that the electron-withdrawing nature of the HN=CH–CH group makes the HB donor (i.e., the imine group) more electron-rich. Concomitantly, the corresponding acceptor loses electron density through the network of conjugated bonds. These two facts weaken the intramolecular HB in **3**. In other words, the π system in this anion hinders intramolecular HB, that is, this HB is more accurately named resonance-impaired hydrogen bond (RIHB).

More specifically, herein, we focus on a comparison of RAHBs and RIHBs, with the aim of providing insights into the factors that cause that a π system to strengthen or weaken a given HB. For this purpose, we have compared the RAHBs in **2** and the RIHB in **3**, with similar intermolecular HBs, CH_2=CH–NH–H···O=CH–CH=CH_2 ($\mathbf{2}_{inter}$) and H_2C=CH–CH=N–H···$^-$O–CH=CH_2 ($\mathbf{3}_{inter}$; Figure 2). Both the HB donors and acceptors in $\mathbf{2}_{inter}$

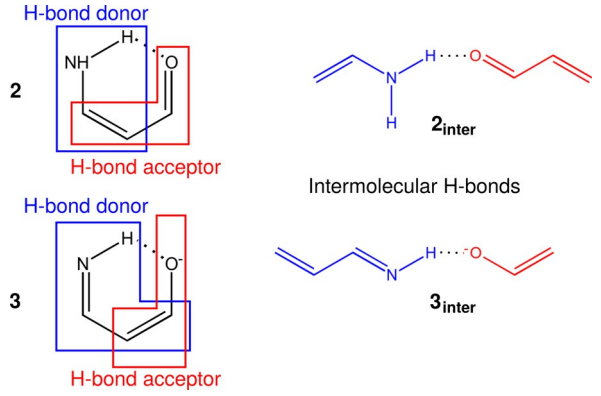

Figure 2. Intermolecular HBs $\mathbf{2}_{inter}$ and $\mathbf{3}_{inter}$ used to examine 1) the RAHB in **2**, and 2) the RIHBs in its conjugated base **3**, respectively. The HB donors are indicated in blue, whereas the HB acceptors are displayed in red.

and $\mathbf{3}_{inter}$ are conjugated for a better comparison with the intramolecular HBs in **2** and **3**. We have used quantum chemical topology tools, namely, the quantum theory of atoms in molecules (QTAIM), the interacting quantum atoms (IQA) partition of the electronic energy and the analysis of the electron localisation function (ELF), to obtain further insights into the factors that stabilise RAHBs and RIHBs. These methods of wave function analyses are based on the first-order reduced density matrix, $\rho_1(\mathbf{r}_1,\mathbf{r}_1')$, and on the one- and two-electron density functions, $\rho_1(\mathbf{r}_1)$ and $\rho_2(\mathbf{r}_1,\mathbf{r}_2)$, respectively. We used these approaches because they have provided valuable information about the nature of HB cooperativity and anticooperativity occurring both across σ and π bonds.[4,5,13,15,16] Thus, our results establish relevant differences between RAHBs and RIHBs, and hence, we expect that they will aid in the understanding of the complicated interplay between HBs and π-conjugated systems.

Methods

The methodologies used for the analysis of RAHBs and RIHBs should be suitable to describe interactions in the long- and short-distance regimes. This circumstance arises because part of the account presented herein concerns the mutual effect between the π-conjugated system and HBs occurring in RAHBs and RIHBs. Hence, we decided to use methods that could account for both HBs and electron delocalisation on the same footing, that is, through the study of scalar fields derived from the electronic state vector, such as the charge distribution $\rho(\mathbf{r})$ and the pair density $\rho_2(\mathbf{r}_1,\mathbf{r}_2)$.

The investigation of these scalar fields is best achieved through real-space theories of chemical bonding, such as QTAIM. This approach is built upon the topology of $\rho(\mathbf{r})$, which allows a partition of three-dimensional space into disjointed regions associated with atoms forming functional groups, molecules and molecular clusters. In this way, QTAIM provides a seamless link between short- and long-range interactions. QTAIM basins can be understood as proper open quantum mechanical subsystems for which one can obtain well-behaved expectation values of Dirac observables.

We can also use QTAIM to analyse changes in the chemical bonding scenario when a given intramolecular HB is formed or dissociated. For this purpose, we have considered the integration of the exchange-correlation hole over the topological atoms to calculate delocalisation indices [DIs; Eq. (1)]:[17]

$$\delta(\Omega,\Omega') = 2\left|\int_{\Omega}\int_{\Omega'}\rho(\mathbf{r}_1)\rho(\mathbf{r}_2)f(\mathbf{r}_1,\mathbf{r}_2)\mathrm{d}\mathbf{r}_1\mathrm{d}\mathbf{r}_2\right| \quad (1)$$

in which $\Omega \neq \Omega'$, that is, Ω and Ω′ are two different atoms, and $f(\mathbf{r}_1,\mathbf{r}_2)$ is the correlation factor that relates the pair density, $\rho_2(\mathbf{r}_1,\mathbf{r}_2)$, and $\rho(\mathbf{r}_1)$ [Eq. (2)]:[18]

$$\rho_2(\mathbf{r}_1,\mathbf{r}_2) = \rho(\mathbf{r}_1)\rho(\mathbf{r}_2)[1+f(\mathbf{r}_1,\mathbf{r}_2)] \quad (2)$$

The DI $\delta(\Omega,\Omega')$ is a measure of the number of electrons shared between two atoms, Ω and Ω′, and therefore, of the covalency of the bond between them.

Finally, electron delocalisation is intimately related to other chemical phenomena, such as aromaticity. We used DIs to compute the following aromaticity indices: 1) $I_{ring}(\mathscr{A})$, a measurement that involves the sum of the σ- and π-electron populations,[19] 2) MCI($\mathscr{A}$), which assess the values of delocalisation in comparison with those of benzene,[20] and 3) $I_{NG}(\mathscr{A})$ together with 4) $I_{NB}(\mathscr{A})$, which utilise the Hückel molecular orbital approximation to match the topological resonance energies per π electron of aromatic annulenes and their ions,[21] within the pseudo-cycles of systems **2** and **3**. We proceeded in this way in virtue of the relationship that can exist between aromaticity, antiaromaticity and HB strength briefly discussed in the Introduction.

Despite the definition of DIs in QTAIM, the theoretical framework of this approach yields only one-atom contributions to the total electronic energy. One is often interested in how the interaction energy between two atoms or functional groups is

© 2017 Wiley-VCH Verlag GmbH & Co. KGaA, Weinheim

affected when it results in a change in the system of interest. The IQA energy partition offers a solution to this situation by considering the one- and two-domain division of the non-relativistic Born–Oppenheimer electronic energy [Eq. (3)]:[22]

$$E = \sum_{X} E^{X}_{net} + \sum_{X>Y} E^{XY}_{int} = \sum_{X} T^{X} + V^{XX}_{ne} + V^{XX}_{ee} + \sum_{X>Y} V^{XY}_{nn} + V^{XY}_{ne} + V^{YX}_{ne} + V^{XY}_{ee} \quad (3)$$

in which E^{X}_{net} and E^{XY}_{int} are the IQA net and interaction energies of atom X and pair XY. The quantity T^{X} represents the contribution to the kinetic energy from basin X. Finally, the terms V^{XY}_{ne} and V^{XY}_{ee} denote 1) the attraction between the nucleus of domain X and the electrons of basin Y, and 2) the repulsion of electrons in X and Y. The conditions X = Y and X ≠ Y correspond to intra- and inter-atomic contributions, respectively, to the electronic energy.

It is possible to obtain further insight into the nature of the interaction between two atoms by considering the Coulombic and exchange-correlation components of electronic repulsion. This allows to the IQA interaction energy between two atoms to be split into classical (or Coulombic; V^{XY}_{cl}) and exchange-correlation (V^{XY}_{xc}) contributions [Eq. (4)]:[22]

$$E^{XY}_{int} = V^{XY}_{cl} + V^{XY}_{xc} \quad (4)$$

The intra-atomic potential energy can also be partitioned, as indicated in Equation (4), into V^{X}_{cl} and V^{X}_{xc}.

Because QTAIM provides an atomic partition of an electronic system, other scalar fields related to the localisability of electrons have shown their ability to partition the 3D space into the chemistry of the traditional core and lone and bonding pairs. One of the best known is ELF, which was introduced by Becke and Edgecombe,[23] and has been extensively used since the work of Savin and Silvi.[24] The ELF, initially defined for Hartree–Fock wave functions only, was further generalised by Savin et al.,[25] who related it to the excess kinetic energy density of an electron system, with respect to the bosonic von Weizsäcker reference. The evolution of ELF basins along a chemical process has been shown to correlate well with standard chemical wisdom, particularly when lone pairs play a significant role, which is the case herein.

Computational Details

Previous studies indicated that hydrogen bonding was well described in second-order Møller–Plesset perturbation theory upon employing augmented Dunning basis sets.[26] Thus, all geometries reported herein were obtained by using the MP2[27] method in its efficient RIJCOSX variant,[28] in conjunction with the aug-cc-pVTZ basis set,[29] as implemented in the Orca software.[30] Harmonic frequency calculations were performed to confirm that the optimised structures indeed corresponded to local minima.

The QTAIM and IQA analyses were made with our Promolden code,[31] with B3LYP/aug-cc-pVTZ electron densities, which were read directly from the Orca output files with the aid of the program Molden2AIM.[32,33] This methodology was successfully used, along with quantum chemical topology, in the study of RAHBs.[34] We considered an approximation to the one- and two-atom terms of the Kohn–Sham exchange-correlation energy[35] to perform the IQA energy partition. The β spheres, with radii of between 0.1 and 0.3 Bohr, were used throughout the computation, along with restricted angular Lebedev quadratures. This range of radii was selected as a compromise between the required accuracy and associated computational cost. There are two choices regarding the size of β spheres in IQA integrations that usually give good results: 1) small β spheres are useful to eliminate nuclear singularities, and 2) large β spheres (with radii typically equal to 90% of the distance to the closest bond critical point) take advantage of the shape of the volume for integration by using a coarser grid with as much space as possible; thus reducing the computational effort. We observed that the former approach resulted in better IQA total energies for the systems studied herein, and hence, it was the procedure chosen in this investigation. Inside the β spheres, 451 mapped radial point trapezoidal quadratures and L expansions truncated at $l = 10$ were employed, while outside the β spheres the number of mapped radial points was increased to 651 and L up to $l = 12$ was used.

ELF analysis was also carried out by using the in-house code Promolden, available upon request.[31] The aromaticity indices, $I_{ring}(\mathscr{A})$, $I_{NG}(\mathscr{A})$, $I_{NB}(\mathscr{A})$ and MCI($\mathscr{A}$), were computed with the software Esi-3D.[36] Finally, the software Avogadro[37] was used to visualise molecular structures.

Results and Discussion

Electronic structure calculations

Table 1 shows the electronic structure results for the formation energy of the HBs in **2** and **3**, along with the respective inter-molecular HBs with which they are compared, namely, $\mathbf{2}_{inter}$ and $\mathbf{3}_{inter}$. As expected, the interaction between the hydrogen-bonded atoms and the π system in the RAHB increases the formation energy of the HB. We estimate the energetic effect of the RAHB to be that shown in Equation (5).

Table 1. Formation energy for the HBs in systems **2**, $\mathbf{2}_{inter}$, **3** and $\mathbf{3}_{inter}$. Values are reported in kcal mol^{-1}.

System	ΔE^{HB}_{form}
2	−7.9
$\mathbf{2}_{inter}$	−3.6
3	−2.6
$\mathbf{3}_{inter}$	−14.3

$$\Delta\Delta E_{RAHB} = \Delta E^{HB}_{form}(\mathbf{2}) - \Delta E^{HB}_{form}(\mathbf{2}_{inter}) = -4.3\ \text{kcal mol}^{-1} \quad (5)$$

On the contrary, the interaction between the HB donor and acceptor in anion **3** reduces the formation of the HB quite noticeably, in comparison with that of the HB in $\mathbf{3}_{inter}$. Simlar to Equation (5), the RIHB effect reduces the magnitude of ΔE^{HB}_{form} as shown in Equation (6).

$$\Delta\Delta E_{RIHB} = \Delta E^{HB}_{form}(\mathbf{3}) - \Delta E^{HB}_{form}(\mathbf{3}_{inter}) = 11.7\ \text{kcal mol}^{-1} \quad (6)$$

© 2017 Wiley-VCH Verlag GmbH & Co. KGaA, Weinheim

Indeed, the absolute value of the formation energy of the intramolecular HB in anion **3**, $|\Delta E_{form}^{RIHB}(\mathbf{3})| = 2.6$ kcal mol^{-1} (Figure 1), is significantly lower than that of the corresponding energies for typical σ-HBs that involve charged species. The magnitudes of ΔE_{form}^{HB} for these systems are usually larger than 10 kcal mol^{-1}, similar to that of $\mathbf{3}_{inter}$ ($\Delta E_{form}^{HB}(\mathbf{3}_{inter}) = 14.3$ kcal mol^{-1}), and can be as large as 30–40 kcal mol^{-1} in strongly bonded, symmetric $[H_2O\cdots H\cdots OH_2]^+$ and $[F\cdots H\cdots F]^-$ molecules.[2]

Not only the energetics, but also the H···O and H···O distances resulting from the formerly described electronic structure calculations, indicate the respective stabilising/destabilising effects of the π system on the RAHBs and RIHBs examined herein. Table 2 reports these parameters for the HBs in **2**, $\mathbf{2}_{inter}$, **3** and $\mathbf{3}_{inter}$. [The angle $\theta = (\measuredangle X{-}H\cdots Y)$ is also a parameter that indicates the strength of the HB X–H···Y. A stronger HB is usually related to a larger value of θ.[2] Nonetheless, the geometric constraints imposed by the pseudo-cycles in **2** and **3** prevent the use of θ to compare the examined RAHBs and RIHBs with those in $\mathbf{2}_{inter}$ and $\mathbf{3}_{inter}$, respectively.] These reults indicate how the surrounding conjugated bonds strengthen/weaken the examined RAHBs/RIHBs.

Table 2. O···H and N···O distances (in Å) for the HBs in systems **2**, $\mathbf{2}_{inter}$, **3** and $\mathbf{3}_{inter}$.

System	*d*(H···O)	*d*(N···O)
2	1.896	2.665
$\mathbf{2}_{inter}$	2.024	3.030
3	2.135	2.979
$\mathbf{3}_{inter}$	1.714	2.752

To obtain a further insight into the reasons underlying the opposite effects found in the intramolecular HBs examined herein, we now dissect our results in light of the wave function analyses performed through the QTAIM, IQA and ELF approaches already summarised.

Quantum chemical topology

RAHBs have previously been characterised through quantum chemical topology as interactions that involve the homogenisation of the DIs through the pseudo-cycle forming the HB structure shown in Figure 3a.[5,16] In other words, the number of shared electrons associated with the double bonds decrease, whereas the number of those related to single bonds show the opposite behaviour; this is in agreement with the arrow-pushing sketches in Figures 1a and b and 4a. On the contrary, the formation of the RIHB makes the DIs through the pseudo-cycle less uniform (Figure 3b), that is, double/single bonds increase/decrease their DIs after the occurrence of this interaction, as shown in Figure 4b. Thus, the π-conjugated channels in RAHBs and RIHBs behave in opposite ways with respect to the effects of bond order in double and single bonds after the formation of the corresponding HBs. Intermolecular HBs used as control systems, $\mathbf{2}_{inter}$ and $\mathbf{3}_{inter}$, have similar behaviour to that of **2** and **3**, respectively, concerning changes in the DIs for single and double bonds, as displayed in Figure S1 in the Supporting Information. We also note that the decrease in the DI associated with the N–H bond, because of the formation of the HB, is larger for the RAHB than that of the RIHB; this is consistent with the fact that the former interaction is a stronger HB.

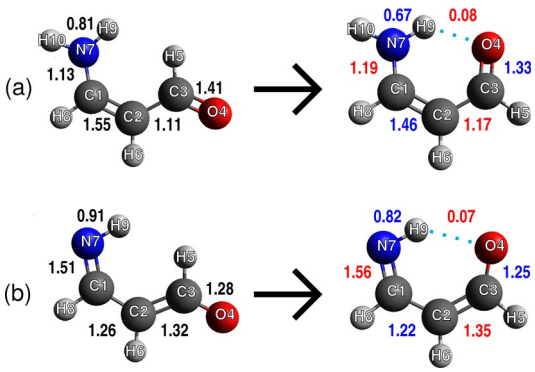

Figure 3. Changes in the DIs across the pseudo-cycles of a) **2** and b) **3** on account of the formation of the RAHBs and RIHBs, respectively. An increase/decrease in δ(X,Y) as a result of the formation of these intramolecular HBs is indicated with red/blue.

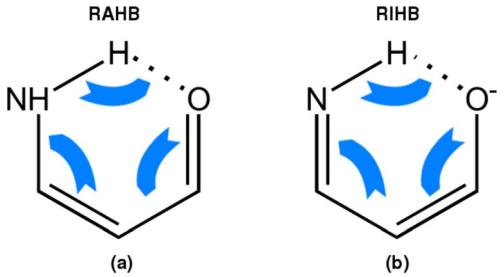

Figure 4. Flow of electron density in the pseudo-cycles of the a) RAHB and b) RIHB investigated.

The changes in the DIs in Figure 3 suggest that system **2** will have a larger aromatic character than that of system **3**. Nevertheless, as shown in Table 3, the well-established multicentred aromaticity indices, $I_{ring}(\mathscr{A})$,[19] which measures the six-centre delocalisation along the direct ring path; MCI($\mathscr{A}$),[20] which adds all other possible paths; as well as their normalised versions, $I_{NG}(\mathscr{A})$ and $I_{NB}(\mathscr{A})$,[21] indicate, to different degrees, that compound **3** is more aromatic than compound **2**. Hence, although normally aromaticity is considered to be a source of

Table 3. Aromaticity indices $I_{ring}(\mathscr{A})$, MCI($\mathscr{A}$), $I_{NG}(\mathscr{A})$ and $I_{NB}(\mathscr{A})$ for the closed conformations of **2** and **3**.

Index	2	3
I_{inter}	0.001211	0.001668
MCI	0.022377	0.023604
I_{NG}	0.001618	0.002265
I_{NB}	0.021824	0.023082

© 2017 Wiley-VCH Verlag GmbH & Co. KGaA, Weinheim

stabilisation, what we have found herein is that the most stable compound is the least aromatic. This surprising result is in close agreement with our previous work, which indicates that the strength of the RAHB, compared with those in non-conjugated carbonyl molecules, does not originate from the resonant structures.[16]

The variations in the DIs indicated in Figure 3, due to the formation of the RAHB and RIHB, are supported by the results of the ELF analysis shown in Figure 5, which reveals several iso-

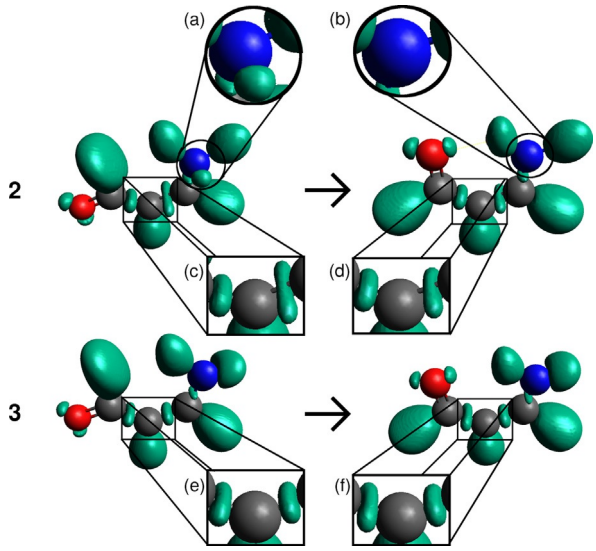

Figure 5. ELF isosurfaces at an isovalue of 0.9 for the RAHB in **2** in its open (a) and closed (b) conformations and the RIHB in **3** in its open (c) and closed (d) dispositions.

surfaces of this scalar field. The electron population associated with a given domain increases with the size of the isosurface. The C1–C2 and C2–C3 bonds (atom numbering is shown in Figure 3) in system **2** are qualitatively more similar upon the formation of the HB, whereas the opposite occurs in the case of anion **3**. Additionally, examination of the ELF in molecule **2** in its open conformer reveals a solitary lone pair (Figure 5 a), which disappears when the RAHB is formed. This result indicates substantial conjugation of this lone pair with the adjacent C–N bond upon formation of the RAHB. Base **3** does not exhibit such a lone pair in either the dissociated or hydrogen-bonded conformations.

As discussed previously,[16] the fact that the RAHB makes the bond orders more uniform through the π system does not imply that the number of delocalised electrons increases with the formation of this HB. Similarly, reduced uniformity in the DIs following the formation of the RIHB in **3** is not accompanied by a decrease in the total number of delocalised electrons. These statements are based on the sum rule obeyed by the localisation and delocalisation indicies shown in Equation (7):

$$N = \sum_{X} \lambda(X) + \frac{1}{2} \sum_{X \neq Y} \delta(X,Y) \qquad (7)$$

in which the total number of electrons in a molecule is partitioned into localised (as measured by λ, the atomic localisation index) and delocalised sets (as measured by the interatomic DIs).

Table 4 shows that the total number of delocalised electrons is slightly reduced after the formation of the RAHB in **2**, whereas the number of delocalised electrons almost remains constant in system **3**, on account of the formation of the RIHB.

Table 4. Change in the number of delocalised electrons and the intra- and intermolecular components of the IQA exchange-correlation energy (reported in kcal mol^{-1}) as a consequence of the formation of the HBs in **2**, $\mathbf{2}_{inter}$, **3** and $\mathbf{3}_{inter}$.

System	$\sum_{A>B} \Delta\delta(A,B)$	$\sum_{A} \Delta V_{xc}^{A}$	$\sum_{A>B} \Delta V_{xc}^{AB}$
2	−0.08	−23.9	17.5
$\mathbf{2}_{inter}$	−0.03	−14.9	6.2
3	0.01	−0.7	4.0
$\mathbf{3}_{inter}$	−0.01	−24.7	14.6

The increase in the number of localised electrons in **2** as a consequence of the RAHB is accompanied by a substantial rise in the intra-atomic component of the IQA exchange-correlation energy, $\Delta|\Sigma_A V_{xc}^A| = 23.9$ kcal mol^{-1}. Interestingly, the interatomic exchange becomes less negative: $\Sigma_{A>B}\Delta V_{xc}^{AB} = 17.5$ kcal mol^{-1}. As previously discussed,[16] an important source of stabilisation from the RAHB comes from the change of the intra-atomic component of electron exchange, rather than inter-atomic exchange, as suggested by the mesomeric structures in Figure 1 a and b. We found similar effects concerning intra $\Sigma_A V_{xc}^A$ and inter $\Sigma_{A>B}\Delta V_{xc}^{AB}$ in the RIHBs examined herein, but these were considerably smaller in magnitude.

The behaviour of the DIs after the generation of an RAHB or RIHB indicates that the pair density is affected in different ways by these interactions. Because the charge distribution can be obtained by integrating $\rho_2(\mathbf{r}_1,\mathbf{r}_2)$, we expect distinct modifications of $\rho(\mathbf{r})$ in RAHBs and RIHBs. For example, the results in Table 5 show that RAHBs and RIHBs involve qualitatively similar changes in QTAIM charges. Nonetheless, the variations in $q(\Omega)$ are more conspicuous for the former HB than those for the latter; this is in agreement with the above comparison of these interactions.

Table 5. Variations in the QTAIM charges in **2** and **3** on account of the formation of the respective RAHBs and RIHBs in these systems. The atomic numbering is shown in Figure 3. Atomic units are used throughout.

Atom	**2**	**3**	Atom	**2**	**3**
C1	0.11	0.04	H6	−0.04	−0.03
C2	−0.04	−0.03	N7	−0.10	−0.03
C3	−0.08	−0.02	H8	0.00	−0.01
O4	−0.04	0.00	H9 (HB)	0.12	0.11
H5	0.04	−0.01	H10	0.01	–
$\sum_{A} \lvert\Delta Q(A)\rvert$	0.58	0.28	–	–	–

© 2017 Wiley-VCH Verlag GmbH & Co. KGaA, Weinheim

The smaller rearrangement of charge distribution in the RIHBs, compared with that in the RAHBs, is consistent with the fact that the absolute values of all components of the IQA decomposition of the formation energy of the former interaction are significantly lower than that of the latter HB (Table 6). We

Table 6. IQA partition of the formation energy of the HBs in **2**, $\mathbf{2}_{inter}$, **3** and $\mathbf{3}_{inter}$. Values are given in kcal mol^{-1}.

System	$\sum_{A>B}\Delta\delta(A,B)$	$\sum_{A}\Delta T^{A}$	$\sum_{A}\Delta V_{cl}^{A}$	$\sum_{A}\Delta V_{xc}^{A}$	$\sum_{A>B}\Delta V_{cl}^{AB}$	$\sum_{A>B}\Delta V_{xc}^{AB}$
2	−0.01	16.88	43.35	−14.26	−58.36	5.52
$\mathbf{2}_{inter}$	0.01	20.39	22.97	−8.46	−38.09	0.51
3	0.03	−3.49	22.42	0.93	−21.56	0.68
$\mathbf{3}_{inter}$	0.04	26.56	36.27	−16.04	−62.56	3.46

stress that even the IQA classical contribution, which jointly takes into account the electrostatics, polarisation and charge-transfer energies in standard energy decomposition analyses is smaller in the examined RIHBs than that in the RAHBs, although the RIHB involves a negatively charged enolate as the HB acceptor. Additionally, results in Table 6 indicate that the magnitude of $\Sigma_{A>B}\Delta V_{cl}^{A>B}$ for the HB $\mathbf{3}_{inter}$, corresponding to the intermolecular interaction of an enolate and an α,β-unsaturated imine, is more than twice the corresponding value for the RIHB in **3**. Table 6 also reveals that the most important sources of stabilisation in the investigated HBs are $\Sigma_{A>B}\Delta V_{cl}^{AB}$ and $\Sigma_{A}\Delta V_{xc}^{A}$; the first component is more important than the second. The order of the absolute values of the change of these components after the formation of the HB is that shown in Equation (8):

$$\begin{aligned}&|\Delta V_{cl}^{AB}|(\mathbf{3}_{inter}) > |\Delta V_{cl}^{AB}|(\mathbf{2}) > |\Delta V_{cl}^{AB}|(\mathbf{2}_{inter}) > |\Delta V_{cl}^{AB}|(\mathbf{3})\\ &|\Delta V_{xc}^{A}|(\mathbf{3}_{inter}) > |\Delta V_{xc}^{A}|(\mathbf{2}) > |\Delta V_{cl}^{A}|(\mathbf{2}_{inter}) > |\Delta V_{cl}^{A}|(\mathbf{3})\end{aligned} \quad (8)$$

which is the same as that of the formation energies discussed in the previous subsection [Eq. (9)].

$$|\Delta E_{form}^{AB}|(\mathbf{3}_{inter}) > |\Delta E_{form}^{AB}|(\mathbf{2}) > |\Delta E_{form}^{AB}|(\mathbf{2}_{inter}) > |\Delta E_{form}^{AB}|(\mathbf{3}) \quad (9)$$

Similar tendencies are observed for the O···H interaction, as reported in Table 7. The magnitude of the exchange-correlation component for the N–H bond decreases in an inverse order to that shown in Equations (8) and (9), to give that shown in Equation (10):

$$|V_{xc}^{N-H}|(\mathbf{3}) > |V_{xc}^{N-H}|(\mathbf{2}_{inter}) > |V_{xc}^{N-H}|(\mathbf{2}) > |V_{xc}^{N-H}|(\mathbf{3}_{inter}) > \quad (10)$$

in agreement with the relative strengths of the HBs considered herein because a more covalent N–H bond indicates a weaker H···O HB.

Table 7. Changes in the IQA energy components, E_{int}^{AB}, V_{cl}^{AB} and V_{xc}^{AB}, for the O···H and N–H bonds because of the formation of the HBs in the examined systems, that is, from the open to the hydrogen-bonded conformations of **2** and **3** (as shown in Figure 3) and from the dissociated to the associated forms for $\mathbf{2}_{inter}$ and $\mathbf{3}_{inter}$. Data are reported in kcal mol^{-1}.

System	O···H			N–H		
	E_{int}^{AB}	V_{cl}^{AB}	V_{xc}^{AB}	E_{int}^{AB}	V_{cl}^{AB}	V_{xc}^{AB}
2	−106.4	−93.7	−12.8	−297.2	−153.9	−143.3
$\mathbf{2}_{inter}$	−74.7	−65.7	−8.9	−277.9	−118.0	−159.9
3	−71.1	−61.6	−9.6	−259.2	−90.4	−168.9
$\mathbf{3}_{inter}$	−126.9	−104.6	−22.3	−273.7	−138.9	−134.8

Conclusion

We have introduced the concept of the RIHB, namely, a HB substantially hindered by the surrounding π system. The consideration of intermolecular HBs as control systems shows that the examined RIHB has a low formation energy, despite a negative charge in the enolate group acting as the HB acceptor. Although typical charged σ-HBs have formation energies that usually surpass 10 kcal mol^{-1}, the corresponding value for the examined RIHBs is $\Delta E_{form}^{RIHB} = -2.6$ kcal mol^{-1}. QTAIM and ELF analyses indicated that RAHBs and RIHB behaved differently with regard to homogenisation of bond orders throughout the pseudo-cycle formed in these interactions. Different aromaticity indices indicated that anion **3** was more aromatic than molecule **2**, despite a stronger RAHB than that of the RIHB. This result is consistent with previous descriptions of RAHBs, in which the stability of this HB is not based on the corresponding mesomeric structures. Instead, both RAHBs and RIHBs become stabilised through intra-atomic exchange and electrostatic effects, as shown by the IQA energy partition. Nonetheless, the magnitude of these effects is larger in an RAHB than it is in an RIHB. We expect, overall, that these results will give valuable insights into the complex interplay between π-conjugated systems and HBs in chemistry.

Acknowledgements

We acknowledge financial support from the Spanish government (grant CTQ-2015-65790-P), as well as computer time from DGTIC/UNAM (grant LANCAD-UNAM-DGTIC-250) T.R-R., E.R.M. and J.M.G.V. are also grateful to CONACyT/México for financial support (grant 253776), a M.Sc. and PhD. scholarships (numbers 308773 and 381483) respectively. T. R.-R. is also thankful to Magdalena Aguilar Araiza, Gladys Cortés Romero and David Vázquez Cuevas for technical support.

Conflict of interest

The authors declare no conflict of interest.

Keywords: aldehydes · conjugation · density functional calculations · hydrogen bonds · pi interactions

[1] S. Scheiner, *Hydrogen Bonding. A Theoretical Perspective*, Oxford University Press, New York, **1997**.

[2] T. Steiner, *Angew. Chem. Int. Ed.* **2002**, *41*, 48; *Angew. Chem.* **2002**, *114*, 50.

© 2017 Wiley-VCH Verlag GmbH & Co. KGaA, Weinheim

[3] K. Liu, J. D. Cruzan, R. J. Saykally, *Science* **1996**, *271*, 929.
[4] J. M. Guevara-Vela, E. Romero-Montalvo, V. A. Mora Gómez, R. Chávez-Calvillo, M. García-Revilla, E. Francisco, A. Martín Pendás, T. Rocha-Rinza, *Phys. Chem. Chem. Phys.* **2016**, *18*, 19557.
[5] E. Romero-Montalvo, J. M. Guevara-Vela, W. E. Vallejo-Narváez, A. Costales, A. Martín Pendás, T. Rocha-Rinza, *Chem. Commun.* **2017**, *53*, 3516.
[6] K. Nauta, R. E. Miller, *Science* **1999**, *283*, 1895.
[7] L. Pauling, *The nature of the chemical bond 3rd ed.*, Cornell University Press, New York, **1960**.
[8] J. I. Wu, J. E. Jackson, P. v. R. Schleyer, *J. Am. Chem. Soc.* **2014**, *136*, 13526.
[9] T. Kakeshpour, J. I. Wu, J. E. Jackson, *J. Am. Chem. Soc.* **2016**, *138*, 3427.
[10] G. Gilli, F. Bellucci, V. Ferretti, V. Bertolasi, *J. Am. Chem. Soc.* **1989**, *111*, 1023.
[11] V. Bertolasi, P. Gilli, V. Ferretti, G. Gilli, *J. Am. Chem. Soc.* **1991**, *113*, 4917.
[12] P. Gilli, V. Bertolasi, V. Ferretti, G. Gilli, *J. Am. Chem. Soc.* **2000**, *122*, 10405.
[13] E. Romero-Montalvo, J. M. Guevara-Vela, A. Costales, A. Martín Pendás, T. Rocha-Rinza, *Phys. Chem. Chem. Phys.* **2017**, *19*, 97.
[14] V. Bertolasi, L. Pretto, G. Gilli, P. Gilli, *Acta Crystallogr.* **2006**, *62*, 850.
[15] J. M. Guevara-Vela, R. Chávez-Calvillo, M. Garca-Revilla, J. Hernández-Trujillo, O. Christiansen, E. Francisco, A. Martín Pendás, T. Rocha-Rinza, *Chem. Eur. J.* **2013**, *19*, 14304.
[16] J. M. Guevara-Vela, E. Romero-Montalvo, A. Costales, A. Martín Pendás, T. Rocha-Rinza, *Phys. Chem. Chem. Phys.* **2016**, *18*, 26383.
[17] X. Fradera, M. A. Austen, R. F. W. Bader, *J. Phys. Chem. A* **1999**, *103*, 304.
[18] W. Koch, M. C. Holthausen, *A Chemist's guide to Density Functional Theory*, Wiley-VCH Verlag, Weinheim, **2001**.
[19] M. Giambiagi, M. S. de Giambiagi, C. D. dos Santos Silva, A. P. de Figueiredo, *Phys. Chem. Chem. Phys.* **2000**, *2*, 3381.
[20] P. Bultinck, R. Ponec, S. Van Damme, *J. Phys. Org. Chem.* **2005**, *18*, 706.
[21] J. Cioslowski, E. Matito, M. Solà, *J. Phys. Chem. A* **2007**, *111*, 6521.
[22] M. A. Blanco, A. Martín Pendás, E. Francisco, *J. Chem. Theory Comput.* **2005**, *1*, 1096.
[23] A. D. Becke, K. E. Edgecombe, *J. Chem. Phys.* **1990**, *92*, 5397.
[24] B. Silvi, A. Savin, *Nature* **1994**, *371*, 683.
[25] A. Savin, R. Nesper, S. Wengert, T. F. Fässler, *Angew. Chem. Int. Ed. Engl.* **1997**, *36*, 1808; *Angew. Chem.* **1997**, *109*, 1892.
[26] C. Pérez, M. T. Muckle, D. P. Zaleski, N. A. Seifert, B. Temelso, G. C. Shields, Z. Kisiel, B. H. Pate, *Science* **2012**, *336*, 897.
[27] C. Møller, M. S. Plesset, *Phys. Rev.* **1934**, *46*, 618.
[28] S. Kossmann, F. Neese, *J. Chem. Theory Comput.* **2010**, *6*, 2325.
[29] T. H. Dunning, *J. Chem. Phys.* **1989**, *90*, 1007.
[30] F. Neese, *WIREs Comput. Mol. Sci.* **2012**, *2*, 73.
[31] A. Martín Pendás, E. Francisco, Promolden. *A QTAIM/IQA code*, University of Oviedo, (unpublished).
[32] Schaftenaar, G, Molden version 5.7, a pre- and post processing program of molecular and electronic structure, **2016**, http://www.cmbi.ru.nl/molden/molden.html.
[33] Zou, W, Molden2Aim, **2016**, http://www.molscience.com/software/Molden2AIM.
[34] S. Wojtulewski, S. J. Grabowski, *J. Mol. Struct.* **2003**, *621*, 285 – 291.
[35] E. Francisco, J. L. Casals-Sainz, T. Rocha-Rinza, A. Martín Pendás, *Theor. Chem. Acc.* **2016**, *135*, 170.
[36] E. Matito, Esi-3D*: Electron Sharing Indices Program for 3D Molecular Space Partitioning* **2015**, Institute of Computational Chemistry and Catalysis, University of Girona, Catalonia, Spain.
[37] M. D. Hanwell, D. E. Curtis, D. C. Lonie, T. Vandermeersch, E. Zurek, G. R. Hutchison, *J. Cheminf.* **2012**, *4*, 17.

Manuscript received: July 24, 2017
Accepted manuscript online: September 5, 2017
Version of record online: October 30, 2017

© 2017 Wiley-VCH Verlag GmbH & Co. KGaA, Weinheim

ChemPubSoc Europe

DOI: 10.1002/cphc.201700940

CHEMPHYSCHEM Articles

VIP *Very Important Paper*

Where Does Electron Correlation Lie? Some Answers from a Real Space Partition

José Luis Casalz-Sainz,[a] José Manuel Guevara-Vela,[a] Evelio Francisco,[a] Tomás Rocha-Rinza,[b] and Ángel Martín Pendás*[a]

We discuss an intra- and interatomic partition of the electron correlation energy (E_{corr}) within the interacting quantum atoms (IQA) approach at the accurate coupled cluster level with single, double, and estimated triple excitations (CCSDT(T)). This division offers a privileged window into the spatial localization of this component of the molecular energy. We show that the total molecular E_{corr} is dominated by the intra-atomic or intra-fragment terms and that interatomic contributions change smoothly from short- to long-range correlation (dispersion). The sign of these interatomic correlation terms differentiate between (i) mainly covalent or (ii) mainly ionic or nonbonded interactions. We propose that this feature may be used to define and examine intramolecular dispersion terms.

1. Introduction

One of the holy grails of contemporary molecular computational chemistry is the appropriate treatment of electron correlation (EC).[1–5] This energetic contribution has turned out to be crucial for the suitable description of many systems and processes in physical chemistry[6–8] and, hence, many efforts have been undertaken to obtain it as accurately as possible both in density functional theory (DFT) and wavefunction methods.

Apart from the purely theoretical and computational problem of obtaining accurate electron correlation energies (E_{corr}), it is interesting to examine where EC resides in real space. Insights into this correlation energy density should be of importance in several branches of molecular physics and quantum chemistry. Not much work has been done in this direction, although the Casimir–Polder expression for E_{corr} provides an important starting point that has been used recently to derive self-consistent van der Waals corrections in DFT.[9] Several mathematical transformations[10] have also been proposed to define correlation densities, but their chemical meaning has not been explored in detail. Here, we do not attempt to develop another correlation energy density, but instead offer a coarse-grained picture of the spatial distribution of electron correlation. We do this by using the atomic partitioning provided by the quantum theory of atoms in molecules (QTAIM) of R. F. W. Bader et al.[11] coupled to the interacting quantum atoms (IQA) approach, which provides an exact decomposition of the total molecular energy into intra- and inter-atomic components.[12,13] The combination of these methods of wavefunction analysis has been used to shed light on a broad range of problems. For example, the nature of covalent,[14,15] metallic,[16–18] as well as noncovalent interactions,[19–28] the origin of steric effects,[29–31] and the study of excited states[32–34] to name a few. IQA/QTAIM provides explicit access to both one- and two-center correlation energy terms that add to the total correlation energy as measured with respect to deviations from the HF energy components.

Early insight on spatial localization of electron correlation in this context was already presented by Gatti and co-workers in 1988.[35] Progress made in this direction was also recently reported by Popelier et al.,[36] who partitioned the second order Møller–Plesset (MP2) correlation energy into IQA intra- and interatomic contributions using QTAIM topological atoms. However, as already pointed out by these workers, the used MP expansions of E_{corr} only contain two-electron terms. Hence, all MP IQA contributions obtained with this approach will be equal to their Hartree–Fock (HF) counterparts except for the exchange-correlation energies. Since the charge distribution itself must also be affected by electron correlation, we have decided to use the coupled cluster with singles, doubles and estimated triples (CCSD(T)) relaxed reduced density matrices (RDM) rather than effective RDMs, which can reproduce the correlated electronic energy but otherwise underestimate the effect of EC on the IQA partition.[37] Additionally, the use of unrelaxed density matrices is not consistent with the computation of other molecular properties because the Hellman–Feynman theorem is not satisfied for nonvariatonal electronic structure methods without the consideration of Lagrangian functions.[38] Despite these limitations, MP2 is known to provide a large part of the correlation energy of simple systems and the partition of E_{corr}(MP2) has already provided valuable insights. For instance,

[a] J. L. Casalz-Sainz, J. M. Guevara-Vela, Prof. E. Francisco, Prof. Á. Martín Pendás
Departament of Analytical and Physical Chemistry, University of Oviedo
E-33006, Oviedo (Spain)
E-mail: angel@fluor.quimica.uniovi.es

[b] Dr. T. Rocha-Rinza
Institute of Chemistry, National Autonomous University of Mexico
Circuito Exterior, Ciudad Universitaria, Delegación Coyoacán C.P. 04510, Mexico City (Mexico)

Supporting Information and the ORCID identification number(s) for the author(s) of this article can be found under: https://doi.org/10.1002/cphc.201700940.

© 2017 Wiley-VCH Verlag GmbH & Co. KGaA, Weinheim

the interpretation that chemical bonds involve charge transfer and exchange in an independent way and, hence, that covalency does not represent the opposite of ionicity (understood in the sense of net charge transfer).[39] We expect that the fully relaxed technique proposed here will add to this growing body of knowledge, helping to shed light on the role of correlation in chemical bonding.[40]

As a by-product of our approach, we also expect to show how EC computed at several levels of theory impacts different energy components in real space. To that end we have compared IQA decompositions at HF, MP2, configuration interaction with singles and doubles (CISD), CCSD, CCSD(T) and almost full configuration interaction (FCI, as coming from the density matrix renormalization group, DMRG) approximations for a set of representative molecules and molecular clusters. These data will be useful to calibrate the sensitivity of the different molecular energy components to electron correlation. Note that the MP2, CCSD and CCSD(T) methods are not variational.

The rest of the paper is organized as follows. Firstly, we briefly review the IQA energy partition and specify the details of the computations performed in this investigation. Later we discuss the physical localization of electron density based on CCSD(T) relaxed densities. Finally, we compare the CCSD(T) results with the IQA splitting based on the different electronic structure methods considered herein. Overall, we offer an insightful spatial localization of correlation energy that can be used to analyze the stabilization that occur through nonbonded interactions in chemistry.

Methods

IQA and Correlation Energy Partition

Real space theories of chemical bonding divide space into either disjointed or overlapping regions endowed with a physically sound meaning.[12,13] According to QTAIM, which falls into the first category, the topology of the electron density yields an exhaustive partition of $\mathfrak{R}^3$ into atomic regions Ω, $\mathfrak{R}^3 = \bigcup_A \Omega_A$.[11] This partitioning can be easily inherited by all the reduced density matrices (*n*RDMs).[13] For instance, the $A_1A_2\ldots A_n$ component of the *n*-th order reduced density (*n*RD) is simply defined as $\rho_n^{A_1A_2\ldots A_n}(\mathbf{r}_1,\mathbf{r}_2,\ldots,\mathbf{r}_n) = \rho_n(\mathbf{r}_1 \in \Omega_{A_1}, \mathbf{r}_2 \in \Omega_{A_2},\ldots,\mathbf{r}_n \in \Omega_{A_n})$.

Because the electronic energy for a Coulomb Hamiltonian depends only on the 1RDM and the 2RD, $E = \mathrm{Tr}\,\hat{h}\rho_1(\mathbf{r}_1,\mathbf{r}_1') + (1/2)\mathrm{Tr}_{12}^{-1}\rho_2(\mathbf{r}_1,\mathbf{r}_2)$, we can write E as a sum of one- and two-domain components. This condition leads to the IQA decomposition [Eq. (1)]:

$$E = \sum_A E_{self}^A + \sum_{A>B} E_{int}^{AB} \qquad (1)$$

In this expression, E_{self}^A is the self-energy of atom A, which adds all the energy terms that depend only on nuclei (*n*) and electrons (e) contained in domain A, while the pairwise additive interatomic energy, E_{int}^{AB}, gathers all contributions containing particles in the A and B regions. In this way, $E_{self}^A = T^A + V_{ne}^{AA} + V_{ee}^{AA}$ and $E_{int}^{AB} = V_{nn}^{AB} + V_{ee}^{AB} + V_{ne}^{AB} + V_{ne}^{BA}$, where we have used a clear notation that needs no more comments.

We obtain a fruitful decomposition of E_{int}^{AB} if we further partition the 2RD into its Coulomb (J) and exchange-correlation (xc) components, $\rho_2(\mathbf{r}_1,\mathbf{r}_2) = \rho_2^J(\mathbf{r}_1,\mathbf{r}_2) + \rho_2^{xc}(\mathbf{r}_1,\mathbf{r}_2)$. In this way, we can separate all terms in E_{int} depending on the one-particle density (that would correspond to the interaction among classical particles) from those calculated from the exchange-correlation density (with no analogue in classical mechanics), so that $E_{int}^{AB} = V_{cl}^{AB} + V_{xc}^{AB}$. The contribution V_{cl}^{AB} is thus immediately associated to the ionic component of a chemical bond, tending asymptotically to Q_AQ_B/R_{AB} for charged species, while V_{xc}^{AB} i.e. the exchange-correlation energy, represents a measure of covalency.[12]

Within this scenario, we start from Löwdin's definition of correlation energy with respect to the Hartree–Fock reference to partition E_{corr} a là IQA [Eq. (2)]:

$$\begin{aligned} E_{corr}^{Löwdin} &= \sum_A (E_{self}^{correlated} - E_{self}^{HF})^A + \sum_{A>B} (E_{int}^{correlated} - E_{int}^{HF})^{AB} \\ &= \sum_A E_{corr}^{self,A} + \sum_{A>B} E_{corr}^{int,AB} = E_{corr}^{self} + E_{corr}^{int} \end{aligned} \qquad (2)$$

where we simply subtract HF IQA quantities from their correlated counterparts. As E_{int} itself, E_{corr}^{int} may be divided into its classical and exchange-correlation contributions, $E_{corr}^{int} = E_{corr}^{int,cl} + E_{corr}^{int,xc}$.

Notice that the above definition provides $E_{corr}^{self,A}$ and $E_{corr}^{int,AB}$ quantities that coincide with those proposed by Popelier et al.[36,39] in the case of their MP2 IQA correlation energy partition. In that unrelaxed formulation only the correlation energy terms included in V_{xc} will be different from their HF analogues. This is not the case in our general implementation, and all one- and two-electron energy components are affected by the inclusion of electron correlation.

Computational Details

We have partitioned the electron correlation energy in a battery of 43 systems (Table 1) at several levels of theory. This set comprises simple molecules with geometries taken from the NIST database[41] and molecular dimers from the S22 and KB49 datasets.[42–44] The geometries of some examples (specified in Table 1) were optimized using the CCSD/aug-cc-pvdz approximation with the Gamess-US program.[45] All geometries can be found in the Supporting Information (SI). Density matrices with the HF, CISD, CCSD and CCSD(T) methods were directly read with the cc-pVDZ basis set from calculations carried out using the PySCF suite.[46] DMRG[47] wavefunctions and their associated density matrices, approaching the FCI level with typical errors smaller than 1 kcal mol^{-1}, were computed with the Block code.[1,4,48–50] All electrons and orbitals were considered in correlated calculations. If the reader is interested in some of the cumbersome expressions of the 2RDMs for these methods we advise that more specialized works are consulted.[37,46,51]

DMRG calculations were done as follows. CASSCF valence orbitals and Edmiston–Ruedenberg split localized orbitals were used as the initial guess in molecules and dimers, respectively. We chose a bond dimension max = 3200/3400 states and used a custom scheduling. In the last set of iterations with M = max, the noise prefactor was suppressed, and we let Block iterate until the change in energy was smaller than 10^{-8} a.u. In all cases, the largest discarded weight was less than or equal to 10^{-8}. Once this energy convergence was reached, a set of extra iterations using the OneDot algorithm were performed to obtain the 2RDM. In every case, the truncation error due to variational loss remained of the order of the TwoDot largest discarded weight. The disposed weights with

© 2017 Wiley-VCH Verlag GmbH & Co. KGaA, Weinheim

Table 1. List of molecules studied in this work. Geometries were taken from the NIST, S22, and KB49 datasets,[42–44] except in some cases where they were optimized as detailed in the text.

Molecule	Geometry	Molecule	Geometry
C_2H_2	NIST	HCN···HF	KB49
Ar_2	NIST	HCN	NIST
Be_2	NIST	HF···ClF	optimized
BH_3	NIST	HF···CO	optimized
C_2	NIST	HF···F2	optimized
CF^+	optimized	HF···H_2O	optimized
$(CH_3F)_2$	KB49	$(HF)_2$	KB49
$(CH_4)_2$	S22	HF···N2	optimized
CH_4···HF	KB49	HF	NIST
CH_4···NH_3	KB49	HNC	NIST
CN^-	NIST	LIF	NIST
CO	NIST	CH3OH	NIST
C_2H_4	NIST	CH_4	NIST
F_2	NIST	N_2	NIST
FCN	NIST	Ne_2	NIST
$(H_2CO)_2$	optimized	NH_3···F_2	optimized
H_2CO	NIST	$(NH_3)_2$	S22
CH_2O_2	NIST	NH_3	NIST
H_2CF^+	optimized	NO^+	NIST
$(H_2O)_2$	optimized	$(NO)_2$	NIST
H_2O	optimized	OC···BH_3	optimized
HCl	NIST		

the most substantial magnitude in the OneDot algorithm fell in the interval 10^{-15}–10^{-10}. We used the Fiedler vector ordering. These settings provide DMRG accuracies of 1.0 kcal mol^{-1} or better.[52–54]

IQA integrations were performed using β-spheres with radii between 0.1 and 0.3 bohr. Restricted angular Lebedev quadratures with 5810 points and 451 points Gauss–Chebyshev mapped radial grids were used inside the β-spheres, with L expansions cut at $l=10$. Outside the β-spheres, extended 5810-point Lebedev, 551- and 651- mapped radial point Gauss–Legendre quadratures, and L expansions up to $l=12$ were selected. Total energies reconstructed from these IQA decompositions differ in less than 1.0 kcal mol^{-1} from those of the parent electronic structure codes, so that each of the computed interactions is thus considerably more accurate than this figure. Note that errors in numerical integrations stem from limitations in the quadratures used, approaching the exact value from above or below and thus tending to accumulation, not cancelation. We consider this accuracy enough for the objectives of this paper. All IQA calculations were done with our in-house code Promolden, available upon request.[55] It is known that for some systems with small interatomic distances, like C_2 and acetylene, the appearance of non-nuclear attractors may depend on the theoretical level used for their description. To avoid these problems, we have always used (thanks to symmetry) the internuclear midplane between these C atoms as interatomic surfaces. IQA computations are CPU intensive but feasible. As an example, the CH_3F dimer requires 2.3 days on 12 standard Xeon processors using around 0.5 Gb disk space.

2. Results and Discussion

2.1. Localization of the CCSD(T) Correlation Energy

We now discuss the intra- and interatomic partition of the correlation energies for the systems addressed in this work at the CCSD(T) level. Table 2 gathers the global E_{corr}^{self} and E_{corr}^{int} contributions, and Tables 3 and 4 contain a finer decomposition of these IQA components into their physical constituents. To simplify the discussion, we consider that A and B in Equation (2) run over atoms for isolated molecules, and over monomers in

Table 2. Partition of the Löwdin CCSD(T) correlation energies according to Equation (2).[a]

System	Self	Int	Total	System	Self	Int	Total
C_2	−0.498809	0.155563	−0.343246	HF···H_2O	−0.424186	−0.003399	−0.427586
CF^+	−0.361418	0.057722	−0.303696	$(HF)_2$	−0.420501	−0.002719	−0.423220
CN^-	−0.448912	0.151339	−0.297573	HF···N_2	−0.528874	−0.002779	−0.531653
CO	−0.437109	0.128281	−0.308828	Ne_2	−0.383820	−0.000050	−0.383870
F_2	−0.499545	0.084036	−0.415509	NH_3···F_2	−0.626559	−0.001640	−0.628199
HCl	−0.191449	0.020562	−0.170887	$(NH_3)_2$	−0.417352	−0.002932	−0.420284
HF	−0.221964	0.011302	−0.210662	$(NO)_2$	−0.885738	0.088935	−0.796803
LiF	−0.217534	0.005486	−0.212048	OC···BH_3	−0.426038	−0.020936	−0.446974
N_2	−0.553463	0.228442	−0.325021	BH_3	−0.125914	0.006540	−0.119373
NO^+	−0.603477	0.251072	−0.352405	C_2H_2	−0.523356	0.235412	−0.287944
Ar_2	−0.315209	−0.000350	−0.315559	C_2H_4	−0.531402	0.211851	−0.319551
Be_2	−0.091713	−0.010124	−0.101838	CH_2O_2	−0.742443	0.209378	−0.533065
$(CH_3F)_2$	−0.732845	−0.001978	−0.734823	CH_3OH	−0.524479	0.148977	−0.375502
$(CH_4)_2$	−0.381721	−0.001667	−0.383388	CH_4	−0.301611	0.110678	−0.190933
CH_4···HF	−0.400637	−0.003070	−0.403707	FCN	−0.740873	0.247006	−0.493867
CH_4···NH_3	−0.399239	−0.001442	−0.400681	H_2CF^+	−0.423656	0.094291	−0.329365
$(H_2CO)_2$	−0.687735	−0.001271	−0.689006	H_2CO	−0.520161	0.173249	−0.346912
$(H_2O)_2$	−0.429695	−0.002489	−0.432184	H_2O	−0.261064	0.044648	−0.216415
HCN···HF	−0.518226	−0.003211	−0.521437	HCN	−0.524103	0.214406	−0.309697
HF···ClF	−0.565216	−0.000817	−0.566033	HNC	−0.470410	0.168882	−0.301528
HF···CO	−0.515506	−0.000964	−0.516470	NH_3	−0.290928	0.082119	−0.208809
HF···F_2	−0.616486	−0.001723	−0.618209				

[a] The entry "self" refers to E_{corr}^{self}, the sum of all the nonequivalent values of $E_{corr}^{self,A} = E_{self}^{CCSD(T),A} - E_{self}^{HF,A}$, where A refers to atoms in the case of isolated molecules and to monomers in the case of dimers. Likewise, the item "int" refers to E_{corr}^{int}, and adds up all the nonequivalent $E_{corr}^{int,AB} = E_{int}^{CCSD(T),AB} - E_{int}^{HF,AB}$ interatomic terms. All data are reported in a.u.

© 2017 Wiley-VCH Verlag GmbH & Co. KGaA, Weinheim

Table 3. Partition of the CCSD(T) E_{corr}^{self} correlation energies into kinetic (*T*) nucleus-electron (NE), Coulomb (J) and exchange-correlation (xc) contributions. The data are given in a.u.

System	*T*	NE	J	xc	System	*T*	NE	J	xc
C_2	0.3528	−0.5025	0.4014	−0.7506	$HF\cdots H_2O$	0.2825	0.3462	−0.2391	−0.7097
CF^+	0.1956	0.2933	−0.3905	−0.4598	$(HF)_2$	0.2147	0.4715	−0.3028	−0.6982
CN^-	0.3985	−0.3564	0.0749	−0.5659	$HF\cdots N_2$	0.5510	−0.2149	0.0559	−0.9036
CO	0.3363	−0.0652	−0.1923	−0.5159	Ne_2	−0.0154	0.6177	−0.3462	−0.6399
F_2	0.4061	−0.1352	0.0118	−0.7822	$NH_3\cdots F_2$	0.6241	−0.1738	0.0014	−1.0613
HCl	0.0556	0.1788	−0.1175	−0.3084	$(NH_3)_2$	0.4148	−0.0089	−0.0599	−0.7157
HF	0.1117	0.2228	−0.2105	−0.3459	$(NO)_2$	1.2592	−1.2795	0.6895	−1.4455
LiF	0.0634	0.4239	−0.3916	−0.3133	$OC\cdots BH_3$	0.4018	−0.1116	−0.0056	−0.7242
N_2	0.4694	−0.4859	0.2556	−0.7926	BH_3	0.0939	−0.0541	0.0120	−0.1777
NO^+	0.5050	−0.4334	0.0786	−0.7537	C_2H_2	0.3745	−0.3286	0.1658	−0.7351
Ar_2	−0.0149	0.3727	−0.1404	−0.5326	C_2H_4	0.3590	−0.2915	0.1650	−0.7638
Be_2	0.0462	−0.0561	0.0790	−0.1608	CH_2O_2	0.5256	0.0764	−0.4312	−0.9132
$(CH_3F)_2$	0.5050	0.3991	−0.3762	−1.2195	CH_3OH	0.3457	−0.0169	−0.1204	−0.7329
$(CH_4)_2$	0.3498	−0.2561	0.0283	−0.6641	CH_4	0.1747	−0.1284	0.0883	−0.4362
$CH_4\cdots HF$	0.2807	0.1169	−0.1404	−0.6812	FCN	0.5272	−0.2003	−0.1463	−0.9214
$CH_4\cdots NH_3$	0.3774	−0.1260	−0.0189	−0.6889	H_2CF^+	0.1876	0.4111	−0.4627	−0.5596
$(H_2CO)_2$	0.6937	0.0245	−0.1770	−1.1414	H_2CO	0.3668	−0.0283	−0.2037	−0.6549
$(H_2O)_2$	0.3602	0.2231	−0.1770	−0.7241	H_2O	0.1897	0.0982	−0.1738	−0.3751
$HCN\cdots HF$	0.5239	−0.1105	−0.0155	−0.8771	HCN	0.4247	−0.3619	0.0696	−0.6565
$HF\cdots ClF$	0.3336	0.1491	−0.1668	−0.9368	HNC	0.3746	−0.2096	−0.0923	−0.5431
$HF\cdots CO$	0.4256	0.1952	−0.1606	−0.8536	NH_3	0.2099	−0.0169	−0.0685	−0.4154
$HF\cdots F_2$	0.4613	0.1892	−0.1994	−1.0326					

Table 4. Partition of the CCSD(T) E_{corr}^{int} correlation energies into electron-nucleus (EN, where electrons are on fragments A and nuclei on fragments B, see Table 2), nucleus-electron (NE, with nuclei on fragments A and nuclei on B), Coulomb (J), classical (cl), and exchange-correlation (xc) contributions. Atomic units are used throughout.

System	EN	NE	J	cl	xc	System	EN	NE	J	cl	xc
C_2	−0.0620	−0.0620	0.0943	−0.0297	0.1852	$HF\cdots H_2O$	−0.0279	0.0164	0.0129	0.0014	−0.0048
CF^+	−0.2959	0.1481	0.2281	0.0803	−0.0226	$(HF)_2$	0.0092	−0.0280	0.0197	0.0009	−0.0036
CN^-	−0.1954	0.1945	0.0990	0.0981	0.0532	$HF\cdots N_2$	−0.0226	−0.0049	0.0273	−0.0002	−0.0026
CO	−0.2914	0.2206	0.1946	0.1238	0.0045	Ne_2	0.0000	0.0000	−0.0000	0.0000	−0.0001
F_2	0.0046	0.0046	−0.0082	0.0010	0.0829	$NH_3\cdots F_2$	0.0279	−0.0110	−0.0168	0.0001	−0.0018
HCl	−0.0827	0.0072	0.0777	0.0022	0.0184	$(NH_3)_2$	0.0460	−0.0446	−0.0009	0.0005	−0.0034
HF	−0.0655	0.0130	0.0689	0.0164	−0.0051	$(NO)_2$	−0.1972	0.1991	−0.0020	0.0000	0.0891
LiF	−0.0293	0.0164	0.0213	0.0084	−0.0028	$OC\cdots BH_3$	−0.1985	0.1379	0.0543	−0.0063	−0.0146
N_2	0.0128	0.0128	−0.0257	−0.0001	0.2285	BH_3	−0.0173	0.0677	−0.0140	0.0364	−0.0299
NO^+	−0.3154	0.3083	0.1033	0.0962	0.1549	C_2H_2	0.0309	−0.0114	−0.0196	−0.0001	0.2356
Ar_2	−0.0000	−0.0000	0.0001	0.0001	−0.0004	C_2H_4	−0.0045	0.0779	−0.0690	0.0043	0.2074
Be_2	−0.0167	−0.0167	0.0317	−0.0017	−0.0084	CH_2O_2	−0.4705	0.2909	0.3533	0.1737	0.0356
$(CH_3F)_2$	−0.1050	0.1136	−0.0075	0.0011	−0.0030	CH_3OH	−0.0941	0.1065	0.0396	0.0520	0.0969
$(CH_4)_2$	−0.0246	0.0250	−0.0006	−0.0002	−0.0016	CH_4	−0.0197	0.0990	−0.0728	0.0065	0.1041
$CH_4\cdots HF$	−0.0002	−0.0172	0.0174	0.0000	−0.0031	FCN	−0.5645	0.4376	0.2765	0.1496	0.0974
$CH_4\cdots NH_3$	−0.0056	0.0066	−0.0008	0.0002	−0.0016	H_2CF^+	−0.2435	0.1278	0.1768	0.0611	0.0331
$(H_2CO)_2$	−0.1828	0.1974	−0.0120	0.0026	−0.0038	H_2CO	0.2190	−0.2626	0.1409	0.0973	0.0760
$(H_2O)_2$	−0.0149	0.0119	0.0038	0.0008	−0.0033	H_2O	0.0356	−0.0953	0.0949	0.0352	0.0095
$HCN\cdots HF$	0.0291	−0.0290	0.0012	0.0013	−0.0044	HCN	−0.2020	0.2149	0.0763	0.0892	0.1252
$HF\cdots ClF$	−0.0328	0.0200	0.0137	0.0009	−0.0016	HNC	0.1695	−0.2053	0.1746	0.1388	0.0300
$HF\cdots CO$	−0.0253	0.0417	−0.0149	0.0015	−0.0024	NH_3	0.0389	−0.0612	0.0483	0.0260	0.0562
$HF\cdots F_2$	−0.0313	0.0002	0.0310	−0.0001	−0.0017						

the case of dimers. A full account of all the IQA results may be found in the Supporting Information.

A first look at Table 2 uncovers that, in the vast majority of the intra-molecular cases showing covalent links, E_{corr}^{int} is positive; i.e. EC decreases the magnitude of E_{int}^{AB}. Moreover, the values of $E_{corr}^{int,xc}$ are also destabilizing in many of the intramolecular interactions shown in Table 4. Although these results might appear counterintuitive, they have a very precise physical origin. Under the action of Fermi correlation only, opposite spin electrons behave as statistically independent effective moieties, and they delocalize freely over larger spatial regions than when Coulomb correlation is also allowed.[56–58] A very natural way to understand this starts by recalling that the Fermi hole[58] (FH) that accompanies an electron excludes same-spin electrons, and thus leaves free room for opposite spin ones. This is the very nature of the Lewis pair, in which

© 2017 Wiley-VCH Verlag GmbH & Co. KGaA, Weinheim

pairs of opposite spin electrons delocalize independently over common regions of space controlled by the size of the Fermi hole. The spatial extent of the latter decreases when Coulomb correlation is switched on and opposite spin electrons are no longer effectively independent from the statistical point of view. Since V_{xc}^{AB} is an energetic measure of interdomain electron delocalization, the consideration of opposite spin correlation decreases the amount of this IQA component.

This picture, typical of mainly covalent interactions, weakens in highly ionic links for which the charge transfer at the HF level is a bit too large, and electron correlation slightly counteracts such density donation, thereby increasing delocalization. These circumstances result in E_{corr}^{int} being only slightly positive in systems such as LiF or BH_3. Note that E_{corr}^{int} acquires a more important role in determining the total value of $E_{corr}^{CCSD(T)}$ as the strength of the involved bonds increase (e.g. the multiple bonds in acetylene, dinitrogen, etc.). We stress how well the sign of E_{corr}^{int} separates weak from strong interactions. Table 2 is separated in an almost binary way into molecules and dimers by this descriptor, classifying $(NO)_2$ as a strongly bound system, as expected.

A second issue concerns long-range interatomic (or interfragment) correlation or dispersion, traditionally defined from perturbation theory as a stabilizing energetic contribution. As our Ar…Ar and Ne…Ne examples show, in these cases, E_{corr}^{int} is feebly negative, so that it is tempting to associate E_{corr}^{int} to dispersion as it takes into account double excitations in which one of the electrons is located on fragment A while the other is attached to monomer B. Care has to be taken, however, because dispersion corrections are well-defined only in standard perturbation theory under the polarization approximation,[59] and several possible expressions for the dispersion energy arise in symmetry-adapted perturbation theories (SAPT).[60] Still, it is reasonable to associate E_{corr}^{int} with real space dispersion when the regions are well separated in space. As these domains approach each other, short-range correlation contributions set in, and E_{corr}^{int} changes from a dispersive-like to an intramolecular-like regime. It should always be taken into account that dispersion and short-range correlation cannot be unequivocally separated in orbital invariant approaches, such as the one considered herein.

Tables 3 and 4 contain a partition of E_{corr}^{self} and E_{corr}^{int} into their kinetic energy (only for E_{corr}^{self}), classical, and exchange-correlation components. Regarding the self-energy terms, the change in kinetic energy is almost always positive, enforced by the satisfaction of the virial theorem and the overall energy lowering. Only in the rare gas dimers does the change in kinetic energy upon inclusion of correlation become negative. This stems from the flagrant violation of the virial theorem suffered by these systems at the Hartree–Fock level for correlated geometries. The intra-atomic exchange-correlation contribution is stabilizing in all cases, being the only component with definite sign. This fact points toward the primary role of exchange-correlation energies in determining the absolute value of E_{corr}. Note that the change in the intra-atomic electron–electron repulsion induced by electron correlation, as measured by the sum of the Coulombic J and xc columns of Table 4, is always negative, but that there are two basic modes in which this decrease is achieved. In nonpolar covalent systems such as C_2, N_2 or C_2H_2, J is positive, and thus, the electron distribution becomes, grossly speaking, more compact upon inclusion of electron correlation. This effect is also evidenced by the negative nucleus-electron values displayed by these systems. The overall decrease in the intra-atomic electron–electron repulsion is then a true two-particle effect, due to increased localization of the electrons in the atomic regions. With fewer electrons delocalized, the atomic densities condense themselves, and the kinetic energy of the electrons rises in turn. On the other hand, many polar molecules such as CO, HF, etc, and also dispersion-bound molecular clusters such as Ar_2 and Ne_2 display negative J values. The Hartree–Fock method provides too compressed densities either because of excessive charge transfer, in the first set, or because of the inability of this approximation to delocalize electrons properly in the second set. In many of these cases the xc component of E_{corr}^{int} is also negative.

We now turn to the interatomic or interfragment contributions considered in Table 4. For strongly covalent systems, the exchange-correlation term generally determines the overall sign of E_{corr}^{int}. In the case of mostly homopolar interactions, such as in CH_4, C_2H_2, N_2, or F_2, the redistribution of the density leads to globally canceling classical contributions, and $E_{corr}^{int,cl}$ becomes considerably smaller than its $E_{corr}^{int,xc}$ companion. An interesting exception is dicarbon, for which correlation contains a stabilizing electrostatic contribution arising from considerably more negative V_{ne}^{AB} (with $A \neq B$) terms not compensated by the increased interelectron Coulombic repulsion. In strongly bound polar systems, correlation tends to decrease polarity from the Hartree–Fock charge distribution, leading to non-negligible destabilizing classical $E_{corr}^{int,cl}$ components. This is the case in CF^+, CO, HF, BH_3, H_2O, HCN, etc. Note that, as commented above, this is normally accompanied by a destabilizing $E_{corr}^{int,xc}$, although a number of notable exceptions, such as the CF^+ and BH_3 molecules arise. A detailed study of BH_3, for instance, shows that it is the poor Hartree–Fock description of the hydride-like basin that leads to the stabilizing exchange-correlation component. Finally, the vast majority of the weakly bound systems are characterized by small $E_{corr}^{int,cl}$ contributions and dominating stabilizing $E_{corr}^{int,xc}$ terms.

Dimers provide an excellent playground to understand how E_{corr} is partitioned. As shown clearly in Table 2, the lion's share of the total correlation energy of a system is always intramonomer (or intra-atomic for molecules) in nature. This is reminiscent of Feynman's conjecture about the role of intra-atomic density distortions as the driving force of dispersion, as discussed by Allen and Tozer.[61] The total value of $E_{corr}^{Löwdin}$ is proportional to the overall number of electrons, and notable exceptions to this rule can be tracked to the multiconfigurational nature of the system (e.g. the NO and Be dimers). Therefore, and in agreement with Popelier et al.,[36,39] a real space partitioning of the correlation energy provides intra-atomic or intrafragment leading terms.

These components are associated with their energy lowering role through electron localization effects, and to a general decrease of the binding energy of strong chemical interactions.

© 2017 Wiley-VCH Verlag GmbH & Co. KGaA, Weinheim

Most importantly, however, the small interfragment components are critical from a chemical perspective. They provide a position space (instead of Fock- or orbital-space) window into the dispersion energy, and also into how this energetic contribution transforms itself into short-range correlation as the distance between the fragments decreases. These features can now be explored with the techniques presented herein and should be the objective of future research, including their comparison with recent methods developed to obtain intramolecular dispersion energies.[62,63] This line of research could prove useful in understanding the behavior of highly crowded molecular environments such as those found in biochemical assemblies, in which short- and long-range correlation effects may not be easily separable.

The intermonomer CCSD(T) E_{corr}^{int} energies should reasonably resemble the $E_{disp} + E_{disp-x}$ dispersion energies in SAPT[64] aside from the effects that penetration, mutual polarization of the fragments, charge transfer, and delocalization of electrons among the monomers may have. As an example, our values of E_{corr}^{int} for the H_2O and HF dimers are almost identical, −0.43 and −0.42 kcal mol^{-1}, respectively. These are clearly different from their SAPT counterparts,[64] −1.33 and −1.12 kcal mol^{-1}, but in decent agreement with the results obtained with the localized molecular orbital energy decomposition analysis (LMOEDA),[65] equal to −0.57 and −0.31 kcal mol^{-1}, in the same order. As we have already discussed in detail,[64] we have to be careful when comparing supermolecular and perturbation approaches to intermolecular interactions.

As a final point, we emphasize that the analysis that we are presenting is but a summary of a great amount of information that may be further scrutinized. To this end, we comment on the detailed CCSD(T) correlation energies obtained in the methane and water molecules. For methane, the total E_{corr} is −119.8 kcal mol^{-1}, with intra-atomic $E_{corr}^{self,A}$ energies equal to −130.07 and −14.7 kcal mol^{-1} for the C and H atoms, respectively. The last value implies that the probability of finding more than one electron on H is nonvanishing, because the correlation energy for a one-electron system equals zero. Our electron distribution functions (EDF) provide an adequate framework to understand this phenomenon.[56,57] As commented, $E_{corr}^{CCSD(T)}$ is indeed dominated by the intra-atomic terms. With the same basis set (including the H-centered primitives), the CCSD(T) correlation energy of the C atom in vacuo is −49.8 kcal mol^{-1}; more than two times smaller than the value obtained within the CH_4 molecule. These results show the sensitivity of E_{corr}^{self} to the electronic environment. Although the average number of electrons in carbon is similar in both cases, the atomic correlation energy is much larger in the molecule because in this latter case the probability of finding a larger number of electrons in the C basin is not negligible.

Regarding the interatomic interactions, the C–H correlation energy is positive, equal to 19.2 kcal mol^{-1}. EC thus makes the C–H bond slightly less covalent, as already commented. More interesting are the H···H interactions for which $E_{corr}^{int,H\cdots H} = -1.2$ kcal mol^{-1} in the CCSD(T) approximation. This value is small but not negligible. It is typical of 1,3-contacts, indicating the relevance of nonbonded interactions in electron correlation and generally in chemistry. In other words, the correlation term behaves differently in the same molecule in (1) bonded interactions such as C–H and (2) nonbonded ones like H···H. In the former case, correlation corrects the excessively delocalized HF picture, yielding a positive E_{corr}^{int}, whereas in the latter $E_{corr}^{int} < 0$. The last-mentioned result suggests once more that E_{corr}^{int} acts as a dispersion-like contribution, and that even in some 1,3-contacts, E_{corr}^{int} is already stabilizing. We have found this picture to be rather general. For instance, in the water molecule, $E_{corr}^{self,A} = -137.6$, −13.1 kcal mol^{-1} for the O and H atoms, respectively, and $E_{corr}^{int} = 16.2$, −1.1 kcal mol^{-1} for the O–H and H···H pairs. The smaller $E_{corr}^{int,H\cdots H}$ value as compared with that of methane depends on the large positive charge of the H atom, equal to 0.58 a.u.

We also note that the smooth change from long-range stabilizing to short-range destabilizing behavior of the EC interaction terms might be related to the existence of several minima in the Coulomb hole, as revealed by accurate calculations of the position intracule in atoms.[66] This deserves further study.

2.2. Comparison of ab initio Methods

Once the basic facts regarding the IQA partition of the EC energy have been presented at the CCSD(T) method, we compare to what extent the different IQA correlation contributions depend on the approximation to the electronic Hamiltonian.

Tables S5 to S47 in the Supporting Information contain the IQA contributions for all the systems at the different ab initio levels considered in this work. We summarize this information using statistical measures. For that purpose, we divide again our dataset into molecular and dimers subsets. In the first subset we report statistics with respect to IQA atomic (T^A, E_{self}^A) and interatomic (V_{xc}^{AB}, V_{cl}^{AB}) components using DMRG as a benchmark. For the dimers subset we consider monomer and intermonomer properties instead of atomic and interatomic IQA values, taking the CCSD(T) values as reference.

Figure 1 shows the mean average error (MAE) together with the mean average percentage error (MAPE) in the molecular subset. Note that CCSD(T) values may be considered as fully converged as compared to the DMRG reference. As expected, the quality of the IQA energetics improves across the HF, MP2, CISD, CCSD, and CCSD(T) series. HF atomic self-energies display the largest absolute errors. However, the corresponding percentage error is low. This does not occur necessarily for each component of the self-energy. All properties depending on the 1RDM (for instance T^A or V_{cl}^{AB}) inherit the HF values at the unrelaxed MP2 level. As discussed in the Introduction section, the description of these properties improves notably when we consider relaxed first-order densities (e.g. at the CISD or CCSD level). The behavior of V_{xc}^{AB} is also interesting: its MAE, even at the HF level, is much smaller than that of V_{cl}^{AB}. Note that this difference is even larger as we go to MP2. This surprising error hierarchy is maintained (particularly in the MAPE) for all the correlated (i.e. not HF) levels of theory employed.

Even at the CCSD(T) level, the interatomic classical interaction is the one displaying the largest MAPE of all of the com-

© 2017 Wiley-VCH Verlag GmbH & Co. KGaA, Weinheim

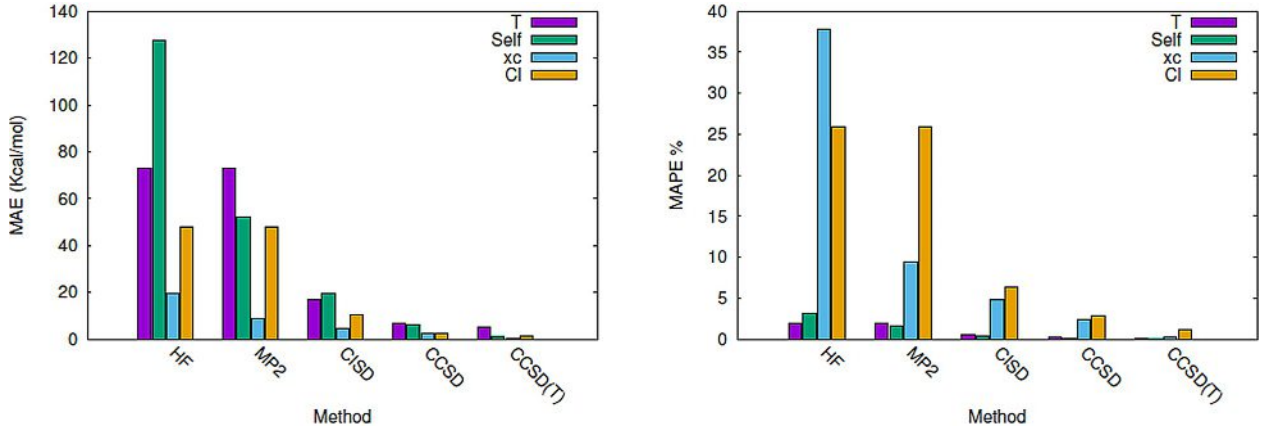

Figure 1. MAE and MAPE errors for selected IQA descriptors in the molecular subset using DMRG data as a reference.

ponents examined. This behavior is rooted in the large magnitude of the classical interaction IQA components.

Figure 2 reports the same data in our set of dimers, this time compared with the CCSD(T) results, taken as a reference. Now, the MAE/MAPE data need to be analyzed simultaneously, because group self-energies are much larger than atomic energies whereas monomer–monomer interactions are considerably smaller than interatomic interactions within a given monomer. Aside from common considerations, we find interesting that interfragment classical and exchange-correlation contributions evolve similarly on improving the quality of the method. Nevertheless, an unexpected tendency for the exchange-correlation terms to be better described than the classical ones develops smoothly again.

Overall, these data confirm that although the use of unrelaxed densities may provide a convenient way to access correlation energies and to partition them, the kinetic and electrostatic energy components cannot be easily neglected if a global picture of the role of electron correlation on molecular electron distributions is needed. In dimers, for instance, percentage errors in the IQA energy components do not drop below 10% with respect to CCSD(T) unless fully relaxed methods such as CISD are used.

3. Conclusions

The intra- and interatomic partitioning of the CCSD(T) correlation energy provides an interesting view of the spatial distribution of $E_{corr}^{Löwdin}$. In agreement with the results of Popelier et al.,[36] the intra-atomic (or intrafragment) components dominate the correlation energy, growing with the average number of electrons contained in a region. On the other hand, the behavior of the interatomic terms is richer and more diverse. For covalent interactions $E_{corr}^{int} > 0$ because of enhanced localization of bonding electrons in their respective atomic domains upon inclusion of correlation. The contrary is true for nonbonded (including mainly ionic) links. A main conclusion of this work is that $E_{corr}^{int} > 0$ evolves smoothly from the short to the long-range limit, and it becomes standard dispersion at large distances. This comportment points towards using E_{corr}^{int} as a physically sound measure of intramolecular dispersion. We propose that the sign of E_{corr}^{int} can be safely used to distinguish between bonded (positive) and nonbonded (negative) interactions. We also expect that the IQA-developments presented herein will provide valuable insights on the role of dispersion in conglomerates of hydrocarbon chains in which short- and long-range correlation effects may not be easily separated.

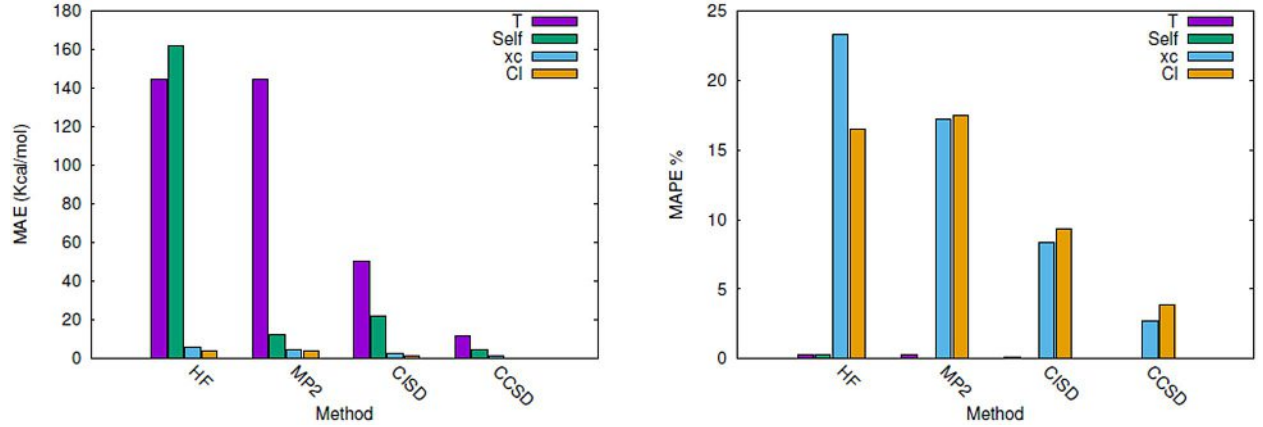

Figure 2. MAE and MAPE errors for relevant IQA quantities in the dimers subset using CCSD(T) data as a reference.

© 2017 Wiley-VCH Verlag GmbH & Co. KGaA, Weinheim

Acknowledgements

We thank the Spanish MINECO, grant CTQ2015-65790-P, the FICyT, grant GRUPIN14-049, and the European Union FEDER funds. J.M.G.V. is also grateful to CONACyT/Mexico for funding (grant 381483). T.R.R. gratefully acknowledges financial support from CONACyT (grant 253776) and DGAPA/UNAM (project IN209715) as well as computer time from DGTIC/UNAM (grant LANCAD/UNAM/DGTIC/250).

Conflict of interest

The authors declare no conflict of interest.

Keywords: ab initio calculations · bond theory · electron localization · electronic structures · noncovalent interactions

[1] G. K.-L. Chan, M. Head-Gordon, *J. Chem. Phys.* **2002**, *116*, 4462 – 4476.
[2] J. Fosso-Tande, T. S. Nguyen, G. Gidofalvi, A. E. Deprince, *J. Chem. Theory Comput.* **2016**, *12*, 2260 – 2271.
[3] N. S. Blunt, S. D. Smart, J. A. F. Kersten, J. S. Spencer, G. H. Booth, A. Alavi, *J. Chem. Phys.* **2015**, *142*, 184107.
[4] S. Guo, M. A. Watson, W. Hu, Q. Sun, G. K. L. Chan, *J. Chem. Theory Comput.* **2016**, *12*, 1583 – 1591.
[5] S. Sharma, A. Alavi, *J. Chem. Phys.* **2015**, *143*, 102815.
[6] S. Vancoillie, P. K. Malmqvist, V. Veryazov, *J. Chem. Theory Comput.* **2016**, *12*, 1647 – 1655.
[7] W. Wu, H. Zhang, B. Braïda, S. Shaik, P. C. Hiberty, *Theor. Chem. Acc.* **2014**, *133*, 1 – 13.
[8] X. He, L. Fusti-Molnar, G. Cui, K. M. Merz, *J. Phys. Chem. B* **2009**, *113*, 5290 – 5300.
[9] A. Tkatchenko, M. Scheffler, *Phys. Rev. Lett.* **2009**, *102*, 073005.
[10] J. Deng, A. T. B. Gilbert, P. M. W. Gill, *J. Chem. Theory Comput.* **2015**, *11*, 1639 – 1644.
[11] R. F. W. Bader, *Atoms in molecules: A Quantum Theory*, Oxford University Press, Oxford, **1990**.
[12] M. A. Blanco, A. Martín Pendás, E. Francisco, *J. Chem. Theory Comput.* **2005**, *1*, 1096 – 1109.
[13] E. Francisco, A. Martín Pendás, M. A. Blanco, *J. Chem. Theory Comput.* **2006**, *2*, 90 – 102.
[14] C. Foroutan-Nejad, Z. Badri, R. Marek, *Phys. Chem. Chem. Phys.* **2015**, *17*, 30670 – 30679.
[15] B. Waerder, S. Steinhauer, J. Bader, B. Neumann, H.-G. Stammler, Y. V. Vishnevskiy, B. Hoge, N. W. Mitzel, *Dalton Trans.* **2015**, *44*, 13347 – 13358.
[16] D. Tiana, E. Francisco, M. A. Blanco, P. Macchi, A. Sironi, A. Martín Pendás, *J. Chem. Theory Comput.* **2010**, *6*, 1064 – 1074.
[17] D. Tiana, E. Francisco, M. A. Blanco, P. Macchi, A. Sironi, A. Martín Pendás, *Phys. Chem. Chem. Phys.* **2011**, *13*, 5068 – 5077.
[18] D. Tiana, E. Francisco, P. Macchi, A. Sironi, A. Martín Pendás, *J. Phys. Chem. A* **2015**, *119*, 2153 – 2160.
[19] Z. Badri, C. Foroutan-Nejad, J. Kozelka, R. Marek, *Phys. Chem. Chem. Phys.* **2015**, *17*, 26183 – 26190.
[20] A. Martín Pendás, M. A. Blanco, E. Francisco, *J. Chem. Phys.* **2006**, *125*, 184112.
[21] J. M. Guevara-Vela, R. Chávez-Calvillo, M. García-Revilla, J. Hernández-Trujillo, O. Christiansen, E. Francisco, A. Martín Pendás, T. Rocha-Rinza, *Chem. Eur. J.* **2013**, *19*, 14304 – 14315.
[22] J. M. Guevara-Vela, E. Romero-Montalvo, V. A. Mora Gomez, R. Chávez-Calvillo, M. García-Revilla, E. Francisco, A. Martín Pendás, T. Rocha-Rinza, *Phys. Chem. Chem. Phys.* **2016**, *18*, 19557 – 19566.
[23] S. Ebrahimi, H. A. Dabbagh, K. Eskandari, *Phys. Chem. Chem. Phys.* **2016**, *18*, 18278 – 18288.
[24] E. Romero-Montalvo, J. M. Guevara-Vela, A. Costales, A. Martín Pendás, T. Rocha-Rinza, *Phys. Chem. Chem. Phys.* **2017**, *19*, 97 – 107.
[25] J. M. Guevara-Vela, E. Romero-Montalvo, A. Costales, A. Martín Pendás, T. Rocha-Rinza, *Phys. Chem. Chem. Phys.* **2016**, *18*, 26383 – 26390.
[26] O. A. Syzgantseva, V. Tognetti, L. Joubert, *J. Phys. Chem. A* **2013**, *117*, 8969 – 8980.
[27] K. Eskandari, M. Lesani, *Chem. Eur. J.* **2015**, *21*, 4739 – 4746.
[28] M. Yahia-Ouahmed, V. Tognetti, L. Joubert, *Comput. Theor. Chem.* **2015**, *1053*, 254 – 262.
[29] A. Martín Pendás, M. A. Blanco, E. Francisco, *J. Comput. Chem.* **2009**, *30*, 98 – 109.
[30] J. Dillen, *Int. J. Quantum Chem.* **2013**, *113*, 2143 – 2153.
[31] F. Cortés-Guzmán, G. Cuevas, A. Martín Pendás, J. Hernández-Trujillo, *Phys. Chem. Chem. Phys.* **2015**, *17*, 19021 – 19029.
[32] D. Ferro-Costas, A. Martín Pendás, L. González, R. Mosquera, *Phys. Chem. Chem. Phys.* **2014**, *16*, 9249 – 9258.
[33] D. Ferro-Costas, E. Francisco, A. Martín Pendás, R. A. Mosquera, *ChemPhysChem* **2016**, *17*, 2666 – 2671.
[34] J. Jara-Cortés, J. M. Guevara-Vela, A. Martín Pendás, J. Hernández-Trujillo, *J. Comput. Chem.* **2017**, *38*, 957 – 970.
[35] P. J. Gatti, C. MacDougall, R. F. W. Bader, *J. Chem. Phys.* **1988**, *88*, 3792.
[36] J. L. McDonagh, M. A. Vincent, P. L. A. Popelier, *Chem. Phys. Lett.* **2016**, *662*, 228 – 234.
[37] F. J. Holguín-Gallego, R. Chávez-Calvillo, M. García-Revilla, E. Francisco, A. Martín Pendás, T. Rocha-Rinza, *J. Comput. Chem.* **2016**, *37*, 1753 – 1765.
[38] T. Helgaker, P. Jørgensen, J. Olsen, *Molecular Electronic Structure theory*, Wiley, Chichester, **2004**.
[39] J. L. McDonagh, A. F. Silva, M. A. Vincent, P. L. A. Popelier, *J. Phys. Chem. Lett.* **2017**, *8*, 1937 – 1942.
[40] T. Thonhauser, V. R. Cooper, S. Li, A. Puzder, P. Hyldgaard, D. C. Langreth, *Phys. Rev. B* **2007**, *76*, 125112.
[41] *NIST Chemistry WebBook, NIST Standard Reference Database Number 69* (Eds.: P. J. Linstrom, W. G. Mallard), National Institute of Standards and Technology, Gaithersburg MD, 20899, **2017**.
[42] P. Jurečka, J. Šponer, J. Černý, P. Hobza, *Phys. Chem. Chem. Phys.* **2006**, *8*, 1985 – 1993.
[43] M. S. Marshall, L. A. Burns, C. D. Sherrill, *J. Chem. Phys.* **2011**, *135*, 194102.
[44] F. O. Kannemann, A. D. Becke, *J. Chem. Theory Comput.* **2010**, *6*, 1081 – 1088.
[45] M. W. Schmidt, K. K. Baldridge, J. A. Boatz, S. T. Elbert, M. S. Gordon, J. H. Jensen, S. Koseki, N. Matsunaga, K. A. Nguyen, S. Su, T. L. Windus, M. Dupuis, J. A. Montgomery, *J. Comput. Chem.* **1993**, *14*, 1347 – 1363.
[46] Q. Sun, T. C. Berkelbach, N. S. Blunt, G. H. Booth, S. Guo, Z. Li, J. Liu, J. McClain, S. Sharma, S. Wouters, G. K.-L. Chan, *The Python-based Simulations of Chemistry Framework (PySCF)*, **2017**. http://arxiv.org/abs/1701.08223.
[47] G. K.-L. Chan, D. Zgid, *Annu. Rep. Comput. Chem.* **2009**, *5*, 149 – 162.
[48] G. K.-L. Chan, *J. Chem. Phys.* **2004**, *120*, 3172 – 3178.
[49] D. Ghosh, J. Hachmann, T. Yanai, G. K. L. Chan, *J. Chem. Phys.* **2008**, *128*, 144117.
[50] S. Sharma, G. K.-L. Chan, *J. Chem. Phys.* **2012**, *136*, 124121.
[51] R. Chávez-Calvillo, M. García-Revilla, E. Francisco, A. Martín Pendás, T. Rocha-Rinza, *Comput. Theor. Chem.* **2015**, *1053*, 90 – 95.
[52] G. K. L. Chan, M. Head-Gordon, *J. Chem. Phys.* **2003**, *118*, 8551 – 8554.
[53] G. K.-L. Chan, M. Kállay, J. Gauss, *J. Chem. Phys.* **2004**, *121*, 6110 – 6116.
[54] R. Olivares-Amaya, W. Hu, N. Nakatani, S. Sharma, J. Yang, G. K. L. Chan, *J. Chem. Phys.* **2015**, *142*, 034102.
[55] A. Martn Pendás, E. Francisco, *Promolden. A QTAIM/IQA code*, unpublished.
[56] E. Francisco, A. Martín Pendás, M. A. Blanco, *J. Chem. Phys.* **2007**, *126*, 094102.
[57] E. Francisco, A. Martín Pendás, M. A. Blanco, *J. Chem. Phys.* **2009**, *131*, 124125.
[58] I. Ruiz, E. Matito, F. J. Holguín-Gallego, E. Francisco, A. Martín Pendás, T. Rocha-Rinza, *Theor. Chem. Acc.* **2016**, *135*, 209.
[59] A. Stone, *The Theory of Intermolecular Forces, of International Series of Monographs on Chemistry*, Clarendon, Oxford, **1997**.
[60] B. Jeziorski, R. Moszynski, K. Szalewicz, *Chem. Rev.* **1994**, *94*, 1887 – 1930.
[61] M. J. Allen, D. J. Tozer, *J. Chem. Phys.* **2002**, *117*, 11113.
[62] R. M. Parrish, J. F. Gonthier, C. Corminbœuf, C. D. Sherrill, *J. Chem. Phys.* **2015**, *143*, 051103.

© 2017 Wiley-VCH Verlag GmbH & Co. KGaA, Weinheim

[63] E. Pastorczak, A. Prlj, J. F. Gonthier, C. Corminboeuf, *J. Chem. Phys.* **2015**, *143*, 224107.
[64] E. Francisco, A. Martín Pendás, *Non-covalent Interactions in Quantum Chemistry and Physics: Theory and Applications*, (Eds.: A. Otero de la Roza, G. di Labio), Elsevier, Amsterdam, **2017**.
[65] P. Su, H. Li, *J. Chem. Phys.* **2009**, *131*, 014102.
[66] J. K. Pearson, P. M. W. Gill, J. M. Ugalde, R. J. Boyd, *Mol. Phys.* **2009**, *107*, 1089.

Manuscript received: August 24, 2017
Revised manuscript received: October 4, 2017
Accepted manuscript online: October 5, 2017
Version of record online: November 15, 2017

© 2017 Wiley-VCH Verlag GmbH & Co. KGaA, Weinheim

ChemPubSoc Europe

DOI: 10.1002/cphc.201800474

CHEMPHYSCHEM Articles

Halogen Bonds in Clathrate Cages: A Real Space Perspective

José Manuel Guevara-Vela,[a] David Ochoa-Resendiz,[b, c] Aurora Costales,[a] Ramón Hernández-Lamoneda,[b] and Ángel Martín Pendás*[a]

In this paper we present real space analyses of the nature of the dihalogen-water cage interactions in the 5^{12} and $5^{12}6^2$ clathrate cages containing chlorine and bromine, respectively. Our Quantum Theory of Atoms in Molecules and Interacting Quantum Atoms results provide strong indications that halogen bonding is present even though the lone pairs of water molecules are already engaged in hydrogen bonding interactions.

1. Introduction

A halogen bond is defined by the IUPAC as a relationship where "…there is evidence of a net attractive interaction between an electrophilic region associated with an halogen atom in a molecular entity an a nucleophilic region in another, or the same, molecular entity".[1] Even though its full understanding is relatively recent, its relevance is already widely recognized in very different fields, such as biomolecules, crystal engineering, or functional systems design.[2]

The nature of guest-host interactions in the case of dihalogen molecules in water clathrate cages[1] has been the subject of recent debate in both experimental[3–5] and theoretical studies.[6–9] The initial interpretation of the observed electronic shifts in ultraviolet and visible spectra of bromine clathrate assumed that halogen bonding could not be responsible since all the water lone-pairs are involved in hydrogen bonding of the water lattice and thus not available for halogen bonding.[3] In contrast the much larger blue-shifts observed in bromine aqueous solutions were consistent with the formation of halogen bonding interactions.[10–13] However evidence of halogen bonding in clathrate cages was strongly suggested in ab initio local correlation calculations through an energy partitioning analysis and calculation of the electronic shifts at selected geometries.[8] In particular the role of the ionic component as indicator of halogen bonding was stressed. This was further confirmed by performing a more thorough calculation of the electronic shifts taking into account the rotational motion of the dihalogen inside the cages.[14] Another important set of experiments probed the structural characteristics of chlorine and bromine clathrates in X-ray measurements.[5] The case of chlorine has a long and interesting history starting with its accidental discovery by sir Humphrey Davy[15] in 1811, followed by the first X-ray determination in 1952 by Pauling and Marsh[16] where using van der Waals radii arguments it was assumed that chlorine would not fit in the smaller dodecahedral cage and the recent detailed study by the group of Ripmeester showing that more than 30% of the 5^{12} dodecahedral cages are occupied[5]. Furthermore in the case of the mixed chlorine and bromine clathrate a strong distortion of the 5^{12} cage and a short Cl–O distance (2.7 Å) together with lengthening of the nearby hydrogen bonds could be an indication of the presence of halogen bonding interactions.

Previous theoretical analyses have focused so far on orbital based energetic partitionings that do not allow for discriminating directly halogen bonds from other types of interactions. In the meantime, a considerable amount of work has shown that spatial features of the electron density ρ, like the position of charge concentration (CC) and charge depletion (CD) regions of the Laplacian of the density, $\nabla^2\rho$, lead to unambiguous descriptors in these systems. For instance, Espinosa and coworkers[17] have shown that halogen bonded synthons, used in crystal engineering, are characterized by a clear match between CC's and CD's that can be interpreted electrostatically, in agreement with the σ-hole paradigm. We are not aware that any of these techniques have been used to date to establish unambiguously the nature of the bonding between dihalogens and clathrate cages. A recent work by Dureckova and coworkers[18] performed a natural bond orbital (NBO)[19] analysis of dichlorine and dibromine clathrate cages with conclusions which are not far from our own. However, NBO results in weakly interacting systems should be taken with care.

We hereby use a battery of methods, that range from the description of the topological features of the electron density in these systems as provided by the quantum theory of atoms in molecules (QTAIM), passing through an orbital free energetic decomposition based on QTAIM basins, the so-called interacting quantum atoms approach (IQA), and including arguments

[a] J. M. Guevara-Vela, A. Costales, Á. Martín Pendás
Departament of Analytical and Physical Chemistry, University of Oviedo, E-33006, Oviedo, Spain
E-mail: ampendas@uniovi.es
[b] D. Ochoa-Resendiz, R. Hernández-Lamoneda
Centro de Investigaciones Químicas, Universidad Autónoma del Estado de Morelos, Av. Universidad 1001, Cuernavaca 62209, Morelos, México.
[c] D. Ochoa-Resendiz
Instituto Tecnológico de Zacatepec, Calz. Tecnológico 27 Zacatepec 62780, Morelos, México.

Supporting information for this article is available on the WWW under https://doi.org/10.1002/cphc.201800474

[1] Clathrates are compounds in which the guest molecule is in a cage formed by the host molecule.

© 2018 Wiley-VCH Verlag GmbH & Co. KGaA, Weinheim

borrowed from the analysis of the electron localization function (ELF) and the non-covalent interaction index (NCI). As we will show, our results provide strong indications that halogen bonding is present even though the water molecules lone pairs are already engaged into hydrogen bonding interactions.

2. Methodology

We have considered a combination of real space analyses that could further advance the understanding of the guest-host relation. The Quantum Theory of Atoms in Molecules (QTAIM), based on the structure of the electron density scalar field, is an appropiate technique in the research of intra-atomic interactions, providing a separation of the molecular real space into disjoint regions. The latter, constructed as the attraction basins of the density, are identified with quantum atoms. All standard quantum-mechanical observables in QTAIM can be decomposed into intra- and (at most) interatomic contributions exactly.[20]

The QTAIM has been extensively used for investigations in diverse problems related with intra- and intermolecular interactions. We can cite, for instance, the nature of endohedral complexes,[21,22] hydrogen bonds[23–25] or photoisomerization[26] processes, the anomeric effect,[27] etc. In this regard, halogen bonding is not unknown to these analyses, having been widely explored by Grabowski,[28] or by Espinosa and coworkers as crystal engineering is concerned.[17] A real space, thus orbital invariant, decomposition of the molecular energy compatible with the QTAIM partitioning is provided by the Interacting Quantum Atoms (IQA) approach.[29,30] IQA writes the total molecular energy as a sum of intra- and interatomic terms that gauge the interaction between atomic domains:

$$E = \sum_{A} E^{A}_{net} + \sum_{A>B} E^{AB}_{int}, \quad (1)$$

where E^{A}_{net} is the net energy of atom A, which contains the kinetic and potential energy terms of all particles contained in domain A, and E^{AB}_{int} is the interaction energy between atoms A and B that gathers all the inter-particle potential energy contributions of particles in domain A with particles in domain B. The interaction energy between two basins can be further separated into a classical component, which is assimilated as the ionic contribution to the interaction V^{AB}_{cl} and an exchange correlation one, V^{AB}_{xc}, which measures the covalent term.

$$E^{AB}_{int} = V^{AB}_{cl} + V^{AB}_{xc} \quad (2).$$

Because of this distinctive ability of separating bonding components as well as reconstructing fully the energy in a pairwise additive manner, IQA has been succesfully employed to scrutinize a variety of phenomena where there is a combination of Coulombic and quantum contributions, like the cooperativity in hydrogen bonds,[31,32] the role of covalency in metal-metal interactions[33] or in halogen bonding.[34–36]

Since lone pairs are an essential part of the accepted σ-hole paradigm that is usually employed to describe halogen bonds, we have also used real space techniques which stress the role of these objects. The laplacian of the density, $\nabla^2\rho$, a field that recovers the atomic shell structure and its symmetry breaking in molecules, has been traditionally used to uncover the position of those objects. However, it is well known that the outer shells are not captured by $\nabla^2\rho$ beyond $Z = 20$ (the calcium atom). Since we are not only dealing with Cl ($Z = 17$), but also with Br ($Z = 35$), we have decided to examine the electron localization function (ELF) of Becke and Edgecombe,[37] which was further popularized in chemistry by Savin and Silvi.[38] This scalar, which can be interpreted as measuring the excess kinetic energy density of an electron system with respect to the bosonic von Weizsäcker reference, provides stunning images of great chemical value by, grossly speaking, locating regions where electrons are localized. It also provides an exhaustive partition of space into regions that are now associated to cores, lone pairs, and bonds instead of atoms. As we will show, ELF provides important insights about the characterization of lone pairs and σ-holes, both essential elements in halogen bonding.

Similarly, contemporary research is continuously emphasizing the role that dispersion forces play in building the overall architecture of molecular aggregates. Given the rather delocalized nature of these interactions, the standard local QTAIM analysis based on descriptors obtained at critical points is not particularly suited to uncover the importance of these forces for a given interaction. To this end, the non covalent interactions index (NCI) introduced by Johnson and coworkers has shown to be particularly useful. The NCI index is also a kinetic energy based descriptor, this time using the reduced density gradient $s(\mathbf{r}) \approx |\nabla\rho(\mathbf{r})|/\rho(\mathbf{r})^{4/3}$. In intermolecular regions, minima of s uncover non-covalent interactions, that can be further classified if the second eigenvalue of the hessian of the electron density (λ_2) is also used. Isosurfaces of the NCI index rainbow-coloured through λ_2, with blue and red corresponding to (very) negative and (very) positive λ_2 values, respectively, provide very intuitive images of intermolecular interactions. Strongly blue isosurfaces are found, for instance, in hydrogen bonds, while strongly red ones tend to uncover sterically crowded regions. The NCI picture of the dihalogen clathrates adds to the global QTAIM, IQA, and ELF descriptions.

3. Computational Details

We have specifically studied Cl_2 and Br_2 molecules confined in the 5^{12} and the $5^{12}6^2$ clathrate cages, respectively. A plot of both systems is shown in Figure 1.

The geometries for the clathrate complexes have been taken from those reported in a previous local correlation study[8] where evidence of halogen bonding was found for the $Cl_2@5^{12}$ cage in the global energy minimum but not in $Br_2@5^{12}6^{12}$, where it appeared at a geometry which does not correspond to a total energy minimum. Using the local correlation energy partitioning analysis in this case, it was possible to establish a clear correlation with the ionic energy component and for this reason the geometry at which this component is minimum is also presented and discussed.

© 2018 Wiley-VCH Verlag GmbH & Co. KGaA, Weinheim

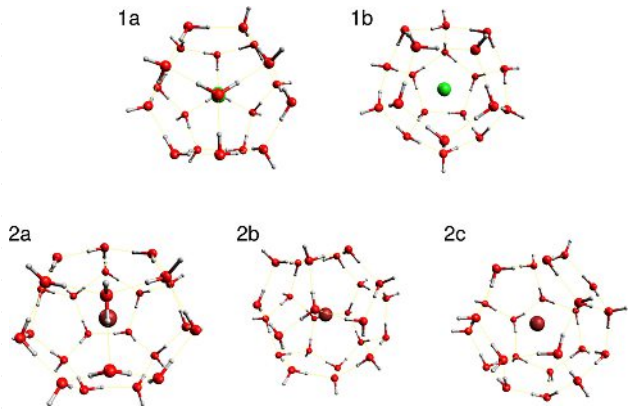

Figure 1. Sketch of the systems studied in this work. Cl_2 in the 5^{12} cage at the global minimum (1a) and maximum (1b) conformations, and Br_2 in the $5^{12}6^2$ cage in three conformations: the global minimum (2a), the conformation at which the ionic energetic component is minimum (2c, see the text for further information), and the global maximum (2c).

The electronic structure calculations necessary to obtain the density were done at the M06-X/aug-cc-pVTZ[39,40] level of theory using the GAUSSIAN09 package.[41] The QTAIM and IQA analyses were carried out with the AIMAll program[42] while the ELF calculations were made using our in house PROMOLDEN code.[43] The IQA computations was done employing an approximately reconstructed second order reduced density matrix.[44]

4. Results and Discussion

4.1. QTAIM Topology

A local QTAIM analysis reveals that in both complexes, regardless of their specific conformation, numerous bond paths exist that link the halogen atoms to the oxygens in the clathrate cage, as shown in Figure 2. Besides being traditionally associated with bonds in simple chemical compounds,[20] in more controvertial or complex situations bond paths are indicators of preferred quantum-mechanical exchange channels between atoms.[45] Their presence here is a first sign of non-negligible interactions between the halogen atoms and some of the oxygens forming the water molecules in the cage.

However, not all the bond paths present in the different conformations should be thought of as equivalent. Actually, their distances and angles with respect to the halogen-halogen axis are very different. On the one hand we have those interactions that fulfil the condition of linearity needed for being considered as halogen bonds, and on the other hand we can gather those that do not, i.e., those that form a considerable angle or are even perpendicular to the halogen-halogen axis. This is shown in Figure 1, where two of the former are highlighted in blue while two of the latter are pointed out in black.

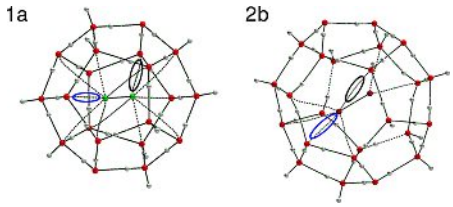

Figure 2. QTAIM bond paths for systems 1a and 2b. In blue we highlight two oxygen-halogen interactions that are (near) colinear to the halogen-halogen bond (Cl61-O4 and Br73-O16). Similarly, two representative of nonlinear interactions are indicated in black (Cl62-O5 and Br73-O7).

Table 1 summarizes the geometrical parameters as well as several bond critical point (BCP) QTAIM descriptors of the interactions that are more likely to be considered as halogen bonds, the Cl61-O4 bond path in 1a and the Br73-O16 one in 2b, together with other oxygen-halogen contacts selected for comparison, and the reference systems Cl_2···H_2O and Br_2···H_2O.

Table 1. Geometric parameters and several local QTAIM properties of some bond paths present in the different conformations examined. ρ_b and $\nabla^2\rho_b$ refer to the values of the electron density and its laplacian at the bond critical point.

System	Pair	Distance/Å	∠OXX/°	ρ_b/a.u.	$\nabla^2\rho_b$/a.u.
Cl_2···H_2O	Cl2···O3	2.771	180.0	0.0157	0.0698
1a	Cl61···O4	2.790	175.2	0.0174	0.0731
	Cl62···O5	3.204	130.3	0.0096	0.0348
1b	Cl61···O18	2.835	133.9	0.0153	0.0696
Br_2···H_2O	Br2···O3	2.796	179.5	0.0181	0.0732
2a	Br74···O7	3.159	165.1	0.0081	0.0334
2b	Br73···O7	4.237	84.2	0.0014	0.0047
	Br73···O16	2.788	167.0	0.0209	0.0803
	Br74···O31	2.895	162.4	0.0176	0.0705
2c	Br73···O31	3.044	141.2	0.0146	0.0548

As the local QTAIM indicators at BCPs are regarded, the density at the bond critical point in these compounds is closely related to the distance between the atoms involved, and thus offers little extra information related to the nature of the interaction. The Laplacian of the density ($\nabla^2\rho$), traditionally used to separated closed-shell (if positive) from shared-shell (if negative) behavior, reproduces this trend, magnifying it. In all of the cases, its small positive value implies weak closed-shell interactions, as expected. All in all, these simple local descriptors do neither confirm nor deny the halogen bond nature of the guest-host bonding. More information can be obtained from the analysis of other scalar fields.

A relevant point regards the effect of halogen bonding on the water molecules that directly participate in these interactions. We have examined this issue by monitoring several QTAIM indicators. For instance, in system 1a the Cl61-O4 interaction involves the O4H55H57 molecule. This is hydrogen-bonded to O8H42H46. The density at the hydrogen bond critical point between these two molecules (that with a shared oxygen lone pair) is 0.0368 au, and its delocalization index 0.088. Similar water molecules with a free lone pair not directly involved in halogen bonding are O15H50H52, with an equivalent density equal to 0.0378 au and DI = 0.097, and O14H26H27, with densities and DIs equal to 0.0368 and 0.088, respectively. These values are almost identical to those in the O4H55H57 molecule. This means that the participation of already hydrogen-bonded lone pairs of water molecules in halogen bonding does not alter essentially

© 2018 Wiley-VCH Verlag GmbH & Co. KGaA, Weinheim

their nature, at least not beyond the variability displayed by other water molecules in the cage not engaged in direct interactions with the halogen atoms.

4.2. ELF Isosurfaces and the Role of Lone Pairs

The importance of the ELF analysis for this study thrives due to its ability to bring into focus the presence of lone pairs. The standard electrostatic model of halogen bonding rests heavily on the geometrical disposition of lone pairs. In typical cases it is the presence of a σ-hole in the halogen, accompanied by a lone pair in the partner that acts as a Lewis base, that is used to recognize the interaction as a halogen bond. Here, the purported saturation of all the lone pairs of the oxygen atoms belonging to the water molecules of the cage, which are engaged in normal hydrogen bonds, forms the basis for denying the presence of halogen bonds.

Figure 3 shows relevant ($\eta = 0.9$ a.u) ElF isosurfaces. It is first interesting to recognize the archetypal halogen bond pattern in the Cl_2···H_2O and Br_2···H_2O complexes. In both cases, the halogen's lone pairs adopt a quasi-cyllindrical arrangement seen in the ELF as a well developed localization torus around the halogen atom. This leaves a region of much smaller η values that can be put in correspondence with the electrostatic potential *sigma*-hole. Clearly, one of the two lone pairs of the oxygen atoms points directly toward the σ-hole. This view is in agreement with a donor-acceptor paradigm, and explains the lock-and-key geometry which is observed. Notice that more subtle effects can also be recognized from a more detailed analysis of the ELF function. For instance, it is clear that the two lone pairs of the donor water molecule cease to be equivalent in the complex, and that some electronic charge is transferred toward the lone pair pointing away from the dihalogen in an attempt to minimize interelectron repulsions.

The ELF isosurfaces of clathrates 1a and 2b show that although the lone pairs of the oxygen atoms of the cage are basically engaged in hydrogen bonds in the expected H_2O(LP)···H–OH manner, the closest X···O contacts involve a lock-and-key distribution of part of a lone pair and the X *sigma*-hole. This lone pair is both participating in a hydrogen bond and in what we will call a partial halogen bond. Notice that these contacts are the same appearing in Table 1 as those with largest densities and laplacians and smallest X–O distances. Moreover, the rest of the oxygens' lone pairs point either outside the clathrate cage or lie vaguely around the halogen's tori, disqualifying these contacts as halogen bonds. The fact that we are using a single cage model raises the question of what changes can be expected if the lone-pairs of the water molecules involved in halogen bonding are saturated. This point has been discussed, first, in reference[8] where it was shown that addition of extra water molecules has the expected effect of decreasing the interaction between the *sigma*-hole and the newly saturated lone-pair but, crucially, the interaction with the lone-pair involved in hydrogen bonding within the single cage remains the same. It is this interaction that retains the main characteristics of a halogen bond. More recently in reference[18] this point was confirmed doing a more exhaustive saturation of the dodecahedral cage and again concluding that the lone-pair involved in hydrogen bonding within the cage shows a strong donor-acceptor interaction as determined in their NBO analysis.

4.3. NCI Isosurfaces and the Delocalized Nature of the X_2Cage Interactions

Figure 4 shows the NCI equivalent to Figure 3. It is first interesting to show that the reference Cl_2···H_2O and Br_2···H_2O complexes develop a rather standard, blue disk-shaped surface between the halogen and the oxygen atom, in complete agreement with the ELF picture that points toward the importance of lone pairs. In the 1a and 2b clathrates the overall image is confirmed. The figure emphasizes how all the water-water hydrogen bonds are well developed, and how this does not preclude the appearance of rather intense blue contact surfaces between the chlorine or bromine atoms and the closest oxygen atoms, again in agreement with the lock and key arrangement found in the ELF. As expected, the NCI index shows that the interaction between the dihalogen and the cage involves a considerable number of the atoms of the cage

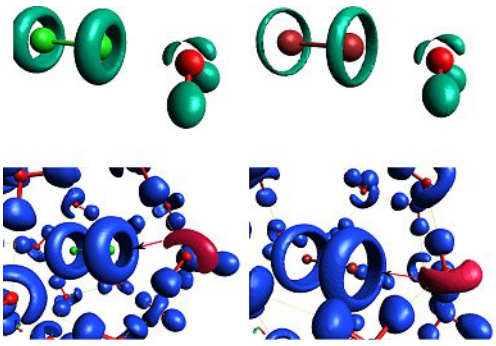

Figure 3. $\eta = 0.9$ ELF isosurfaces for the Cl_2···H_2O and Br_2···H_2O complexes (top, from left to right), and for the relevant parts of systems 1a and 2b (bottom, also from left to right). In this case, an arrow shows how the oxygens's lone pairs involved in halogen bonding (in red) point twoard the appropriate σ-holes.

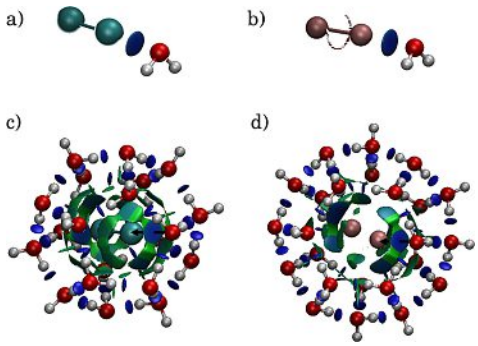

Figure 4. NCI isosurfaces for the Cl_2···H_2O and Br_2···H_2O complexes (top, from left to right), and for systems 1a and 2b (bottom, also from left to right). The attractive surface corresponding to the oxygen-halogen interaction is intersected by a black arrow pointong from the O to the X atom.

© 2018 Wiley-VCH Verlag GmbH & Co. KGaA, Weinheim

(notice the extended nature of the isosurfaces), but it is also clear that the most attractive ones are those that have been previously identified as potential halogen bonds.

In this sense, both the ELF and NCI descriptions provide compatible interpretations favouring the existence of halogen bonding in the 1a and 2b conformers.

4.4. IQA Interaction Energies

Although both a standard QTAIM analysis at BCPs as well as the chemical images provided by the ELF and NCI agree with a non-negligible role of halogen bonding in the stabilization of the 1a and 2b clathrates, a more convincing argument coming from energetic descriptors can also be put forward. To that end we have used the IQA approach to dissect the features of individual interatomic interactions, specifically as their relative strength with respect to the $X_2\cdots H_2O$ systems are regarded. A summary of our results can be found in Table 2.

Table 2. Relevant IQA descriptors between selected oxygen-halogen interactions. Energies in kcal/mol and delocalization indices in au.

System	Interaction	$E_{int^{AB}}$	$V_{cl^{AB}}$	$V_{xc^{AB}}$	DI(A,B)
$Cl_2\cdots H_2O$	Cl2–O3	−24.48	−10.36	−14.12	0.131
1a	Cl61–O4	−21.74	−7.20	−14.54	0.131
	Cl62–O5	−5.61	0.63	−6.25	0.063
1b	Cl61–O18	−12.12	−1.60	−10.52	0.092
$Br_2\cdots H_2O$	Br2–O3	−34.07	−17.06	−17.01	0.158
2a	Br74–O7	−13.30	−7.02	−6.18	0.060
2b	Br73–O7	−2.06	−1.35	−0.70	0.009
	Br73–O16	−37.78	−19.49	−18.29	0.165
	Br74–O31	−19.61	−5.36	−14.24	0.133
2c	Br73–O31	−14.62	−3.61	−11.01	0.106

It is firstly noteworthy that in the isolated $X_2\cdots H_2O$ complexes, the direct halogen-oxygen IQA interaction energy is non-negligible, about −24 and −34 kcal/mol in the chlorine and bromine compounds. Even more interesting is noticing that both the electrostatic (classical) and covalent (exchange-correlation) contributions are important. V_{cl} is slightly more relevant in $Br_2\cdots H_2O$, in agreement with the increased intensity of the σ-hole in this case. The importance of V_{xc} is in line with previous IQA work on hydrogen bonding.[46] In more traditional molecular orbital descriptions, this can be read as an important overlap contribution. When other factors are equal, the exchange-correlation term of a given weak interaction is then mostly dependent on the distance between the atoms involved. Thus, although V_{xc} is essential for the final energetic stabilization of the complex, in a sense the IQA marker of the presence of a halogen bond is a strong and attractive $V_{cl_{AB}}$.

Although not surprising to the electrostatic potential connoisseur, the stabilizing (negative) values of V_{cl} reported in the Table require further explanation, since both the halogen atoms and the corresponding oxygens bear a negative QTAIM net charge. Since the monopole-monopole electrostatic contribution usually dominates, a negative V_{cl} can only be the result of large counteracting dipole and quadrupole terms, i.e. of considerable density polarizations. For instance, in the Cl61-O4 interaction of the 1a conformer, the QTAIM charges are −0.008 and −1.295 au for the Cl and O atoms, respectively. This provides a monopole-monopole term equal to 1.3 kcal/mol, in sharp contrast with the exact electrostatics, −7.20 kcal/mol. Notice that ascribing this difference to further order multipolar terms has a more qualitative than quantitative nature. Actually, the multipolar interaction in this type of interactions does not converge to the exact value, since the condition for its proper convergence is not fulfilled.

The charge polarizations can be pictorially attributed to the lone pair/σ-hole interaction. A corroboration is found for the Cl62-O5 atomic pair in the 1a conformer, where the classical part of the interaction energy is sligthly positive as in this case the interaction occurs between an oxygen's lone pair and the lone pairs of the adjacent chlorine atom.

As the clathrate cages are formed and the water molecules engage in hydrogen bonding, the closest halogen-oxygen interactions are modified. As the data displayed in the Table shows, this new environment decreases the Cl61-O4 E_{int} in the Cl 5^{12} cage to about −22 kcal/mol. This 2.7 kcal/mol destabilization is basically due to V_{cl}, and is probably associated to a non-ideal geometry with respect to the $Cl_2\cdots H_2O$ case. The Cl62-O5 pair, with a larger Cl–O distance and a non-aligned σ-hole, oxygen pair results in a slightly positive V_{cl}, as already commented, and a much smaller exchange contribution. If we restrict to the Cl61-O4 pair, the IQA energetic description fully agrees with a Cl···O halogen bond, slightly weaker than that in the reference complex.

Similar conclusions can be drawn from the bromine cages. Since the Br73-O16 pair has a slightly smaller Br–O distance than that found in the isolated $Br_2\cdots H_2O$ complex, both the electrostatic and exchange components of the interaction increase slightly, V_{cl} feeling a slightly stronger effect. Overall, the Br–O V_{cl} term almost doubles its chlorine counterpart. The large interaction energy is again the result of combining a larger σ-hole for the bromine atom, and a more flexible geometry afforded by a bigger clathrate cage. Again, the Br73-O16 interaction cannot and should not be distinguished from the widely accepted halogen bonding found in $Br_2\cdots H_2O$.

Another indication of the role that exchange-correlation plays in this type of halogen bonding comes from the direct two-center integration of the exchange-correlation density, which provides the delocalization index, DI.[47] DIs are real space generalizations of bond orders, and show how many pairs of electrons are shared between two atomic basins. Relevant DI values in Table 2 show a well known parallel behavior with V_{xc} values. What is more important to us here, is that the halogen-oxygen bond orders may display values as large as 0.16 (in the Br74-O31 interaction in cage 2b). These are not fully developed covalent interactions (the DI in H_2 is 1.0), but are comparable to those found in traditional hydrogen bonds (the DI for the H,O interaction in the water dimer is close to 0.07 au). This is an independent proof of the halogen-cage electron exchange.

© 2018 Wiley-VCH Verlag GmbH & Co. KGaA, Weinheim

ChemPubSoc Europe

DOI: 10.1002/ejic.201800567

EurJIC European Journal of Inorganic Chemistry

Full Paper

Gold Phosphine Complexes

Stability and *trans* Influence in Fluorinated Gold(I) Coordination Compounds

Guillermo Moreno-Alcántar,*[a] Hugo Hernández-Toledo,[a] José Manuel Guevara-Vela,[b] Tomás Rocha-Rinza,[c] Ángel Martín Pendás,[b] Marcos Flores-Álamo,[a] and Hugo Torrens*[a]

Abstract: We examined the Au–P and Au–X chemical bonding scenario throughout the series of compounds of the general formula [AuX(L_P)] wherein L_P is triphenylphosphine or a fluorinated phosphine [PPh_F = $P(C_6H_5)_2(C_6F_5)$ **1**, $P(C_6H_5)(C_6F_5)_2$ **2** and $P(C_6F_5)_3$ **3**] and X is chloride or a fluorinated thiolate [SR_F = SCF_3 **a**, SCH_2CF_3 **b**, SC_6F_5 **c**, $SC_6F_4(CF_3)$-4 **d**]. We found that the increase of the fluorination degree or the replacement of Cl^- by a ^-SR_F ligand decreases the stability of the compound. Furthermore, this substitution shifts the ^{31}P-NMR signals to low field, which indicates differences in the electronegativity of the phosphorus due to the distinct *trans* influences of the Cl^- and ^-SR_F species. These effects correlate with the charge of the gold atom coordinated to phosphorus. Our investigation shows the high potential of fluorination as a strategy for the modulation of the properties of gold compounds, for example in catalysis, and the applicability of quantum chemical topology studies in the explanation of these features.

Introduction

Gold(I) tris(pentafluorophenyl)phosphine complexes have been extensively used as catalysts in organic conversions.[1–8] In contrast, the applications and properties of the related partially fluorinated phosphines have been relatively unexplored.[9–11] This circumstance occurs despite the interesting opportunities for the analysis of the ligand-induced influences over the catalytic center that these compounds offer.

One of these effects is the *trans* influence, i.e., the set of modifications that one ligand induces over the metal bond to the ligand in its *trans* position, which concerns the stability, reactivity and properties of coordination compounds.[12] The understanding and use of this effect is one of the pillars for the improvement of synthetic and predictive capabilities of inorganic chemists. Particularly, the *trans* influence, can be studied in different ways.[13–17] If the atom of the ligand interacting directly with the metal center is an NMR active species, this technique becomes a powerful tool to get insights into this phenomenon.[18–20] Because gold(I) coordination compounds commonly exhibit linear geometries, they are ideal systems to study the *trans* influences among different ligands.[20,21]

Given this background, we investigated the *trans* influence that anionic ligands exert over phosphorus atoms in gold phosphine complexes. More specifically, we synthesized and characterized the three fluorophosphine gold(I) derivatives [AuCl(PPh_F)] with PPh_F = $P(C_6H_5)_2(C_6F_5)$ **1**, $P(C_6H_5)(C_6F_5)_2$ **2** and $P(C_6F_5)_3$ **3**. We also obtained the previously unreported crystal X-ray structures of compounds **1** and **2**. In addition, we prepared 8 new derivatives via the substitution of chloride in **1** and **2** with fluorinated thiolates, yielding the compounds with the general formula [Au(SR_F)(PPh_F)] (where SR_F = SCF_3 **a**, SCH_2CF_3 **b**, SC_6F_5 **c**, $SC_6F_4(CF_3)$-4 **d**). We report the crystal structures of compounds [$AuSCF_3(P(C_6H_5)_2(C_6F_5))$] **1a** and [$AuSCH_2CF_3$ $(P(C_6H_5)_2(C_6F_5))$] **1b** as well. We also synthesized the analogous derivatives of triphenylphosphine [$AuSR_F(PPh_3)$].

Later, we studied the relative stability of the three fluorinated-phosphine gold(I) chloride derivatives (1, 2 and 3) by ^{31}P-NMR spectroscopy. Finally, we performed electronic structure and quantum chemical calculations to investigate the chemical bonding scenario within these systems. Overall, our results show how the techniques employed herein can prove useful in the study of the *trans* effect in gold(I) phosphine complexes.

Results and Discussion

Chloro(fluorophosphine)gold(I) compounds [AuCl(PPh_F)] were prepared by the reaction of chloro(tetrahydrothiophene)gold(I) with the corresponding fluorinated phosphine. The synthesis and experimental handling of the thiolate derivatives of compounds **1**, **2** and **3** show that compounds **1x** are the most stable as they can be further characterized and crystallized. Compounds **2x** are less stable and even if they can be characterized, their short lifetimes and low stability did not allow us to obtain crystals. Finally, thiolate derivatives of **3** could not be identified. To further examine the relative stability of the chloro(fluorophosphine)gold(I) compounds (**1**, **2** and **3**), we performed li-

[a] *Faculty of Chemistry, Universidad Nacional Autónoma de México, Ciudad Universitaria, Coyoacán, México, 04510*
E-mail: lgma@comunidad.unam.mx, torrens@unam.mx
https://quimica.unam.mx/
[b] *Department of Physical and Analytical Chemistry, Universidad de Oviedo, Julián Clavería 8, Oviedo, Spain. E-33006*
[c] *Institute of Chemistry, Universidad Nacional Autónoma de México, Ciudad Universitaria, Coyoacán, México, 04510*
Supporting information and ORCID(s) from the author(s) for this article are available on the WWW under https://doi.org/10.1002/ejic.201800567.

© 2018 Wiley-VCH Verlag GmbH & Co. KGaA, Weinheim

gand-substitution reactions starting from compound **3**. Figure 1 shows the ^{31}P-NMR spectra of the reaction system in [D]chloroform. The uppermost spectrum corresponds to a solution of compound **3** (–35.4 ppm). The addition of a stoichiometric amount of $P(C_6H_5)(C_6F_5)_2$ to this solution yields $P(C_6F_5)_3$ (–76.5 ppm) and forms compound **2** (–8.5 ppm). Further addition of $P(C_6H_5)_2(C_6F_5)$ to the system results in the production of $P(C_6H_5)(C_6F_5)_2$ (–48.1 ppm) and compound **1** (δ =12.4 ppm). Finally, when we added triphenylphosphine to the last-mentioned solution, we detected the formation of [AuCl(PPh_3)] (δ = 31.1 ppm) and $P(C_6H_5)_2(C_6F_5)$ (–25.2 ppm). The coordination of phosphorus to the gold center unshields the ^{31}P nucleus resulting in a signal displaced to low field as compared to the free phosphine, this seems to be a general behavior in phosphine-gold(I) complexes.[22] We performed geometry optimizations of the systems of interest in gas phase and in solution with density functional theory (see the Computational details section). The results indicate that the process of ligand exchange is thermodynamically favored in both phases, and therefore we refer only to the results computed in solution phase in the rest of the paper. Scheme 1 reports the calculated ΔG for the three successive substitution reactions. Additionally, Figure 2 shows a correlation between cumulative ΔG values and the ^{31}P-NMR chemical shift of the product. We note that shielded phosphorus atoms give place to thermodynamically less stable compounds

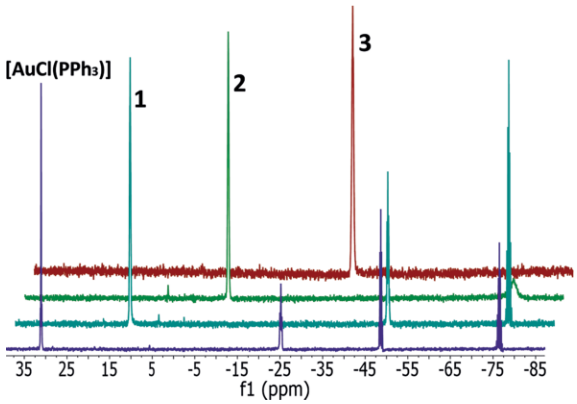

Figure 1. Sequence of phosphine substitution reactions starting with compound **3** (top) monitored by ^{31}P-NMR in $CDCl_3$.

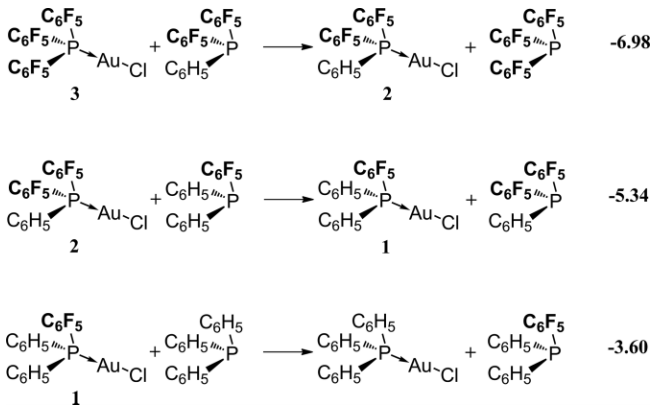

Scheme 1. Calculated ΔG values [kcal/mol] for the consecutive phosphine substitution reactions.

than unshielded P nuclei. this observed trend in stability is consistent with that observed in TGA results (FigureS13–S16 in the SI).

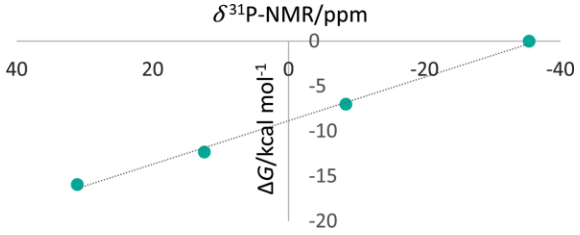

Figure 2. Correlation between the cumulative change in Gibbs free energy associated to the phosphine substitution reactions of Scheme 1 and the ^{31}P-NMR shift of the product. ($CDCl_3$).

The shielding of the ^{31}P nuclei is directly related to the equilibrium electronegativity of the atom in the molecule,[23] a more electronegative phosphorus center is expected to be a worse σ-donor ligand and vice versa, then the shielding on the phosphine P atom will be related to the strength of the Au–P bond to be formed. The weaker the gold phosphorus bond, the easier the substitution of the ligand, as observed for the largest values of ΔG for the substitutions reactions presented in Scheme 1. Moreover, the coordination of the phosphine to gold also increases the shielding of P, and thereby its equilibrium electronegativity, as discussed below.

Figure 3 shows the crystal structures of compounds **1**, **2** and **3**. The three systems show similar conformations. The gold coordination geometry is almost linear and bond angles and distances are similar in the three monomeric units. Selected bond lengths and angles are shown in Table 1. P–Au and Au–Cl dis-

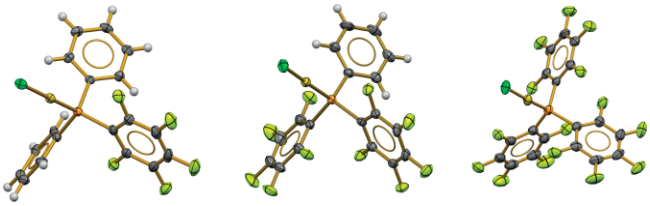

Figure 3. ORTEP diagrams at 50 % probability level of the X-ray structures of compounds **1**–**3**. Colour code: orange, P; golden, Au; green, Cl; gray, C; white, H.

Table 1. Experimental and calculated Au–P and Au–Cl bond lengths along with the P–Au–Cl bond angle for compounds **1**–**3** and [AuCl(PPh_3)].

Compound		D_{Au-P}	D_{Au-Cl}	$\theta_{P-Au-Cl}$
[AuCl(PPh_3)][a]	Exp.	2.228(1)	2.288(1)	179.17
	Calc.	2.2356	2.3069	179.79
1	Exp.	2.224(1)	2.278(1)	178.48
		2.229(1)	2.281(1)	
	Calc.	2.2325	2.3014	179.47
2	Exp.	2.222(1)	2.276(1)	173.75
		2.227(1)	2.280(1)	174.83
	Calc.	2.2277	2.2890	177.83
3[b]	Exp.	2.206(1)	2.269(1)	172.69
		2.215(1)	2.271(1)	176.54
	Calc.	2.2277	2.2890	179.88

[a] Experimental distances reported by Dunstan, 2014[24] and. [b] Chen, 2013.[25]

© 2018 Wiley-VCH Verlag GmbH & Co. KGaA, Weinheim

Table 2. QTAIM analysis of systems **1** to **3**.

Compound	DI	$\rho(\mathbf{r}_{BCP})$	$\nabla^2\rho(\mathbf{r}_{BCP})$	ε	V	G	$\lvert V\rvert/G$	q_{Au}	δ = ^{31}P (ppm)
[AuCl(PPh3)]	1.0597	0.1280	0.0291	0.0006	−0.1500	0.0787	1.91	0.0239	31.1[a]
1	1.0586	0.1284	0.0379	0.0051	−0.1526	0.0810	1.88	0.0538	12.4
2	1.0614	0.1287	0.0488	0.0136	−0.1557	0.0839	1.86	0.0923	−8.5
3	1.0497	0.1284	0.0591	0.0002	−0.1572	0.0860	1.83	0.1289	−35.4
[Au(SCF_3)(PPh_3)]	0.9996	0.1211	0.0455	0.0369	−0.1386	0.0750	1.85	−0.0294	38.1
1a	0.9965	0.1212	0.0544	0.0440	−0.1407	0.0771	1.82	−0.0040	15.7
2a	0.9944	0.1210	0.0647	0.0529	−0.1428	0.0795	1.80	0.0282	1.3
3a	0.9976	0.1213	0.0749	0.0408	−0.1457	0.0822	1.77	0.0590	[a]
[Au(SCH_2CF_3)(PPh_3)]	0.9966	0.1202	0.0546	0.0415	−0.1462	0.0762	1.92	−0.0588	35.94
1b	0.9960	0.1204	0.0627	0.0442	−0.1431	0.0784	1.83	−0.0343	25.86
2b	0.9941	0.1202	0.0728	0.0582	−0.1410	0.0806	1.75	−0.0023	7.82
3b	0.9983	0.1206	0.0822	0.0335	−0.1387	0.0834	1.66	0.0298	[a]
[Au(SC_6F_5)(PPh_3)]	1.0072	0.1221	0.0449	0.0365	−0.1411	0.0761	1.85	−0.0474	35.00
1c	1.0011	0.1216	0.0553	0.0540	−0.1429	0.0783	1.83	−0.0128	20.40
2c	1.0037	0.1218	0.0651	0.0540	−0.1455	0.0809	1.80	0.0196	−3.28
3c	1.0002	0.1215	0.0769	0.0301	−0.1468	0.0830	1.77	0.0485	[a]
[Au($SC_6F_4(CF_3)$-4)(PPh_3)]	1.0068	0.1221	0.0428	0.0366	−0.1408	0.0758	1.86	−0.0347	35.09
1d	1.0048	0.1223	0.0516	0.0324	−0.1429	0.0779	1.83	−0.0110	17.95
2d	1.0028	0.1219	0.0632	0.0535	−0.1453	0.0806	1.80	0.0322	−5.68
3d	1.0013	0.1218	0.0743	0.0302	−0.1467	0.0826	1.78	0.0619	[a]

[a] Compounds **3a**–**d** have not been isolated. [a] Dunstan,2014.[24]

tances are affected by the changes in the fluorination of the phosphine ligand. Both bonds show the same trend with respect to the degree of fluorination of the ligand, i.e. the most fluorinated phosphine results in the shortest bonds. Whilst these changes are rather subtle for the Au–P bond lengths, the corresponding variations for the Au–Cl interaction are more pronounced. These results evidence the different *trans* influence of the phosphines considered in this investigation. The shortest Au–Cl bond corresponds to the most fluorinated phosphine. This effect could result from the diminution of electron density at the Au center indicated by its QTAIM charge (Table 2). This rise in q_{Au} increases gold electrophilicity and it causes that the metallic center attracts electron density from the chlorine atom more efficiently.

The slight variations in the Au–P distances are baffling. The successive changes in Gibbs free energy in Scheme 1 indicate that the most fluorinated phosphine is associated with the weakest Au–P bond. But, in contrast with the common assumption about the relationship between bond length and bond strength (first suggested by Pauling),[26] the Au–P distance does not increase as the Au–P bond becomes weaker. Furthermore the widespread notion that π-acceptor ligands tend to make stronger bonds[27] contrasts with the preference of the gold atom for the worst π-acceptor of the group of ligands. A detailed analysis of systems **1** to **3** using the QTAIM (Table 2) gives valuable insights about the features of the Au–P chemical bonds. First, the value of the electronic density at the Bond Critical Point (BCP) $\rho(\mathbf{r}_{BCP})$ is essentially equal for the four analyzed compounds. Second, the delocalization Index (DI), which is a measure of the number of electron pairs shared by two atoms, decreases slightly with fluorination, indicating a small reduction of the degree of covalency of the bond. Third, $\nabla^2\rho(\mathbf{r}_{BCP})$, increases with the fluorination degree of the ligand (the Laplacian of the electron density being an indicator of the covalent or closed shell character of a bond). Fourth, the relation between the potential ($|V|$) and kinetic energy (G) at the BCP, also indicates that the Au–P bond is intermediate between a covalent and a closed shell interaction. Both parameters [$\nabla^2\rho(\mathbf{r}_{BCP})$ and $|V|/G$] indicate a decrease in the covalent character and a rise of the closed shell nature of the Au–P bond as the degree of fluorination of the ligands is increased. Thus, the lack of change in the Au–P distances could be explained considering that while the covalent character of the bond decreases the coulombic attraction increases maintaining the length of the bond nearly constant.

We observe the same trend concerning the covalent and closed shell features of the Au–P bond in compounds **1a**–**d** and **2a**–**d** with respect to the fluorination degree of the ligands. Our results suggest that this reduction in covalency is related to a decrease in the stability of the examined compounds.

Tong et al.[23] found that there is a good correlation between the ^{31}P-NMR chemical shift and the atomic equilibrium electronegativity of the P atom. This parameter can be estimated as the sum of the group electronegativities of the moieties bonded to phosphorus. The shielding of the P atom increases with the electronegativity of this atom. This behavior is consistent throughout these phosphines and their complexes. We found a good indicator of P equilibrium electronegativity in the QTAIM charge observed in the gold atom. The change of fluorinated electronegative phenyl groups for less electronegative phenyl fragments reduces the equilibrium atomic electronegativity of the P atom. This circumstance influences the electron density distribution of the P–Au bond and this effect can be directly observed on q_{Au}.

Figure 4 shows the plot of the Au atom charge as a function of the ^{31}P-NMR chemical shift for all the investigated compounds. The different colors indicate the distinct anionic li-

© 2018 Wiley-VCH Verlag GmbH & Co. KGaA, Weinheim

gands bonded to gold. The distance between the lines evidences the different *trans* influences of chlorine and fluorothiolate ligands. The difference in the *y*-intercept of the straight lines shown in Figure 4 is produced by the change in the shielding of the phosphorus atom due to the differences of the ligands in *trans* positions. The atomic equilibrium electronegativity of the phosphorus atom is smaller when the anionic ligand is a fluorothiolate as revealed by the low field chemical shift of the phosphorus atom which is related to a less positive charge of the Au atom. This result can be rationalized in view of the larger electron donor character of sulfur with respect to chlorine. Because S provides more electron density to Au, it decreases more markedly the electronegativity of the metal center. Therefore, the P equilibrium electronegativity is reduced as well, a condition which unshields the P nuclei. Small variations are observed within the different thiolate derivatives with changes in the fluorinated moiety since the effect over the ^{31}P nucleus diminishes with the distance between P and R_F groups.

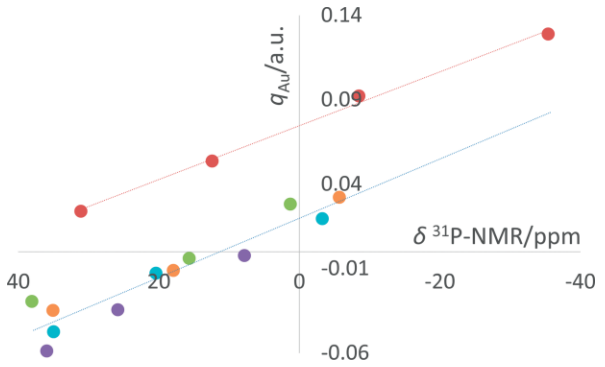

Figure 4. Relation between the gold atom charge and the ^{31}P-NMR chemical shift ($CDCl_3$). Colour code for anionic ligands: red, chloride; green, $^-SCF_3$; purple, $^-SCH_2CF_3$; orange, $^-SC_6F_4(CF_3)$-4; blue, $^-SC_6F_5$.

The Au–P and Au–S distance changes in the crystal structures of compounds **1a** and **1b** (Figure 5) are inconsequential and do not reflect the marked differences observed in the δ = ^{31}P-NMR for these systems. We performed theoretical analyses of the phosphine exchange reactions for the compounds of the type [Au(SR_F)(PPh_F)] in a similar way that it was done for the chlorine adducts. We found that the most stable compounds are formed by the less fluorinated phosphines regardless of the considered thiolate ligand. Additionally, Figure 6 shows the cumulative ΔG of the phosphine substitution reactions for the

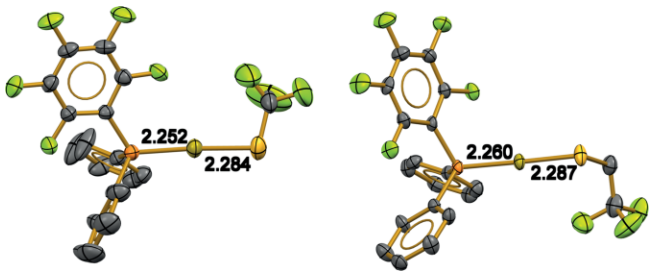

Figure 5. ORTEP diagrams at 40 % probability level of the X-ray structures of compounds **1a** and **1b**. Colour code: orange, P; golden, Au; yellow, S; green, F; gray, C. Hydrogen atoms were omitted for clarity.

different anionic ligands as a function of the ^{31}P-NMR chemical shift. These plots reveal that the exchange of Cl^- for ^-SR_F anionic ligands reduces the stability of the compounds into the same phosphine family. By extrapolating the observed trend for the PPh_3 derivatives, **1a**–**d** and **2a**–**d** to the not isolated compounds **3a**–**d**, we could expect that the stability decreases with respect to that of compound **3** a condition which explains the problematic isolation of these complexes.[64] The introduction of the thiolate groups also decreases the covalent character of the Au–P bond as it can be seen in the values of $\nabla^2\rho(\mathbf{r}_{BCP})$ and $|V|/G$, and hence, the stability of the examined compounds is directly affected by the covalent character of the Au–P bond.

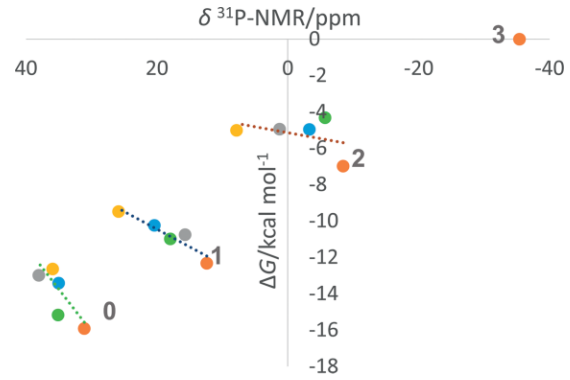

Figure 6. Correlation of ΔG for the phosphine substitution reaction and ^{31}P-NMR chemical shift in $CDCl_3$. The label indicates the phosphine in the data cluster, $P(C_6H_5)_3$ **0**, $P(C_6H_5)_2(C_6F_5)$ **1**, $P(C_6H_5)(C_6F_5)_2$ **2** and $P(C_6F_5)_3$ **3**, [AuX(PPh3)]. The colour code for the anionic ligands is as follows: orange, chloride; gray, $^-SCF_3$; yellow, $^-SCH_2CF_3$; green, $^-SC_6F_4(CF_3)$-4; blue, $^-SC_6F_5$.

The charge of the Au center in the unstable compounds **3a**–**d** is positive. The subsequent reduction of the fluorination degree in the phosphines increases the electronic density over the gold center to the point that Au is slightly negative within triphenylphosphine compounds. The positive charge in the gold atoms of the set **3x** make them good electrophilic centers.

We proceed to discuss now the dissociative or associative nature of the mechanism of substitution of the considered phosphines as shown in Scheme 2. On the one hand, the above-mentioned gold positive charge, the low coordinating nature of the solvent ($CDCl_3$ in the experiment) and the known stability of some three-coordinate gold species[28,29] are factors that support an associative process for the reaction of ligand substitution. Additionally, the dissociation energy of the phosphine from compound **3** has a calculated energetic barrier of 45.2 kcal/mol, a condition which suggests that this process is not plausible under the experimental conditions.[65] These results suggest an associative process in which after the nucleophilic attack of the less fluorinated phosphine, the dissociation of the more fluorinated phosphine (which is less covalently bound to the gold center) occurs, thereby forming the product of the reaction. On the other hand, we did not find NMR evidence of either the three-coordinate species (TCS) related to the associative mechanism or the free phosphine linked to the dissociative mechanism (Spectra available in the SI). We point out that it is possible that the signals of these species could not necessarily be detectable in the case that only a small frac-

© 2018 Wiley-VCH Verlag GmbH & Co. KGaA, Weinheim

tion of the complexes dissociate or the concentration of the TCS intermediary is too low. A rapid equilibrium of the TCS with free and coordinated phosphine would also impair the detection of the first two-mentioned species. Overall, our analysis suggests an associative mechanism but a dissociative process cannot be conclusively discarded.

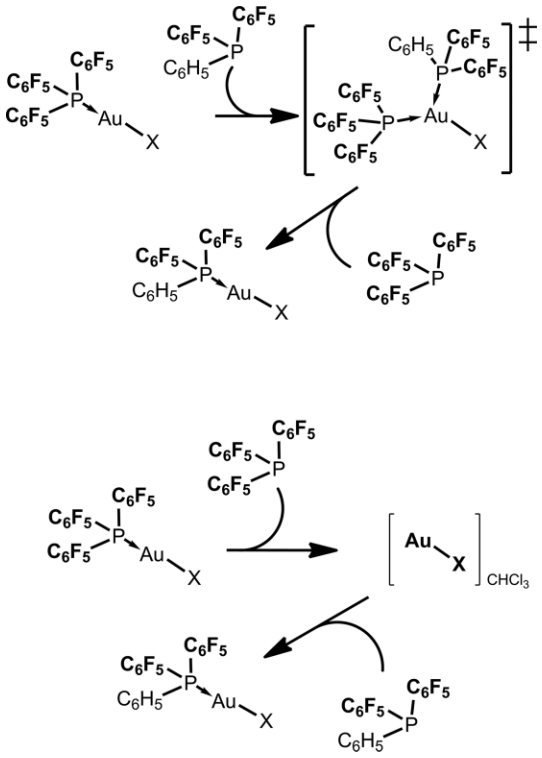

Scheme 2. Proposed associative (top) and dissociative (bottom) mechanisms for the phosphine substitution reaction.

The catalytic activity of gold adducts is strongly influenced by the electronic environment of the Au centers.[1,21,30–34] The results of this investigation indicate that such catalytic activity could be modulated via the fluorination of the ligands. When the shielding of the phosphorus atom rises, the positive charge of the gold atom increases, and the compound becomes more susceptible to suffer nucleophilic attacks in the Au center. These conditions are indicative of an enhanced reactivity of the catalyst, but concomitantly, a decrease in its stability. Conversely, a reduction of the fluorination degree must give more stable compounds resulting in a higher selectivity.

Conclusions

We investigated the stability and *trans* influence in a series of gold compounds bearing fluorinated phosphines and thiolates. A rise in the fluorination degree of the ligands in the compounds shields the P nuclei. This change is related to the increase of the phosphorus equilibrium electronegativity. The change of chlorine for a thiolate changes the ^{31}P-NMR chemical shift to low field due to the *trans* influence of the ligand along the Au–P bond. This influence is evidenced by the observed trends in the QTAIM charge of the gold atom. The electron density topological analyses of the examined systems show that the fluorination of the phosphines and the inclusion of fluorinated thiolate ligands decrease the covalent character of the Au–P bond. This circumstance is related with the loss of stability of the molecules of interest for this work. Overall, the observed variations in the electronic environment of the gold center could be used to modulate the selectivity and activity of the examined systems as potential catalysts via the valuable explanatory power of the QTAIM methodology.

Experimental Section

Instrumentation: Melting points were obtained using a Fisher–Johns apparatus. Infrared spectra were recorded on a Perkin–Elmer FTIR/FIR Spectrum 400 spectrometer in the range of 4000 to 400 cm^{-1} using Attenuated Total Reflectance. Elemental analyses were performed using a Thermo Scientific Flash 2000 Analyser at 950 °C. ^{1}H and ^{13}C NMR spectra were registered on a 9.4 T Varian VNMRS spectrometer while ^{19}F and ^{31}P{^{1}H} NMR were obtained on a 7.0 T Oxford Spectrometer. Chemical shifts are in ppm relative to internal TMS δ = 0 ppm (^{1}H) and to external references of $CFCl_3$ (for ^{19}F) and H_3PO_4 (for ^{31}P) at 0 ppm. *J* values are given in Hz, all spectra were collected from fresh solutions under sealed N_2 atmosphere. Positive-ion fast atom bombardment mass spectrometry spectra were recorded on an MStation JMS-700 mass spectrometer operated at an acceleration voltage of 10 kV. Samples were desorbed from a 3-nitrobenzyl alcohol matrix by 3 keV xenon atoms employing the matrix ions as the reference material.

All thiols and phosphines were purchased from Sigma–Aldrich Co. and used without further purification. Chlorotetrahydrothiophene-gold(I) [AuCl(tht)],[35] [AuCl(PPh$_3$)],[36] [AuCl{P(C$_6$F$_5$)}] (**3**),[25] [Au(SC$_6$F$_5$)(PPh$_3$)][37] and $AgSCF_3$[38] were prepared following the procedures reported in the literature. Lead thiolates[39] were obtained by the reaction of stoichiometrical quantities of lead acetate dissolved in an excess of deionized water with the corresponding thiol dissolved in a small amount of methanol. $AgSCF_3$ is used as source of $^{-}SCF_3$ because the equivalent lead thiolate is unstable.

Synthesis: Because compounds **1** and **2** were synthesized in similar ways, only the synthesis of **1** is explained in detail.

Compound 1 [AuCl{P(C$_6$H$_5$)$_2$(C$_6$F$_5$)}]: 822 mg (2.56 mmol) of [AuCl(tht)] (tht = tetrahydrotiophene) were stirred in 50 mL of dichloromethane at room temperature together with 903 mg (2.56 mmol) of P(C$_6$H$_5$)$_2$(C$_6$F$_5$) for 3 h. The formed colorless solution was reduced in volume to about 5 mL and an excess of hexane was added forming a white powder. Yield 91 % (1.31 g, 2.33 mmol); m.p. 169–171 °C (from hexane/$CHCl_3$). $C_{18}H_{10}AuClF_5P$ (584.66): calcd. C 36.98, H 1.7; found C 37.2, H 2.1. FTIR: $\tilde{\nu}_{max}$ = 534.70 and 688.12 (P–C), 1025.48 (P–Au), 745.05, 1436.54 and 1644.23 (C=C), 979.39, 1093.36, 1478.42 and 1516.93 (C–F), 3055.16 and 3038.06 (C–H$_{ar}$) cm^{-1}. Mass spectrum *M*/*z*: 584 (M^{+}, 5 %), 549 ppm ([Au(PPh$_F$)]$^{+}$, 100). δ ^{19}F (282 MHz. $CDCl_3$; $CFCl_3$): –126.9 (2 F, m, oF), –148.3 (1 F, m, pF), –160.4 ppm (2 F, m, mF); δ^{31}P{^{1}H} (122 MHz, $CDCl_3$, H_3PO_4): 18.6 ppm (1P, t, $^{3}J_{FP}$ = 15.70 Hz, PR_3). Multi-day slow evaporation of solutions of the compound in dichloromethane gave X-ray suitable crystals.

Compound 2 [AuCl{P(C$_6$H$_5$)(C$_6$F$_5$)$_2$}]: 82 % (1.22 g, 1.82 mmol), m.p. 171–173 °C (from hexane/CH_2Cl_2). $C_{18}H_5AuClF_{10}P$ (674.61): calcd. C 30.6, H 0.7; found C 30.9, H 1.1. FTIR: $\tilde{\nu}_{max}$ = 523.51 and 688.84 (P–C), 1025.52 (P–Au), 745.26, 1438.24 and 1644.96 (C=C), 977.73, 1094.20, 1474.94 and 1520.19 (C–F), 3049.79 and 2935.53

© 2018 Wiley-VCH Verlag GmbH & Co. KGaA, Weinheim

(C–H_{ar}) cm^{-1}. Mass spectrum *M/z*: 792 (15 %), 639 ([Au(PPh_F)]$^+$, 100). δ^{19}F (282 MHz. $CDCl_3$; $CFCl_3$): –127.4 (2 F, m, oF), –143.6 (1 F, m, pF), –157.3 ppm (2 F, m, mF); $\delta^{31}P\{^1H\}$ (122 MHz, $CDCl_3$, H_3PO_4): –5.9 ppm (1P, m, PR_3).

[Au(SCF_3)(PPh_3)]: 150 mg (0.256 mmol) of [AuCl(PPh_3)] in 20 mL of dichloromethane and 53.6 mg (0.256 mmol) of $AgSCF_3$ were mixed under continuous stirring in a 50 mL Schlenk flask. After 3 h, the formed white suspension was filtered off to obtain solid, white AgCl and a clear solution whose volume was diminished until about 2 mL by reduced pressure evaporation. An excess of hexane was added to the last-mentioned solution and a white powder was formed. Yield 80 % (114.7 mg, 0.205 mmol), m.p. 109–110 °C. $C_{19}H_{15}AuF_3PS$ (560.32): calcd. C 40.7, H 2.7; found C 40.9, H 2.9. FTIR: $\tilde{\nu}_{max}$ = 689.82 and 997.53 (P–C), 1026.34 (P–Au), 1435.35 and 1479.88 (C=C), 1078.11 br (C–F), 3054.83 and 3073.18 (C–H_{ar}) cm^{-1}. Mass spectrum *m/z*: 459 ([Au(PPh_F)]$^+$, 100 %). δ^1H (400 MHz. $CDCl_3$; TMS) 7.7–7.6 ppm (m, 15 H, PPh_3); δ^{19}F (282 MHz. $CDCl_3$; $CFCl_3$): –19.0 (3 F, s, CF_3); $\delta^{31}P\{^1H\}$ (122 MHz, $CDCl_3$, H_3PO_4): 38.1 ppm (1P, s, PR_3).

Compound 1a [Au(SCF_3){P(C_6H_5)$_2$(C_6F_5)}]: 117 mg (0.2 mmol) of **1** in 20 mL of dichloromethane and 42 mg (0.2 mmol) of $AgSCF_3$ were mixed under continuous stirring in a 50 mL round Schlenk flask under N_2 atmosphere. After 3 h, the formed white suspension was filtered off to obtain solid, white AgCl and a clear solution whose volume was diminished until about 2 mL by reduced pressure evaporation. An excess of hexane was added to the last-mentioned solution and a white powder was formed. Yield 89 %, m.p. 169–171 °C (from hexane/$CHCl_3$). $C_{18}H_{10}AuClF_5P$ (584.66): calcd. C 37.0, H 1.7; found C 37.2, H 2.0. FTIR: $\tilde{\nu}_{max}$ = 534.70 and 688.12 (P–C), 1025.48 (P–Au), 745.05, 1436.54 and 1644.23 (C=C), 979.39, 1093.36, 1478.42 and 1516.93 (C–F), 3055.16 and 3038.06 (C–H_{ar}) cm^{-1}. Mass spectrum *m/z*: 549 ([Au(PPh_F)]$^+$, 17 %). δ^{19}F (282 MHz. $CDCl_3$; $CFCl_3$): –126.9 (2 F, m, oF), –148.3 (1 F, m, pF), –160.4 ppm (2 F, m, mF); $\delta^{31}P\{^1H\}$ (122 MHz, $CDCl_3$, H_3PO_4): 18.6 ppm (1P, t, $^3J_{P-F}$ = 15.7 Hz, PR_3).

Compound 2a [Au(SCF_3){P(C_6H_5)(C_6F_5)$_2$}]: The protocol for the synthesis of this compound is equivalent to that of compound **1a** with the difference that it starts with the mixing of 135 mg of **2** with 42 mg (0.2 mmol) of $AgSCF_3$. Yield 67 % decomposes at 124 °C. $C_{19}H_5AuF_{10}PS$ (683.23): calcd. C 30.8, H 0.7; found C 31.1, H 1.0. FTIR: $\tilde{\nu}_{max}$ = 520.19 and 688.05 (P–C), 741.30, 1439.15 and 1644.19 (C=C), 979.83, 1081.75, 1475.45 and 1522.98 (C–F), 3053.44 and 2965.42 (C–H_{ar}) cm^{-1}. Mass spectrum *m/z*: 741({M + 1}$^+$, 10 %), 639(100), 442(31), 562(4), 936(8), 275(47). δ^{19}F (282 MHz. $CDCl_3$; $CFCl_3$): –20.3(3 F, s, SCF_3), –127.4 (2 F, m, oF), –143.5 (1 F, m, pF), –157.2 ppm (2 F, m, mF); $\delta^{31}P\{^1H\}$ (122 MHz, $CDCl_3$, H_3PO_4): 1.3 ppm (1P, s, PR_3).

Compounds [Au(SR_F)(PPh_3)] [with R_F = CH_2CF_3 and $C_6F_4(CF_3)$-4], **1b**–**d** and **2b**–**d** were synthesized in an analogous way to [Au(SCF_3)(PPh_3)], 1a and 2a respectively but using the corresponding lead thiolates.

[Au(SCH_2CF_3)(PPh_3)]: White powder (146 mg, 88 %). $C_{20}H_{17}AuF_3PS$ (574.35): calcd. C 41.8, H 3.0; found C 41.6, H 3.1. Mass spectrum *m/z*: 459 ([Au(PPh_F)]$^+$, 45 %). δ^1H (400 MHz. $CDCl_3$; TMS) 7.6–7.4 (m, 15 H, PPh_3), 3.5 (q, 2 H, $^3J_{H,F}$ = 9.9 Hz, CH_2), δ^{19}F (282 MHz. $CDCl_3$; $CFCl_3$): –70.8 ppm (3 F, t, $^3J_{F,H}$ = 9.9 Hz, CF_3); $\delta^{31}P\{^1H\}$ (122 MHz, $CDCl_3$, H_3PO_4): 35.9 ppm (1P, s, PPh_3).

[Au($SC_6F_4(CF_3)$-4)(PPh_3)]: White powder (120 mg, 96 %). $C_{25}H_{15}AuF_7PS$ (708.38): calcd. C 42.4, H 2.1; found C 42.3, H 2.1. Mass spectrum *m/z*: 459 ([Au(PPh_F)]$^+$, 28 %). δ^1H (400 MHz. $CDCl_3$; TMS) 7.6 –7.5 (m, 15 H, PPh_3); δ^{19}F (282 MHz. $CDCl_3$; $CFCl_3$): –58.5 to –58.2 (3 F, m, CF_3), –134.2 (2 F, m, oF), –146.8 ppm (2 F, m, mF); $\delta^{31}P\{^1H\}$ (122 MHz, $CDCl_3$, H_3PO_4): 35.1 ppm (1P, s, PPh_3).

Compound 1b [Au(SCH_2CF_3){P(C_6H_5)$_2$(C_6F_5)}]: Yellowish powder (155 mg, 87 %) decomposes at 126 °C. $C_{20}H_{12}AuF_8PS$ (664.30): calcd. C 36.16, H 1.82; found C 35.8, H 1.6. FTIR: $\tilde{\nu}_{max}$ = 526.32 and 692.98 (P–C), 1027.76 (P–Au), 748.91, 1438.37 and 1643.35 (C=C), 979.70, 1090.28, 1477.93 and 1516.84 (C–F), 3077.93 and 2953.43 (C–H_{ar}), 2923.87 (C– H) cm^{-1}. Mass spectrum *M/z*: 665 ({M + 1}$^+$, 10 %), 549 (100), 352 (5), 275 (9), 183 (18). δ^{19}F (282 MHz. $CDCl_3$; CF_3CO_2H): –68.2 (3 F, t, $^3J_{HF}$ = 9.83 Hz, CF_3), –125.9 (2 F, m, oF), –145.2 (1 F, m, pF), –158.0 ppm (2 F, m, mF); $\delta^{31}P\{^1H\}$ (122 MHz, $CDCl_3$, H_3PO_4): 22.0 ppm (1P, s, PR_3).

Compound 1c [Au(SC_6F_5){P(C_6H_5)$_2$(C_6F_5)}]: Yellowish powder (172 mg, 91 %) decomposes at 145 °C. $C_{24}H_{10}AuF_{10}PS$ (748.32): calcd. C 38.52, H 1.35; found C 38.8, H 1.2. FTIR: $\tilde{\nu}_{max}$ = 531.69 and 689.03 (P–C), 1025.43 (P–Au), 740.27, 1437.22 and 1644.41 (C=C), 979.81, 1078.21, 1478.42 and 1523.68 (C–F), 3077.93 and 2958.61 (C– H_{ar}) cm^{-1}. Mass spectrum *m/z*: 748 (M$^+$, 20 %) 549 (100), 472 (6), 275 (25), 199 (28). δ^{19}F (282 MHz. $CDCl_3$; CF_3CO_2H): –132.91 (2 F, m, oF(SC_6F_5)), –162.6 [1 F, m, pF(SC_6F_5)] and –164.6 [2 F, m, mF(SC_6F_5)], –126.2 [2 F, m, oF(C_6F_5)], –145.3 [1 F, m, pF(C_6F_5)], –158.3 ppm [2 F, m, mF(C_6F_5)]; $\delta^{31}P\{^1H\}$ (122 MHz, $CDCl_3$, H_3PO_4): 20.4 ppm (1P, s, PR_3).

Compound 1d [Au{$SC_6F_4(CF_3)$-4}{P(C_6H_5)$_2$(C_6F_5)}]: White powder (172 mg, 84 %) decomposes at 120 °C. $C_{24}H_{10}AuF_{10}PS$ (748.32): calcd. C 37.61, H 1.26; found C 36.85, H 1.19. FTIR: $\tilde{\nu}_{max}$ = 518.01 and 688.22 (P–C), 1025.70 (P–Au), 744.93, 1437.52 and 1644.48 (C=C), 979.57, 1093.84, 1478.22 and 1518.34 (C–F), 3055.81 and 1587.66 (C– H_{ar}) cm^{-1}. Mass spectrum *M/z*: 798 (M$^+$, 3 %), 549 (100), 352 (19), 183 (73). δ^{19}F (282 MHz. $CDCl_3$; CF_3CO_2H): –58.5 (3 F, s, CF_3), –134.4 [2 F, m, oF($SC_6F_4CF_3$)], –146.8 [2 F, m, mF($SC_6F_4CF_3$)], –128.8 [2 F, m, oF(C_6F_5)], –147.5 [1 F, m, pF(C_6F_5)], –160.7 ppm [2 F, m, mF(C_6F_5)]; $\delta^{31}P\{^1H\}$ (122 MHz, $CDCl_3$, H_3PO_4): 18.0 ppm (1P, s, PR_3).

Compound 2b [Au(SCH_2CF_3){P(C_6H_5)(C_6F_5)$_2$}]: Yellowish oil (103 mg, 61 %) air sensitive. Mass spectrum *M/z*: 950 ({M + Au}$^+$, 5 %), 639 (100), 442 (16), 562 (3), 459 (16). δ^{19}F (282 MHz. $CDCl_3$; CF_3CO_2H): –68.4 (3 F, t, J_{HF} = 9.7 MHz, SCF_3), –128.5 [4 F, m, oF(C_6F_5)], –148.8 [2 F, m, pF(C_6F_5)], –159.7 ppm [4 F, m, mF(C_6F_5)]; $\delta^{31}P\{^1H\}$ (122 MHz, $CDCl_3$, H_3PO_4): 7.8 ppm (1P, s, PR_3).

Compound 2c [Au(SC_6F_5){P(C_6H_5)(C_6F_5)$_2$}]: Colorless oil (99 mg, 66 %) air sensitive. Mass spectrum *M/z*: 1035 ({M + Au}$^+$, 7 %), 639 (100). δ^{19}F (282 MHz. $CDCl_3$; CF_3CO_2H): –132.49 [2 F, m, oF(SC_6F_5)], –161.7 [1 F, m, pF(SC_6F_5)], –163.9 [2 F, m, mF(SC_6F_5)], –127.1 [4 F, m, oF(C_6F_5)], –143.5 [2 F, m, pF(C_6F_5)], –157.1 ppm [4 F, m, mF(C_6F_5)]; $\delta^{31}P\{^1H\}$ (122 MHz, $CDCl_3$, H_3PO_4): –3.3 ppm (1P, s, PR_3).

Compound 2d [Au{$SC_6F_4(CF_3)$-4}{P(C_6H_5)(C_6F_5)$_2$}]: Yellowish oil (91 mg, 70 %), air sensitive. Mass spectrum *M/z*: 1085 ({M + Au}$^+$, 5 %), 639 (100). δ^{19}F (282 MHz. $CDCl_3$; CF_3CO_2H): –58.6 (3 F, s, CF_3), –134.5 [2 F, m, oF($SC_6F_4CF_3$)], –146.5 [2 F, m, mF($SC_6F_4CF_3$)], –130.0 [4 F, m, oF(C_6F_5)], –146.5 [2 F, m, pF(C_6F_5)], –160.0 ppm [4 F, m, mF(C_6F_5)]; $\delta^{31}P\{^1H\}$ (122 MHz, $CDCl_3$, H_3PO_4): –5.7 ppm (1P, s, PR_3).

Computational Details: Geometry optimizations were carried out using Density Functional Theory along with the Zeroth Order Regular Approximation Hamiltonian.[40,41] We utilized the combination of the BP86 exchange-correlation functional,[42,43] the def2-TZVP-ZORA basis set[44] and the Grimme's dispersion correction.[45,46] In order to speed up the computations, we consider the RI approximation together with the SARC auxiliary basis set.[47–49] For the solution phase estimations we used the conductor-like polarizable continuum model[50] where the cavities were built using the GEPOL algorithm[51–53] [Selected radii (bohr):Au 2.8029, S 3.0818, P 2.9798,

© 2018 Wiley-VCH Verlag GmbH & Co. KGaA, Weinheim

F 2.2503, C 2.7795, H 1.4566]. We performed all the electronic structure calculations in the ORCA program.[54] This methodology has been successfully employed in the description of metal-metal as well as metal-ligand bonding by others[55–57] and in our own research.[58,59] The Quantum Theory of Atoms in Molecules (QTAIM) methodology was used to investigate the chemical bonding scenario in the examined systems. QTAIM is a wave function analysis approach based on the topology of the charge distribution $\rho(r)$ and results in an exhaustive partition of space into disjoint regions that can be identified with the atoms of chemistry.[60,61] The AIMAll package was used to perform the QTAIM analyses.[62]

CCDC 1587377 (for **1**), 1587378 (for **1a**), 1587379 (for **1b**), and 1587380 (for **2**) contain the supplementary crystallographic data for this paper. These data can be obtained free of charge from The Cambridge Crystallographic Data Centre.

Acknowledgments

We acknowledge the technical support of USAII at the School of Chemistry, UNAM. We are also thankful to DGAPA-UNAM, CONACYT-Mexico and the Spanish Government for funding through the projects IN210818, CB-2012/177498 and CTQ-2015-65790-P respectively, along with PhD scholarships 270993 (G. M. A.) and 381483 (J. M. G. V). We also express our gratitude to DGTIC/UNAM for supercomputer resources (project LANCAD-UNAM-DGTIC-250) together with Rosa Isela del Villar for the NMR facilities and Luis Turcio-García for experimental assistance. We want to acknowledge the comments of the referees of the paper concerning the associative and dissociative nature of the phosphine substitutions discussed herein. The issues raised by these anonymous colleagues were very useful to improve our discussion in this regard.

Keywords: Gold · Phosphine ligands · Fluorine · Thiolates

[1] S.-H. Shin, *Bull. Korean Chem. Soc.* **2005**, *26*, 1925–1926.
[2] C. Nieto-Oberhuber, M. P. Muñoz, S. López, E. Jiménez-Núñez, C. Nevado, E. Herrero-Gómez, M. Raducan, A. M. Echavarren, *Chem. Eur. J.* **2006**, *12*, 1677–1693.
[3] J. Y. Cheong, D. Im, M. Lee, W. Lim, Y. H. Rhee, *J. Org. Chem.* **2011**, *76*, 324–327.
[4] J.-E. Kang, H.-B. Kim, J.-W. Lee, S. Shin, *Org. Lett.* **2006**, *8*, 3537–3540.
[5] J. Schießl, J. Schulmeister, A. Doppiu, E. Wörner, M. Rudolph, R. Karch, A. S. K. Hashmi, *Adv. Synth. Catal.* **2018**, *360*, 2493–2502.
[6] A. C. Shaikh, D. S. Ranade, P. R. Rajamohanan, P. P. Kulkarni, N. T. Patil, *Angew. Chem. Int. Ed.* **2017**, *56*, 757–761; *Angew. Chem.* **2017**, *129*, 775.
[7] J. Kim, W. Jeong, Y. H. Rhee, *Org. Lett.* **2017**, *19*, 242–245.
[8] A. W. McCarter, M. Sommer, J. M. Percy, C. Jamieson, A. R. Kennedy, D. J. Hirst, *J. Org. Chem.* **2018**, acs.joc.8b01121.
[9] J. S. Charlton, D. I. Nichols, *J. Chem. Soc. A* **1970**, *0*, 1484–1488.
[10] D. I. Nichols, *J. Chem. Soc. A* **1970**, *0*, 1216–1217.
[11] H. Schmidbaur, A. Schier, in *Categ. 1, Organometallics* (Ed.: O'Neil), Georg Thieme Verlag, Stuttgart, **2004**, pp. 691–761.
[12] T. G. Appleton, H. C. Clark, L. E. Manzer, *Coord. Chem. Rev.* **1973**, *10*, 335–422.
[13] S. Boonseng, G. Roffe, R. Jones, G. Tizzard, S. Coles, J. Spencer, H. Cox, *Inorganics* **2016**, *4*, 25.
[14] A. O. Ogweno, S. O. Ojwach, M. P. Akerman, *Dalton Trans.* **2014**, *43*, 1228–1237.
[15] H. Niu, R. J. Mangan, A. V. Protchenko, N. Phillips, W. Unkrig, C. Friedmann, E. L. Kolychev, R. Tirfoin, J. Hicks, S. Aldridge, *Dalton Trans.* **2018**, *47*, 7445–7455.
[16] M. Carmona, L. Tejedor, R. Rodríguez, V. Passarelli, F. J. Lahoz, P. García-Orduña, D. Carmona, *Chem. Eur. J.* **2017**, *23*, 14532–14546.
[17] D. Mendola, N. Saleh, N. Vanthuyne, C. Roussel, L. Toupet, F. Castiglione, T. Caronna, A. Mele, J. Crassous, *Angew. Chem. Int. Ed.* **2014**, *53*, 5786–5790; *Angew. Chem.* **2014**, *126*, 5896.
[18] R. Cervantes, J. Tiburcio, H. Torrens, *New J. Chem.* **2015**, *39*, 631–638.
[19] L. Rocchigiani, J. Fernandez-Cestau, I. Chambrier, P. Hrobárik, M. Bochmann, *J. Am. Chem. Soc.* **2018**, *140*, 8287–8302.
[20] A. H. Greif, P. Hrobárik, M. Kaupp, *Chem. Eur. J.* **2017**, *23*, 9790–9803.
[21] A. Y. Sokolov, O. V. Sizova, *Russ. J. Gen. Chem.* **2010**, *80*, 1223–1231.
[22] L. Pazderski, in *Annu. Reports NMR Spectrosc.*, Academic Press, **2013**, pp. 33–179.
[23] J. Tong, S. Liu, S. Zhang, S. Z. Li, *Spectrochim. Acta Part A* **2007**, *67*, 837–846.
[24] S. P. C. Dunstan, P. C. Healy, A. N. Sobolev, E. R. T. Tiekink, A. H. White, M. L. Williams, *J. Mol. Struct.* **2014**, *1072*, 253–259.
[25] H. W. Chen, E. R. T. Tiekink, *Acta Crystallogr., Sect. E Struct. Rep. Online* **2003**, *59*, m50–m52.
[26] L. Pauling, K. S. Pitzer, *J. Am. Chem. Soc.* **1960**, *82*, 4121–4121.
[27] R. H. Crabtree, *The Organometallic Chemistry of the Transition Metals*, Wiley-Interscience, New Jersey, **2005**.
[28] M. C. Gimeno, A. Laguna, *Chem. Rev.* **1997**, *97*, 511–522.
[29] P. Sinha, A. K. Wilson, M. A. Omary, *J. Am. Chem. Soc.* **2005**, *127*, 12488–12489.
[30] D. Zuccaccia, L. Belpassi, A. Macchioni, F. Tarantelli, *Eur. J. Inorg. Chem.* **2013**, *2013*, 4121–4135.
[31] A. S. K. Hashmi, *Angew. Chem. Int. Ed.* **2008**, *47*, 6754–6756; *Angew. Chem.* **2008**, *120*, 6856.
[32] D. Ding, T. Mou, M. Feng, X. Jiang, *J. Am. Chem. Soc.* **2016**, *138*, 5218–5221.
[33] L. Biasiolo, A. Del Zotto, D. Zuccaccia, *Organometallics* **2015**, *34*, 1759–1765.
[34] D. Benitez, N. D. Shapiro, E. Tkatchouk, Y. Wang, W. A. Goddard, F. D. Toste, *Nat. Chem.* **2009**, *1*, 482–486.
[35] T. Mathieson, A. Schier, H. Schmidbaur, *J. Chem. Soc., Dalton Trans.* **2001**, 1196–1200.
[36] J. P. Fackler Jr., B. E. Douglas, S. L. Holt Jr., J. H. Worrell, R. N. Grimes, R. J. Angelici, *Inorganic Syntheses*, John Wiley & Sons, Inc., Hoboken, NJ, USA, **1990**.
[37] E. Delgado, E. Hernandez, *Polyhedron* **1992**, *11*, 3135–3138.
[38] H. J. Emeléus, D. E. MacDuffie, *J. Chem. Soc.* **1961**, *0*, 2572–2600.
[39] M. E. Peach, *Can. J. Chem.* **1968**, *46*, 2699–2706.
[40] E. Van Lenthe, E. J. Baerends, J. G. Snijders, *J. Chem. Phys.* **1993**, *99*, 4597–4610.
[41] C. van Wüllen, *J. Chem. Phys.* **1998**, *109*, 392–399.
[42] M. Levy, J. P. Perdew, *J. Chem. Phys.* **1986**, *84*, 4519–4523.
[43] A. D. Becke, *Phys. Rev. A* **1988**, *38*, 3098–3100.
[44] F. Weigend, R. Ahlrichs, *Phys. Chem. Chem. Phys.* **2005**, *7*, 3297.
[45] S. Grimme, S. Ehrlich, L. Goerigk, *J. Comput. Chem.* **2011**, *32*, 1456–1465.
[46] S. Grimme, J. Antony, S. Ehrlich, H. Krieg, *J. Chem. Phys.* **2010**, *132*, 154104.
[47] O. Vahtras, J. Almlöf, M. W. Feyereisen, *Chem. Phys. Lett.* **1993**, *213*, 514–518.
[48] F. Neese, *J. Comput. Chem.* **2003**, *24*, 1740–1747.
[49] D. A. Pantazis, X.-Y. Chen, C. R. Landis, F. Neese, *J. Chem. Theory Comput.* **2008**, *4*, 908–919.
[50] V. Barone, M. Cossi, *J. Phys. Chem. A* **1998**, *102*, 1995–2001.
[51] J. L. Pascual-ahuir, E. Silla, I. Tuñon, *J. Comput. Chem.* **1994**, *15*, 1127–1138.
[52] E. Silla, I. Tuñón, J. L. Pascual-Ahuir, *J. Comput. Chem.* **1991**, *12*, 1077–1088.
[53] J. L. Pascual-Ahuir, E. Silla, *J. Comput. Chem.* **1990**, *11*, 1047–1060.
[54] F. Neese, *Wiley Interdiscip. Rev. Comput. Mol. Sci.* **2017**, e1327.
[55] L. J. Farrugia, H. M. Senn, *J. Phys. Chem. A* **2010**, *114*, 13418–13433.
[56] L. J. Farrugia, C. Evans, H. M. Senn, M. M. Hänninen, R. Sillanpää, *Organometallics* **2012**, *31*, 2559–2570.
[57] L. C. Forfar, D. Zeng, M. Green, J. E. McGrady, C. A. Russell, *Chem. Eur. J.* **2016**, *22*, 5397–5403.

© 2018 Wiley-VCH Verlag GmbH & Co. KGaA, Weinheim

[58] G. Moreno-Alcántar, J. M. Guevara-Vela, R. Delgadillo-Ruíz, T. Rocha-Rinza, Á. Martín Pendás, M. Flores-Álamo, H. Torrens, *New J. Chem.* **2017**, *41*, 10537–10541.
[59] G. Moreno-Alcántar, K. Hess, J. M. Guevara-Vela, T. Rocha-Rinza, Á. Martín Pendás, M. Flores-Álamo, H. Torrens, *Dalton Trans.* **2017**, *46*, 12456–12465.
[60] R. F. W. Bader, *Acc. Chem. Res.* **1985**, *18*, 9–15.
[61] R. F. W. Bader, *Atoms in Molecules: A Quantum Theory*, Clarendon Press, **1990**.
[62] T. A. Keith, **2016**, *AIMAll* (version 12.06.03) 2016.
[63] R. E. Bachman, S. A. Bodolosky-Bettis, *Z. Naturforsch. B* **2009**, *64*, 1491–1499.
[64] We (Hernández-Toledo, Moreno-Alcántar and Torrens) studied the route of decomposition of compound **3c**. When we tried to synthesize it, a gray insoluble powder was isolated, IR and EA indicate that this product is the polymeric gold(I) thiolate $[Au(SC_6F_5)]_n$.[63] Attempts to synthesize complexes **3a**, **3b** and **3d** give similar results. This indicates that when the degree of fluorination of the phosphine increases, the gold center interacts with the lone pair of sulfur rather than with those of the phosphine, forming a more stable thiolate.
[65] Figure S13 in the SI shows the barriers for dissociation of compounds **2**, **3**, and [AuCl(PPh3)]. Unfortunately, we were not able to compute the corresponding results for compound **1** or the TS structure of the associative mechanism for a suitable comparison.

Received: May 8, 2018

 © 2018 Wiley-VCH Verlag GmbH & Co. KGaA, Weinheim

Capítulo 6

Informe sobre el Factor de Impacto de las Publicaciones Presentadas

En virtud de la actual normativa para estudios de doctorado de la Universidad de Oviedo, las tesis depositadas bajo la modalidad de compendio de publicaciones deben incluir un informe con el factor de impacto de cada una de los artículos que la conforman. En el caso del presente trabajo, las nueve publicaciones aceptadas o enviadas se recogen en 8 revistas científicas indizadas en la base de datos Journal Citation Reports del ISI e incluidas en la categorÃa de revistas de Química Física o de áreas de conocimiento afines. La tabla 6.1 contiene los datos correspondientes.

Tabla 6.1: Datos de las revistas donde se publicaron los artículos resultantes de este trabajo de tesis. Factor de impacto (FI) y ranking para el año de publicación del artículo.

Revista	FI	Categoría	Ranking
Chem. Comm.	6.290	Chemistry - Multidisciplinary	28/170
Chem. Eur. J.	5.160	Chemistry - Multidisciplinary	37/170
Dalton Trans.	4.099	Chemistry - Inorganic and nuclear	6/45
J. Comput. Chem.	3.221	Chemistry - Multidisciplinary	63/170
New J. Chem.	3.201	Chemistry - Multidisciplinary	65/170
ChemPhysChem	2.947	Physics - Atomic, Mol. Chem.	11/37
Eur. J. Inorg. Chem.	2.507	Chemistry - Inorganic and nuclear	14/45
Theor. Chem. Acc.	1.545	Chemistry - Physical	106/146

Bibliografía

[1] R. Xirau, *Introduccion a la Historia de la Filosofia*, UNAM, **2019**.

[2] S. Greenblatt, *The Swerve: How the World Became Modern*, W. W. Norton & Company, **2011**.

[3] S. J. Linden, *The Alchemy Reader: From Hermes Trismegistus to Isaac Newton*, Cambridge University Press, **2003**.

[4] S. Drake, *Galileo at Work: His Scientific Biography*, Dover Publications, **2003**.

[5] N. W. Best, *Found. Chem.* **2015**, *17*, 137–151.

[6] R. Siegfried, *From Elements to Atoms: A History of Chemical Composition (Transactions of the Americal Philosophical Society, Vol. 92, Pt. 4)*, American Philosophical Society, **2002**.

[7] D. Mendelejeff, *Z. Chem.* **1896**, *12*, 405–406.

[8] *Annual Register*, University of Chicago, **1896**.

[9] P. F. Dahl, *Flash of the Cathode Rays: A History of J J Thomson's Electron*, CRC Press, **1997**.

[10] *Nobel Laureates in Chemistry, 1901-1992 (History of Modern Chemical Sciences)*, Wiley-VCH, **1993**.

[11] J. D. Olsen, J. D. Olsen, K. T. McDonald, K. T. McDonald, *Classical Lifetime of a Bohr Atom*, `http://www.physics.princeton.edu/ mcdonald/examples/orbitdecay.pdf`, Fecha de acceso: 2 de abril de 2019.

[12] W. V. der Kloot, *Notes Rec.* **2011**, *65*, 393–410.

[13] D. R. Hartree, W. Hartree, *Proc. Royal Soc. A* **1935**, *150*, 9–33.

[14] L. González, D. Escudero, L. Serrano-Andrés, *ChemPhysChem* **2011**, *13*, 28–51.

[15] G. Schreckenbach, G. A. Shamov, *Acc. Chem. Res.* **2010**, *43*, 19–29.

[16] P. L. A. Popelier in *Intermolecular Forces and Clusters I*, Springer Berlin Heidelberg, **2005**, pp. 1–56.

[17] P. L. A. Popelier, *Applications of Topological Methods in Molecular Chemistry*, Springer International Publishing, **2016**.

[18] A. Szabo, N. S. Ostlund, *Modern Quantum Chemistry: Introduction to Advanced Electronic Structure Theory (Dover Books on Chemistry)*, Dover Publications, **1996**.

[19] I. N. Levine, *Quantum Chemistry*, Prentice Hall, **1999**.

[20] G. B. Arfken, H. J. Weber, F. Harris, *Mathematical Methods for Physicists*, Academic Press, **2000**.

[21] T. Helgaker, P. Jørgensen, J. Olsen, *Molecular Electronic-Structure Theory*, John Wiley & Sons, Ltd, **2000**.

[22] P. Hohenberg, W. Kohn, *Phys. Rev.* **1964**, *136*, B864–B871.

[23] M. Levy, *Proc. Natl. Acad. Sci. USA* **1979**, *76*, 6062–6065.

[24] W. Kohn, L. J. Sham, *Phys. Rev.* **1965**, *140*, A1133–A1138.

[25] A. D. Becke, *J. Chem. Phys.* **1996**, *104*, 1040–1046.

[26] Y. Zhao, D. G. Truhlar, *Theor. Chem. Acc.* **2007**, *120*, 215–241.

[27] R. F. W. Bader, *Atoms in Molecules: A Quantum Theory*, Oxford University Press, **1991**.

[28] C. F. Matta, R. J. Boyd, *The Quantum Theory of Atoms in Molecules: From Solid State to DNA and Drug Design*, Wiley-VCH, **2007**.

[29] R. F. W. Bader, *J. Phys. Chem. A* **1998**, *102*, 7314–7323.

[30] C. F. Matta, J. Hernández-Trujillo, T.-H. Tang, R. F. W. Bader, *Chem.: Eur. J.* **2003**, *9*, 1940–1951.

[31] J. Hernández-Trujillo, C. F. Matta, *Struct. Chem.* **2007**, *18*, 849–857.

[32] J. Poater, M. Solà, F. M. Bickelhaupt, *Chem.: Eur. J.* **2006**, *12*, 2889–2895.

[33] D. Cremer, E. Kraka, *Angew. Chem. Int. Ed.* **1984**, *23*, 627–628.

[34] E. Espinosa, I. Alkorta, J. Elguero, E. Molins, *J. Chem. Phys.* **2002**, *117*, 5529–5542.

[35] X. Fradera, M. A. Austen, R. F. W. Bader, *J. Phys. Chem. A* **1999**, *103*, 304–314.

[36] M. A. Blanco, A. Martín Pendás, E. Francisco, *J. Chem. Theory Comput.* **2005**, *1*, 1096–1109.

[37] E. Francisco, J. L. Casals-Sainz, T. Rocha-Rinza, A. Martín Pendás, *Theor. Chem. Acc.* **2016**, *135*.

[38] E. R. Johnson, S. Keinan, P. Mori-Sánchez, J. Contreras-García, A. J. Cohen, W. Yang, *J. Amer. Chem. Soc.* **2010**, *132*, 6498–6506.

[39] A. Zupan, K. Burke, M. Ernzerhof, J. P. Perdew, *J. Chem. Phys.* **1997**, *106*, 10184–10193.

[40] A. J. Cohen, P. Mori-Sanchez, W. Yang, *Science* **2008**, *321*, 792–794.

[41] J. Contreras-García, E. R. Johnson, S. Keinan, R. Chaudret, J.-P. Piquemal, D. N. Beratan, W. Yang, *J. Chem. Theory Comput.* **2011**, *7*, 625–632.

[42] E. Romero-Montalvo, J. M. Guevara-Vela, W. E. Vallejo Narváez, A. Costales, Á. Martín Pendás, M. Hernández-Rodríguez, T. Rocha-Rinza, *Chemical Communications* **2017**, *53*, 3516–3519.

[43] J. M. Guevara-Vela, E. Romero-Montalvo, A. del Río-Lima, Á. Martín Pendás, tarcos Hernández-Rodríguez, T. Rocha-Rinza, *Chem.: Eur. J.* **2017**, *23*, 16605–16611.

[44] J. M. Guevara-Vela, D. Ochoa-Resendiz, A. Costales, R. Hernández-Lamoneda, Á. Martín Pendás, *ChemPhysChem* **2018**, *19*, 2512–2517.

[45] G. Moreno-Alcántar, K. Hess, J. M. Guevara-Vela, T. Rocha-Rinza, Á. Martín Pendás, M. Flores-Álamo, H. Torrens, *Dalton Trans.* **2017**, *46*, 12456–12465.

[46] G. Moreno-Alcántar, J. M. Guevara-Vela, R. Delgadillo-Ruíz, T. Rocha-Rinza, Á. Martín Pendás, M. Flores-Álamo, H. Torrens, *New J. Chem.* **2017**, *41*, 10537–10541.

[47] G. Moreno-Alcántar, H. Hernández-Toledo, J. M. Guevara-Vela, T. Rocha-Rinza, Á. Martín Pendás, M. Flores-Álamo, H. Torrens, *Eur. J. Inorg. Chem.* **2018**, *2018*, 4413–4420.

[48] J. M. Guevara-Vela, T. Rocha-Rinza, Á. Martín Pendás, *Theor. Chem. Acc.* **2017**, *136*.

[49] J. L. Casalz-Sainz, J. M. Guevara-Vela, E. Francisco, T. Rocha-Rinza, Á. MartínPendás, *ChemPhysChem* **2017**, *18*, 3553–3561.

[50] A. Stone, *The Theory of Intermolecular Forces*, of *International Series of Monographs on Chemistry*, Clarendon Press, **1997**.

[51] K. Müller-Dethlefs, P. Hobza, *Chem. Rev.* **2000**, *100*, 143–168.

[52] J. M. Guevara-Vela, R. Chávez-Calvillo, M. García-Revilla, J. Hernández-Trujillo, O. Christiansen, E. Francisco, Á. Martín Pendás, T. Rocha-Rinza, *Chem.: Eur. J.* **2013**, *19*, 14304–14315.

[53] J. M. Guevara-Vela, E. Romero-Montalvo, V. A. M. Gómez, R. Chávez-Calvillo, M. García-Revilla, E. Francisco, Á. Martín Pendás, T. Rocha-Rinza, *Phys. Chem. Chem. Phys.* **2016**, *18*, 19557–19566.

[54] J. M. Guevara-Vela, E. Romero-Montalvo, A. Costales, Á. Martín Pendás, T. Rocha-Rinza, *Phys. Chem. Chem. Phys.* **2016**, *18*, 26383–26390.

[55] E. Romero-Montalvo, J. M. Guevara-Vela, A. Costales, Á. Martín Pendás, T. Rocha-Rinza, *Phys. Chem. Chem. Phys.* **2017**, *19*, 97–107.

[56] T. Steiner, *Angew. Chem. Int. Ed.* **2002**, *41*, 48–76.

[57] K. Morokuma, C. Muguruma, *J. Amer. Chem. Soc.* **1994**, *116*, 10316–10317.

[58] L. J. Larson, M. Kuno, F.-M. Tao, *J. Chem. Phys.* **2000**, *112*, 8830–8838.

[59] C. E. Kolb, J. T. Jayne, D. R. Worsnop, M. J. Molina, R. F. Meads, A. A. Viggiano, *J. Amer. Chem. Soc.* **1994**, *116*, 10314–10315.

[60] T. Loerting, K. R. Liedl, *Proc. Natl. Acad. Sci. USA* **2000**, *97*, 8874–8878.

[61] B. J. Mhin, S. J. Lee, K. S. Kim, *Phys. Rev. A* **1993**, *48*, 3764–3770.

[62] C. Møller, M. S. Plesset, *Phys. Rev.* **1934**, *46*, 618–622.

[63] T. H. Dunning, *J. Chem. Phys.* **1989**, *90*, 1007–1023.

[64] M. J. Frisch, G. W. Trucks, H. B. Schlegel, G. E. Scuseria, M. A. Robb, J. R. Cheeseman, G. Scalmani, V. Barone, B. Mennucci, G. A. Petersson, H. Nakatsuji, M. Caricato, X. Li, H. P. Hratchian, A. F. Izmaylov, J. Bloino, G. Zheng, J. L. Sonnenberg, M. Hada, M. Ehara, K. Toyota, R. Fukuda, J. Hasegawa, M. Ishida, T. Nakajima, Y. Honda, O. Kitao, H. Nakai, T. Vreven, J. A. Montgomery, Jr., J. E. Peralta, F. Ogliaro, M. Bearpark, J. J. Heyd, E. Brothers, K. N. Kudin, V. N. Staroverov, R. Kobayashi, J. Normand, K. Raghavachari, A. Rendell, J. C. Burant, S. S. Iyengar, J. Tomasi, M. Cossi, N. Rega, J. M. Millam, M. Klene, J. E. Knox, J. B. Cross, V. Bakken, C. Adamo, J. Jaramillo, R. Gomperts, R. E. Stratmann, O. Yazyev, A. J. Austin, R. Cammi, C. Pomelli, J. W. Ochterski, R. L. Martin, K. Morokuma, V. G. Zakrzewski, G. A. Voth, P. Salvador, J. J. Dannenberg, S. Dapprich, A. D. Daniels, Ö.. Farkas, J. B. Foresman, J. V. Ortiz, J. Cioslowski, D. J. Fox, *Gaussian 09 Revision C.1*, Gaussian Inc. Wallingford CT 2009.

[65] T. A. Keith, *AIMAll, Version 16.01.09*, **2016**, TK Gristmill Software, aim.tkgristmill.com.

[66] A. Müller, *Phys. Lett. A* **1984**, *105*, 446–452.

[67] T. Okino, Y. Hoashi, Y. Takemoto, *J. Amer. Chem. Soc.* **2003**, *125*, 12672–12673.

[68] W.-Y. Siau, J. Wang, *Catal. Sci. Technol.* **2011**, *1*, 1298.

[69] X. Fang, C.-J. Wang, *ChemComm* **2015**, *51*, 1185–1197.

[70] Y. Wang, H. Lu, P.-F. Xu, *Acc. Chem. Res.* **2015**, *48*, 1832–1844.

[71] G. S. Hammond, *J. Amer. Chem. Soc.* **1955**, *77*, 334–338.

[72] J. Clayden, N. Greeves, S. Warren, P. Wothers, *Organic Chemistry*, Oxford University Press, **2000**.

[73] J. I. Wu, J. E. Jackson, P. von Ragué Schleyer, *J. Amer. Chem. Soc.* **2014**, *136*, 13526–13529.

[74] J. R. Lane, J. Contreras-García, J.-P. Piquemal, B. J. Miller, H. G. Kjaergaard, *J. Chem. Theory Comput.* **2013**, *9*, 3263–3266.

[75] G. Gilli, F. Bellucci, V. Ferretti, V. Bertolasi, *J. Amer. Chem. Soc.* **1989**, *111*, 1023–1028.

[76] V. Bertolasi, P. Gilli, V. Ferretti, G. Gilli, *J. Amer. Chem. Soc.* **1991**, *113*, 4917–4925.

[77] S. Kossmann, F. Neese, *J. Chem. Theory Comput.* **2010**, *6*, 2325–2338.

[78] F. Neese, *Wiley Interdiscip. Rev. Comput. Mol. Sci.* **2011**, *2*, 73–78.

[79] A. Martín Pendás, E. Francisco, *Promolden. A QTAIM/IQA code (unpublished).*

[80] E. Matito, *ESI-3D: Electron Sharing Indices Program for 3D Molecular Space Partitioning*, **2015**, Institute of Computational Chemistry and Catalysis, University of Girona, Catalonia, Spain.

[81] M. Giambiagi, M. S. de Giambiagi, C. D. dos Santos Silva, A. P. de Figueiredo, *Phys. Chem. Chem. Phys.* **2000**, *2*, 3381–3392.

[82] P. Bultinck, R. Ponec, S. V. Damme, *J. Phys. Org. Chem.* **2005**, *18*, 706–718.

[83] J. Cioslowski, E. Matito, M. Solà, *J. Phys. Chem. A* **2007**, *111*, 6521–6525.

[84] G. R. Desiraju, P. S. Ho, L. Kloo, A. C. Legon, R. Marquardt, P. Metrangolo, P. Politzer, G. Resnati, K. Rissanen, *Pure and Applied Chemistry* **2013**, *85*, 1711–1713.

[85] G. Kerenskaya, I. U. Goldschleger, V. A. Apkarian, K. C. Janda, *J. Phys. Chem. A* **2006**, *110*, 13792–13798.

[86] I. U. Goldschleger, G. Kerenskaya, V. Senekerimyan, K. C. Janda, V. A. Apkarian, *Phys. Chem. Chem. Phys.* **2008**, *10*, 7226.

[87] K. A. Udachin, S. Alavi, J. A. Ripmeester, *J. Phys. Chem. C* **2013**, *117*, 14176–14182.

[88] H. Dureckova, T. K. Woo, S. Alavi, *J. Chem. Phys.* **2016**, *144*, 044501.

[89] R. Franklin-Mergarejo, J. Rubayo-Soneira, N. Halberstadt, K. C. Janda, V. A. Apkarian, *J. Chem. Phys.* **2016**, *144*, 054307.

[90] D. Ochoa-Resendiz, F. A. Batista-Romero, R. Hernández-Lamoneda, *J. Chem. Phys.* **2016**, *145*, 161104.

[91] F. A. Batista-Romero, P. Pajón-Suárez, O. Roncero, R. Hernández-Lamoneda, *J. Chem. Phys.* **2017**, *147*, 154301.

[92] F. A. Batista-Romero, A. Gamboa-Suárez, R. Hernández-Lamoneda, K. C. Janda, *J. Chem. Phys.* **2017**, *146*, 144311.

[93] Á. Martín Pendás, E. Francisco, M. A. Blanco, C. Gatti, *Chem.: Eur. J.* **2007**, *13*, 9362–9371.

[94] A. Martín Pendás, M. A. Blanco, E. Francisco, *J. Chem. Phys.* **2006**, *125*, 184112.

[95] C. A. Gaggioli, G. Ciancaleoni, D. Zuccaccia, G. Bistoni, L. Belpassi, F. Tarantelli, P. Belanzoni, *Organometallics* **2016**, *35*, 2275–2285.

[96] D. J. Gorin, F. D. Toste, *Nature* **2007**, *446*, 395–403.

[97] A. M. Echavarren, *Nat. Chem.* **2009**, *1*, 431–433.

[98] A. M. Echavarren, A. S. K. Hashmi, F. D. Toste, *Advanced Synthesis & Catalysis* **2016**, *358*, 1347–1347.

[99] V. W.-W. Yam, E. C.-C. Cheng, *Chem. Soc. Rev.* **2008**, *37*, 1806.

[100] M. C. Blanco, J. Cámara, M. C. Gimeno, A. Laguna, S. L. James, M. C. Lagunas, M. D. Villacampa, *Angew. Chem. Int. Ed.* **2012**, *51*, 9777–9779.

[101] R. Chaudret, B. de Courcy, J. Contreras-García, E. Gloaguen, A. Zehnacker-Rentien, M. Mons, J.-P. Piquemal, *Phys. Chem. Chem. Phys.* **2014**, *16*, 9876.

[102] M. Alonso, T. Woller, F. J. Martín-Martínez, J. Contreras-García, P. Geerlings, F. De Proft, *Chem.: Eur. J.* **2014**, *20*, 4931–4941.

[103] M. Levy, J. P. Perdew, *J. Chem. Phys.* **1986**, *84*, 4519–4523.

[104] A. D. Becke, *J. Chem. Phys.* **1988**, *88*, 2547–2553.

[105] D. A. Pantazis, X.-Y. Chen, C. R. Landis, F. Neese, *J. Chem. Theory Comput.* **2008**, *4*, 908–919.

[106] E. van Lenthe, E. J. Baerends, J. G. Snijders, *J. Chem. Phys.* **1993**, *99*, 4597–4610.

[107] C. van Wüllen, *J. Chem. Phys.* **1998**, *109*, 392–399.

[108] C. R. Groom, I. J. Bruno, M. P. Lightfoot, S. C. Ward, *Acta Crystallogr. B Struct. Sci. Cryst. Eng. Mater.* **2016**, *72*, 171–179.

[109] J. E. True, T. D. Thomas, R. W. Winter, G. L. Gard, *Inorg. Chem.* **2003**, *42*, 4437–4441.

[110] V. Barone, M. Cossi, *J. Phys. Chem. A* **1998**, *102*, 1995–2001.

[111] O. Vahtras, J. Almlöf, M. Feyereisen, *Chem. Phys. Lett.* **1993**, *213*, 514–518.

[112] F. Neese, *J. Comput. Chem.* **2003**, *24*, 1740–1747.

[113] F. Neese, F. Wennmohs, A. Hansen, U. Becker, *Chem. Phys.* **2009**, *356*, 98–109.

[114] F. Weigend, A. Köhn, C. Hättig, *J. Chem. Phys.* **2002**, *116*, 3175–3183.

[115] S. Kossmann, F. Neese, *Chem. Phys. Lett.* **2009**, *481*, 240–243.

[116] F. Cortés-Guzmán, R. Bader, *Coord. Chem. Rev.* **2005**, *249*, 633–662.

[117] J. Segarra-Martí, M. Merchán, D. Roca-Sanjuán, *J. Chem. Phys.* **2012**, *136*, 244306.

[118] F. Weigend, R. Ahlrichs, *Phys. Chem. Chem. Phys.* **2005**, *7*, 3297.

[119] S. Vancoillie, P. Å. Malmqvist, V. Veryazov, *J. Chem. Theory Comput.* **2016**, *12*, 1647–1655.

[120] X. He, L. Fusti-Molnar, G. Cui, K. M. Merz, *J. Phys. Chem. B* **2009**, *113*, 5290–5300.

[121] C. Gatti, P. J. MacDougall, R. F. W. Bader, *J. Chem. Phys.* **1988**, *88*, 3792–3804.

[122] J. L. McDonagh, M. A. Vincent, P. L. Popelier, *Chem. Phys. Lett.* **2016**, *662*, 228–234.

[123] P. J. Linstrom, W. G. Mallard (Eds.), *NIST Chemistry WebBook, NIST Standard Reference Database Number 69*, National Institute of Standards and Technology, Gaithersburg MD, 20899, **2017**.

[124] P. Jurečka, J. Šponer, J. Černý, P. Hobza, *Phys. Chem. Chem. Phys.* **2006**, *8*, 1985–1993.

[125] M. S. Marshall, L. A. Burns, C. D. Sherrill, *J. Chem. Phys.* **2011**, *135*, 194102.

[126] F. O. Kannemann, A. D. Becke, *J. Chem. Theory Comput.* **2010**, *6*, 1081–1088.

[127] M. W. Schmidt, K. K. Baldridge, J. A. Boatz, S. T. Elbert, M. S. Gordon, J. H. Jensen, S. Koseki, N. Matsunaga, K. A. Nguyen, S. Su, T. L. Windus, M. Dupuis, J. A. Montgomery, *J. Comput. Chem.* **1993**, *14*, 1347–1363.

[128] Q. Sun, T. C. Berkelbach, N. S. Blunt, G. H. Booth, S. Guo, Z. Li, J. Liu, J. McClain, S. Sharma, S. Wouters, G. K.-L. Chan, *The Python-based Simulations of Chemistry Framework (PySCF)*, **2017**. `http://arxiv.org/abs/1701.08223`.

[129] G. K.-L. Chan, D. Zgid in *Annual Reports in Computational Chemistry*, Elsevier, **2009**, pp. 149–162.

[130] G. K.-L. Chan, M. Head-Gordon, *The Journal of Chemical Physics* **2002**, *116*, 4462–4476.

[131] G. K.-L. Chan, *J. Chem. Phys.* **2004**, *120*, 3172–3178.

[132] D. Ghosh, J. Hachmann, T. Yanai, G. K.-L. Chan, *J. Chem. Phys.* **2008**, *128*, 144117.

[133] S. Sharma, G. K.-L. Chan, *J. Chem. Phys.* **2012**, *136*, 124121.

[134] S. Guo, M. A. Watson, W. Hu, Q. Sun, G. K.-L. Chan, *J. Chem. Theory Comput.* **2016**, *12*, 1583–1591.

[135] E. Francisco, A. Martín Pendás, M. A.Blanco, *J. Chem. Phys.* **2007**, *126*, 094102.

[136] E. Francisco, A. Martín Pendás, M. A.Blanco, *The Journal of Chemical Physics* **2009**, *131*, 124125.

[137] I. Ruiz, E. Matito, F. J. Holguín-Gallego, E. Francisco, Á. Martín Pendás, T. Rocha-Rinza, *Theor. Chem. Acc.* **2016**, *135*.

[138] M. J. Allen, D. J. Tozer, *J. Chem. Phys.* **2002**, *117*, 11113–11120.

[139] J. K. Pearson, P. M. Gill, J. M. Ugalde, R. J. Boyd, *Mol. Phys.* **2009**, *107*, 1089–1093.

[140] M. Rodríguez-Mayorga, E. Ramos-Cordoba, X. Lopez, M. Solà, J. M. Ugalde, E. Matito, *ChemistryOpen* **2019**, *8*, 411–417.

[141] D. Rumsfeld, *Known and Unknown: A Memoir*, Sentinel, **2012**.